STUDIES ON THIRD-ORDER NONLINEAR OPTICAL PROPERTIES OF TRANSITION METAL OXIDE THIN FILMS PREPARED BY SOL-GEL METHOD(Dissertation_全文)

AUTHOR(S):

Hashimoto, Tadanori

STUDIES ON THIRD-ORDER NONLINEAR OPTICAL PROPERTIES OF TRANSITION METAL OXIDE THIN FILMS PREPARED BY SOL-GEL METHOD

TADANORI HASHIMOTO

1994

STUDIES ON THIRD-ORDER NONLINEAR OPTICAL PROPERTIES OF TRANSITION METAL OXIDE THIN FILMS PREPARED BY SOL-GEL METHOD

CONTENTS

GENERAL INTRODUCTION

This thesis presents the results of studies on the third-order nonlinear optical properties of transition metal oxide thin films prepared by the sol-gel method. In this study, the third-order nonlinear optical susceptibility, $\chi^{(3)}$, of the sol-gel derived simple and complex oxides containing Ti, V, Nb, Ta, Fe and Pb has been measured by the third-harmonic generation (THG) method and the results have been discussed on the basis of the linear optical properties, microscopic local structures and electronic structures of these oxides.

The present information-carrying capacity of optical communications is limited not only by the transmission of media but also by the speed of electronics. [1] Nonlinear optical devices can switch and process signal in the time range (10^{-15} s) inaccessible to electronics (10^{-12} s) without converting it to electronic form. Such nonlinear optical devices are based on the nonlinear optical phenomena of materials, e.g., change in refractive index and/or absorption coefficient caused by an electric field as will be described below.

Optical response of a material is generally described in the approximation of interaction of electric dipole with the radiation. [2] In this model, the electric field of radiation induces a polarization in the material. When the material is subject to a strong electric field by high power laser, the macroscopic nonlinear polarization of the material, P, can be expressed as a power series in the electric field, E, as follows: [3]

$$P = P_0 + \chi^{(1)} \cdot E + \chi^{(2)} \cdot E \cdot E + \chi^{(3)} \cdot E \cdot E \cdot E + \cdots , \quad (1)$$

where P_0 is the spontaneous polarization of the material, and $\chi^{(1)}$ and $\chi^{(n)}$ ($n \geq 2$) are the linear and nth-order nonlinear optical susceptibilities,

respectively. P, P_0 and E are vectors, and $\chi^{(n)}$ (n≥1) is (n+1)th-rank tensors. Analogously, the microscopic nonlinear polarization of the molecule, p, can be given using permanent dipole moment, μ, and linear polarizability, $\alpha^{(1)}$, and nth-hyperpolarizabilities, $\alpha^{(n+1)}$ (n≥1), as a power series in the electric field.

For diluted media, $\chi^{(n)}$ is related with $\alpha^{(n)}$ as follows: [2]

$$\chi^{(n)} = N\alpha^{(n)} , \tag{2}$$

where N is the number of atoms or molecules per unit volume. In condensed matters, however, the induced dipole-dipole interaction becomes important and leads to the so-called local-field correction. The $\chi^{(n)}$ is no longer simply proportional to $\alpha^{(n)}$ but represented as follows: [2]

$$\chi^{(n)} = f^{(n)}N\alpha^{(n)} , \tag{3-a}$$

and

$$f^{(n)} = \left[\frac{n_{\omega_1}^2+2}{3}\right]\left[\frac{n_{\omega_2}^2+2}{3}\right]\left[\frac{n_{\omega_3}^2+2}{3}\right]\cdots\left[\frac{n_{\omega_n}^2+2}{3}\right] , \tag{3-b}$$

where $f^{(n)}$ is the Lorentz local-field correction factor for $\chi^{(n)}$ and n_{ω_n} the refractive index at ω_n.

The nth-order nonlinear optical susceptibility, $\chi^{(n)}$, is dependent on the frequencies of the interacting lights and complex. Strictly speaking, one should specify the $\chi^{(n)}$ dispersion as $\chi^{(n)}(-\omega_{n+1};\omega_1,\omega_2,\omega_3,\cdots\omega_n)$ ($\omega_{n+1}=\omega_1+\omega_2+\omega_3+\cdots+\omega_n$). This dispersion also cautions one to be careful in comparing the $\chi^{(n)}$ obtained by the various techniques. For example, one measures $\chi^{(3)}(-3\omega;\omega,\omega,\omega)$ by the third-harmonic generation (THG) method and $\chi^{(3)}(-\omega;\omega,\omega,-\omega)$

by the degenerate four-wave mixing (DFWM) method. The complex $\chi^{(3)}$ is observed as follows: [4]

$$\chi^{(3)} = \sqrt{[Re\chi^{(3)}]^2+[Im\chi^{(3)}]^2} . \tag{4}$$

where $Re\chi^{(3)}$ and $Im\chi^{(3)}$ are the real and imaginary parts of the complex $\chi^{(3)}$, respectively. Therefore, the two $\chi^{(3)}$ values measured by the THG and DFWM are not expected to be identical because of the dispersion effect and complex nature. However, a qualitative correlation of the two $\chi^{(3)}$ values serves a purpose to identify if one measured a nonresonant, or real $\chi^{(3)}$.

Some physical processes can contribute to nonlinear optical response: "electronic"-arising from induced distortions of the electron orbit about the nuclei (response time 10^{-14}-10^{-16} s); "nuclear"-optically induced change in the motion of the nuclei (response time 10^{-12} s); "electrostriction"-electric field induced strain (response time 10^{-7}-10^{-9} s) and "thermal"-resulting from absorption (response time 10^{-1} s). [5] Therefore, the determination of response time is very important not only in understanding the origin of optical nonlinearity but also in device applications. The nonresonant optical nonlinearities, which involve only virtual electronic states as intermediate levels for interaction, have the fastest response time limited only by the laser pulse width. However, some resonant optical nonlinearities can also have extremely fast response time, when the exited state relaxation is ultrafast as can be seen for materials such as semiconductor- [6-8] and metal- [9-11] doped glasses.

The influence of the spatial symmetry of material on the (n+1)th-rank nonlinear optical susceptibility tensor, $\chi^{(n)}$, is presented. $\chi^{(n)}$ must be invariant under the symmetry operations that transform it into itself. This yields a number of relations between the components of $\chi^{(n)}$, from which one can extract the independent and non-zero components [2]. A practically

important consequence is that $\chi^{(2n)}$ is zero for material with inversion symmetry, while $\chi^{(2n-1)}$ have non-zero components for all materials ($n \geq 1$). Since the higher-order nonlinear optical susceptibilities than $\chi^{(3)}$ are too small to be observed, second- and third-order nonlinear optical phenomena are significant in practical application. Table 1 summarizes second- and third-order nonlinear phenomena. [5, 12] This thesis concerns third-order nonlinear optical phenomena and the $\chi^{(3)}$ has been determined as $\chi^{(3)}(-3\omega;\omega,\omega,\omega)$ by the THG method.

The THG process is the generation of light at frequency, 3ω, by nonlinear interaction of a material and a laser light at frequency, ω. The THG intensity from a transparent slab, $I_{3\omega}$, can be expressed as follows: [3]

$$I_{3\omega} \propto [\chi^{(3)}]^2 I_\omega^3 \ell^2 \frac{\sin^2\left(\frac{\pi \ell}{2\ell_c}\right)}{\left(\frac{\pi \ell}{2\ell_c}\right)^2}, \qquad (5)$$

where the coherence length, $\ell_c = \lambda/[6(n_{3\omega} - n_\omega)]$, is the distance over which the bound third-harmonic wave and the free third-harmonic wave accumulate a phase-mismatch of π and is regarded as effective interaction path length. The bound third-harmonic wave is a nonlinear electric field in the material, which is oscillating at 3ω that is driven by the fundamental field. Even though its frequency is 3ω, it propagates with the same velocity as the fundamental wave. The free third-harmonic wave at 3ω propagates with a velocity dependent on the refractive index at 3ω. The above expression is appropriate to the case of nonphase-matched THG.

In isotropic materials far from resonance, the refractive index shows normal dispersion, i.e., n_ω increases with increasing frequency, leading to $n_{3\omega}$

Table 1. Second- and third-order nonlinear optical phenomena. (ω=0 indicates the DC electric field.)

Frequencies of incident fields	Frequencies of fields generated by material polarization	Susceptibility	Process or method of measurement
ω_1,ω_2	$\omega_3=\omega_1\pm\omega_2$	$\chi^{(2)}(-\omega_3;\omega_1,\pm\omega_2)$	Three-wave sum and difference-frequency mixing
ω_1	$2\omega_1$	$\chi^{(2)}(-2\omega_1;\omega_1,\omega_1)$	Second-harmonic generation (SHG)
ω_1	0	$\chi^{(2)}(0;\omega_1,-\omega_1)$	Inverse linear electrooptic effect (Optical rectification)
$0,\omega_1$	ω_1	$\chi^{(2)}(-\omega_1;0,\omega_1)$	Linear electrooptic effect (Pockels effect)
ω_1,	$\omega_2,\omega_3(\omega_2+\omega_3=\omega_1)$	$\chi^{(2)}(-\omega_3;\omega_1,-\omega_2)$	Three-wave parametric gain and oscillator
$\omega_1,\omega_2,\omega_3$	$\omega_4=\pm\omega_1\pm\omega_2\pm\omega_3$	$\chi^{(3)}(-\omega_4;\pm\omega_1,\pm\omega_2,\pm\omega_3)$	Four-wave sum and difference-frequency mixing
ω_1	$3\omega_1$	$\chi^{(3)}(-3\omega_1;\omega_1,\omega_1,\omega_1)$	Third-harmonic generation (THG)
ω_1	ω_1	$\chi^{(3)}(-\omega_1;\omega_1,\omega_1,-\omega_1)$	Optical Kerr effect, Degenerate four-wave mixing (DFWM), Time-resolved interferometry (TRI), Two-photon absorption (TPA), Z-scan
ω_1,ω_2	$\omega_3=2\omega_1-\omega_2$	$\chi^{(3)}(-\omega_3;\omega_1,\omega_1,-\omega_2)$	Nearly degenerate three-wave mixing (TWM), Coherent anti-Stokes Raman scattering (CARS)
ω_1	ω_2	$\chi^{(3)}(-\omega_2;\omega_1,-\omega_1,\omega_2)$	Stimulated Raman and Brillouin scattering
$0,\omega_1$	$2\omega_1$	$\chi^{(3)}(-2\omega_1;0,\omega_1,\omega_1)$	Electric field induced second-harmonic generation (EFISH)
$0,\omega_1$	ω_1	$\chi^{(3)}(-\omega_1;0,0,\omega_1)$	Nonlinear electrooptic effect (DC Kerr effect)
$\omega_1,\omega_2,$ ω_1	$\omega_3,\omega_4(\omega_3+\omega_4=\omega_1+\omega_2),$ $\omega_2,\omega_3,\omega_4(\omega_2+\omega_3+\omega_4=\omega_1)$	$\chi^{(3)}(-\omega_4;\omega_1,\omega_2,-\omega_3),$ $\chi^{(3)}(-\omega_4;\omega_1,-\omega_2,-\omega_3)$	Four-wave parametric gain and oscillator

$> n_\omega$. Phase-matching ($n_{3\omega}=n_\omega$) in the THG can be achieved by using the birefringence of uniaxial or biaxial crystal compensated for the dispersion of the refractive index, or by anomalous dispersion associated with a resonance. Anomalous dispersion due to electronic resonances has been used to achieve phase-matched THG in gases [2] and liquids [13].

Measurements of the THG intensity and ℓ_c of a sample in comparison with that for a reference material with known $\chi^{(3)}$ and ℓ_c allow us to determine $\chi^{(3)}$ of the sample. Generally speaking, nonphase-matched THG measurement requires to vary the phase-mismatch, $\Delta\psi$, continuously to extract the maximum THG intensity and ℓ_c from the observed fringe. This can be accomplished easily by rotating a slab sample or by translating a wedged sample. In this thesis, the former is utilized.

For the case of rotating a slab sample, the fringes (often referred to as Maker fringes [14]) become more closely spaced as the rotation angle, θ, is increased, because the sample length increases nonlinearly with the incident angle. The THG intensity of the fringes also decreases with increasing θ, because of the increased reflection loss of the fundamental light at larger incident angles.

The representative third-order nonlinear optical materials include "inorganic crystals" (e.g. PbO [5, 15], TiO_2 [5, 15, 16] AlGaAs/AlAs superlattice [17]), "inorganic amorphous materials" (e.g. TeO_2 [18], chalcogenide glass [19], Au-doped glass [10, 11]) and "organic molecules" (e.g. polyacetylene [20], polydiacetylene [21], C_{60} [22]). So far, $\chi^{(3)}$ data of inorganic crystals are not so sufficient compared with organic molecules and even with inorganic amorphous materials, although it is considered that $\chi^{(3)}$ of oxide crystals is useful for interpreting that of oxide glasses including the corresponding oxide components. Table 2 summarizes the $\chi^{(3)}$ values of oxide crystals and SiO_2 glass often used as standard, which were measured with

Table 2. $\chi^{(3)}$ values of oxide crystals measured with near-infrared fundamental lights by means of various techniques.

Sample	Refractive index	$\chi^{(3)}$ / 10^{-14} esu	Method of measurement	References
MgO	n(1064)=1.72	2.9	TWM (1064)*	16
CaO	n(1064)=1.83	10	TWM (1064)	16
SrO	n(1064)=1.81	9.8	TWM (1064)	16
ZnO	n(1064)=1.96-1.99	48-53	TWM (1064)	16
PbO	n(?)=2.6	1400	DFWM (1064)**	5,15
Al_2O_3	n(1064)=1.75 n(589)=1.77	2.2-2.4 2.0	TWM (1064) TRI (1064)***	16 23
Ga_2O_3	n(1064)=1.96	12	TWM (1064)	16
Y_2O_3	n(1064)=1.92	11	TWM (1064)	16
Er_2O_3	n(1064)=1.96	9.4	TWM (1064)	16
SiO_2	n(1064)=1.53-1.54 n(1064)=1.53-1.54	1.8-2.0 3.8	TWM (1064) THG (1907)****	16 24
SiO_2 glass	n(1064)=1.45 n(589)=1.46 n(636)=1.46	1.3 1.5 2.8	TWM (1064) TRI (1064) THG (1907)	16 23 25
SnO_2	n(530)=2.00-2.11	500	THG (1064)	26
TiO_2	n(1064)=2.48	150 310	TWM (1064) DFWM (1064)	16 5,15
ZrO_2	n(1064)=2.12	13	TWM (1064)	16
$LiNbO_3$	n(633)=2.26	39	TRI (840)	27
$KTaO_3$	n(1064)=2.25	69	TWM (1064)	16
$BeAl_2O_4$	n(1064)=1.73 n(589)=1.74	2.8 1.5	TWM (1064) TRI (1064)	16 23
$MgAl_2O_4$	n(1064)=1.72	2.7	TWM (1064)	16
$CaCO_3$	n(1064)=1.48-1.64	1.3-1.9	TWM (1064)	16
$CaWO_4$	n(1064)=1.89-1.91	8.4-11	TWM (1064)	16
$SrTiO_3$	n(1064)=2.31	66	TWM (1064)	16
β-BaB_2O_4	n(633)=1.63	0.46	THG (1054)	28
$YAlO_3$	n(1064)=1.93	7.0	TWM (1064)	16
$Y_3Al_5O_{12}$	n(1064)=1.82 n(589)=1.84	5.2 6.2	TWM (1064) TRI (1064)	16 23
$Y_3Ga_5O_{12}$	n(1064)=1.91	11	TWM (1064)	16
$Gd_3Ga_5O_{12}$	n(1064)=1.95	12	TWM (1064)	16

The number in parentheses denotes wavelength in nm unit., *: Nearly degenerate three-wave mixing, **: Degenerate four-wave mixing, ***: Time-resolved interferometry, ****: Third-harmonic generation

near–infrared fundamental lights by means of various techniques. [5, 15, 16, 23–28]

There are known several empirical and theoretical models to predict $\chi^{(3)}$ in terms of linear optical properties.

In the visible and near–infrared region, i.e. far from resonances, linear and third–order nonlinear optical susceptibilities are related to each other by Miller's rule [29, 30]

$$\chi^{(3)} = [\chi^{(1)}]^4 \times 10^{-10} \ (esu) \ , \tag{6–a}$$

and

$$\chi^{(1)} = \frac{n^2-1}{4\pi} \ . \tag{6–b}$$

It should be noted that this empirical equation can be used for any types of $\chi^{(3)}$ such as $\chi^{(3)}(-3\omega;\omega,\omega,\omega)$ and $\chi^{(3)}(-\omega;\omega,\omega,-\omega)$ if one considers dependence of $\chi^{(3)}(-\omega_4;\omega_1,\omega_2,\omega_3)$ on frequencies of interacting lights. This prediction suggests that materials with high refractive index have a high third–order nonlinear optical susceptibility, in accordance with more complicated Boling's empirical equation in this respect [31].

One can expect that enhancement in $\chi^{(3)}$ occurs when any frequency of the interacting lights approaches that of a one–, two– or three–photon resonance as in the case shown in Figure 1 as follows: [32]

$$\chi^{(3)}(-3\omega;\omega,\omega,\omega) \propto \frac{N}{\hbar^3} \sum_{gnmn'} \rho(g) F(\omega) \Omega_{gn} \Omega_{nm} \Omega_{mn'} \Omega_{n'g} \ (esu) \ , \tag{7–a}$$

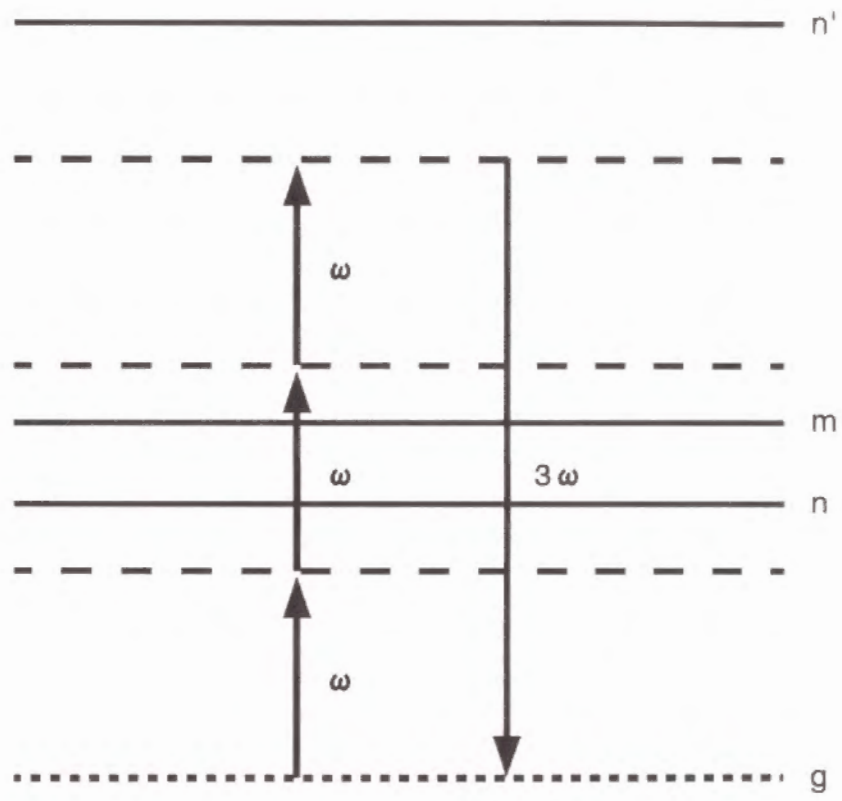

Fig. 1. Schematic representation of third–harmonic generation process. Solid, broken and dotted lines represent exited, virtual and ground states, respectively.

and

$$F(\omega) = \frac{1}{(E_{ng}-3\omega)(E_{mg}-2\omega)(E_{n'g}-\omega)} + \frac{1}{(E_{ng}+\omega)(E_{mg}-2\omega)(E_{n'g}-\omega)} + \frac{1}{(E_{ng}+\omega)(E_{mg}+2\omega)(E_{n'g}-\omega)} + \frac{1}{(E_{ng}+\omega)(E_{mg}+2\omega)(E_{n'g}+3\omega)}, \quad (7\text{-b})$$

where $\rho(g)$, E_{ij} and Ω_{ij} are the density matrix element of fundamental state, the energy difference between states i and j in $\hbar$ ($=h/2\pi$, h: Planck's constant) units and the transition matrix elements, respectively. Some transition metal oxides show *d* electron-derived spectra in the visible region. Therefore, it is expected that $\chi^{(3)}$ may be enhanced by three- photon resonance or near three-photon resonance at 633 nm in this study using near-infrared fundamental light at 1900 nm.

Transition metal oxides are considered to be promising nonlinear optical materials, because most of them meet the above requirements. However, the $\chi^{(3)}$ of transition metal oxides has not been measured so far except $\chi^{(3)}(-\omega;\omega,\omega,-\omega)$ of ZnO, Y_2O_3, TiO_2 and ZrO_2 as shown in Table 2, because most of transition metal oxides are not commercially available in the form of single crystal. Therefore, transparent polycrystalline films are used in this study.

A number of film fabrication techniques such as sol-gel technique, vacuum deposition, sputtering and chemical vapor deposition (CVD) are known. Since the sol-gel method is advantageous for preparing optically transparent oriented and unoriented polycrystalline and amorphous thin films because of low processing temperature, easy coating of large surface and small film thickness [33], this method is applied for preparing transparent polycrystalline films in this study.

Thus, the third-order nonlinear optical properties of transition metal oxides thin films prepared by the sol-gel method are focused on in this study. This study has been undertaken aiming at finding linear optical properties (refractive index and optical band gap, etc.), microscopic local structures (bond length, valence of cation and coordination number, etc.) and electronic structures determining $\chi^{(3)}$ of transition metal oxides using the THG method.

This thesis consists of General Introduction, five Chapters and Summary.

In General Introduction, background and purpose of this study are described.

In Chapter 1, the results of the third-order nonlinear optical properties of TiO_2 thin films are presented. The effects of TiO_2 polymorph (rutile and anatase) and porosity of the TiO_2 films on $\chi^{(3)}$ are discussed. Comparison of the measured $\chi^{(3)}$ with the calculated $\chi^{(3)}$ for TiO_2 polymorphs is given on the basis of three models which relate $\chi^{(3)}$ to linear optical properties. The results of phase-matching for the THG of rutile single crystal (110) are also described from the viewpoint of the practical application in optical devices.

In Chapter 2, the results of the third-order nonlinear optical properties of V_2O_5, Nb_2O_5 and Ta_2O_5 thin films are described. The effect of the local structures (metal-oxygen bond length and valence of cation) on $\chi^{(3)}$ of transition metal oxides with empty *d* orbitals is discussed in comparison with non-transition metal oxides.

In Chapter 3, the results of the third-order nonlinear optical properties of α-Fe_2O_3, γ-Fe_2O_3 and Fe_3O_4 thin films are presented. First, the effects of corundum isomorph (α-Fe_2O_3 and α-Al_2O_3) on $\chi^{(3)}$ are described. Second, $\chi^{(3)}$ of iron oxides (α-Fe_2O_3 and γ-Fe_2O_3) is discussed in terms of superexchange interaction between Fe^{3+} and Fe^{3+} ions though O^{2-} ions.

In Chapter 4, the results of the third-order nonlinear optical properties of $FeTiO_3$ thin films are described. The effect of Fe ions (valence and coordination number) on $\chi^{(3)}$ is discussed in terms of the microscopic second-hyperpolarizability, γ.

In Chapter 5, the results of the third-order nonlinear optical properties of Pb-complex perovskite thin films are presented. Comparison between measured and theoretical $\chi^{(3)}$ is made for complex oxides such as $Pb(Fe_{1/2}Nb_{1/2})O_3$ and $Pb_3Nb_4O_{13}$. Here, the theoretical $\chi^{(3)}$ is calculated based on the second-hyperpolarizabilities of constituent ions which one in turn obtained from $\chi^{(3)}$ of single oxides studied in Chapters 1 to 5.

In Summary, the results of this study described in Chapters 1 to 5 are summarized.

References

[1] E. M. Vogel, *J. Am. Ceram. Soc.*, **72**, 719 (1989).

[2] Y. R. Shen, "The Principles of Nonlinear Optics", John Wiley & Sons, New York (1984).

[3] J. W. Perry, "Materials for Nonlinear Optics, Chemical Perspectives", ed. by S. R. Marder, J. E. Sohn and G. D. Stucky, American Chemical Society, Washington, D. C. (1991) p. 67.

[4] K. S. Wong, S. G. Han and Z. V. Vardeny, *J. Appl. Phys.*, **70**, 1896 (1991).

[5] E. M. Vogel, M. J. Weber and D. M. Krol, *Phys. Chem. Glasses*, **32**, 231 (1991).

[6] R. K. Jain and R. C. Lind, *J. Opt. Soc. Am.*, **73**, 647 (1983).

[7] M. Nogami, K. Nagasaka and M. Takata, *J. Non-Cryst. Solids*, **122**, 101 (1990).

[8] S. Kaneko, H. Nasu, T. Ikegami, J. Matsuoka and K. Kamiya, *Jpn. J. Appl. Phys.*, **31**, 2206 (1992).

[9] D. Ricard, P. Roussignol and C. Flytzanis, *Opt. Lett.*, **10**, 511 (1985).

[10] J. Matsuoka, R. Mizutani, H. Nasu and K. Kamiya, *J. Ceram. Soc. Jpn.*, **100**, 599 (1992).

[11] H. Kozuka and S. Sakka, *Chem. Mater.*, **5**, 222 (1993).

[12] B. S. Wherrett, "Nonlinear Optics", ed. by P. G. Harper and B. S. Wherrett, Academic Press, London (1977) p. 1.

[13] P. P. Bey, J. F. Giuliani and H. Rabin, *IEEE J. Quant. Electron.*, **QE-4**, 932 (1968).

[14] P. D. Maker, R. W. Terhune, M. Nisenoff and C. M. Savage, *Phys. Rev. Lett.*, **8**, 21 (1962).

[15] E. M. Vogel, S. G. Kosinski, D. M. Krol, J. L. Jackel, S. R. Friberg, M. K. Oliver and J. D. Powers, *J. Non-Cryst. Solids*, **107**, 244 (1989).

[16] R. Adair, L. L. Chase and S. A. Payne, *Phys. Rev. B*, **39**, 3337 (1989).

[17] H. Kobayashi, H. Iwamura and K. Kubodera, *J. Appl. Phys.*, **65**, 5202 (1989).

[18] S. H. Kim, T. Yoko and S. Sakka, *J. Am. Ceram. Soc.*, **76**, 2486 (1993).

[19] H. Nasu, K. Kubodera, M. Kobayashi, M. Nakamura and K. Kamiya, *J. Am. Ceram. Soc.*, **73**, 1794 (1990).

[20] F. Krausz, E. Wintner and G. Leising, *Phys. Rev. B*, **39**, 3701 (1989).

[21] T. Kanetake, K. Ishikawa, T. Hasegawa, T. Koda, K. Takeda, M. Hasegawa, K. Kubodera and H. Kobayashi, *Appl. Phys. Lett,*, **54**, 2287 (1989).

[22] J. S. Meth, H. Vanherzeele and Y. Wang, *Chem. Phys. Lett.*, **197**, 26 (1992).

[23] M. J. Weber, D. Milam and W. L. Smith, *Opt. Engng.*, **17**, 463 (1978).

[24] G. R. Meredith, *Phys. Rev. B.*, **24**, 5522 (1981).

[25] G. R. Meredith, B. Buchalter and C. Hanzlik, *J. Chem. Phys.*, **78**, 1533 (1983).

[26] Y. Watanabe, M. Sakai, M. Takata, N. Ueda and H. Kawazoe, *Ferroelectrics*, **131**, 111 (1992).

[27] A. Lattes, H. A. Haus, F. J. Leonberger and E. P. Ippen, *IEEE J. Quant. Electron*, **QE-19**, 1718 (1983).

[28] P. Qiu and A. Penzkofer, *Appl. Phys. B*, **45**, 225 (1988).

[29] C. C. Wang, *Phys. Rev. B*, **2**, 2045 (1970).

[30] R. C. Miller, *Appl. Phys. Lett.*, **5**, 17 (1964).

[31] N. L. Boling, A. J. Glass, A. Owyoung, *IEEE J. Quant. Electron.*, **QE-14**, 601 (1978).

[32] F. Kajzar and J. Messier, "Nonlinear Optical Properties of Organic Molecules and Crystals, **2**", ed. by D. S. Chemla and J. Zyss, Academic Press, New York (1987) p. 51.

[33] S. Sakka and T. Yoko, "Structure and Bonding **77**; Chemistry, Spectroscopy and Applications of Sol-Gel Glasses", ed. by R. Reisfeld and C. K. Jørgensen, Springer-Verlag, Berlin (1992) p. 89.

CHAPTER 1. THIRD-ORDER NONLINEAR OPTICAL PROPERTIES OF TiO_2 THIN FILMS

SECTION 1.1 EFFECT OF TiO_2 POLYMORPH (RUTILE AND ANATASE) ON $\chi^{(3)}$

1. Introduction

A material with high refractive index should exhibit a high third-order nonlinear optical susceptibility, $\chi^{(3)}$, on the basis of Miller's rule [1, 2]. TiO_2 is then considered to be a promising nonlinear optical (NLO) material because of the high refractive index more than 2.5 [3] and high transparency in the visible region. In fact, $\chi^{(3)}$ values of 1.5×10^{-12} esu and 3.1×10^{-12} esu for a TiO_2 single crystal, which were measured by nearly degenerate three-wave mixing (TWM) [4] and degenerate four-wave mixing (DFWM) [5, 6] methods, respectively, have been reported. There are, however, no comparative studies on the third-order nonlinear optical properties of TiO_2 polymorphs except a theoretical study by Lines [7] dealing with the contribution of empty *d* orbital as well as *sp* orbitals to linear and nonlinear optical properties.

In this section, the results of the preparation of TiO_2 thin films of rutile and anatase phases on SiO_2 glass substrates by the sol-gel method and the third-order nonlinear optical properties investigated by the THG method are presented. The effects of TiO_2 polymorph (rutile and anatase) and porosity of the TiO_2 films on $\chi^{(3)}$ are discussed. For TiO_2 polymorphs comparison of $\chi^{(3)}$ between measured and calculated values are given on the basis of three models which relate $\chi^{(3)}$ to linear optical properties.

2. Experimental

2.1 Preparation of TiO_2 Thin Films

TiO_2 thin films were prepared by the sol-gel method. As starting solutions, $Ti(OC_3H_7^i)_4$-*i*-C_3H_7OH-H_2O-$HN(CH_2CH_2OH)_2$ and $Ti(OC_3H_7^i)_4$-*i*-C_3H_7OH-H_2O-HNO_3 solutions were selected for rutile and anatase films, respectively. The chemical compositions of the solutions were 1:20:1:1 and 1:20:1:0.1 in molar ratio, respectively. The difference between these two solutions is whether the solution includes diethanolamine ($HN(CH_2CH_2OH)_2$, DEA) or HNO_3. In the former solution, titanium tetraisopropoxide ($Ti(OC_3H_7^i)_4$, TTIP) was first dissolved in a solution of DEA and half of a prescribed amount of isopropyl alcohol (*i*-C_3H_7OH). Then, the solution was mixed with a solution of H_2O and the remainder of *i*-C_3H_7OH. For the latter solution, TTIP was first diluted by half of a prescribed amount of *i*-C_3H_7OH. Then, the solution was mixed with a solution of HNO_3aq containing a given amount of H_2O and the remainder of *i*-C_3H_7OH. Both coating solutions were allowed to stand at 30 °C for 2 h prior to use.

Dip-coating was used for film formation. A SiO_2 glass substrate was immersed in a coating solution, and pulled up at a rate of 3 cm min^{-1}. The films were heated at 400, 500, 650 or 800 °C for 10 min immediately after each coating procedure. This cycle was repeated 10 times to attain the desired film thickness of ~0.3 μm. To enhance the laser-induced damage threshold (LIDT) [8], a SiO_2 coating was further applied onto the TiO_2 films. Otherwise, a part of TiO_2 films peeled off upon laser irradiation. In the present coating process, films are formed on both surfaces of the SiO_2 glass substrate. The TiO_2 and additional SiO_2 films on one surface were removed afterwards to minimize the interference effect [9] of THG lights in the THG measurement.

2.2 Characterization of TiO_2 Thin Films

The crystalline phases precipitated in the TiO_2 thin films were identified by X-ray diffraction method using CuKα radiation. The refractive indices of TiO_2 films were determined by an ellipsometer in the wavelength region

from 500 to 1000 nm. The ellipsometry measurement also gave the film thickness. The absorption spectra of TiO_2 films with and without additional SiO_2 coating were measured in the wavelength region from 200 to 2000 nm by a UV-visible spectrophotometer.

THG measurements of TiO_2 thin films were made by means of a nonlinear optical measurement apparatus (Tokyo Instruments, Inc., Tokyo, Japan). The Q-switched Nd:YAG laser was operated at the fundamental wavelength of 1064 nm with a pump pulse duration of 10 ns and a peak power density of 200 MW cm^{-2}. The laser frequency at 1900 nm was obtained directly by stimulated Raman scattering in a high pressure hydrogen cell, which was excited by the Nd:YAG line at 1064 nm. The THG light at 633 nm, which was isolated by a monochromator, was detected by a photomultiplier connected to a box-car integrator. The sample was mounted on a goniometer and rotated at 0.25° intervals from −40 to +40° by a computer-controlled stepper motor with respect to the axis perpendicular to the incident light.

In both absorption spectrum and THG measurements, the samples were irradiated from the side without films.

3. Results

3.1 Crystallization Behavior

Figure 1 shows the X-ray diffraction patterns of TiO_2 thin films prepared from solutions containing (a) DEA and (b) HNO_3 by the sol-gel method. The crystalline phases precipitated in the sol-gel derived rutile and anatase thin films were identified referring to JCPDS-FILE 21-1276 (tetragonal) and 21-1272 (tetragonal), respectively. Preferable orientation is not seen for rutile and anatase films. The films prepared from a solution containing DEA were amorphous below 500 °C, and consisted of a mixture

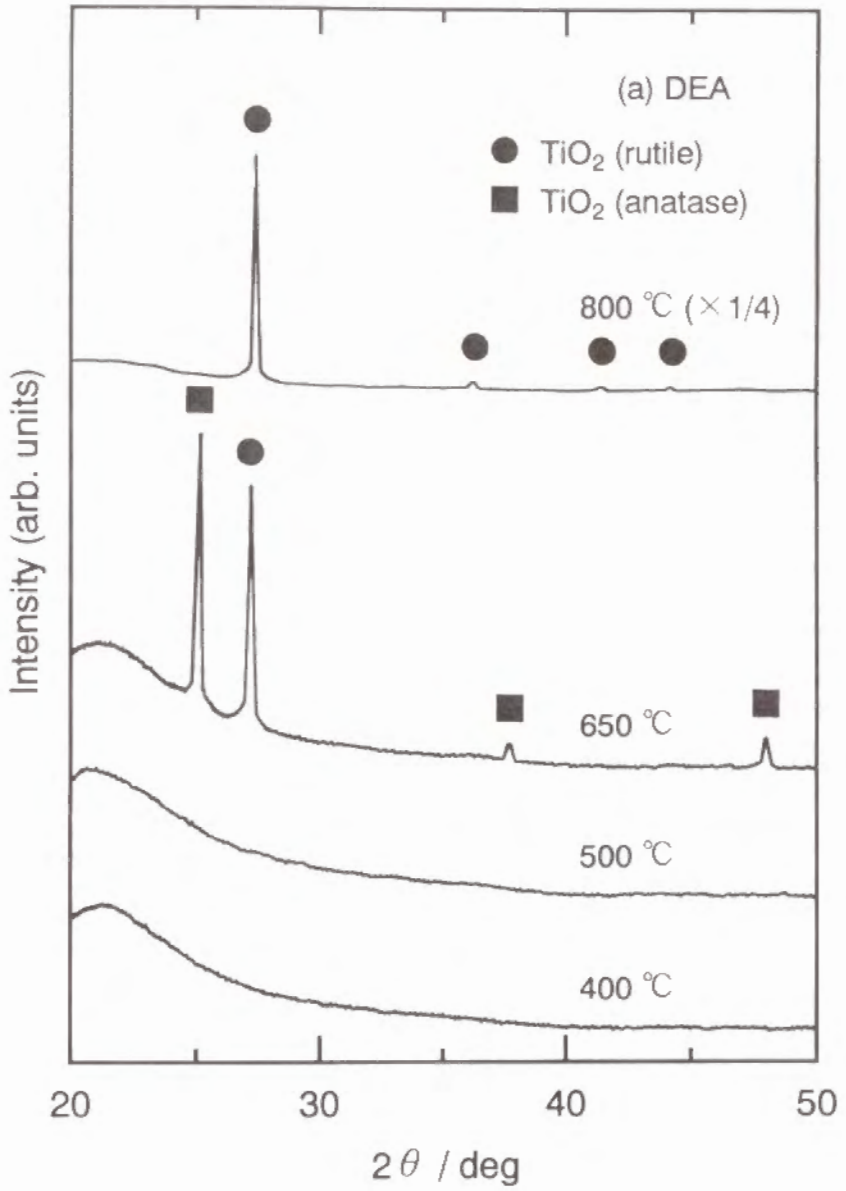

Fig. 1(a). X-ray diffraction patterns of TiO_2 thin films prepared from solutions containing DEA by the sol-gel method.

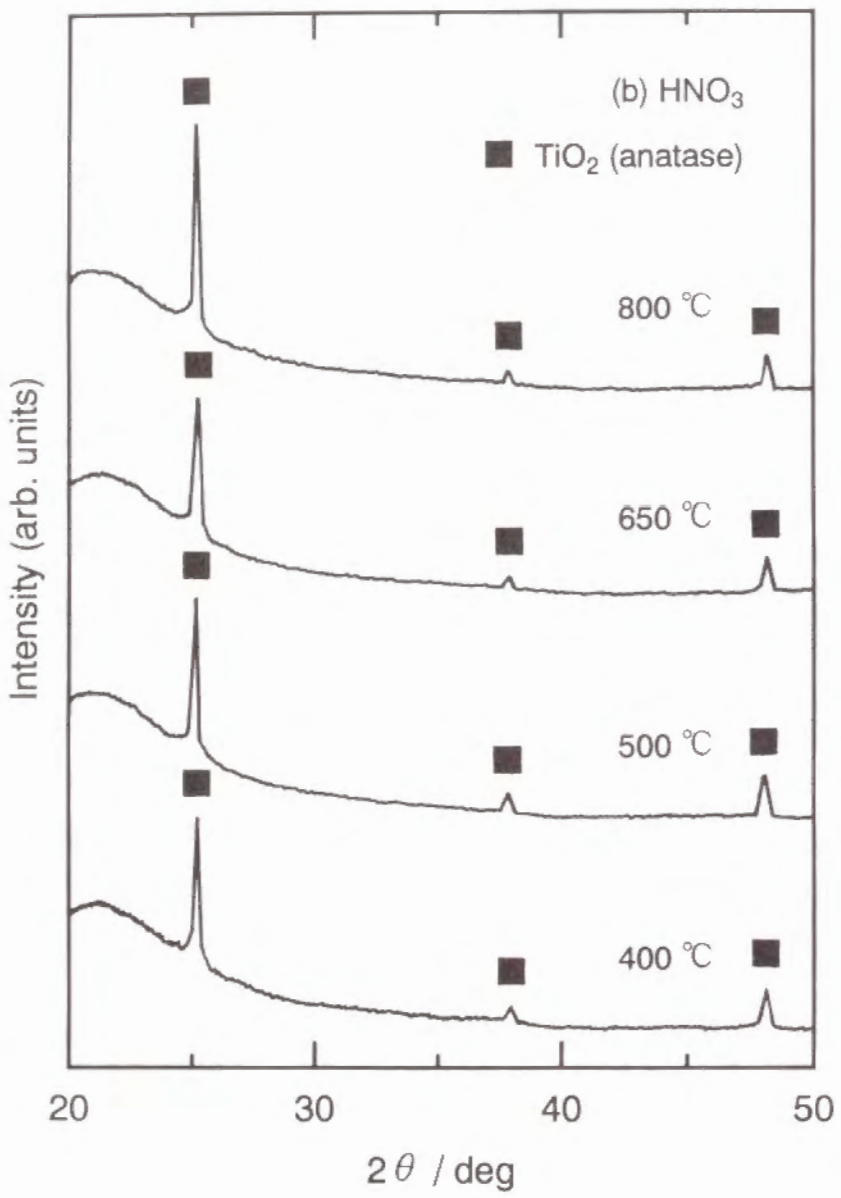

Fig. 1(b). X-ray diffraction patterns of TiO_2 thin films prepared from solutions containing HNO_3 by the sol-gel method.

of anatase and rutile phases at 650 °C and a single phase of rutile at 800 °C. On the other hand, the films prepared from a solution containing HNO_3 were crystallized into a single phase of anatase at 400 °C and no changes in the crystalline phase and the X-ray diffraction peak intensity were seen above 500 °C. The crystallite sizes in the TiO_2 films prepared from the solutions containing DEA and HNO_3 were 40-45 nm and 35-40 nm, respectively.

Rutile and anatase films which were prepared by heating at 800 °C were selected for measurements of various optical properties.

3.2 Refractive Index and Optical Transmittance

The wavelength dependencies of refractive index, n, for TiO_2 thin films are shown in Figure 2. It is seen that the refractive indices of both TiO_2 films decrease with increasing wavelength and the refractive index of rutile films is higher than that of anatase films as well known. Figure 3 presents linear plots of $(n^2-1)^{-1}$ versus E^2 for TiO_2 thin films based on Wemple's equation [10]

$$\frac{1}{n^2-1} = \frac{E_0}{E_d} - \frac{E^2}{E_0 E_d}, \qquad (1)$$

where E, E_0 and E_d are the photon energy, the average oscillator energy and dispersion energy in eV unit, respectively. E_0 and E_d are important optical properties of materials [10]. The refractive indices were estimated as $n_{3\omega}$= 2.40 at 633 nm and n_ω=2.27 at 1900 nm, and the coherence length, ℓ_c=1.9/[6($n_{3\omega}$-n_ω)], was 2.3 μm for the rutile films. In a similar manner, $n_{3\omega}$, n_ω and ℓ_c for the anatase films were estimated as 2.29, 2.16 and 2.4 μm, respectively. The thickness of the TiO_2 films obtained by 10 dippings was typically 0.30-0.35 μm.

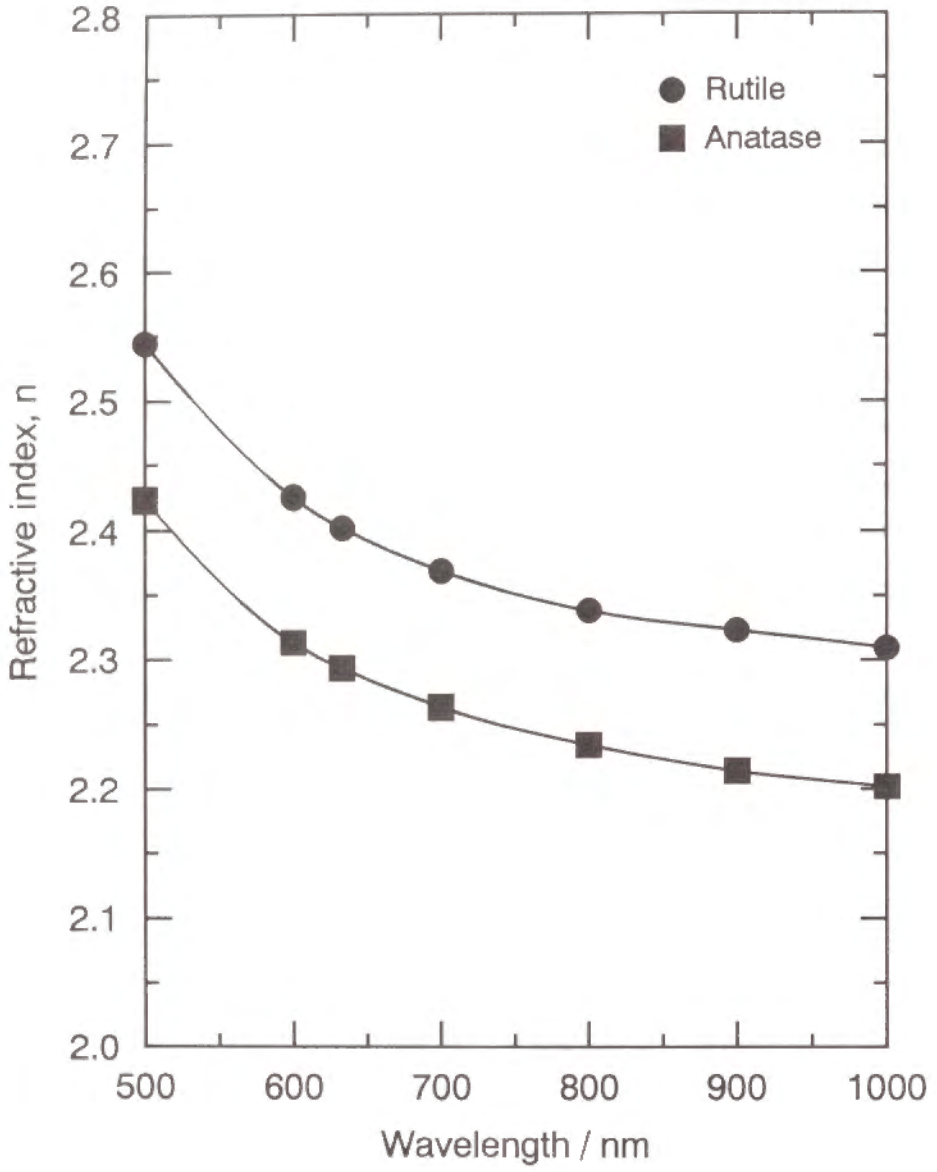

Fig. 2. Wavelength dependencies of refractive index, n, for TiO_2 thin films.

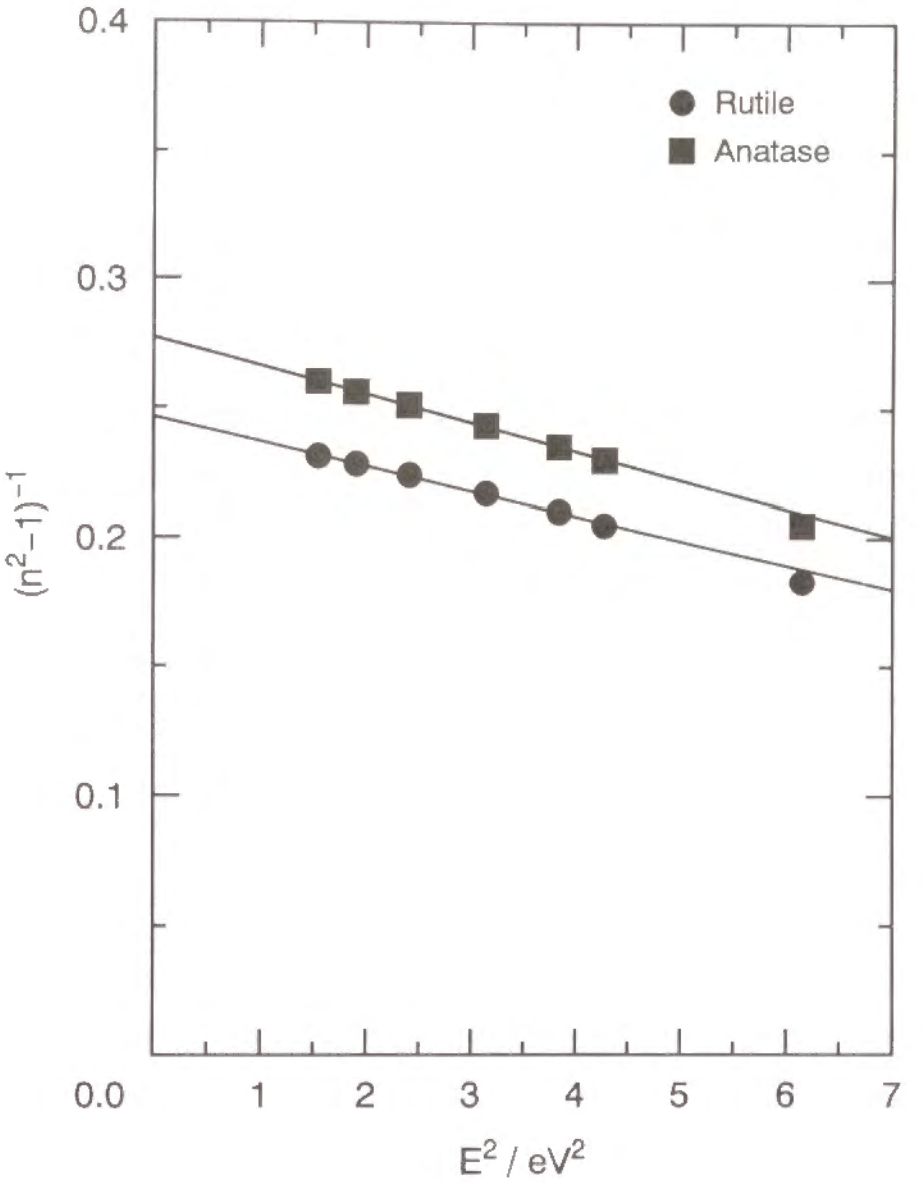

Fig. 3. Linear plots of $(n^2-1)^{-1}$ versus E^2 for TiO_2 thin films.

From refractive indices, n_s and n_p, of single crystals [3, 11] and porous thin films, the porosities, p, of both TiO_2 films can be estimated as follows [12]:

$$p = \left(1 - \frac{n_p^2 - 1}{n_s^2 - 1}\right) \times 100 \ (\%) \ , \tag{2-a}$$

and

$$n_s = \sqrt[3]{n_o^2 n_e} \ , \tag{2-b}$$

where n_s corresponds to a radius of refractive index sphere having the same volume as that of a refractive index ellipsoid with the two n_o radii and one n_e radius (o: ordinary ray, e: extraordinary ray) for uniaxial crystals such as rutile and anatase. The porosities of rutile and anatase films were estimated as 22.6 and 19.9 %, respectively.

Figure 4 shows the absorption spectra of TiO_2 thin films with and without additional SiO_2 coating. All spectra have a number of mountains and troughs arising from the interference of light. The larger amplitude of interference spectra of rutile films compared with anatase films results from the higher refractive index of the former. It is seen that the additional SiO_2 coating reduces the optical loss due to reflection especially in the wavelength region above ~400 nm. The optical band gaps, E_g, of rutile and anatase films were estimated to be 3.0 and 3.2 eV, respectively, corresponding to an energy between the conduction band, which predominantly has a Ti 3*d* character, and the O 2*p* valence band [13]. These values are in good accordance with those

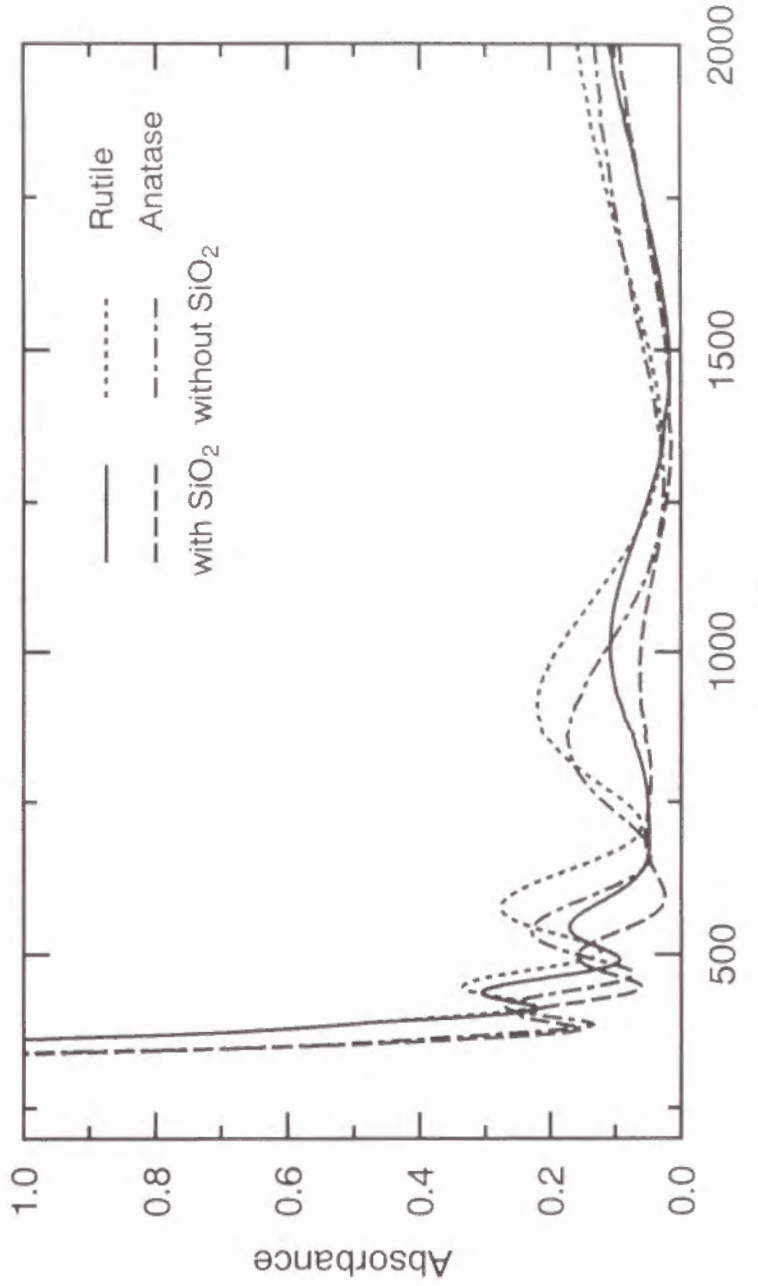

Fig. 4. Absorption spectra of TiO_2 thin films with and without additional SiO_2 coating.

reported previously [14].

3.3 Evaluation of $\chi^{(3)}$ Values

The THG intensities as a function of the rotation angle are given for (a) rutile films, (b) anatase films and (c) SiO_2 glass in Figure 5. The THG intensity patterns of both TiO_2 films clearly show the interference between the THG lights from TiO_2 films and SiO_2 glass substrate as previously reported [9]. The THG intensity was obtained by the least squares method as solid line in Fig. 5.

In the present study, $\chi^{(3)}$ values were determined by the equation [15]

$$\chi^{(3)}_{film} = \frac{2}{\pi}\chi^{(3)}_{SiO_2}\frac{\ell_{c,\,SiO_2}}{\ell}\sqrt{\frac{I_{3\omega,\,film}}{I_{3\omega,\,SiO_2}}}\sqrt{\frac{n^3_{\omega,\,film}n_{3\omega,\,film}T^3_{\omega,\,SiO_2}T_{3\omega,\,SiO_2}}{n^3_{\omega,\,SiO_2}n_{3\omega,\,SiO_2}T^3_{\omega,\,film}T_{3\omega,\,film}}}\ (esu)\ , \qquad (3)$$

where I denotes the THG peak intensity. The film thickness is used for ℓ, because the film thickness is less than the coherence length. The values of $\chi^{(3)}_{SiO_2}=2.8\times10^{-14}$ esu and $\ell_{c,SiO_2}=18.1\ \mu$m were used for SiO_2 glass as both standard sample and substrate [16].

The intensity of THG signal generated from TiO_2 films was determined by the equation [9]

$$I_{film} = \frac{I_{max}+I_{min}}{2} - \frac{I_{substrate}}{2} = \frac{I_{max}+I_{min}}{2} - \frac{I_{SiO_2}}{2}\ , \qquad (4)$$

where I_{max} and I_{min} are the upper and lower envelopes of the superimposed THG intensity pattern. The THG light from the additional SiO_2 coating on the TiO_2 films was neglected, because the $\chi^{(3)}_{SiO_2}$ is low and the thickness of SiO_2 coating (less than ~0.2 μm) is much smaller than the coherence length.

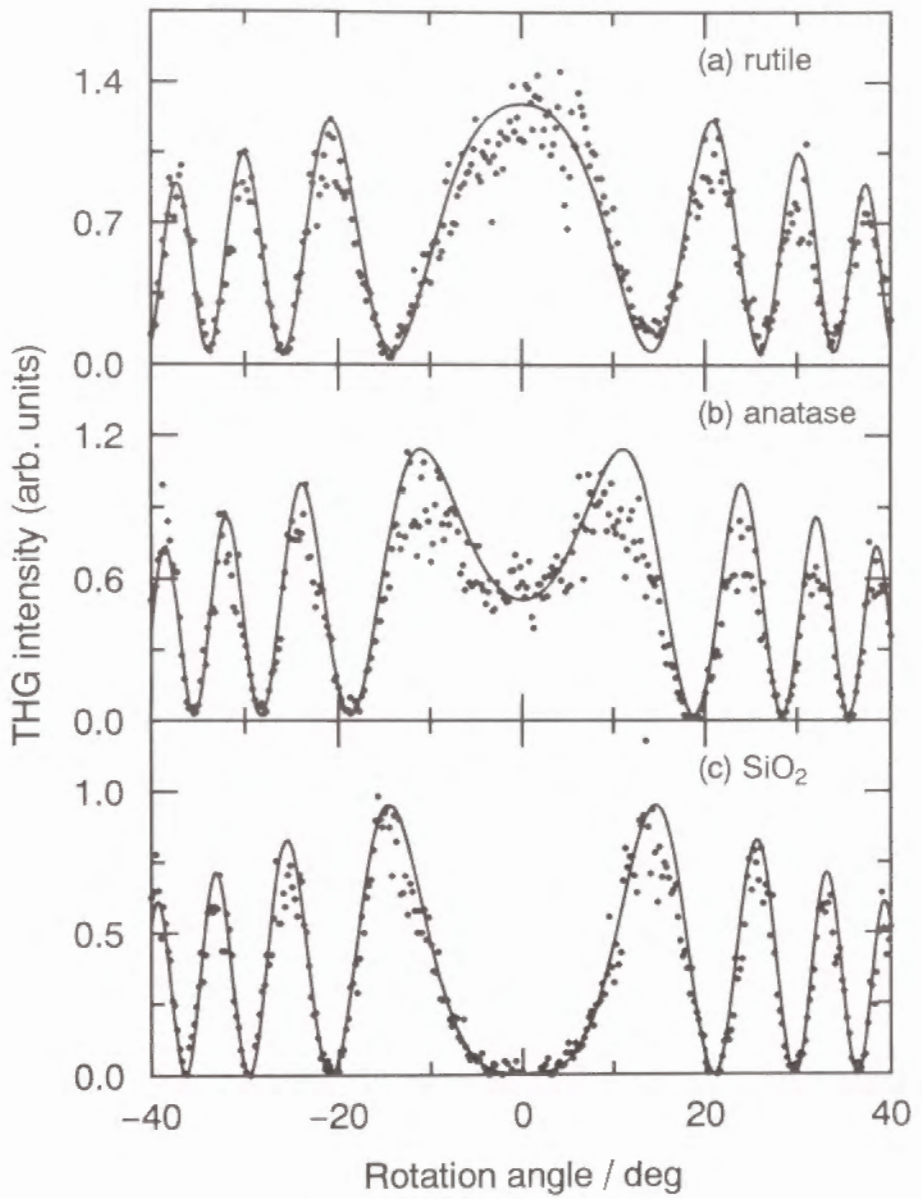

Fig. 5. THG intensities as a function of rotation angle for (a) rutile films, (b) anatase films and (c) SiO_2 glass. Solid curves are computed using the least squares method.

The $\chi^{(3)}$ values of rutile and anatase films were determined to be 1.4×10^{-12} and 9.7×10^{-13} esu, respectively. Table 1 summarizes the optical properties of TiO_2 thin films.

The accuracy of the present THG measurement for thin film samples is estimated to be $\chi^{(3)}\ell=3\times10^{-13}$ esu μm from the weakest THG intensity that can be resolved into two components of films and substrate. This value agrees with the value of 3×10^{-13} esu μm reported by Kubodera et at. [9].

4. Discussion

Rutile [3] and anatase [11] have values of ~0.3 and –0.1, respectively, for the birefringence, $\Delta n=n_e-n_o$. This means that TiO_2 has a large optical anisotropy. However, in the present sol–gel derived TiO_2 thin films crystallites are very small in size and randomly oriented, as seen in Fig. 1, and so the films can be regarded as almost optically isotropic material. Therefore, the present analysis and interpretation concerning the refractive index and $\chi^{(3)}$ are made based on the isotropic values.

4.1 Relation between $\chi^{(3)}$ and Refractive Index, n

It is possible to estimate $\chi^{(3)}$ of a material from refractive index, n, according to Miller's rule [1, 2]

$$\chi^{(3)} = [\chi^{(1)}]^4\times10^{-10}\ (esu)\ , \tag{5–a}$$

and

$$\chi^{(1)} = \frac{n^2-1}{4\pi}\ . \tag{5–b}$$

Table 1. Optical properties of TiO_2 thin films.

Compound	$n_{3\omega}$	n_ω	$T_{3\omega}$ / %	T_ω / %	E_0 / eV	E_d / eV	E_g / eV	p / %	$\frac{I_{3\omega,film}}{I_{3\omega,SiO_2}}$	ℓ_c / μm	ℓ / μm	$\chi^{(3)}$ / esu
Rutile	2.40 (2.68)	2.27 (2.53)	86.5	81.0	5.1 (5.2)	20.7 (27.6)	3.0	22.6	0.22	2.3	0.35	1.4×10^{-12}
Anatase	2.29 (2.51)	2.16 (2.40)	91.3	82.6	5.0 (5.7)	18.1 (26.6)	3.2	19.9	0.10	2.4	0.30	9.7×10^{-13}

The physical meanings of all the notations in the table are described in the section 3.

Transmittances are values of TiO_2 thin films with additional SiO_2 coating.

The data in parentheses are the values of single crystals calculated by Wemple's equation under the isotropic assumption.

The $\chi^{(3)}$ values of 1.2×10^{-12} and 7.3×10^{-13} esu, which are predicted by Miller's rule for rutile and anatase thin films, respectively, as in the third row of Table 2, are in good accordance with the measured $\chi^{(3)}$ values, 1.4×10^{-12} and 9.7×10^{-13} esu, as in the first row.

Since the present sol–gel derived TiO_2 thin films are porous in nature, it is of essence to estimate the $\chi^{(3)}_{dense}$ values of hypothetical dense films corrected for porosity, p. This can be accomplished by combining Eqs. (2) and (5) as follows:

$$\chi^{(3)}_{dense} = \chi^{(3)}_{porous}\left(\frac{100}{100-p}\right)^4 (esu) \ . \qquad (6)$$

The $\chi^{(3)}_{dense}$ values of 4.0×10^{-12} and 2.4×10^{-12} esu for rutile and anatase dense films, respectively, as in the second row of Table 2 are ~100 times as high as $\chi^{(3)}$ of SiO_2 glass as standard sample, 2.8×10^{-14} esu. The $\chi^{(3)}_{dense}$ value of rutile is in reasonable accordance with $\chi^{(3)}(-\omega;\omega,\omega,-\omega)$ of 1.5×10^{-12} esu (TWM) [4] and 3.1×10^{-12} esu (DFWM) [5, 6] reported previously if one assumes that the $\chi^{(3)}(-\omega;\omega,\omega,-\omega)$ corresponds to $\chi^{(3)}(-3\omega;\omega,\omega,\omega)$ obtained by the THG method.

Figure 6 shows a relation between $\chi^{(3)}$ and refractive index, n_ω, at 1900 nm for TiO_2 thin films and other nonlinear optical materials reported so far [15–22]. It is seen that inorganic materials with high refractive index inherently exhibit high optical nonlinearity.

The $\chi^{(3)}$ values of organic polymers such as polydiacetylene (PDA) [20] and poly(2,5–dimethoxy *p*–phenylene vinylene) (MO–PPV) [21] deviate from the relation to a considerable extent, due to the enhancement by the so–called three–photon resonance or near three–photon resonance [23]. Since the measured $\chi^{(3)}$ includes the significant contribution of the imaginary part, there

Table 2. Comparison of the measured $\chi^{(3)}$ with the calculated $\chi^{(3)}$ for TiO_2 thin films on the basis of three models.

	$\chi^{(3)}$ / esu	
	Rutile	Anatase
Measured value (porous)	1.4×10^{-12}	9.7×10^{-13}
Corrected value (dense)	4.0×10^{-12}	2.4×10^{-12}
Miller's rule (porous)	1.2×10^{-12}	7.3×10^{-13}
Miller's rule (dense)	3.4×10^{-12}	2.1×10^{-12}
Band gap model	3.4×10^{-12}	2.3×10^{-12}
Lines' model (porous)	2.3×10^{-12}	1.7×10^{-12}
Lines' model (dense)	4.7×10^{-12}	2.7×10^{-12}

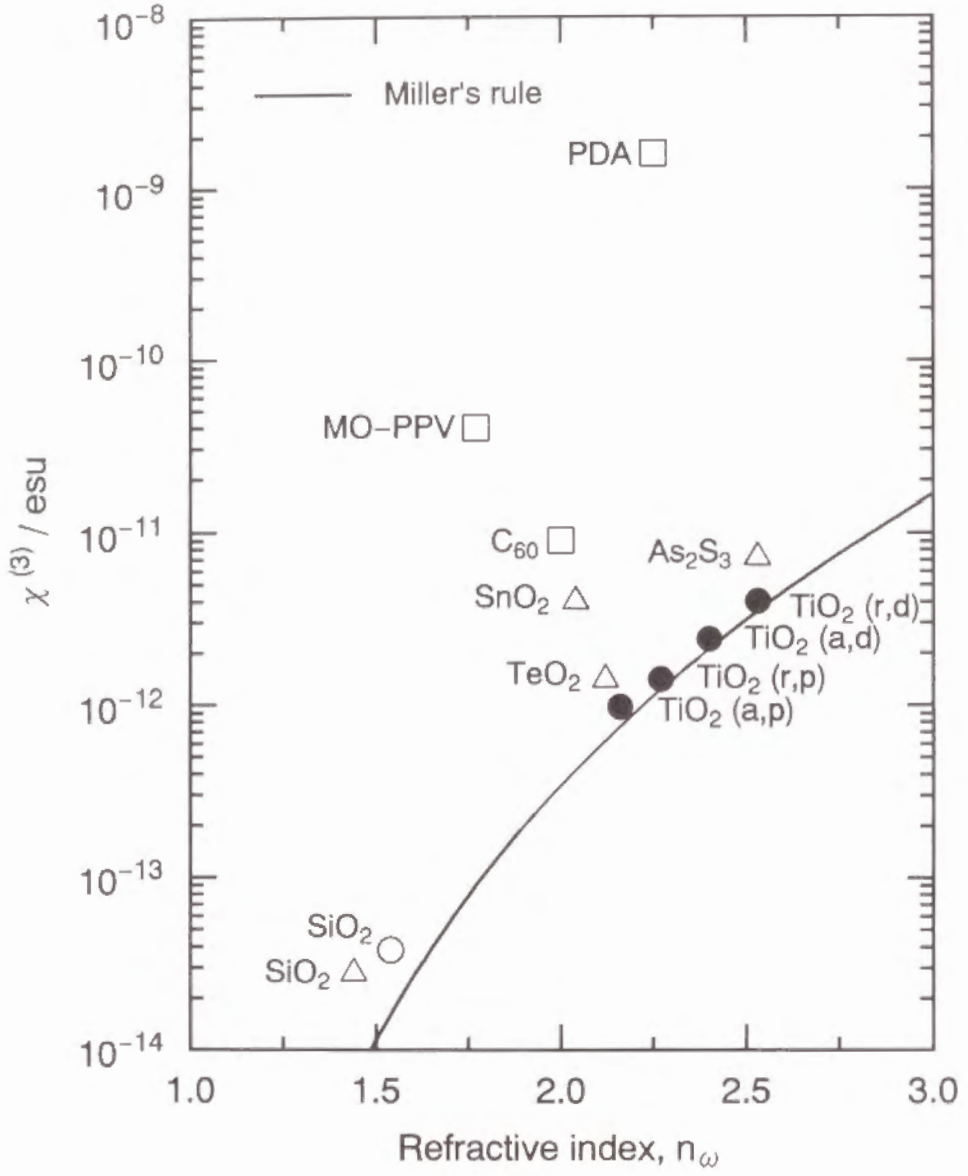

Fig. 6. Relation between $\chi^{(3)}$ and refractive index, n_ω, for TiO_2 thin films together with other NLO materials. Circles, triangles and squares denote inorganic crystals, inorganic amorphous materials and organic materials, respectively. Closed circles are the data measured in the present study. Letters of r, a, d and p in parentheses denote rutile, anatase, dense and porous, respectively. PDA: polydiacetylene, MO–PPV: poly(2,5–dimethoxy *p*–phenylene vinylene).

are no simple relations between $\chi^{(3)}$ and refractive index for these organic materials, that is, Miller's rule does not hold.

4.2 Relation between $\chi^{(3)}$ and Optical Band Gap, E_g

One can expect that an enhancement in $\chi^{(3)}(-3\omega;\omega,\omega,\omega)$ occurs when in a material a frequency of interacting light approaches either one of one–, two– or three–photon resonance frequencies according to the relation [23]

$$\chi^{(3)}(-3\omega;\omega,\omega,\omega) \propto \frac{N}{\hbar^3}\sum_{gnmn'} \rho(g)F(\omega)\Omega_{gn}\Omega_{nm}\Omega_{mn'}\Omega_{n'g}\ (esu)\ , \tag{7–a}$$

and

$$F(\omega) = \frac{1}{(E_{ng}-3\omega)(E_{mg}-2\omega)(E_{n'g}-\omega)} + \frac{1}{(E_{ng}+\omega)(E_{mg}-2\omega)(E_{n'g}-\omega)} + \frac{1}{(E_{ng}+\omega)(E_{mg}+2\omega)(E_{n'g}-\omega)} + \frac{1}{(E_{ng}+\omega)(E_{mg}+2\omega)(E_{n'g}+3\omega)}\ , \tag{7–b}$$

where $\rho(g)$, E_{ij} and Ω_{ij} are the density matrix element of fundamental state, the energy difference between states i and j in $\hbar$ (=h/2π, h: Planck's constant) unit and the transition matrix elements between states i and j, respectively. For materials having optical band gap, E_g, higher than three–photon energy, 3ω, the three–photon resonance makes the greatest contribution to the enhancement of $\chi^{(3)}$. Then, to a good approximation, the most significant term due to the three–photon resonance in Eq. (7) may be expressed as follows:

$$\chi^{(3)} = \frac{A}{(E_g-1.96)(E_g-1.31)(E_g-0.65)}\ (esu)\ (E_g>1.96)\ , \tag{8}$$

where A is the phenomenological constant.

Figure 7 gives a relation between $\chi^{(3)}$ and optical band gap, E_g, for TiO_2 thin films and other nonlinear optical materials shown in Fig. 6. In Fig. 7, for organic materials the absorption edge of exciton absorption is used instead of E_g. Taking into account that E_g should not depend on the porosity, the corrected $\chi^{(3)}$ values for TiO_2 thin films are plotted as a function of E_g. In this figure, the $\chi^{(3)}$ values of these materials show a clear tendency to increase asymptotically as the E_g approaches 1.96 eV corresponding to the photon energy of THG signal. This change obeys Eq. (8) when the parameter, A, takes a value of 1.4×10^{-11}. From this equation, $\chi^{(3)}$ values were estimated to be 3.4×10^{-12} and 2.3×10^{-12} esu for rutile and anatase, respectively, as in the fifth row of Table 2, which are also in good accordance with the corrected $\chi^{(3)}$ values, 4.0×10^{-12} and 2.4×10^{-12} esu, as in the second row.

4.3 Calculation of $\chi^{(3)}$ Based on Lines' Model

Lines introduced a bond–orbital theory dealing with the contribution of empty *d* orbital in addition to *sp* orbitals to linear and nonlinear optical properties, giving the following equation to estimate $\chi^{(3)}$ [7, 24]:

$$\chi^{(3)} = \frac{2.5\times10^{-12}\ell_b^2(n_\omega^2-1)f_L^3E_S^6}{3\pi[E_S^2-E^2]^4}\ (esu)\ , \tag{9}$$

where ℓ_b denotes the bond length between cation and anion, $f_L=(n_\omega{}^2+2)/3$ the Lorentz local–field correction factor, E_S the Sellmeier gap which is in practice

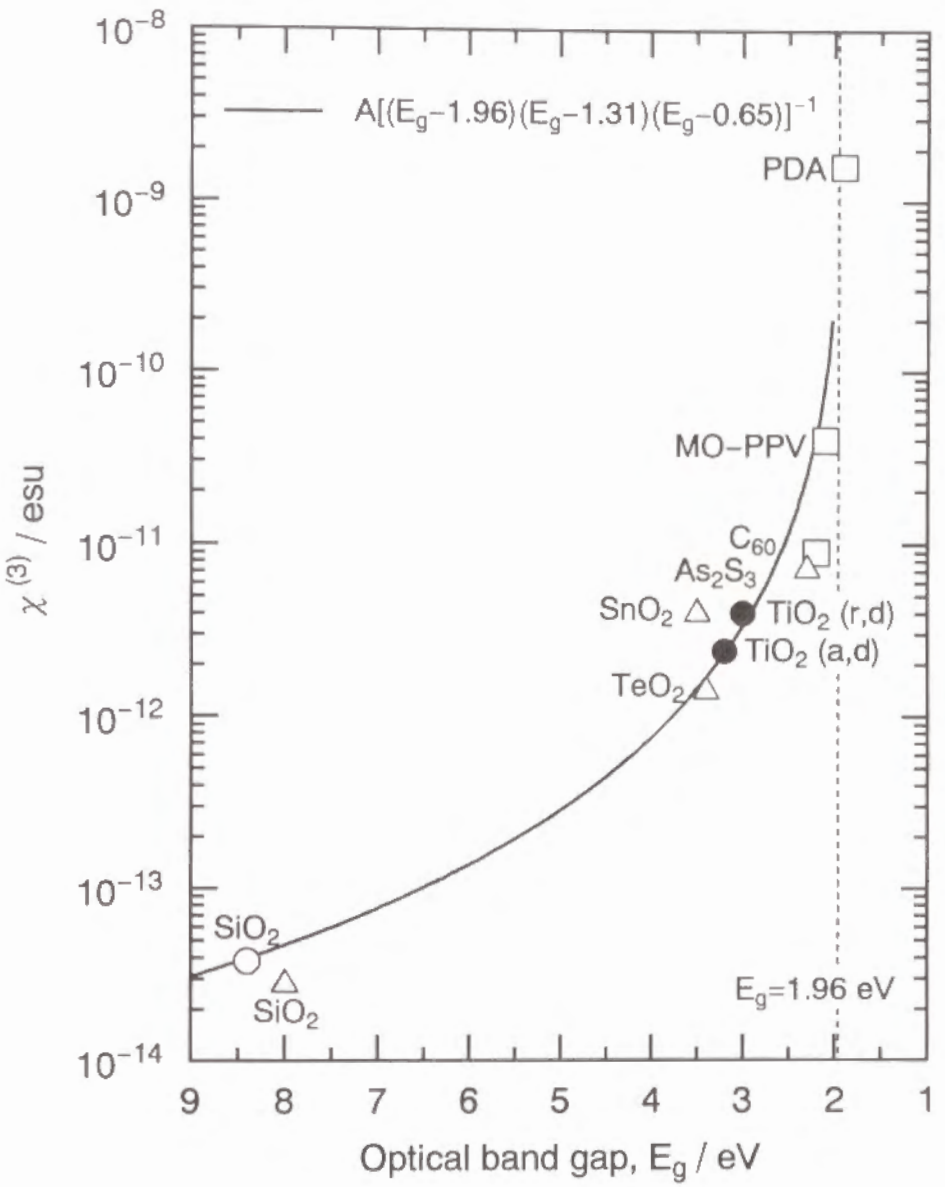

Fig. 7. Relation between $\chi^{(3)}$ and optical band gap, E_g, for TiO_2 thin films together with other NLO materials. Notations are the same as in Fig. 6.

equal to the average oscillator energy, E_0, in Eq. (1). From Eq. (9), one can obtain $\chi^{(3)}$ values of 4.7×10^{-12} and 2.7×10^{-12} esu for rutile and anatase dense films, respectively, as in the seventh row of Table 2, which are in good accordance with the corrected values, 4.0×10^{-12} and 2.4×10^{-12} esu, as in the second row.

Therefore, the much higher $\chi^{(3)}$ values of both TiO_2 polymorphs compared with SiO_2 glass can be ascribed to the higher refractive index and the narrower optical band gap or Sellmeier gap of the former, which all result from the significant contribution of Ti 3*d* orbital due to the large *p*–*d* overlapping caused by the short Ti–O bond length of 0.195–0.196 nm [25].

4.4 Comparison of $\chi^{(3)}$ between Rutile and Anatase

The difference in crystal structure between two TiO_2 polymorphs is that the two edges shared TiO_6 octahedra form straight chains in rutile, as distinct from the zigzag chains consisting of four edges shared TiO_6 octahedra in anatase as seen from Figure 8. A band structure calculation reveals that the straight chains of TiO_6 octahedra in rutile give rise to two important results of the broader t_{2g} part of Ti 3*d* conduction band which lies around −9.5 eV of the density of states (DOS), and the higher DOS around the bottom of the conduction band compared with anatase (Figure 9) [25]. On the other hand, the noticeable difference in O 2*p* valence band around −15.5 eV between both TiO_2 polymorphs is not seen. The broader conduction band explains the narrower optical band gap, and the higher refractive index due to the higher optical transition probability of rutile than that of anatase. The higher DOS around the bottom of conduction band also gives rise to the higher optical transition probability of rutile compared with anatase. In fact, it has been reported that the optical transition between O 2*p* valence band and Ti 3*d* conduction band is direct for rutile, whereas it is indirect for anatase [26].

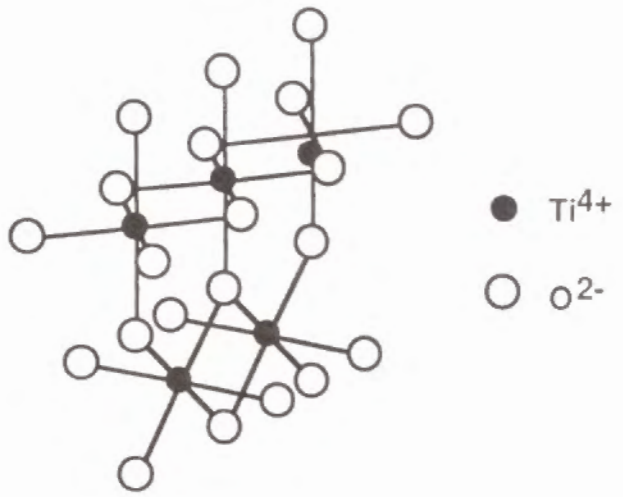

(a) rutile

(b) anatase

Fig. 8. Structures of (a) rutile and (b) anatase.

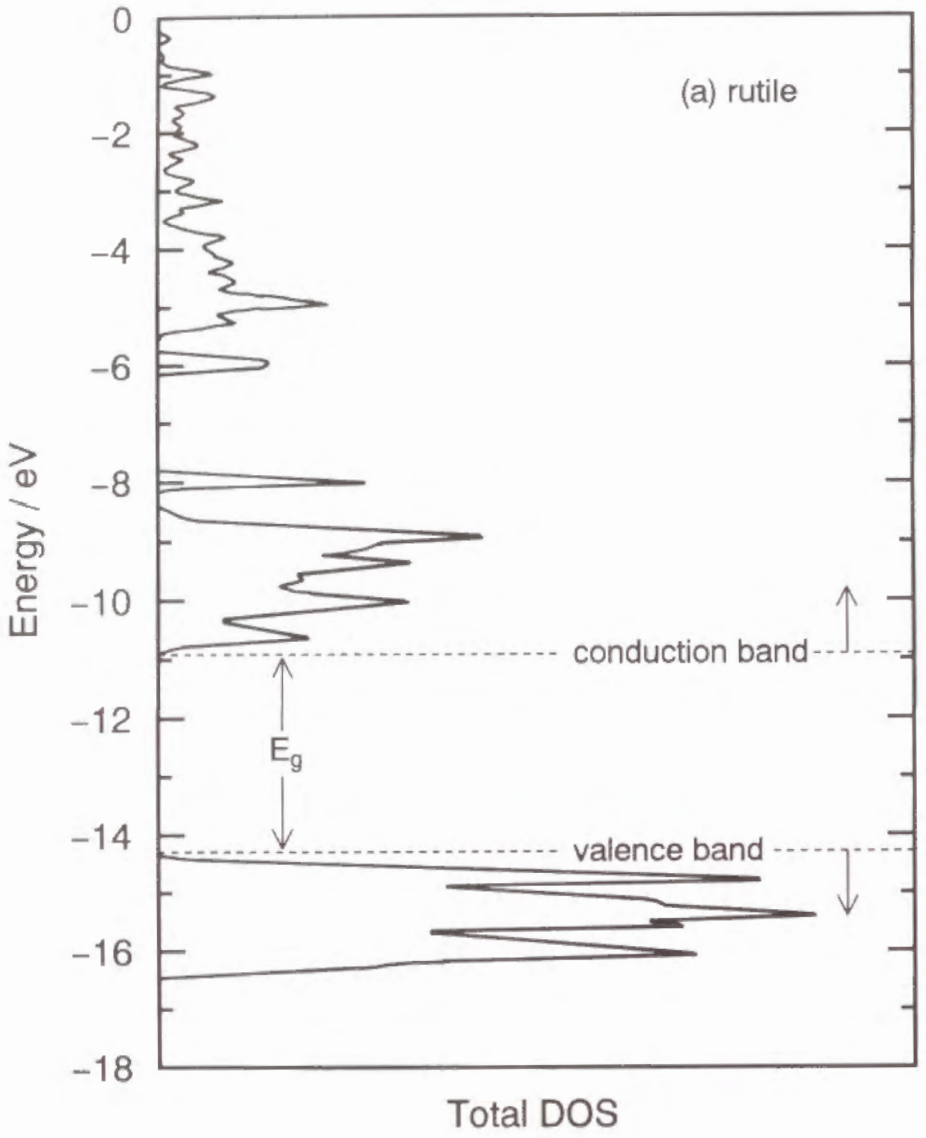

Fig. 9(a). Density of states (DOS) for rutile.

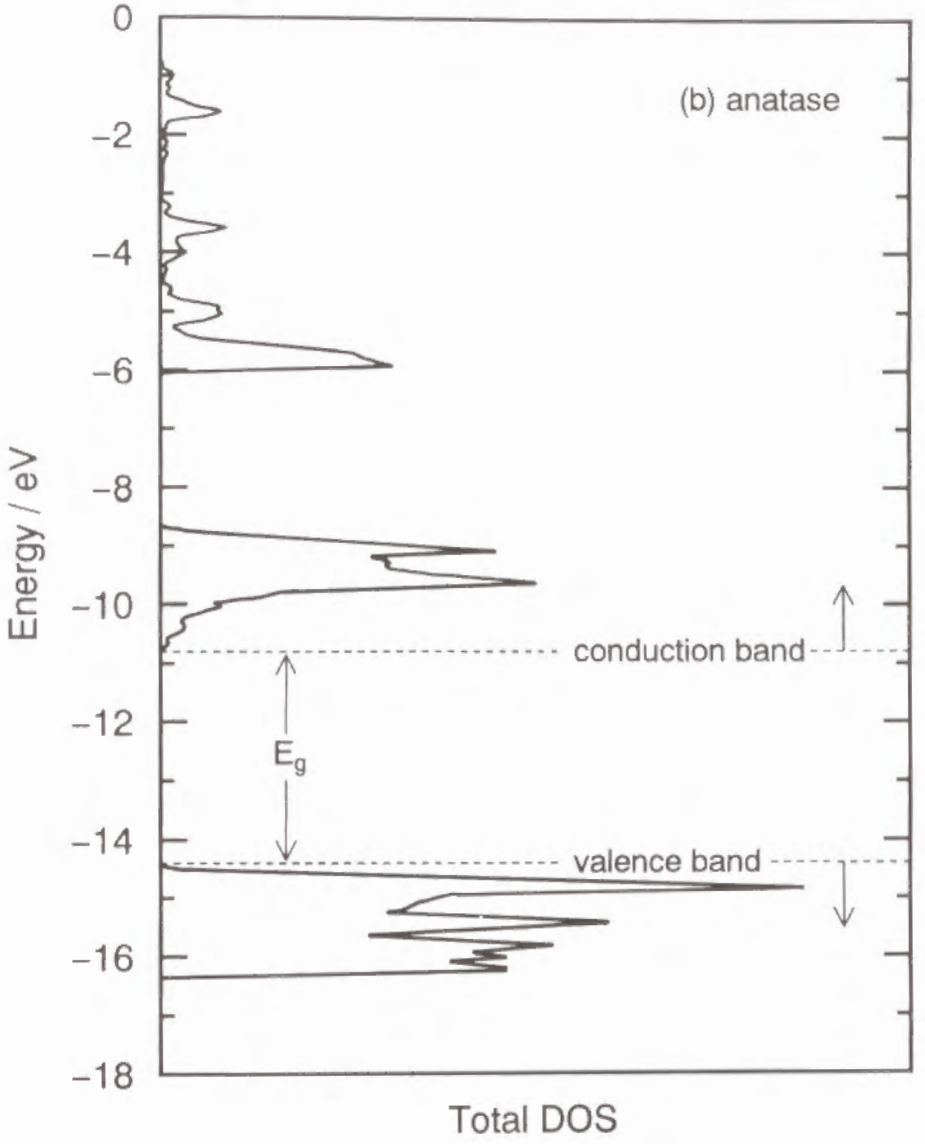

Fig. 9(b). Density of states (DOS) for anatase.

Since the THG process requires the same parity as linear optical transition, the higher $F(\omega)$ and Ω_{ij} in Eq. (7) resulting from the characteristic DOS of rutile is considered to be responsible for the slightly higher $\chi^{(3)}$ value of rutile compared with anatase.

5. Conclusion

In this section, the third-order nonlinear optical properties of the sol-gel derived TiO_2 thin films of rutile and anatase phases have been investigated by the THG method. Chiefly, the effects of TiO_2 polymorph (rutile and anatase) and porosity on $\chi^{(3)}$ has been examined. The following results were obtained.

(1) The measured $\chi^{(3)}$ values of rutile and anatase thin films were 1.4×10^{-12} and 9.7×10^{-13} esu, respectively. The $\chi^{(3)}$ values corrected for porosity were 4.0×10^{-12} (rutile) and 2.4×10^{-12} esu (anatase), which are ~100 times as high as that of SiO_2 glass.

(2) The much higher $\chi^{(3)}$ values of both TiO_2 polymorphs compared with SiO_2 glass were ascribed to the higher refractive index and the narrower optical band gap of the former due to the significant contribution of Ti 3*d* orbital as a result of the large *p*–*d* overlapping caused by the short Ti–O bond length of 0.195–0.196 nm.

(3) The slightly higher $\chi^{(3)}$ value of rutile compared with anatase was also attributed to the higher refractive index and the narrower optical band gap of the former, which both possibly arise from the broader Ti 3*d* conduction band as a result of the formation of the straight chains of TiO_6 octahedra in rutile, as distinct from the zigzag chains of TiO_6 octahedra in anatase.

References

[1] R. C. Miller, *Appl. Phys. Lett.*, **5**, 17 (1964).

[2] C. C. Wang, *Phys. Rev. B*, **2**, 2045 (1970).

[3] J. R. DeVore, *J. Opt. Soc. Am.*, **41**, 416 (1951).

[4] R. Adair, L. L. Chase and S. A. Payne, *Phys. Rev. B*, **39**, 3337 (1989).

[5] E. M. Vogel, S. G. Kosinski, D. M. Krol, J. L. Jackel, S. R. Friberg, M. K. Oliver and J. D. Powers, *J. Non-Cryst. Solids*, **107**, 244 (1989).

[6] E. M. Vogel, M. J. Weber and D. M. Krol, *Phys. Chem. Glasses*, **32**, 231 (1991).

[7] M. E. Lines, *Phys. Rev. B*, **43**, 11978 (1991).

[8] K. H. Guenther, T. W. Humpherys, J. Balmer, J. R. Bettis, E. Casparis, J. Ebert, M. Eichner, A. H. Guenther, E. Kiesel, R. Kuehnel, D. Milam, W. Ryseck, S. C. Seitel, A. F. Stewart, H. Weber, H. P. Weber, G. R. Wirtenson and R. M. Wood, *Appl. Opt.*, **23**, 3743 (1984).

[9] K. Kubodera and H. Kobayashi, *Mol. Cryst. Liq. Cryst.*, **182A**, 103 (1990).

[10] S. H. Wemple, *J. Chem. Phys.*, **67**, 2151 (1977).

[11] H. E. Merwin, "International Critical Tables of Numerical Data, Physics, Chemistry and Technology, **VII**", ed. by E. W. Washburn, C. J. West, N. E. Dorsey and M. D. Ring, (1931) p. 16.

[12] B. E. Yoldas, *Appl. Opt.*, **19**, 1425 (1980).

[13] K. Vos, *J. Phys. C*, **10**, 3917 (1977).

[14] M. Grätzel and F. P. Rotzinger, *Chem. Phys. Lett.*, **118**, 474 (1985).

[15] H. Nasu, K. Kubodera, M. Kobayashi, M. Nakamura and K. Kamiya, *J. Am. Ceram. Soc.*, **73**, 1794 (1990).

[16] G. R. Meredith, B. Buchalter and C. Hanzlik, *J. Chem. Phys.*, **78**, 1533 (1983).

[17] G. R. Meredith, *Phys. Rev. B*, **24**, 5522 (1981).

[18] N. Ueda, H. Kawazoe, Y. Watanabe, M. Takata, M. Yamane and K. Kubodera, *Appl. Phys. Lett.*, **59**, 502 (1991).

[19] S. H. Kim, T. Yoko and S. Sakka, *J. Am. Ceram. Soc.*, **76**, 2486 (1993).

[20] T. Kanetake, K. Ishikawa, T. Hasegawa, T. Koda, K. Takeda, M. Hasegawa, K. Kubodera and H. Kobayashi, *Appl. Phys. Lett,*, **54**, 2287 (1989).

[21] T. Kurihara, Y. Mori, T. Kaino, H. Murata, N. Takada, T. Tsutsui and S. Saito, *Chem. Phys. Lett.*, **183**, 534 (1991).

[22] J. S. Meth, H. Vanherzeele and Y. Wang, *Chem. Phys. Lett.*, **197**, 26 (1992).

[23] F. Kajzar and J. Messier, "Nonlinear Optical Properties of Organic Molecules and Crystals, **2**", ed. by D. S. Chemla and J. Zyss, Academic Press, New York (1987) p. 51.

[24] M. E. Lines, *Phys Rev. B*, **41**, 3383 (1990).

[25] J. K. Burdett, T. Hughbanks, G. J. Miller, J. W. Richardson, Jr. and J. V. Smith, *J. Am. Chem. Soc.*, **109**, 3639 (1987).

[26] T. Yoko, A. Yuasa, K. Kamiya and S. Sakka, *J. Electrochem. Soc.*, **138**, 2279 (1991).

SECTION 1.2 PHASE-MATCHING OF RUTILE SINGLE CRYSTAL

1. Introduction

In Section 1.1, it was presented that TiO_2 has high $\chi^{(3)}$ of 10^{-12} esu. In order to take efficiently the THG light out of the TiO_2, phase-matching between fundamental and THG waves generated from TiO_2 are necessary.

In this section, the results of phase-matching for the THG of rutile single crystal (110) are described from the viewpoint of the practical application in optical devices.

2. Experimental

2.1 Rutile Single Crystal

Rutile single crystal (110) was obtained from Scimarec Co., Ltd. The sample of 740 μm in thickness was used for the measurements.

2.2 Phase-Matching of Rutile Single Crystal

THG measurements of rutile single crystal (110) were made by means of a nonlinear optical measurement apparatus (Tokyo Instruments, Inc., Tokyo, Japan). For phase-matching rutile single crystal (110) was mounted in such way that the optic axis (z or c-axis) is perpendicular to the rotation axis.

3. Results

The THG intensity of rutile single crystal (110) relative to SiO_2 glass as a function of rotation angle is shown in Figure 1. A drastic increase in THG intensity is observed at ~$\pm$40 °, the peak intensity being ~1.7×10^5 times as high as the nonphase-matched THG intensity of SiO_2 glass. The THG

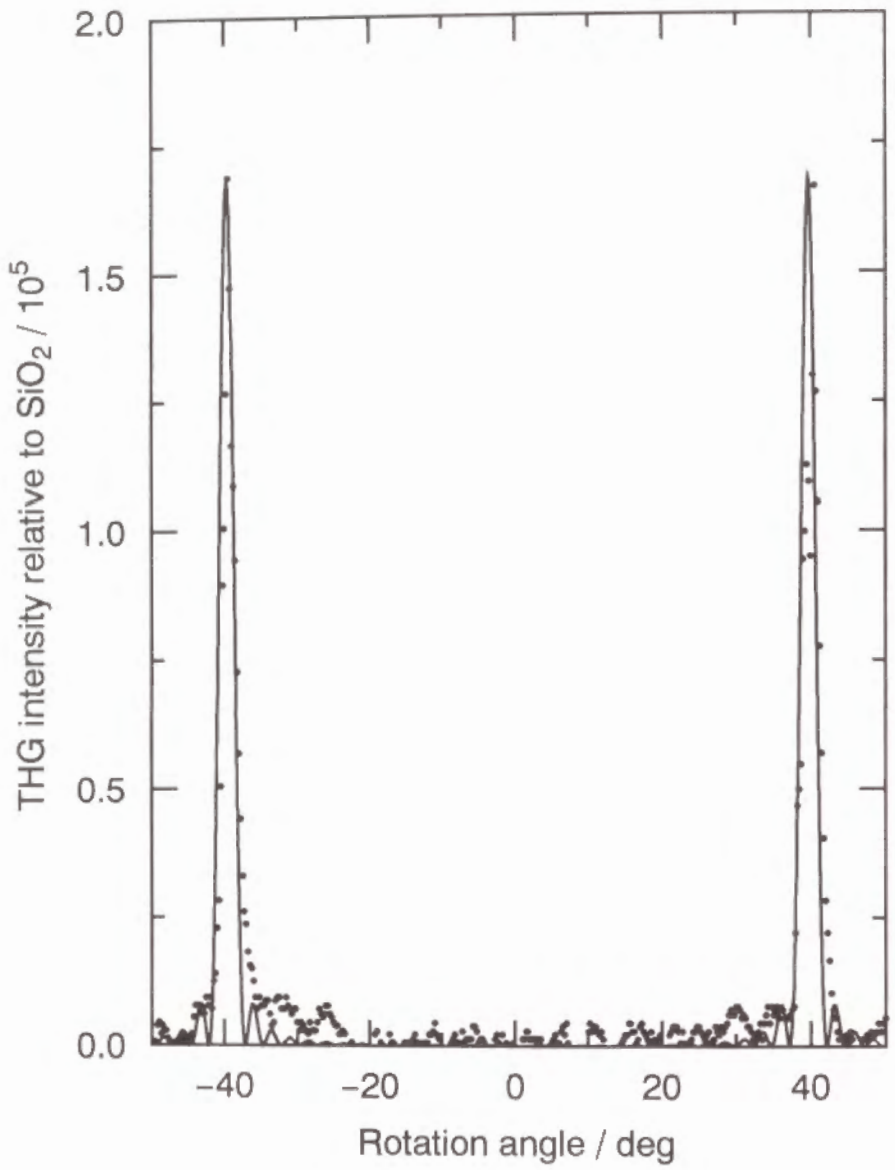

Fig. 1. THG intensity as a function of rotation angle for rutile (110) single crystal.

light at 633 nm is so intense that one can see the red light by eyes.

4. Discussion

A technique that is used widely to satisfy the phase−matching requirement, $n_\omega=n_{3\omega}$, makes use of the natural birefringence of anisotropic crystals. In rutile single crystal, the wavelength dependence of refractive index for ordinary and extraordinary rays in nm unit is given by [1]

$$n_o^2 = 5.913+\frac{2.441\times10^5}{\lambda^2-0.803\times10^5}\ , \qquad (1\text{−a})$$

and

$$n_e^2 = 7.197+\frac{3.322\times10^5}{\lambda^2-0.843\times10^5}\ . \qquad (1\text{−b})$$

Figure 2 represents these relations. It should be noted that the refractive index for extraordinary ray depends on the angle, ϕ, between the propagation vector of light and the crystal optic axis (z or c axis) and varies from $n_e(\phi=0)=n_o$ to $n_e(\phi=90)=n_e$ (Figure 3) according to the next relation [2]

$$\frac{1}{n_e^2(\phi)} = \frac{\cos^2\phi}{n_o^2}+\frac{\sin^2\phi}{n_e^2}\ . \qquad (2)$$

It is seen from the Figs. 2 and 3 that the so−called Type I phase−matching [3], in which three incident lights of all e rays at ω are converted to THG light of an o ray, can be achieved at $n_{e,\omega}(\phi_m)=n_{o,3\omega}$ for positive ($n_e>n_o$) uniaxial

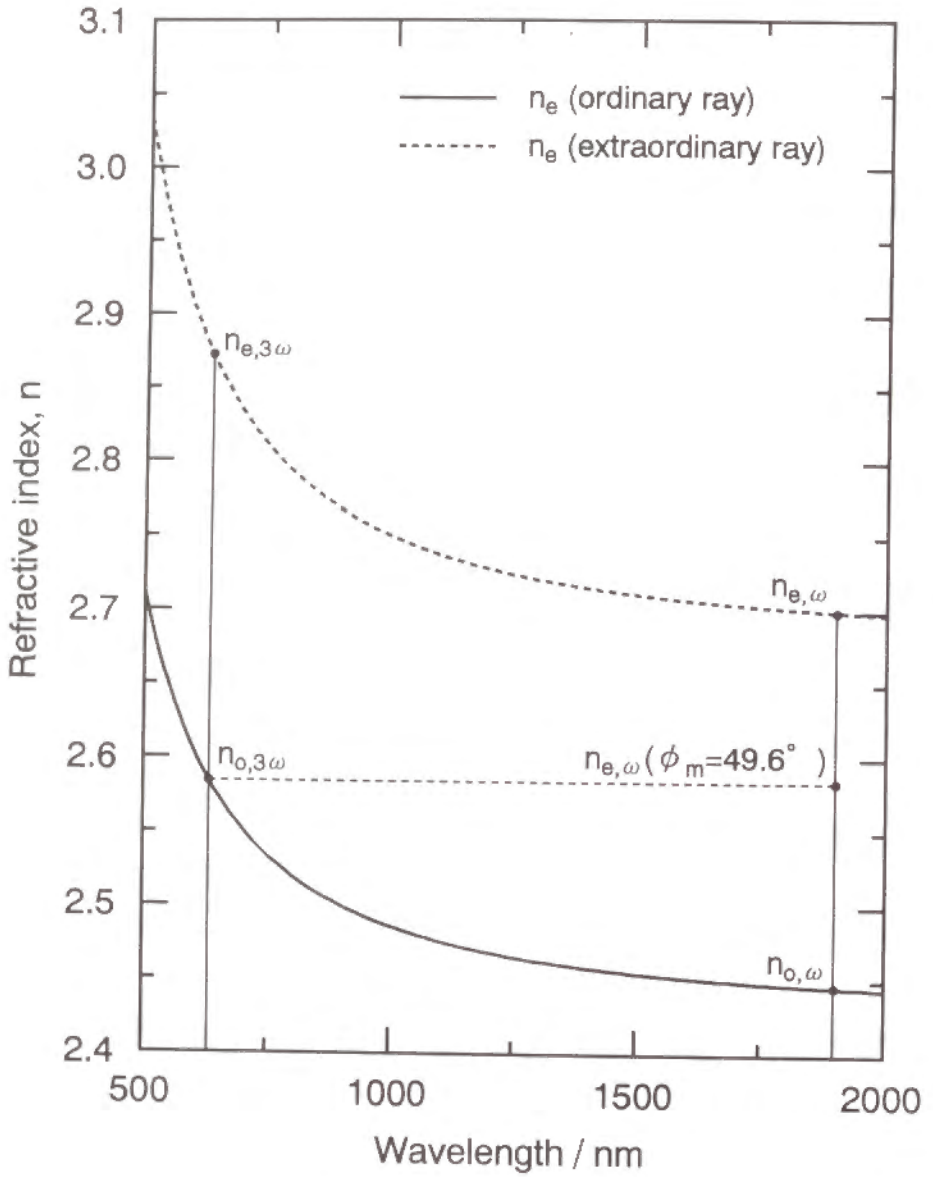

Fig. 2. Wavelength dependencies of refractive index for the ordinary and extraordinary rays in rutile single crystal.

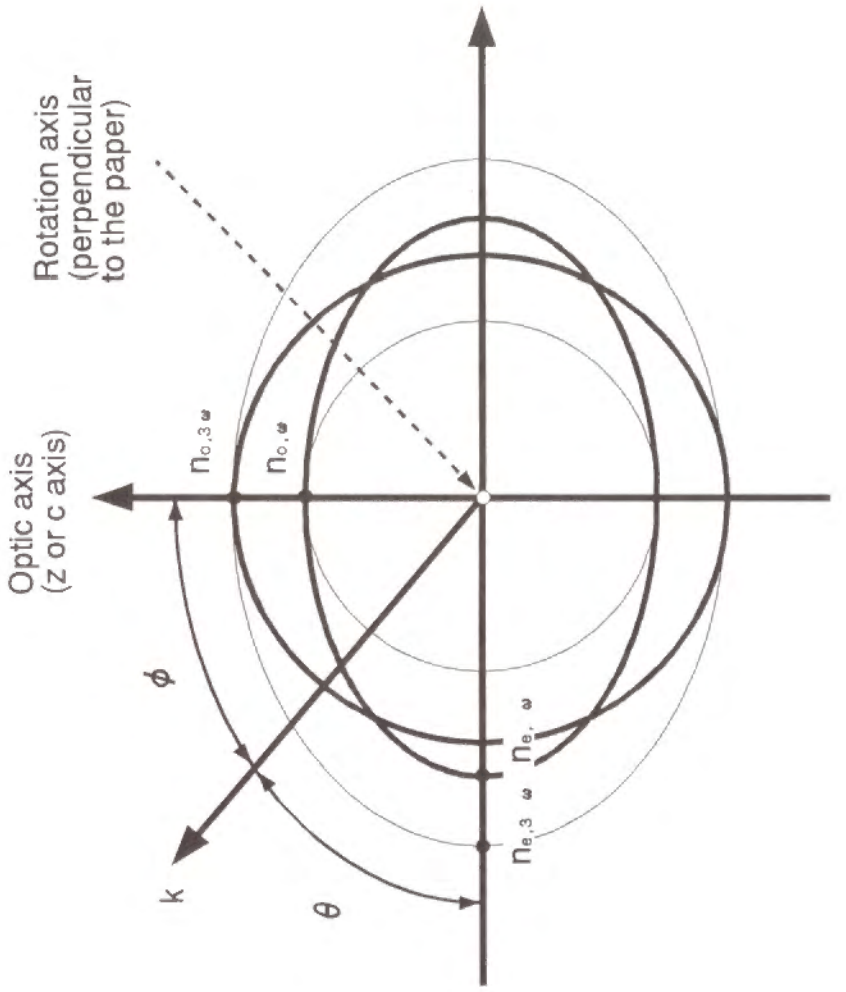

Fig. 3. Surfaces of refractive index ellipsoid for the ordinary and extraordinary rays in a positive ($n_e>n_o$) uniaxial crystal, showing the top view of a sample mounted in the present THG measurement. **k**: propagation vector of incident light, Φ: angle between optic axis and **k**, θ: incident angle.

rutile crystal. Therefore, the phase-matching angle, ϕ_m, is determined by the next equation

$$\frac{\cos^2\phi_m}{n^2_{o,\,\omega}}+\frac{\sin^2\phi_m}{n^2_{e,\,\omega}} = \frac{1}{n^2_{o,\,3\omega}} \quad . \tag{3}$$

Solving for ϕ_m

$$\phi_m = \sin^{-1}\sqrt{\frac{n^{-2}_{o,\,3\omega}-n^{-2}_{o,\,\omega}}{n^{-2}_{e,\,\omega}-n^{-2}_{o,\,\omega}}} = \sin^{-1}\sqrt{\frac{2.584^{-2}-2.446^{-2}}{2.700^{-2}-2.446^{-2}}} = 49.6^\circ \quad . \tag{4}$$

The relation between incident angle, θ, and ϕ in the THG measurement is given from Fig. 3 as follows

$$\theta+\phi = 90^\circ \quad . \tag{5}$$

Therefore, phase-matching can be attained at θ_m=40.4 ° in good accordance with the values at θ_m=39.7 ° experimentally determined by the least squares fitting [2] of the next relation

$$\frac{I_{3\omega,\,TiO_2}}{I_{3\omega,\,SiO_2}} = \frac{B\sin^2[C(\theta-\theta_m)]}{[C(\theta-\theta_m)]^2} \quad , \tag{6}$$

where B and C are the fitting parameters.

The very strong THG light from rutile single crystal is based on the high $\chi^{(3)}$ and transparency in the visible and near infrared wavelength region, proving that TiO_2 is one of the most promising nonlinear optical materials.

5. Conclusion

In this section, phase-matching for the THG of rutile single crystal (110) have been investigated. As a result, third-harmonic generation with a visible red light was clearly observed, indicating that TiO_2 is one of the most promising NLO materials.

References

[1] J. R. DeVore, *J. Opt. Soc. Am.*, **41**, 416 (1951).

[2] "Optical Waves in Crystals", ed. by A. Yariv and P. Yeh, John Wiley & Sons, New York (1983) p. 504.

[3] S. Singh, "Handbook of Laser Science and Technology, **III**, Optical Materials: Part 1", ed. by M. J. Weber, CRC Press, Boca Raton, FL, (1986) p. 3.

CHAPTER 2. THIRD-ORDER NONLINEAR OPTICAL PROPERTIES OF V_2O_5, Nb_2O_5 AND Ta_2O_5 THIN FILMS

1. Introduction

As described in Chapter 1, the third-order nonlinear optical susceptibilities, $\chi^{(3)}$, of transition metal oxides with the high refractive index, such as TiO_2, were on the order of 10^{-12} esu, which is higher than that of SiO_2 glass by two orders of magnitude. This was ascribed to the high refractive index of transition metal oxides on the basis of Miller's rule [1, 2] which predicts that a material with the high refractive index shows the high $\chi^{(3)}$. On the other hand, the resonance or near-resonance effect is also an important factor determining $\chi^{(3)}$. In fact, $\chi^{(3)}$ increases asymptotically, as the optical band gap approaches the three-photon energy as stated in Chapter 1. Transition metal oxides are considered to be the promising nonlinear optical (NLO) materials, because most of them can meet the above two demands.

Since electrons in many transition metal oxides are localized at the metal and the nearest neighboring oxygens, the electronic spectra and even magnetic properties can be described in terms of the electronic structures of coordination polyhedra of metal cations [3-5]. This implies that $\chi^{(3)}$ of transition metal oxides can be also expressed by the local structures including metal-oxygen bond length and valence of metal cation. Lines [6] has dealt with the contribution of the empty *d* orbitals as well as *sp* orbitals to the linear and nonlinear optical properties based on the bond-orbital theory. Lines' model gives a prediction that transition metal oxides with the shortest average bond length, ℓ_b, show the highest $\chi^{(3)}$. Taking these things into account, V_2O_5, Nb_2O_5 and Ta_2O_5 are selected as the present target materials,

because V_2O_5 (ℓ_b=0.183 nm) is one of transition metal oxides with the shortest ℓ_b, and Nb_2O_5 (ℓ_b=0.200 nm) and Ta_2O_5 (ℓ_b=0.204 nm) have the much longer ℓ_b than V_2O_5 while these transition metals belong to the same VA group as vanadium.

In this chapter, the results of preparation of V_2O_5, Nb_2O_5 and Ta_2O_5 thin films on SiO_2 glass substrates by the sol-gel method and the third-order nonlinear optical properties investigated by the THG method are described. The effect of the local structures (metal-oxygen bond length and valence of cation) on $\chi^{(3)}$ of transition metal oxides with empty *d* orbitals is discussed in comparison with non-transition metal oxides.

2. Experimental

2.1 Preparation of V_2O_5, Nb_2O_5 and Ta_2O_5 Thin Films

V_2O_5, Nb_2O_5 and Ta_2O_5 thin films were prepared by the sol-gel method. As starting solutions, $VO(CH(COCH_3)_2)_2$-$CH_3OCH_2CH_2OH$-HNO_3, $Nb(OC_2H_5)_5$-$CH_3OCH_2CH_2OH$-H_2O-HNO_3 and $Ta(OC_2H_5)_5$-$CH_3OCH_2CH_2OH$-H_2O-HNO_3 solutions were selected for V_2O_5, Nb_2O_5 and Ta_2O_5 films, respectively. The chemical compositions of the solutions were 1:50:1, 1:15:1.5:0.1 and 1:20:1.5:0.1 in molar ratio, respectively. In V_2O_5 solution, vanadium oxyacetylacetonate ($VO(CH(COCH_3)_2)_2$) was dissolved in a solution of 2-methoxyethanol ($CH_3OCH_2CH_2OH$) and HNO_3aq (~15 N). For Nb_2O_5 (or Ta_2O_5) solution, niobium pentaethoxide ($Nb(OC_2H_5)_5$) (or tantalum pentaethoxide ($Ta(OC_2H_5)_5$)) was first diluted by half of a prescribed amount of $CH_3OCH_2CH_2OH$. Then, the solution was mixed with a solution of HNO_3aq containing a given amount of H_2O and the remainder of $CH_3OCH_2CH_2OH$. V_2O_5 and Nb_2O_5 (or Ta_2O_5) coating solutions were allowed to stand at 60 and 30 °C for 2 h prior to use, respectively.

Dip-coating was used for the film formation. A SiO_2 glass substrate was immersed in a coating solution, and pulled up at a rate of 3 cm min^{-1}. The films were heated at 500 and 800 °C for 10 min immediately after each coating procedure for V_2O_5 and Nb_2O_5 (or Ta_2O_5), respectively. This cycle was repeated 6 and 15 times to attain the desired film thickness for V_2O_5, and Nb_2O_5 (or Ta_2O_5), respectively.

2.2 Characterization of V_2O_5, Nb_2O_5 and Ta_2O_5 Thin Films

For reason mentioned in Chapter 1, an SiO_2 coating was further applied onto the V_2O_5, Nb_2O_5 and Ta_2O_5 films and then the V_2O_5, Nb_2O_5 and Ta_2O_5 and additional SiO_2 films on one face were removed. These films were characterized by X-ray diffraction, ellipsometry, UV-visible spectrophotometry and THG measurements as gone into details in Chapter 1.

3. Results

3.1 Crystallization Behavior

Figure 1 shows the X-ray diffraction patterns of (a) V_2O_5, (b) Nb_2O_5 and (c) Ta_2O_5 thin films prepared by the sol-gel method. The crystalline phases precipitated in the sol-gel derived V_2O_5, Nb_2O_5 and Ta_2O_5 thin films were identified referring to JCPDS-FILE 41-1426 (orthorhombic), 27-1003 (orthorhombic) and 18-1304 (hexagonal), respectively. Preferable orientation along the (001) plane is seen for V_2O_5 films while not for Nb_2O_5 and Ta_2O_5 films. The crystallite sizes in the V_2O_5, Nb_2O_5 and Ta_2O_5 films were ~40, ~45 and ~20 nm, respectively.

3.2 Refractive Index and Optical Transmittance

The wavelength dependencies of refractive index, n, for V_2O_5, Nb_2O_5 and Ta_2O_5 thin films are shown in Figure 2. It is seen that the refractive indices of V_2O_5, Nb_2O_5 and Ta_2O_5 films decrease with increasing wavelength

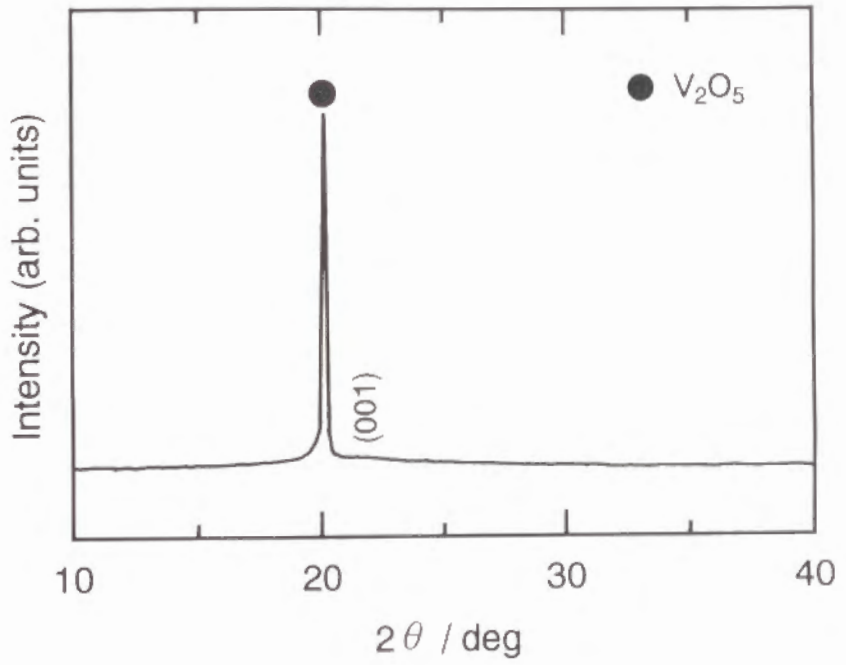

Fig. 1(a). X-ray diffraction pattern of V_2O_5 thin films prepared by the sol-gel method.

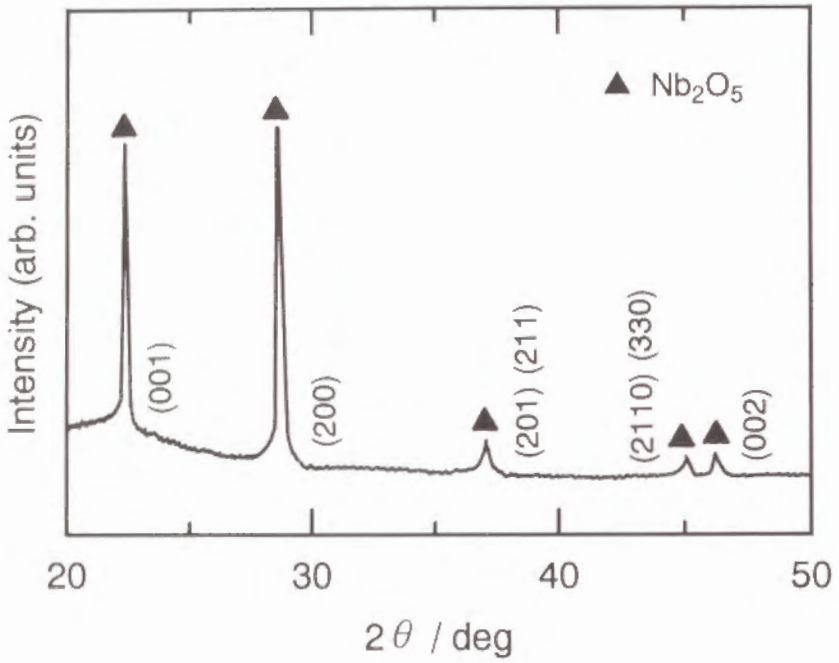

Fig. 1(b). X-ray diffraction pattern of Nb_2O_5 thin films prepared by the sol-gel method.

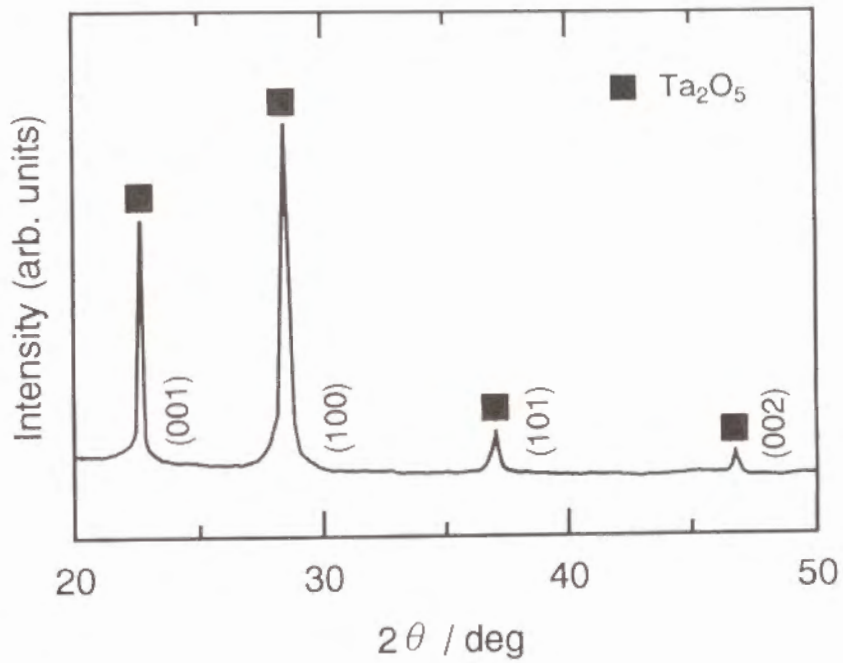

Fig. 1(c). X-ray diffraction pattern of Ta_2O_5 thin films prepared by the sol-gel method.

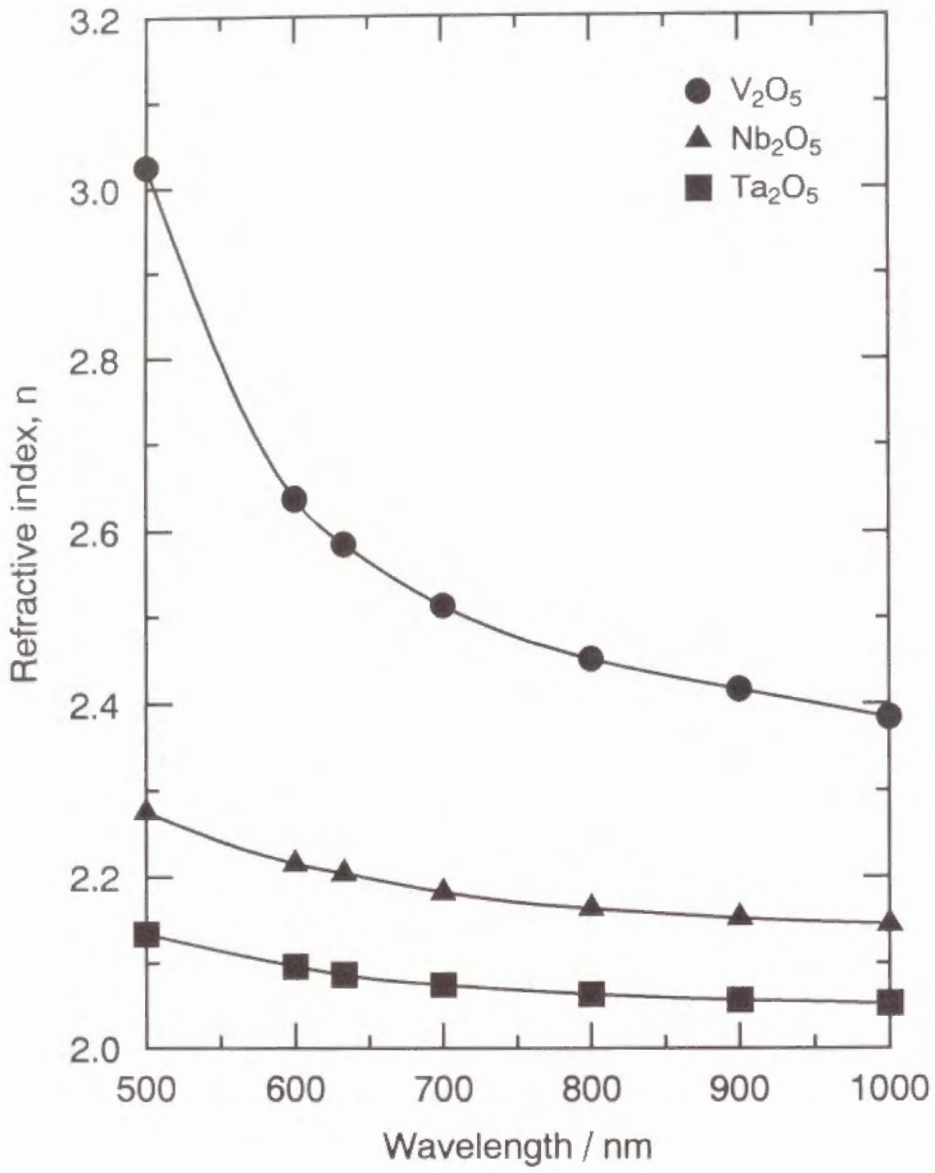

Fig. 2. Wavelength dependencies of refractive index, n, for V_2O_5, Nb_2O_5 and Ta_2O_5 thin films.

as well known. Figure 3 presents the linear plots of $(n^2-1)^{-1}$ versus E^2 for V_2O_5, Nb_2O_5 and Ta_2O_5 thin films based on Wemple's equation [9]

$$\frac{1}{n^2-1} = \frac{E_0}{E_d} - \frac{E^2}{E_0 E_d}, \tag{1}$$

where E, E_0 and E_d are the photon energy, the average oscillator energy and dispersion energy in eV unit, respectively. E_0 and E_d are important optical properties of materials [9]. The refractive indices were estimated as $n_{3\omega}$=2.59 at 633 nm and n_ω=2.31 at 1900 nm, and the coherence length, ℓ_c=1.9/[6($n_{3\omega}$–n_ω)], was 1.1 μm for V_2O_5 films. In a similar manner, $n_{3\omega}$, n_ω and ℓ_c for Nb_2O_5 films were estimated as 2.20, 2.12 and 3.6, and for Ta_2O_5 films 2.09, 2.03 and 6.1 μm, respectively. The thickness of the V_2O_5, Nb_2O_5 and Ta_2O_5 films obtained by 6, 15 and 15 dippings was 0.08, 0.74 and 0.57 μm, respectively.

Figure 4 shows the absorption spectra of V_2O_5, Nb_2O_5 and Ta_2O_5 thin films with and without additional SiO_2 coating. All spectra have a number of mountains and troughs arising from the interference of light. It is seen that the additional SiO_2 coating reduces the optical loss due to the reflection, especially in the wavelength region above ~500 nm. The optical band gaps, E_g, of V_2O_5, Nb_2O_5 and Ta_2O_5 films were estimated to be 2.5, 3.2 and 4.2 eV, respectively.

3.3 Evaluation of $\chi^{(3)}$ Values

The THG intensities as a function of the rotation angle for (a) V_2O_5 films, (b) Nb_2O_5 films, (c) Ta_2O_5 films and (d) SiO_2 glass are given in Figure 5. The THG intensity patterns of V_2O_5, Nb_2O_5 and Ta_2O_5 films clearly show the interference between the THG lights from V_2O_5 (or Nb_2O_5 and Ta_2O_5)

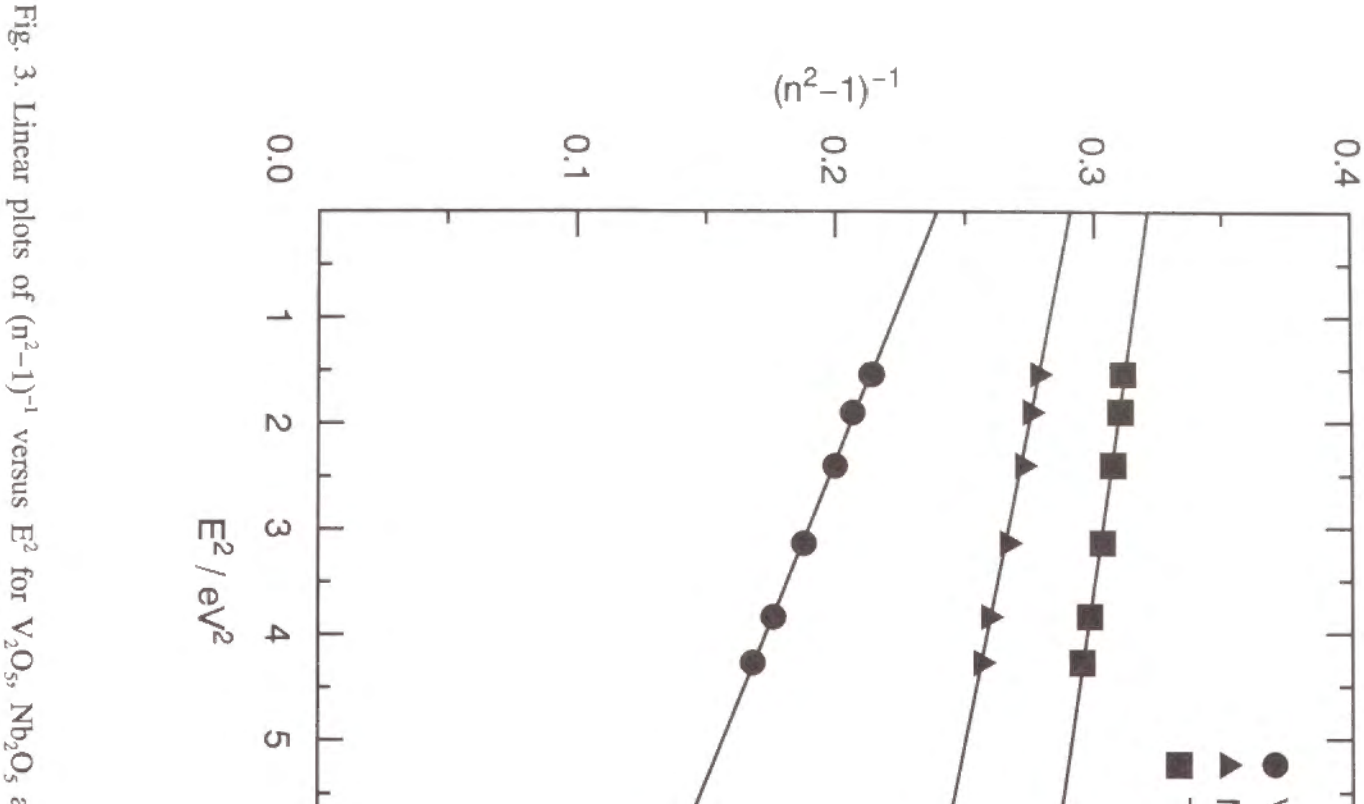

Fig. 3. Linear plots of $(n^2-1)^{-1}$ versus E^2 for V_2O_5, Nb_2O_5 and Ta_2O_5 thin films.

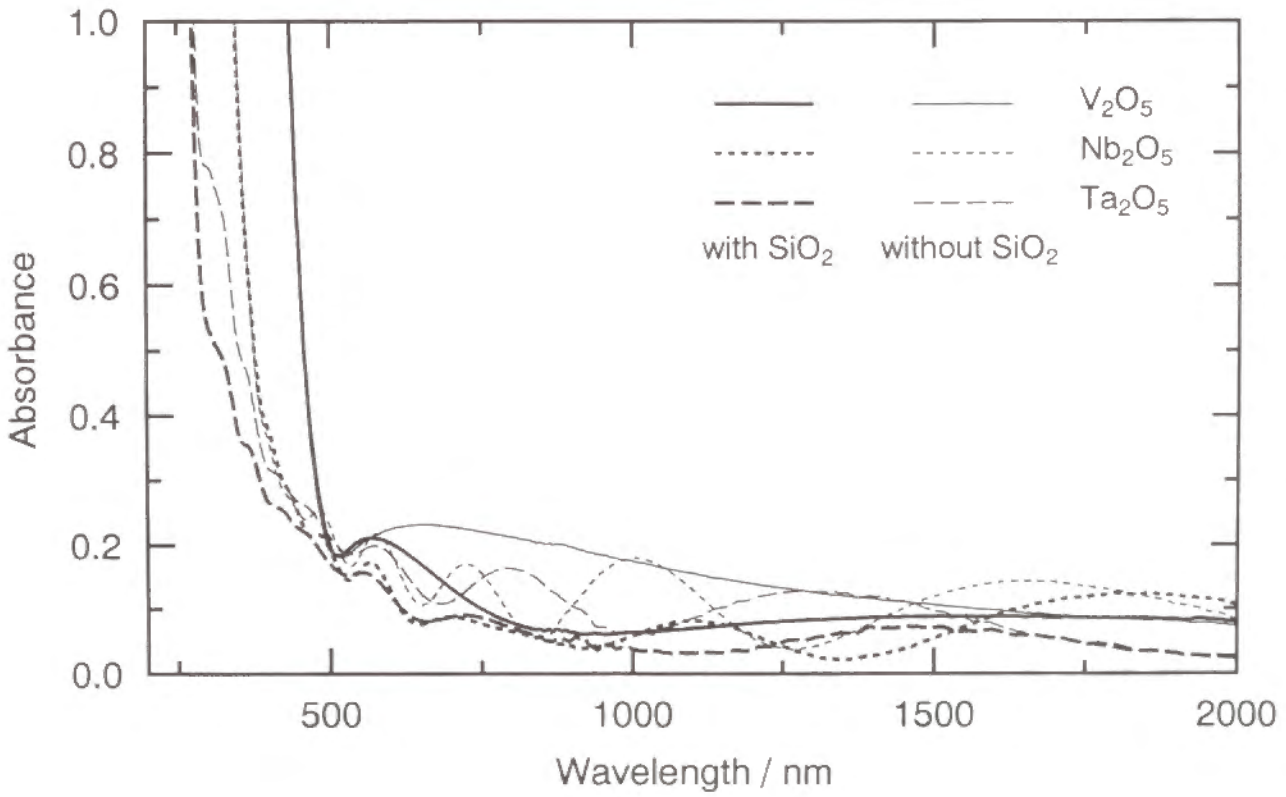

Fig. 4. Absorption spectra of V_2O_5, Nb_2O_5 and Ta_2O_5 thin films with and without additional SiO_2 coating.

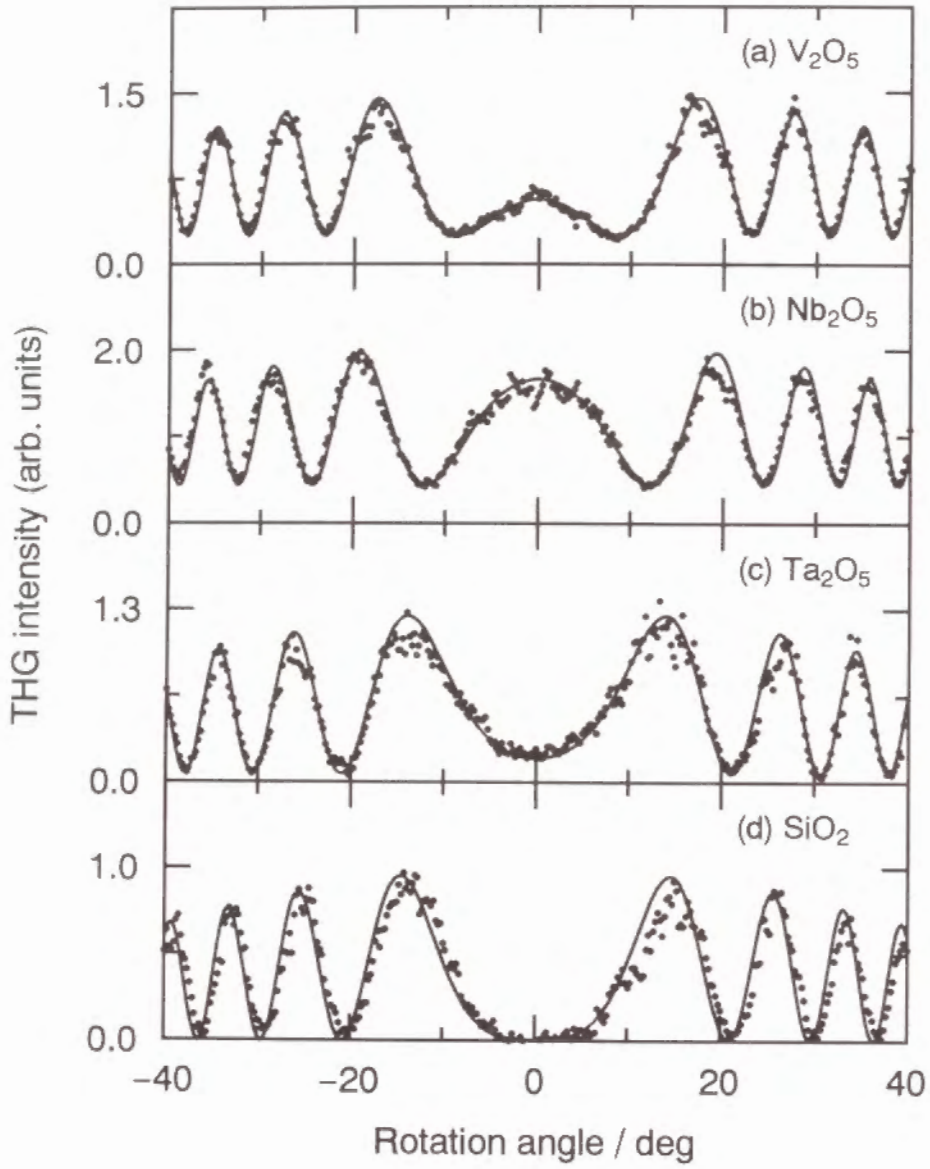

Fig. 5. THG intensities as a function of rotation angle for (a) V_2O_5 films, (b) Nb_2O_5 films, (c) Ta_2O_5 films and (d) SiO_2 glass. Solid curves are computed using the least squares method.

films and SiO_2 glass substrate as previously reported [8]. The THG intensities were obtained by the least squares method as solid curves in Fig. 5.

In the present study, $\chi^{(3)}$ was determined by the equation [10]

$$\chi^{(3)}_{film} = \frac{2}{\pi}\chi^{(3)}_{SiO_2}\frac{\ell_{c,\,SiO_2}}{\ell}\sqrt{\frac{I_{3\omega,\,film}}{I_{3\omega,\,SiO_2}}}\sqrt{\frac{n^3_{\omega,\,film}n_{3\omega,\,film}T^3_{\omega,\,SiO_2}T_{3\omega,\,SiO_2}}{n^3_{\omega,\,SiO_2}n_{3\omega,\,SiO_2}T^3_{\omega,\,film}T_{3\omega,\,film}}}\ (esu)\ , \qquad (2)$$

where I denotes the THG peak intensity, ℓ the film thickness and T the transmittance. The values of $\chi^{(3)}_{SiO_2}=2.8\times10^{-14}$ esu and $\ell_{c,SiO_2}=18.1\ \mu$m were used for SiO_2 glass as both standard sample and substrate [11].

The intensities of the THG signals generated from V_2O_5, Nb_2O_5 and Ta_2O_5 films were determined by the equation [8]

$$I_{film} = \frac{I_{max}+I_{min}}{2} - \frac{I_{substrate}}{2} = \frac{I_{max}+I_{min}}{2} - \frac{I_{SiO_2}}{2}\ , \qquad (3)$$

where I_{max} and I_{min} are the upper and lower envelopes of the superimposed THG intensity pattern, respectively. The THG light from the additional SiO_2 coating on V_2O_5 (or Nb_2O_5 and Ta_2O_5) films was neglected, because $\chi^{(3)}_{SiO_2}$ itself is very small and moreover the thickness of SiO_2 coating (less than ~0.2 μm) is much smaller than the coherence length. The $\chi^{(3)}$ values of V_2O_5, Nb_2O_5 and Ta_2O_5 films were determined to be 1.1×10^{-11}, 1.3×10^{-12} and 6.1×10^{-13} esu, respectively. Table 1 summarizes the optical properties of V_2O_5, Nb_2O_5 and Ta_2O_5 thin films.

Table 1. Optical properties of V_2O_5, Nb_2O_5 and Ta_2O_5 thin films.

Compound	$n_{3\omega}$	n_ω	$T_{3\omega}$ / %	T_ω / %	E_0 / eV	E_d / eV	E_g / eV	$\frac{I_{3\omega,film}}{I_{3\omega,SiO_2}}$	ℓ_c / μm	ℓ / μm	$\chi^{(3)}$ / esu
V_2O_5	2.59	2.31	65.5	81.5	3.8	16.0	2.5	0.39	1.1	0.08	1.1×10^{-11}
Nb_2O_5	2.20	2.12	83.2	75.4	6.0	20.7	3.2	0.77	3.6	0.74	1.3×10^{-12}
Ta_2O_5	2.09	2.03	93.9	81.6	7.3	22.8	4.2	0.19	6.1	0.57	6.1×10^{-13}

The physical meanings of all the notations in the table are described in the section 3.
Transmittances are values for V_2O_5, Nb_2O_5 and Ta_2O_5 thin films with additional SiO_2 coating.

4. Discussion

4.1 Relation between $\chi^{(3)}$ and Refractive Index, n

It is possible to estimate $\chi^{(3)}$ of a material from refractive index, n, according to Miller's rule [1, 2]

$$\chi^{(3)} = [\chi^{(1)}]^4\times10^{-10}\ (esu)\ , \tag{4–a}$$

and

$$\chi^{(1)} = \frac{n^2-1}{4\pi}\ . \tag{4–b}$$

The $\chi^{(3)}$ values of 1.4×10^{-12}, 5.9×10^{-13} and 3.9×10^{-13} esu, which are predicted by Miller's rule for V_2O_5, Nb_2O_5 and Ta_2O_5 thin films, respectively, as in the second row of Table 2, are not in good accordance with the measured ones, 1.1×10^{-11}, 1.3×10^{-12} and 6.1×10^{-13} esu, as in the first row.

Figure 6 shows a relation between $\chi^{(3)}$ and refractive index, n_ω, at 1900 nm for V_2O_5, Nb_2O_5 and Ta_2O_5 thin films together with other NLO materials reported so far [10–17]. There is seen a clear tendency that inorganic materials with the high refractive index inherently exhibit the high $\chi^{(3)}$.

$\chi^{(3)}$ of organic polymers such as polydiacetylene (PDA) [15] and poly(2,5–dimethoxy *p*–phenylene vinylene) (MO–PPV) [16] deviates from the relation to a considerable extent due to the enhancement by the so–called three–photon resonance or near three–photon resonance [18]. In such case, $\chi^{(3)}$ is complex and there are no simple relations between $\chi^{(3)}$ and refractive index, that is, Miller's rule no longer holds.

Table 2. Comparison of the measured $\chi^{(3)}$ with the calculated $\chi^{(3)}$ for V_2O_5, Nb_2O_5 and Ta_2O_5 thin films on the basis of three models.

	$\chi^{(3)}$ / esu		
	V_2O_5	Nb_2O_5	Ta_2O_5
Measured value	1.1×10^{-11}	1.3×10^{-12}	6.1×10^{-13}
Miller's rule	1.4×10^{-12}	5.9×10^{-13}	3.9×10^{-13}
Band gap model	1.2×10^{-11}	2.3×10^{-12}	6.1×10^{-13}
Lines' model	4.3×10^{-12}	1.1×10^{-12}	5.7×10^{-13}

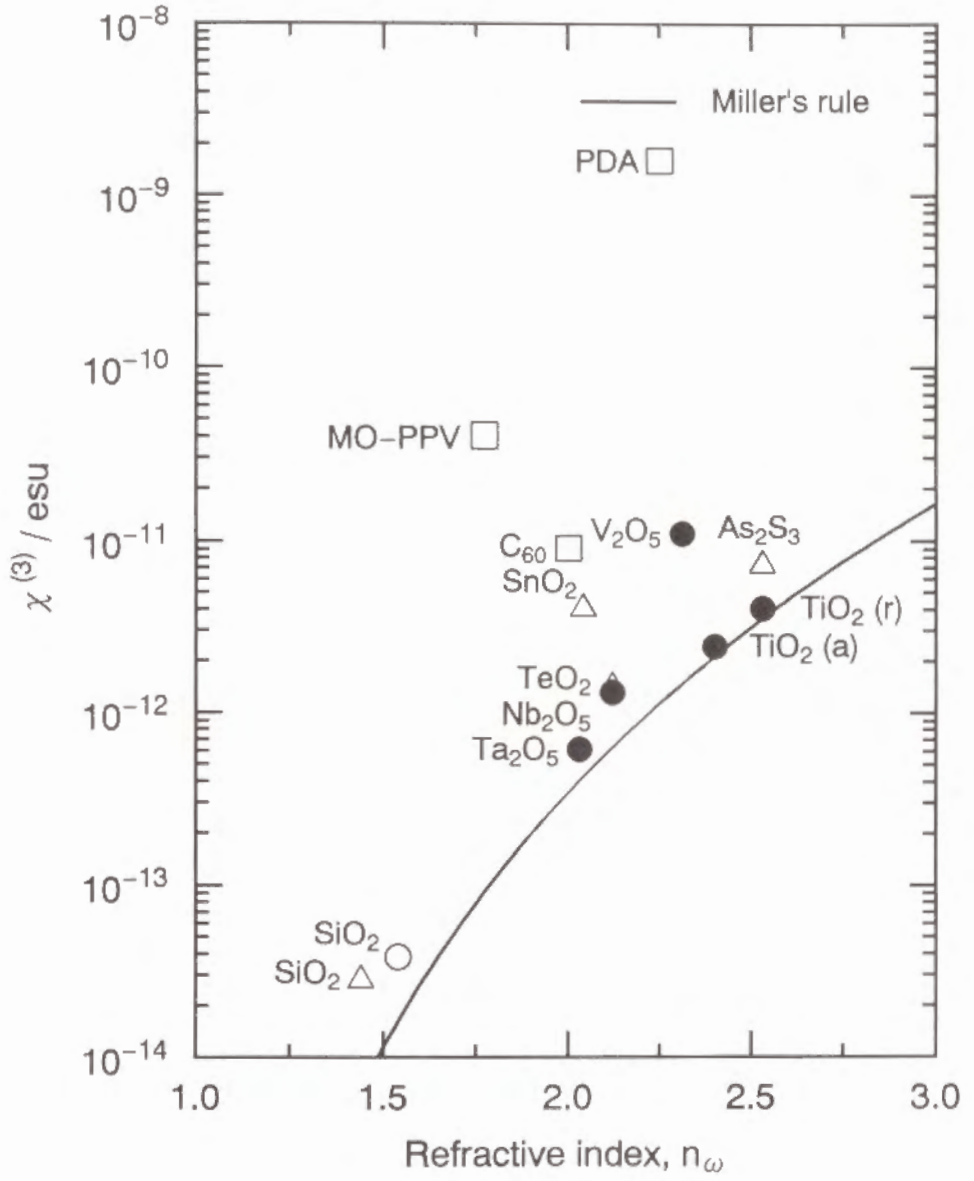

Fig. 6. Relation between $\chi^{(3)}$ and refractive index, n_ω, at 1900 nm for V_2O_5, Nb_2O_5 and Ta_2O_5 thin films together with other NLO materials. Circles, triangles and squares denote inorganic crystals, inorganic amorphous materials and organic materials, respectively. Closed circles are the data measured in the present study. Letters of r and a in parentheses denote rutile and anatase, respectively. PDA: polydiacetylene, MO-PPV: poly(2,5-dimethoxy *p*-phenylene vinylene).

4.2 Relation between $\chi^{(3)}$ and Optical Band Gap, E_g

One can expect that an enhancement in $\chi^{(3)}(-3\omega;\omega,\omega,\omega)$ occurs when a frequency of interacting light approaches either one of one-, two- or three-photon resonance frequency according to the relation [18]

$$\chi^{(3)}(-3\omega;\omega,\omega,\omega) \propto \frac{N}{\hbar^3}\sum_{gnmn'}\rho(g)F(\omega)\Omega_{gn}\Omega_{nm}\Omega_{mn'}\Omega_{n'g}\ (esu)\ , \qquad (5\text{-a})$$

and

$$F(\omega) = \frac{1}{(E_{ng}-3\omega)(E_{mg}-2\omega)(E_{n'g}-\omega)} + \frac{1}{(E_{ng}+\omega)(E_{mg}-2\omega)(E_{n'g}-\omega)} + \frac{1}{(E_{ng}+\omega)(E_{mg}+2\omega)(E_{n'g}-\omega)} + \frac{1}{(E_{ng}+\omega)(E_{mg}+2\omega)(E_{n'g}+3\omega)}\ , \qquad (5\text{-b})$$

where $\rho(g)$, E_{ij} and Ω_{ij} are the density matrix element of fundamental state, the energy difference between states i and j in $\hbar$ (=h/2π, h: Planck's constant) unit and the transition matrix elements between states i and j, respectively. For materials having optical band gap, E_g, higher than three-photon energy, $3\hbar\omega$, the three-photon resonance makes the greatest contribution to the enhancement of $\chi^{(3)}$. Then, to a good approximation, the most significant term due to the three-photon resonance in Eq. (5) may be expressed as follows:

$$\chi^{(3)} = \frac{A}{(E_g-1.96)(E_g-1.31)(E_g-0.65)}\ (esu)\ (E_g>1.96)\ , \qquad (6)$$

where A is the phenomenological constant.

Figure 7 gives a relation between $\chi^{(3)}$ and optical band gap, E_g, for V_2O_5, Nb_2O_5 and Ta_2O_5 thin films together with NLO materials shown in Fig. 6. In Fig. 7, the absorption edge of exciton absorption for some materials is used instead of E_g. It is clear from Fig. 7 that $\chi^{(3)}$ of these materials increases asymptotically as the E_g approaches 1.96 eV corresponding to the three-photon energy. This change obeys Eq. (6) when the parameter, A, takes a value of 1.4×10^{-11}. From Eq. (6), the $\chi^{(3)}$ values were estimated to be 1.2×10^{-11}, 2.3×10^{-12} and 6.1×10^{-13} esu for V_2O_5, Nb_2O_5 and Ta_2O_5, respectively, as in the third row of Table 2, which are in excellent accordance with the measured ones, 1.1×10^{-11}, 1.3×10^{-12} and 6.1×10^{-13} esu, as in the first row.

4.3 Calculation of $\chi^{(3)}$ Based on Lines' Model

Lines introduced a bond-orbital theory to deal with the contribution of the empty *d* orbitals in addition to *sp* orbitals to the linear and nonlinear optical properties, giving the following equation to estimate $\chi^{(3)}$ [6, 19]:

$$\chi^{(3)} = \frac{2.5\times10^{-12}\ell_b^2(n_\omega^2-1)f_L^3E_S^6}{3\pi[E_S^2-E^2]^4}\ (esu)\ , \qquad (7)$$

where ℓ_b denotes the average bond length, $f_L=(n_\omega^2+2)/3$ the Lorentz local-field correction factor, E_S the Sellmeier gap which is in practice equal to the average oscillator energy, E_0, in Eq. (1). It is known that E_s/E_g is ~2 over a wide range of insulators and semiconductors with $E_s \geq 4$ eV. [20] From Eq. (7), one can obtain the $\chi^{(3)}$ values of 4.3×10^{-12}, 1.1×10^{-12} and 5.7×10^{-13} esu for V_2O_5, Nb_2O_5 and Ta_2O_5 films, respectively, as in the fourth row of Table 2, which are in reasonable accordance with the measured ones, 1.1×10^{-11}, 1.3×10^{-12} and 6.1×10^{-13} esu, as in the second row.

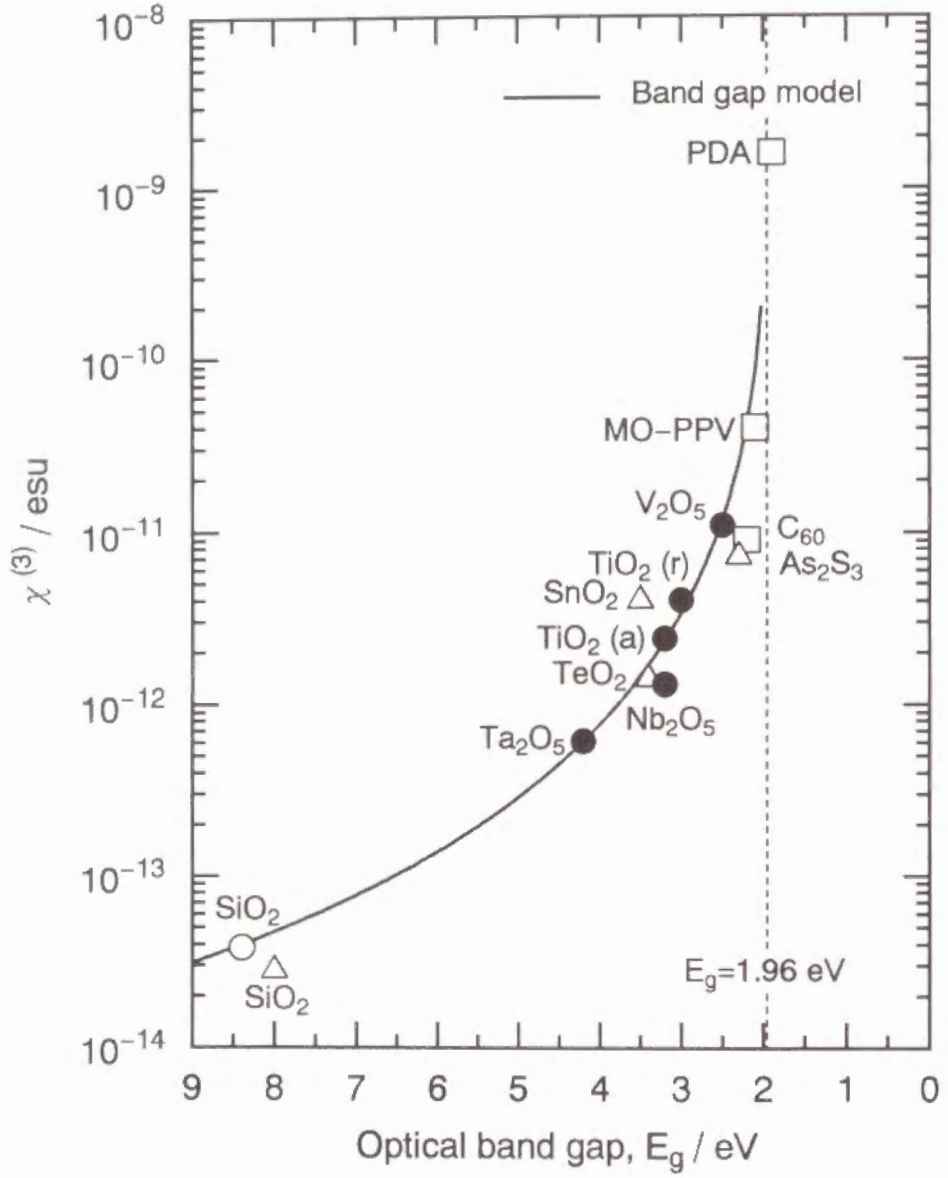

Fig. 7. Relation between $\chi^{(3)}$ and optical band gap, E_g, for V_2O_5, Nb_2O_5 and Ta_2O_5 thin films together with other NLO materials. Notations are the same as in Fig. 6.

Figure 8 shows the comparison of the measured $\chi^{(3)}$(meas.) with the calculated $\chi^{(3)}$(calc.) on the basis of three models for NLO materials cited in Figs. 6 and 7. It is obvious that the consistency between them increases in the order:

Miller's rule < band gap model < Lines' model.

This means that $\chi^{(3)}$ of a material depends on the optical band gap rather than the refractive index, if one takes into consideration that Miller's rule, band gap model and Lines' model deal with n, E_g, and both E_s (or E_g) and n, respectively.

4.4 Effect of Metal–Oxygen Bond Length on $\chi^{(3)}$ of Transition Metal and Non–Transition Metal Oxides

Relations between Sellmeier gap, E_s, and bond length, ℓ_b, for transition metal (T.M.) and non–transition metal oxides are shown in Figure 9–(a). [6, 9] In non–transition metal oxides, E_s increases with decreasing ℓ_b, which can be interpreted in terms of the electronic repulsion between the bonding and antibonding orbitals. On the contrary, E_s of transition metal oxides decreases almost linearly with decreasing ℓ_b according to the equation [6]:

$$E_S = 15(\ell_b - 1.6)\ (eV). \tag{8}$$

This phenomenon can be explained by considering that overlapping between the empty d orbitals of transition metal and O $2p$ orbitals, $\langle d|p\rangle$, becomes large with decreasing ℓ_b, and E_s is dominated by the resultant broadening of both conduction and valence bands rather than the electronic repulsion between the bonding and antibonding orbitals. [6] It is also seen from Fig. 9–(a) that the influence of the metal–oxygen bond length on E_s of transition metal oxides is much larger than that of the valence and coordination number of metal cation.

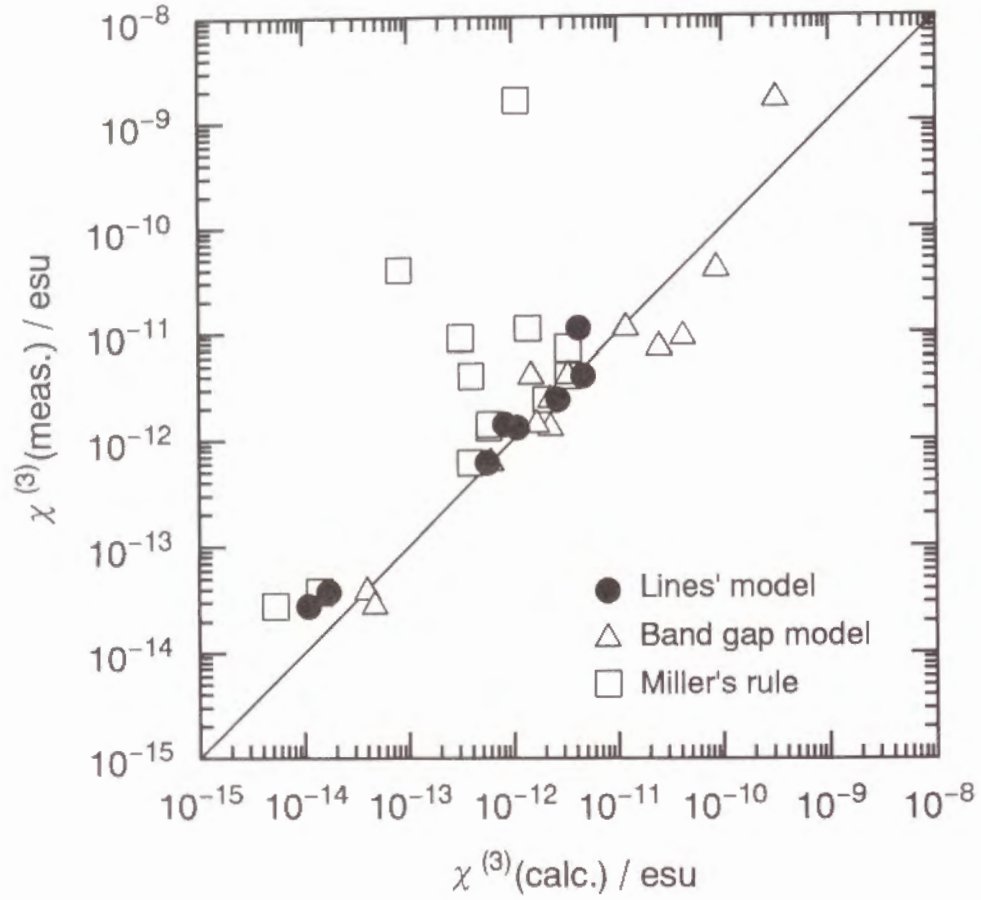

Fig. 8. Comparison of the measured $\chi^{(3)}$(meas.) with the calculated $\chi^{(3)}$(calc.) on the basis of three models for NLO materials cited in Figs. 6 and 7.

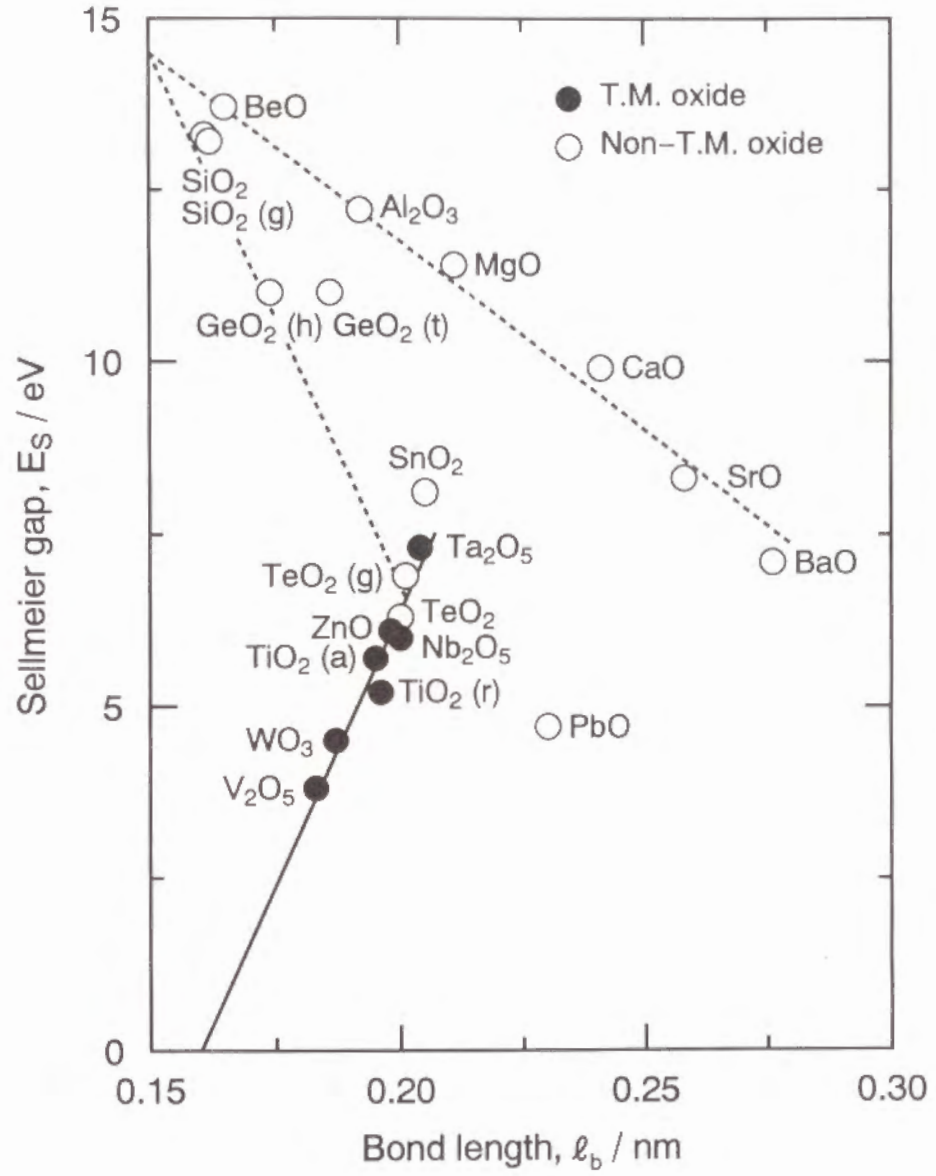

Fig. 9(a). Relations between Sellmeier gap, E_s and bond length, ℓ_b, for transition metal (T.M.) and non–transition metal oxides.

Relations between refractive index, n_ω, and ℓ_b for oxides plotted in Fig. 9–(b) are given. [6, 9] For non–transition metal oxides, n decreases with an decrease of ℓ_b while n of transition metal oxides increases with an decrease of ℓ_b.

Figure 9–(c) shows relations between $\chi^{(3)}$(calc.) calculated from Eq. (7) and ℓ_b for oxides plotted in Figs. 9–(a) and 9–(b). E_s of Sc_2O_3, HfO_2, ZrO_2, Y_2O_3, CeO_2 and La_2O_3 was calculated from Eq. (8). It is expected from Fig. 9–(c) that transition metal oxides with the shortest ℓ_b show the highest $\chi^{(3)}$ while non–transition metal oxides with the longest ℓ_b do the highest $\chi^{(3)}$. This is attributed to the fact that $\chi^{(3)}$ of a material is enhanced by the optical band gap (or Sellmeier gap) close to the resonance photon energy and the high refractive index, which can be achieved by the shortest and longest ℓ_b for transition metal and non–transition metal oxides, respectively.

In fact, the $\chi^{(3)}$ values of V_2O_5, Nb_2O_5 and Ta_2O_5 thin films were 1.1×10^{-11}, 1.3×10^{-12} and 6.1×10^{-13} esu, respectively, which corresponds to an increase of the average bond length in the order of V–O (ℓ_b=0.183 nm), Nb–O (ℓ_b=0.200 nm) and Ta–O (ℓ_b=0.204 nm). The relation also applies to TiO_2 polymorphs ($\chi^{(3)}=4.0\times10^{-12}$ esu, ℓ_b=0.196 nm for rutile: $\chi^{(3)}=2.4\times10^{-12}$ esu, ℓ_b=0.195 nm for anatase) with different valence of metal cation. The results indicate that $\chi^{(3)}$ of these transition metal oxides with the empty *d* orbitals is dominated mainly by the metal–oxygen bond length rather than the valence of metal cation. However, it should be noted that the shortest bond length in coordination polyhedra of transition metal cations does not always contribute to the enhancement of $\chi^{(3)}$. As mentioned above, $\chi^{(3)}$ of rutile is higher than that of anatase. In both TiO_2 polymorphs, the average bond lengths are almost the same (0.196 nm for rutile, 0.195 nm for anatase) and the shortest bond length in the former is smaller than that in the latter (0.195 nm for rutile, 0.193 nm for anatase). The presence of the shortest bond length, or the

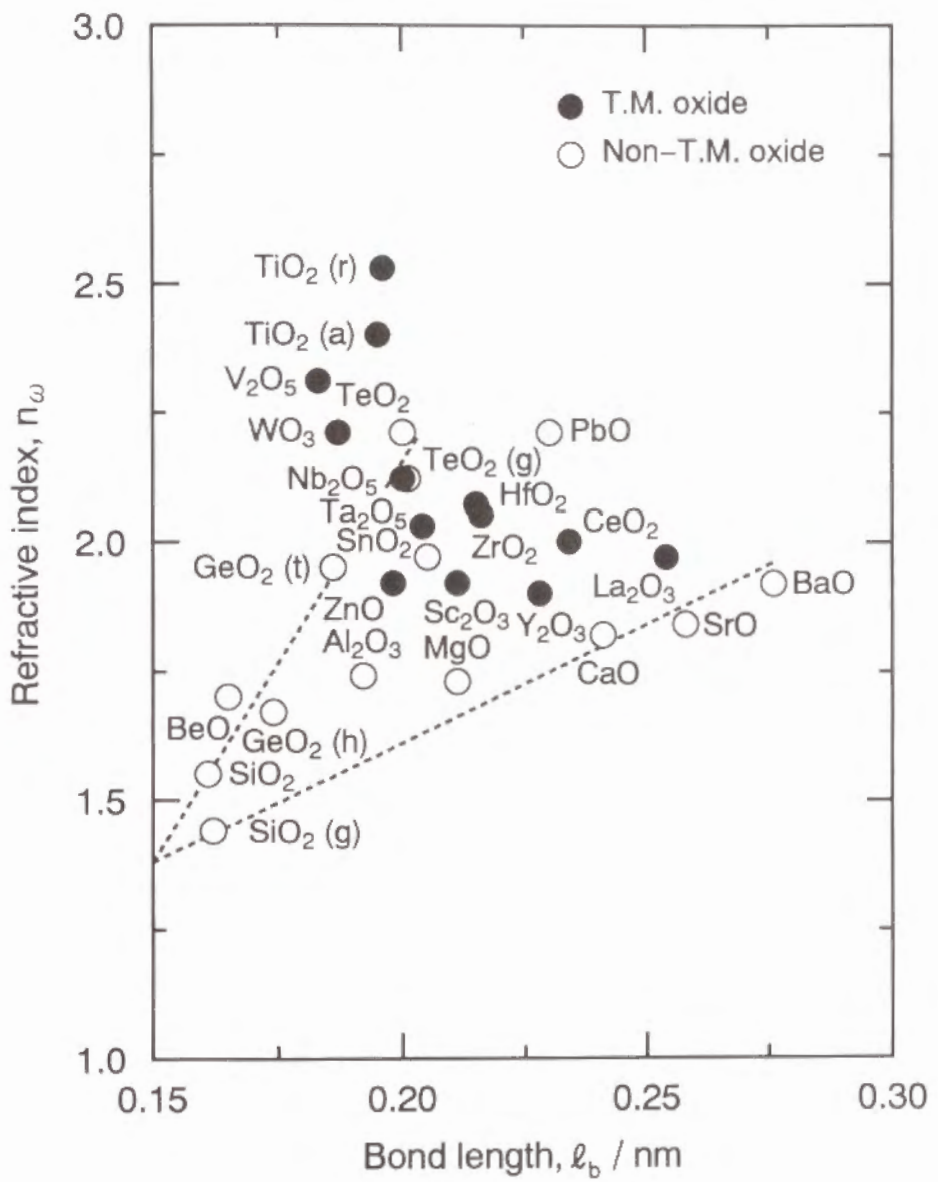

Fig. 9(b). Relations between refractive index, n_ω and bond length, ℓ_b, for transition metal (T.M.) and non–transition metal oxides.

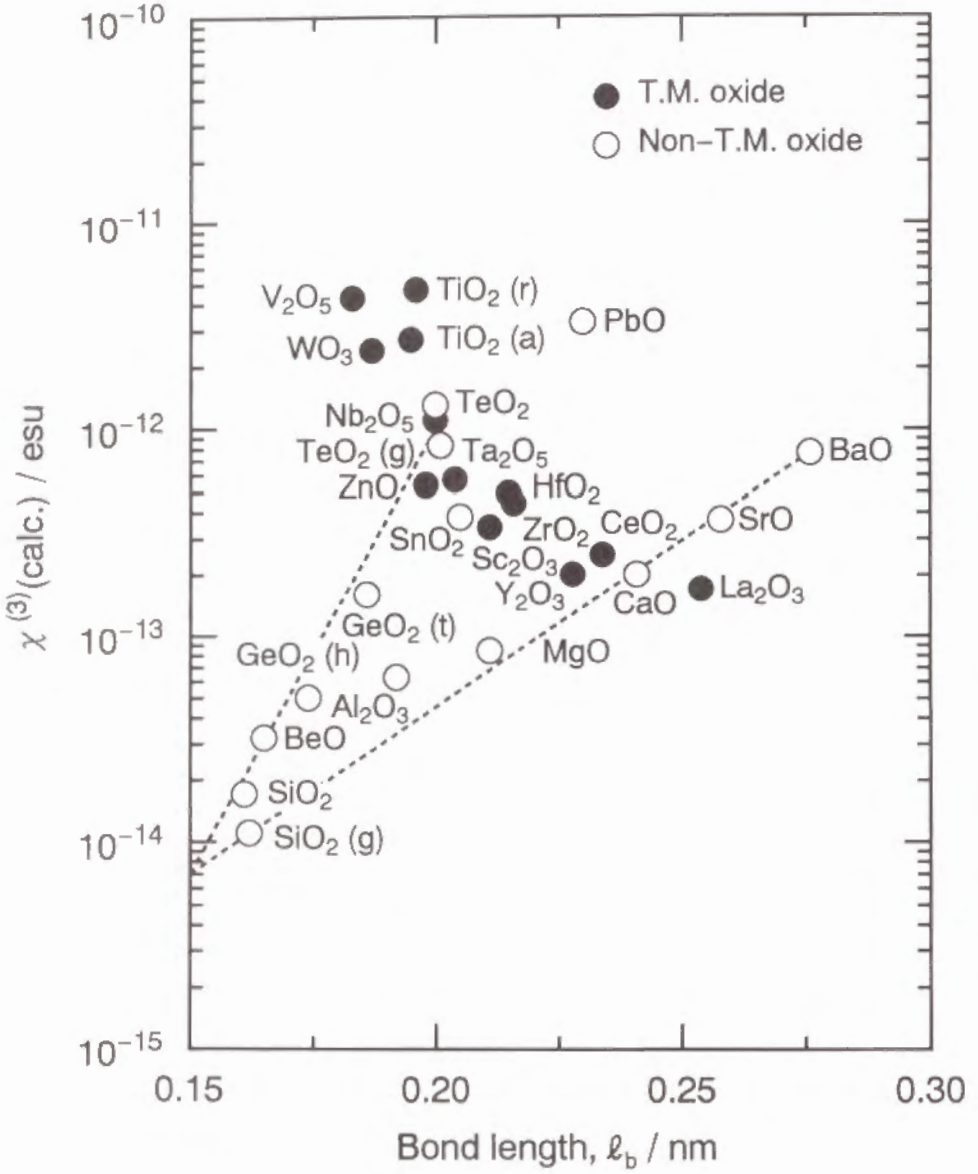

Fig. 9(c). Relations between $\chi^{(3)}$(calc.) and bond length, ℓ_b, for transition metal (T.M.) and non–transition metal oxides.

low symmetry of coordination polyhedra of metal cations may reduce the overlapping between *d* orbitals of transition metal and O 2*p* orbitals.

Lines states that the contribution of *d* orbitals to the linear and nonlinear optical properties is negligible for $\ell_b > 0.23$ nm, but it increases rapidly for $\ell_b < 0.20$ nm. [6] In fact, $\chi^{(3)}$ of transition metal oxides seems to be much higher than those of non–transition metal oxides especially, for $\ell_b < 0.20$ nm as clearly seen from Fig. 9–(c). Therefore, compounds including small transition metals and large non–transition metals such as Pb–containing perovskites are also considered to be promising NLO materials, for which preparation and characterization are on the way in this laboratory.

5. Conclusion

In this chapter, the third–order nonlinear optical properties of the sol–gel derived V_2O_5, Nb_2O_5 and Ta_2O_5 thin films have been investigated by the THG method. Mainly, the effect of the local structures (metal–oxygen bond length and valence of cation) on $\chi^{(3)}$ of transition metal oxides with empty *d* orbitals have been examined in comparison with non–transition metal oxides. The following results were obtained.

(1) The $\chi^{(3)}$ values of V_2O_5, Nb_2O_5 and Ta_2O_5 thin films are 1.1×10^{-11}, 1.3×10^{-12} and 6.1×10^{-13} esu, respectively, which is in reverse relation to an increase of the average bond length in the order of V–O (ℓ_b=0.183 nm), Nb–O (ℓ_b=0.200 nm) and Ta–O (ℓ_b=0.204 nm).

(2) The above relation is also applicable to TiO_2 polymorphs ($\chi^{(3)}$=4.0×10^{-12} esu, ℓ_b=0.196 nm for rutile: $\chi^{(3)}=2.4\times10^{-12}$ esu, ℓ_b=0.195 nm for anatase) with different valence of metal cation from the above metal cations. The results indicate that $\chi^{(3)}$ of these transition metal oxides with the empty *d* orbitals is dominated mainly by the metal–oxygen bond length rather than the valence of metal cation.

(3) It is predicted on the basis of Lines' model that transition metal oxides with the shortest ℓ_b have the highest $\chi^{(3)}$ while non-transition metal oxides with the longest ℓ_b do the highest $\chi^{(3)}$.

References

[1] R. C. Miller, *Appl. Phys. Lett.*, **5**, 17 (1964).

[2] C. C. Wang, *Phys. Rev. B*, **2**, 2045 (1970).

[3] D. M. Sherman, *Phys. Chem. Minerals*, **12**, 161 (1985).

[4] J. A. Tossell, in "Chemical Bonding and Spectroscopy in Mineral Chemistry", ed. by F. J. Berry and D. J. Vaughan, Chapman and Hall, London (1985) p. 1.

[5] D. J. Vaughan, in "Chemical Bonding and Spectroscopy in Mineral Chemistry", ed. by F. J. Berry and D. J. Vaughan, Chapman and Hall, London (1985) p. 251.

[6] M. E. Lines, *Phys. Rev. B*, **43**, 11978 (1991).

[7] K. H. Guenther, T. W. Humpherys, J. Balmer, J. R. Bettis, E. Casparis, J. Ebert, M. Eichner, A. H. Guenther, E. Kiesel, R. Kuehnel, D. Milam, W. Ryseck, S. C. Seitel, A. F. Stewart, H. Weber, H. P. Weber, G. R. Wirtenson and R. M. Wood, *Appl. Opt.*, **23**, 3743 (1984).

[8] K. Kubodera and H. Kobayashi, *Mol. Cryst. Liq. Cryst.*, **182A**, 103 (1990).

[9] S. H. Wemple, *J. Chem. Phys.*, **67**, 2151 (1977).

[10] H. Nasu, K. Kubodera, M. Kobayashi, M. Nakamura and K. Kamiya, *J. Am. Ceram. Soc.*, **73**, 1794 (1990).

[11] G. R. Meredith, B. Buchalter and C. Hanzlik, *J. Chem. Phys.*, **78**, 1533 (1983).

[12] G. R. Meredith, *Phys. Rev. B*, **24**, 5522 (1981).

[13] N. Ueda, H. Kawazoe, Y. Watanabe, M. Takata, M. Yamane and K. Kubodera, *Appl. Phys. Lett.*, **59**, 502 (1991).

[14] S. H. Kim, T. Yoko and S. Sakka, *J. Am. Ceram. Soc.*, **76**, 2486 (1993).

[15] T. Kanetake, K. Ishikawa, T. Hasegawa, T. Koda, K. Takeda, M. Hasegawa, K. Kubodera and H. Kobayashi, *Appl. Phys. Lett.*, **54**, 2287 (1989).

[16] T. Kurihara, Y. Mori, T. Kaino, H. Murata, N. Takada, T. Tsutsui and S. Saito, *Chem. Phys. Lett.*, **183**, 534 (1991).

[17] J. S. Meth, H. Vanherzeele and Y. Wang, *Chem. Phys. Lett.*, **197**, 26 (1992).

[18] F. Kajzar and J. Messier, in "Nonlinear Optical Properties of Organic Molecules and Crystals, **2**", ed. by D. S. Chemla and J. Zyss, Academic Press, New York (1987) p. 51.

[19] M. E. Lines, *Phys Rev. B*, **41**, 3383 (1990).

[20] M. E. Lines, *J. Appl. Phys.*, **69**, 6876 (1991).

CHAPTER 3. THIRD-ORDER NONLINEAR OPTICAL PROPERTIES OF α-Fe_2O_3, γ-Fe_2O_3 AND Fe_3O_4 THIN FILMS

SECTION 3.1 EFFECT OF CORUNDUM ISOMORPH (α-Fe_2O_3 AND α-Al_2O_3) ON $\chi^{(3)}$

1. Introduction

As presented in Chapters 1 and 2, the third-order nonlinear optical susceptibility, $\chi^{(3)}$, of transition metal oxides with empty *d* orbitals in a form of thin films such as and TiO_2, V_2O_5, Nb_2O_5 and Ta_2O_5 is as high as 10^{-12} to 10^{-11} esu, which is higher than that of SiO_2 glass by two to three orders of magnitude. As a result, it was concluded that the high $\chi^{(3)}$ of materials containing transition metal oxides is attributed to the high refractive index and the optical band gap close to the three-photon energy. Since they generally satisfy the above two requirements, transition metal oxides with partly filled *d* orbitals, especially, α-Fe_2O_3 (n~3 and E_g~2 eV) are also considered to be promising nonlinear optical (NLO) materials.

There have been no comparative studies on $\chi^{(3)}$ of inorganic oxides with the same structure and quite different optical properties such as refractive index and band gap. For this purpose, α-Al_2O_3 was selected, which has the same corundum crystal structure as α-Fe_2O_3.

In this section, the results of the preparation of α-Fe_2O_3 thin films on SiO_2 glass substrates by the sol-gel method and the third-order nonlinear optical properties of α-Fe_2O_3 thin films and α-Al_2O_3 single crystal $(11\bar{2}0)$ studied by the THG method are presented. The effect of corundum isomorph (α-Fe_2O_3 and α-Al_2O_3) on $\chi^{(3)}$ is described.

2. Experimental

2.1 Preparation of α-Fe_2O_3 thin films

α-Fe_2O_3 thin films were prepared by the sol-gel method. Iron (III) nitrate enneahydrate ($Fe(NO_3)_3 \cdot 9H_2O$) was dissolved in a mixture of

2-methoxyethanol ($CH_3OCH_2CH_2OH$) and 2,4-pentanedione ($CH_3COCH_2COCH_3$) and allowed to stand for 2 h at 30 °C. The molar ratios of 2-methoxyethanol and 2,4-pentanedione to iron nitrate enneahydrate were 20 and 2, respectively. Dip-coating was used for film formation. A SiO_2 glass substrate was immersed into a coating solution, and pulled up at a rate of 3 cm min^{-1}. The films were heated at 800 °C for 10 min immediately after each coating procedure. This cycle was repeated 4 times to attain the desired film thickness.

2.2 α-Al_2O_3 Single Crystal

α-Al_2O_3 single crystal ($11\bar{2}0$) was supplied by Kyocera, Inc. The sample of 320 μm in thickness was used for the measurement.

2.3 Characterization of α-Fe_2O_3 Thin Films and α-Al_2O_3 Single Crystal

For reason mentioned in Chapter 1, an SiO_2 coating was further applied onto the α-Fe_2O_3 films and then the α-Fe_2O_3 and additional SiO_2 films on one face were removed. α-Fe_2O_3 films and α-Al_2O_3 single crystal were characterized by X-ray diffraction, ellipsometry, UV-visible spectrophotometry and THG measurements as gone into details in Chapter 1.

3. Results

3.1 Crystallization Behavior

Figure 1 shows the X-ray diffraction pattern of α-Fe_2O_3 thin films prepared by the sol-gel method. The crystalline phase precipitated in the sol-gel derived α-Fe_2O_3 thin films was identified referring to JCPDS-FILE 33-0664 (hexagonal). Preferable orientation along the (001) plane is not seen for α-Fe_2O_3 films. The crystallite size in the α-Fe_2O_3 films was ~35 nm.

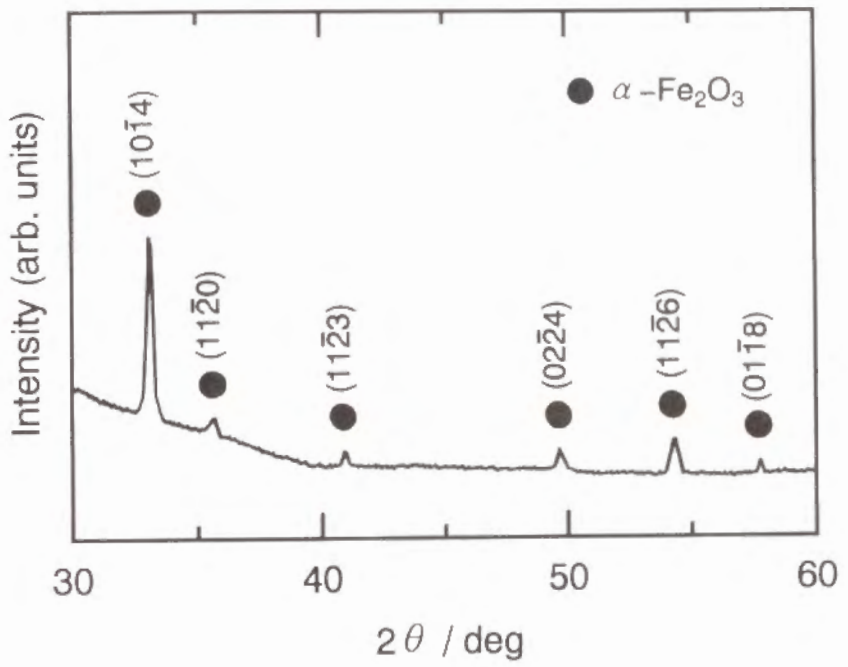

Fig. 1. X-ray diffraction pattern of α-Fe_2O_3 thin films prepared by the sol-gel method.

3.2 Refractive Index and Optical Transmittance

The wavelength dependencies of refractive index, n, for α–Fe_2O_3 thin films and α–Al_2O_3 single crystal are shown in Figure 2. It can be seen that the refractive index of α–Fe_2O_3 films strongly depends on the wavelength in contrast with that of α–Al_2O_3 single crystal which remains almost unchanged within the wavelength range in this measurement. Figure 3 presents the linear plots of $(n^2-1)^{-1}$ versus E^2 for α–Fe_2O_3 thin films and α–Al_2O_3 single crystal based on Wemple's equation [1]

$$\frac{1}{n^2-1} = \frac{E_0}{E_d} - \frac{E^2}{E_0 E_d}, \qquad (1)$$

where E, E_0 and E_d are the photon energy, the average oscillator energy and dispersion energy in eV unit, respectively. E_0 and E_d are important optical properties of materials [1]. The refractive indices were estimated as $n_{3\omega}$=3.00 at 633 nm and n_ω=2.57 at 1900 nm, and the coherence length, ℓ_c=1.9/[6($n_{3\omega}$–n_ω)], was 0.7 μm for α–Fe_2O_3 films. In a similar manner, $n_{3\omega}$, n_ω and ℓ_c for α–Al_2O_3 single crystal were estimated as 1.77, 1.74 and 11.3 μm, respectively. The thickness of the α–Fe_2O_3 films obtained by 4 dippings was 0.07 μm.

Figure 4 shows the absorption spectra of α–Fe_2O_3 thin films with and without additional SiO_2 coating and α–Al_2O_3 single crystal. Most spectra have no mountains and troughs arising from the interference of light due to the small film thickness. It is seen that the additional SiO_2 coating effectively reduces the optical loss due to reflection at the surface especially in the wavelength region above ~600 nm. The optical band gap, E_g, of α–Fe_2O_3 films was estimated to be 2.1 eV. E_g of α–Al_2O_3 was cited to be 7.3 eV [2], which is beyond the measurable wavelength region in the present study.

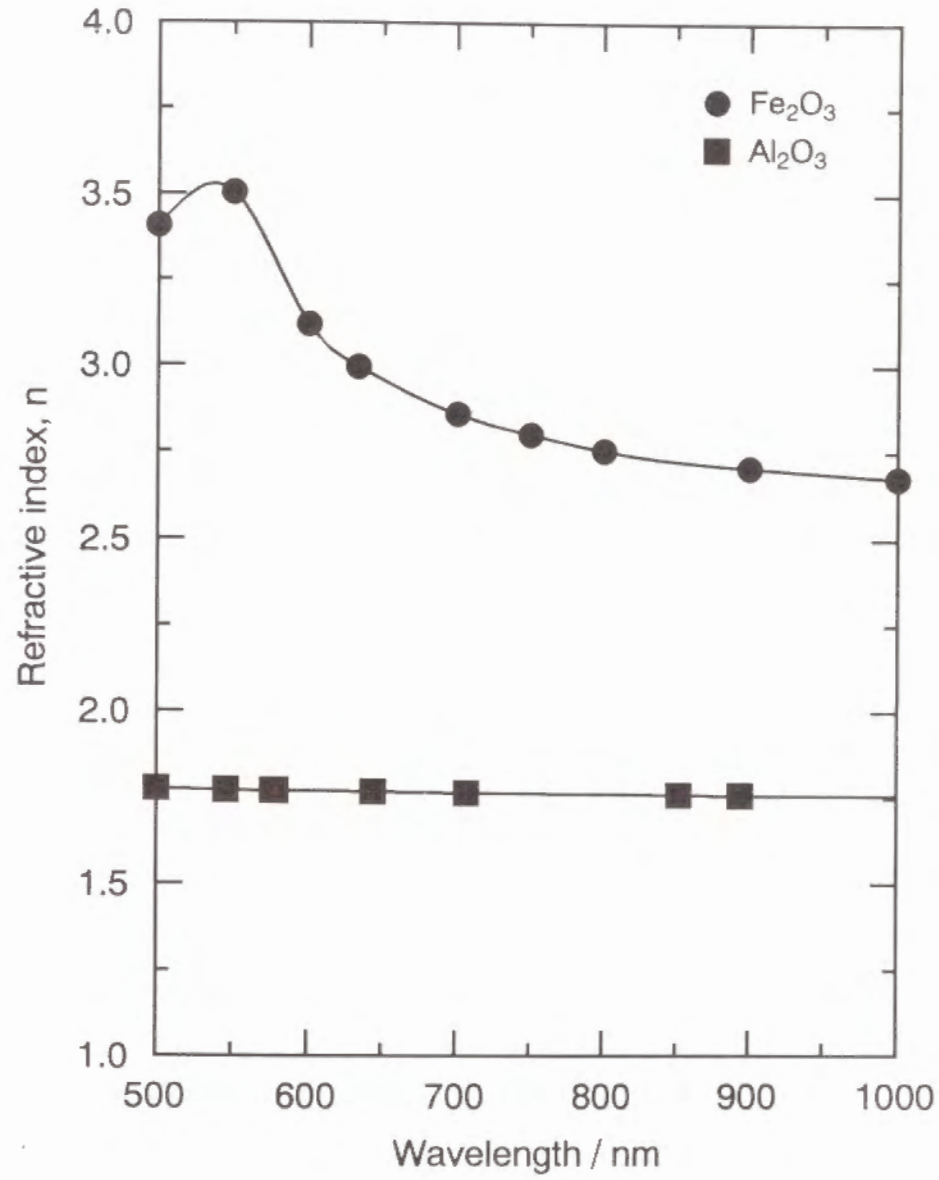

Fig. 2. Wavelength dependencies of refractive index, n, for α–Fe_2O_3 thin films and α–Al_2O_3 single crystal.

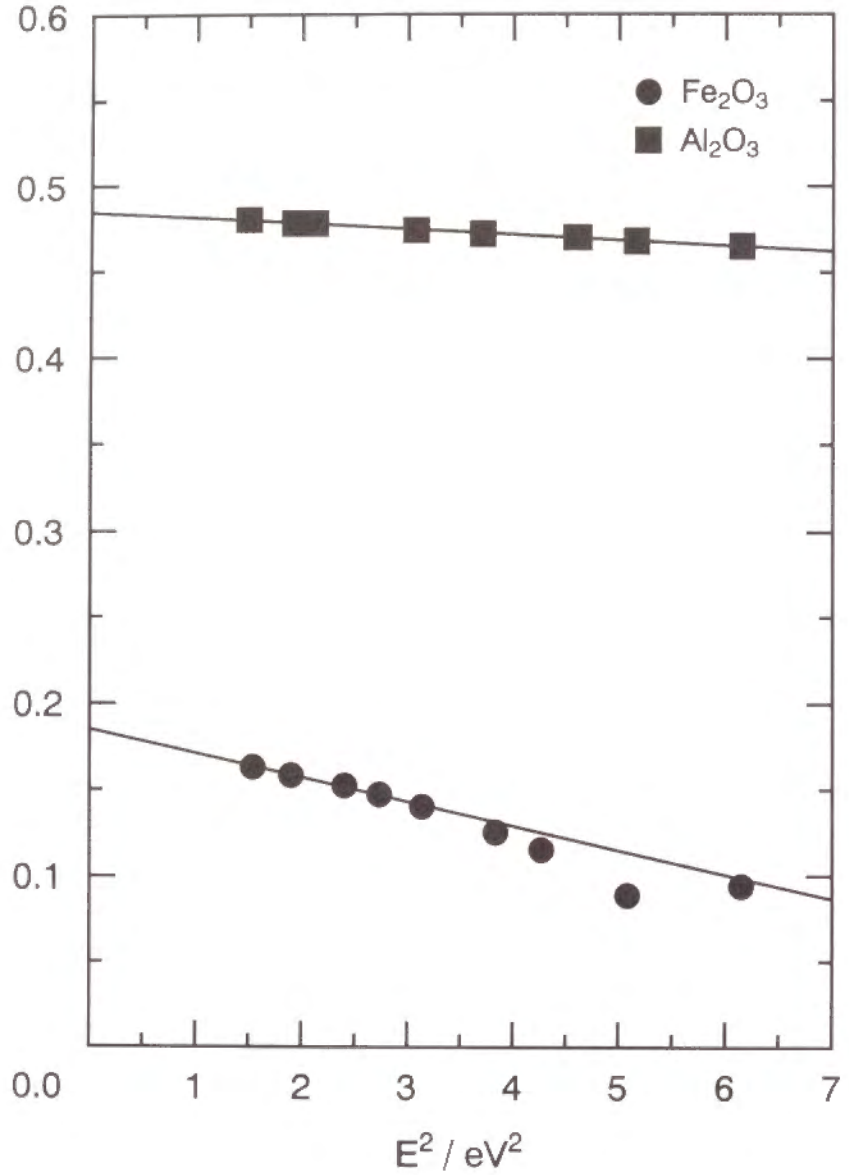

Fig. 3. Linear plots of $(n^2-1)^{-1}$ versus E^2 for α–Fe_2O_3 thin films and α–Al_2O_3 single crystal.

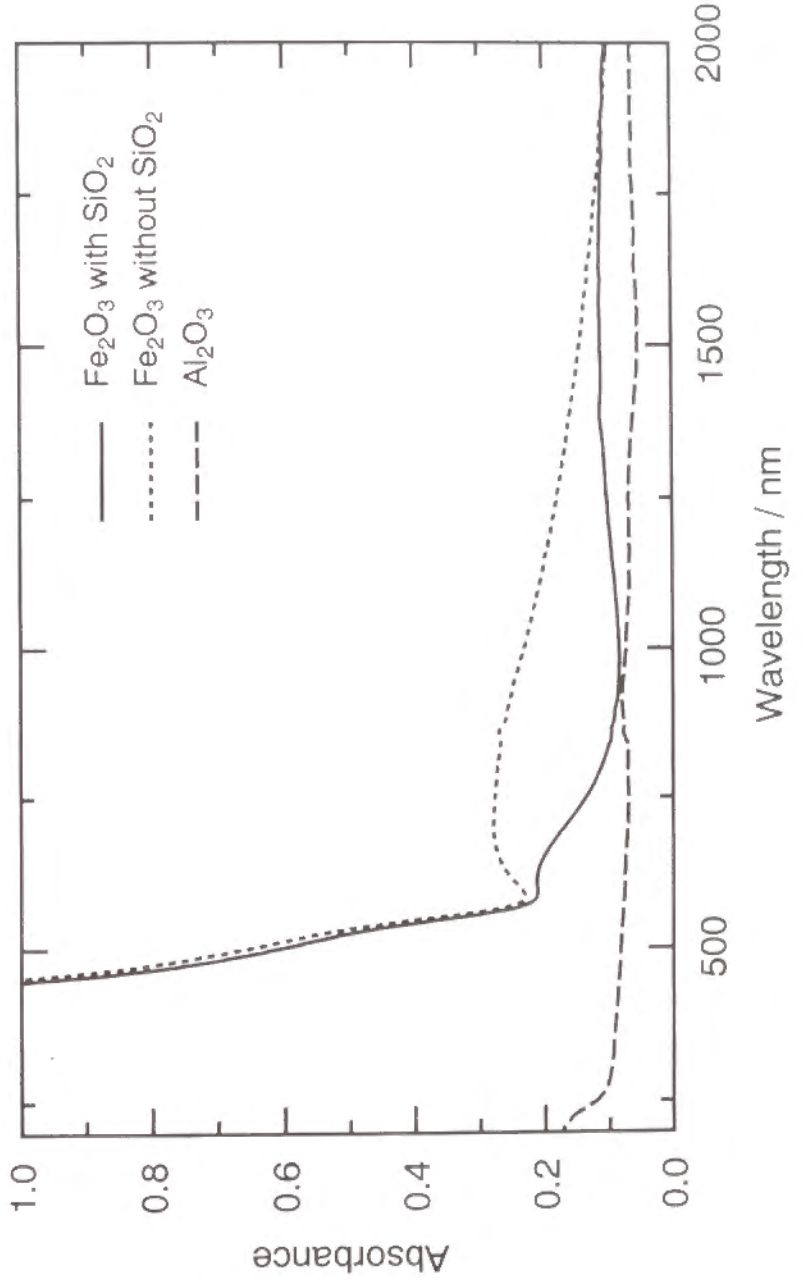

Fig. 4. Absorption spectra of α–Fe_2O_3 thin films with and without additional SiO_2 coating and α–Al_2O_3 single crystal.

3.3 Evaluation of $\chi^{(3)}$ Values

The THG intensities as a function of the rotation angle for (a) α–Fe_2O_3 films, (b) α–Al_2O_3 single crystal, (c) SiO_2 glass are given in Figure 5. The THG intensity pattern of α–Fe_2O_3 films clearly shows the interference between the THG lights from α–Fe_2O_3 films and SiO_2 glass substrate as previously reported [3], while a well-defined Maker fringe pattern was not obtained for α–Al_2O_3 single crystal owing to the small sample thickness. The THG intensity was obtained by the least squares method as solid curve in Fig. 5.

In the present study, $\chi^{(3)}$ was determined by the equation [4]

$$\chi^{(3)}_{film} = \frac{2}{\pi}\chi^{(3)}_{SiO_2}\frac{\ell_{c,\,SiO_2}}{\ell}\sqrt{\frac{I_{3\omega,\,film}}{I_{3\omega,\,SiO_2}}}\sqrt{\frac{n^3_{\omega,\,film}n_{3\omega,\,film}T^3_{\omega,\,SiO_2}T_{3\omega,\,SiO_2}}{n^3_{\omega,\,SiO_2}n_{3\omega,\,SiO_2}T^3_{\omega,\,film}T_{3\omega,\,film}}}\ (esu)\ , \qquad (2)$$

where I denotes the THG peak intensity. The film thickness is used for ℓ, because the film thickness is less than the coherence length. The values of $\chi^{(3)}_{SiO_2}=2.8\times10^{-14}$ esu and $\ell_{c,SiO_2}=18.1$ μm were used for SiO_2 glass as both standard sample and substrate [5].

The intensity of THG signals generated from α–Fe_2O_3 films was determined by the equation [3]

$$I_{film} = \frac{I_{max}+I_{min}}{2} - \frac{I_{substrate}}{2} = \frac{I_{max}+I_{min}}{2} - \frac{I_{SiO_2}}{2}\ , \qquad (3)$$

where I_{max} and I_{min} are the upper and lower envelopes, respectively, of the superimposed THG intensity pattern. The THG light from the additional SiO_2 coating on the α–Fe_2O_3 films was neglected, because $\chi^{(3)}_{SiO_2}$ itself is very small

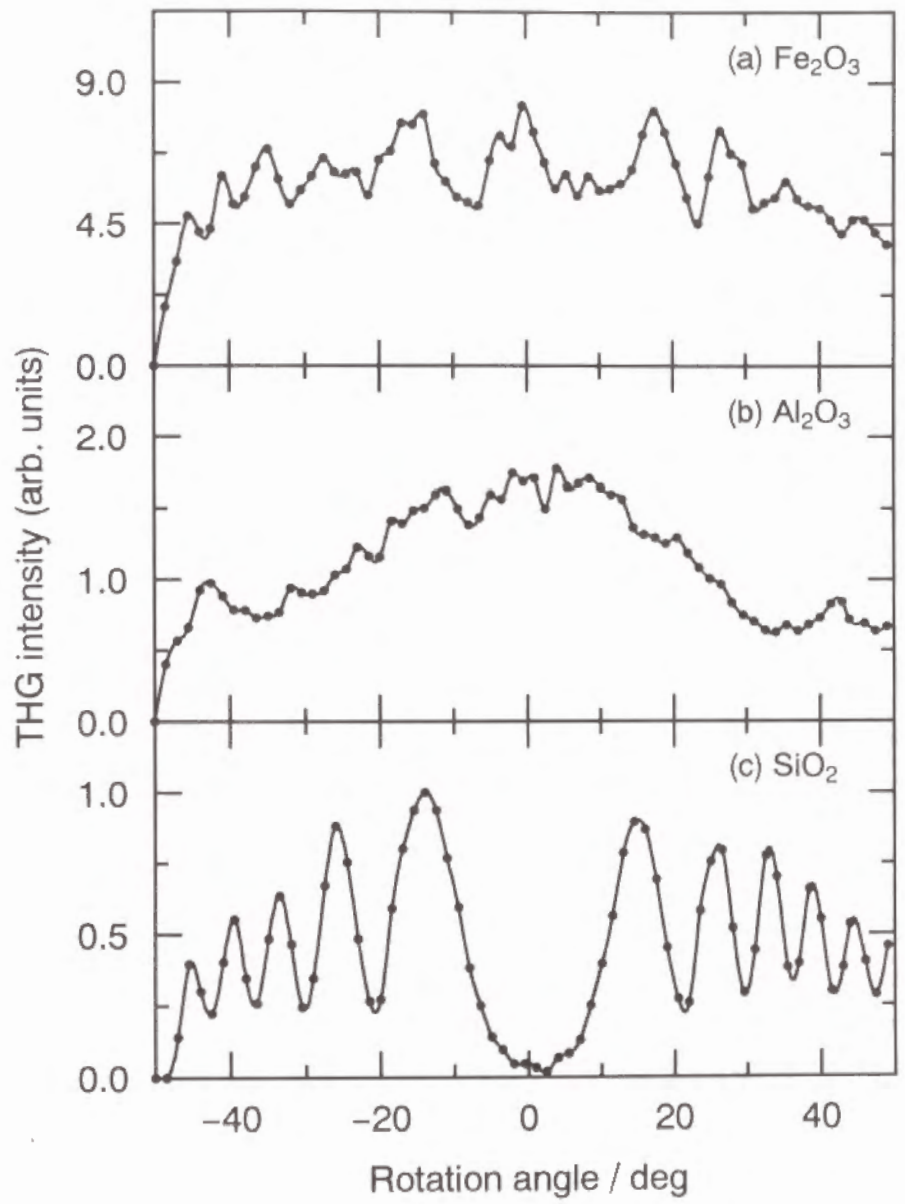

Fig. 5. THG intensities as a function of rotation angle for (a) α–Fe_2O_3 films, (b) α–Al_2O_3 single crystal, (c) SiO_2 glass. Solid curves are computed using the least squares method.

and moreover the thickness of SiO_2 coating (less than ~0.2 μm) is much smaller than the coherence length (18.1 μm). The $\chi^{(3)}$ values of α–Fe_2O_3 films and α–Al_2O_3 single crystal were determined to be 5.8×10^{-11} and 1.0×10^{-13} esu, respectively. Table 1 summarizes the obtained optical properties of α–Fe_2O_3 thin films and α–Al_2O_3 single crystal.

4. Discussion

4.1 Relation between $\chi^{(3)}$ and Refractive Index, n

One can roughly predict $\chi^{(3)}$ of a material from refractive index, n, based on Miller's rule [6, 7]

$$\chi^{(3)} = [\chi^{(1)}]^4\times10^{-10}\ (esu)\ , \qquad (4\text{–a})$$

and

$$\chi^{(1)} = \frac{n^2-1}{4\pi}\ . \qquad (4\text{–b})$$

The $\chi^{(3)}$ values of 3.9×10^{-12} and 6.7×10^{-14} esu, which are predicted by Miller's rule for α–Fe_2O_3 thin films and α–Al_2O_3, respectively, as in the second row of Table 2, are inconsistent with the measured ones, 5.8×10^{-11} and 1.0×10^{-13} esu, as in the first row.

Figure 6 shows a relation between $\chi^{(3)}$ and refractive index, n_ω, at 1900 nm for α–Fe_2O_3 thin films and α–Al_2O_3 single crystal together with other NLO materials reported so far [4, 5, 8–13]. It is found that the α–Fe_2O_3 is one of the inorganic materials with the largest $\chi^{(3)}$ values as expected from generalized Miller's rule. Inorganic materials with the high refractive index tend to exhibit high $\chi^{(3)}$ while $\chi^{(3)}$ of organic polymers such as polydiacetylene

Table 1. Optical properties of α–Fe_2O_3 thin films and α–Al_2O_3 single crystal.

Compound	$n_{3\omega}$	n_ω	$T_{3\omega}$ / %	T_ω / %	E_0 / eV	E_d / eV	E_g / eV	$\frac{I_{3\omega,film}}{I_{3\omega,SiO_2}}$	ℓ_c / μm	ℓ / μm	$\chi^{(3)}$ / esu
α–Fe_2O_3	3.00	2.57	62.4	78.2	3.6	19.4	2.1	5.98	0.7	0.07	5.8×10^{-11}
α–Al_2O_3	1.77	1.74	83.8	86.5	12.2	25.2	7.3	1.60	11.3	320	1.0×10^{-13}

The physical meanings of all the notations in the table are described in the section 3.
Transmittance of α–Fe_2O_3 is value for thin films with additional SiO_2 coating.

Table 2. Comparison of the measured $\chi^{(3)}$ with the calculated $\chi^{(3)}$ for α–Fe_2O_3 thin films and α–Al_2O_3 single crystal on the basis of three models.

	$\chi^{(3)}$ / esu	
	α–Fe_2O_3	α–Al_2O_3
Measured value	5.8×10^{-11}	1.0×10^{-13}
Miller's rule	3.9×10^{-12}	6.7×10^{-14}
Band gap model	8.7×10^{-11}	6.6×10^{-14}
Lines' model	1.3×10^{-11}	6.3×10^{-14}

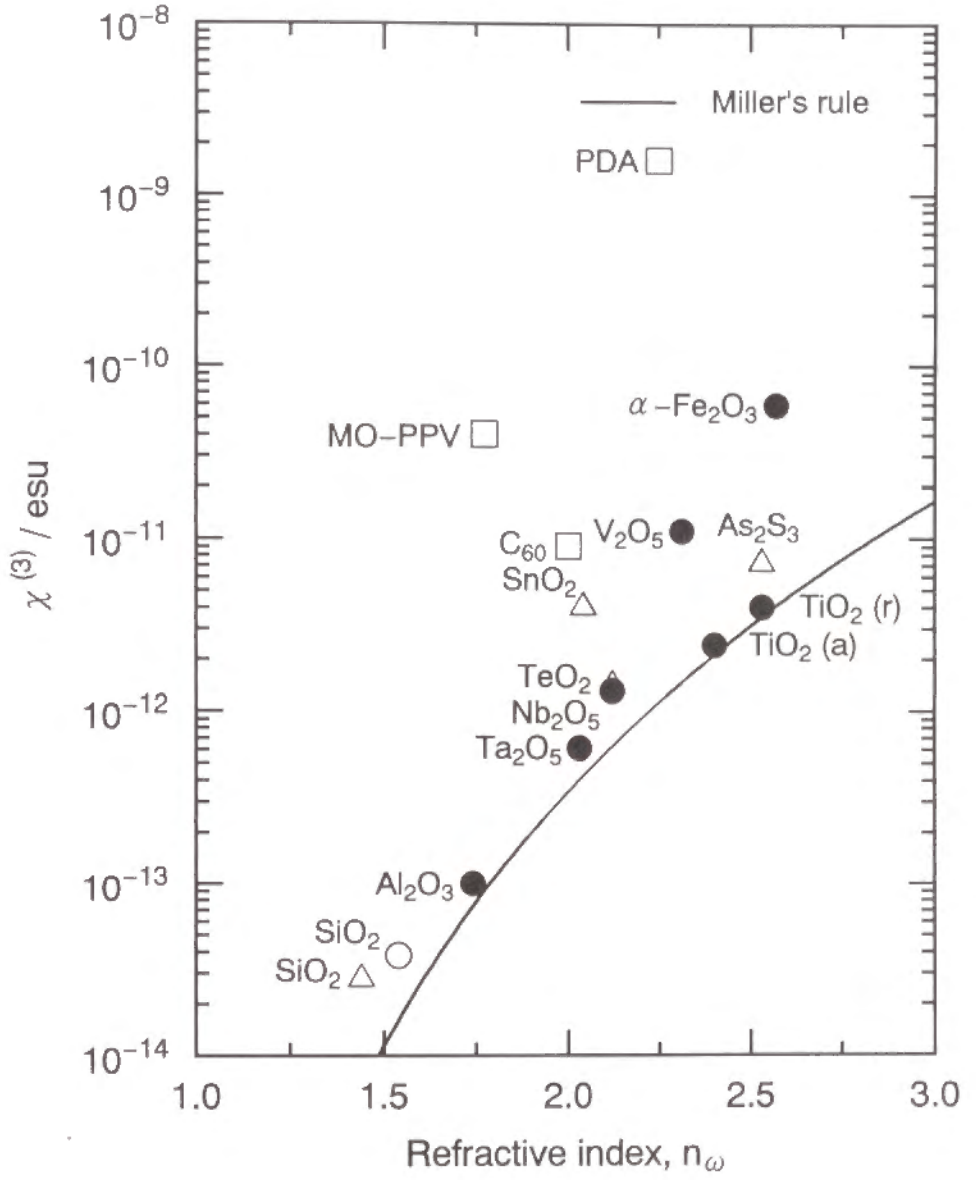

Fig. 6. Relation between $\chi^{(3)}$ and refractive index, n_ω, at 1900 nm for α–Fe_2O_3 thin film and α–Al_2O_3 single crystal together with other NLO materials. Circles, triangles and squares denote inorganic crystals, inorganic amorphous materials and organic materials, respectively. Closed circles are data measured in the present study. Letters of r and a in parentheses denote rutile and anatase, respectively. PDA: polydiacetylene, MO–PPV: poly(2,5–dimethoxy *p*–phenylene vinylene).

(PDA) [11] and poly(2,5-dimethoxy *p*-phenylene vinylene) (MO-PPV) [12] deviates from Miller's rule to a considerable extent. The latter is due to the enhancement by the "so-called" three-photon resonance or near three-photon resonance [14].

4.2 Relation between $\chi^{(3)}$ and Optical Band Gap, E_g

An enhancement in $\chi^{(3)}(-3\omega;\omega,\omega,\omega)$ occurs when a frequency of interacting light approaches either one of one-, two- or three-photon resonance frequency according to the relation [14]

$$\chi^{(3)}(-3\omega;\omega,\omega,\omega) \propto \frac{N}{\hbar^3}\sum_{gnmn'}\rho(g)F(\omega)\Omega_{gn}\Omega_{nm}\Omega_{mn'}\Omega_{n'g}\ (esu)\ , \tag{5-a}$$

and

$$F(\omega) = \frac{1}{(E_{ng}-3\omega)(E_{mg}-2\omega)(E_{n'g}-\omega)}+\frac{1}{(E_{ng}+\omega)(E_{mg}-2\omega)(E_{n'g}-\omega)} + \frac{1}{(E_{ng}+\omega)(E_{mg}+2\omega)(E_{n'g}-\omega)}+\frac{1}{(E_{ng}+\omega)(E_{mg}+2\omega)(E_{n'g}+3\omega)}\ , \tag{5-b}$$

where $\rho(g)$, E_{ij} and Ω_{ij} are the density matrix element of fundamental state, the energy difference between states i and j in $\hbar$ ($=h/2\pi$, h: Planck's constant) unit and the transition matrix elements between states i and j, respectively. If the three-photon resonance is dominant in the THG process as in the case of optical band gap, E_g, higher than three-photon energy, $3\hbar\omega$, one can obtain the most significant term due to the three-photon resonance in Eq. (5) as follows:

$$\chi^{(3)} = \frac{A}{(E_g-1.96)(E_g-1.31)(E_g-0.65)}\ (esu)\ (E_g>1.96)\ , \tag{6}$$

where A is the phenomenological constant and a laser light of 1900 nm (0.65 eV) is used as incident beam.

Figure 7 gives a relation between $\chi^{(3)}$ and optical band gap, E_g, for α-Fe_2O_3 thin films and α-Al_2O_3 single crystal together with other NLO materials shown in Fig. 6. For some organic materials, the absorption edge of exciton absorption for some materials is used instead of E_g. It is clear from Fig. 7 that $\chi^{(3)}$ of these materials increases asymptotically as the E_g approaches 1.96 eV corresponding to the three-photon energy in the present case. This change obeys Eq. (6) as shown in the figure by a solid line when the parameter, A, takes a value of 1.4×10^{-11} determined in Chapter 1. From Eq. (6), the $\chi^{(3)}$ values were estimated to be 8.7×10^{-11} and 6.6×10^{-14} esu for α-Fe_2O_3 and α-Al_2O_3, respectively, as in the third row of Table 2, which are in reasonable accordance with the measured ones, 5.8×10^{-11} and 1.0×10^{-13} esu, as in the first row.

4.3 Calculation of $\chi^{(3)}$ Based on Lines' Model

Recently, Lines has proposed a model dealing with the contribution of the empty *d* orbitals in addition to *sp* orbitals to the linear and nonlinear optical properties based on a bond-orbital theory as follows [15, 16]:

$$\chi^{(3)} = \frac{2.5\times10^{-12}\theta_b^2(n_\omega^2-1)f_L^3E_S^6}{3\pi[E_S^2-E^2]^4}\ (esu)\ , \tag{7}$$

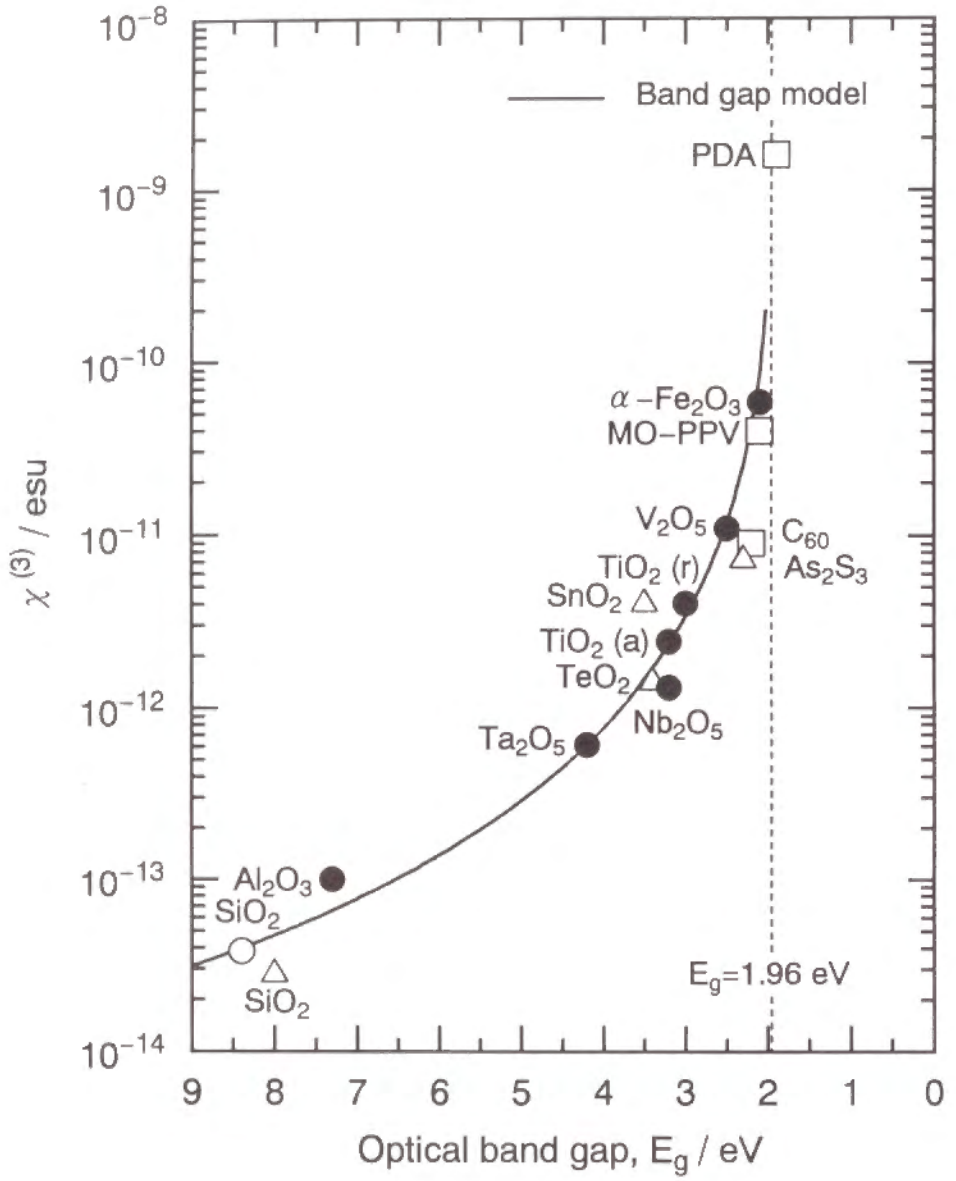

Fig. 7. Relation between $\chi^{(3)}$ and optical band gap, E_g, for α–Fe_2O_3 thin films and α–Al_2O_3 single crystal together with other NLO materials. Notations are the same as in Fig. 6.

where ℓ_b denotes the average bond length, $f_L=(n_\omega^2+2)/3$ the Lorentz local–field correction factor, E_S the Sellmeier gap which is in practice equal to the average oscillator energy, E_0, in Eq. (1). It is known that E_s/E_g is ~2 over a wide range of insulators and semiconductors with $E_s \geq 4$ eV. [17] From Eq. (7), one can obtain the $\chi^{(3)}$ values of 1.3×10^{-11} and 6.3×10^{-14} esu for α–Fe_2O_3 films and α–Al_2O_3 single crystal, respectively, as in the fourth row of Table 2, which are not in accordance with the measured ones, 5.8×10^{-11} and 1.0×10^{-13} esu, as in the second row. Such large discrepancies indicate the improper application of Lines' model to these iron oxides with partially occupied *d* orbitals as expected [15, 16].

4.4 Comparison of $\chi^{(3)}$ between α–Fe_2O_3 and α–Al_2O_3

α–Al_2O_3 has the same crystal structure as α–Fe_2O_3, but their optical properties such as the refractive index and band gap are largely different. Therefore, it is interesting to compare their $\chi^{(3)}$.

The $\chi^{(3)}$ value of α–Al_2O_3 single crystal was 1.0×10^{-13} esu, which is nearly three orders of magnitude lower than for α–Fe_2O_3 and only two to three times larger than that for SiO_2 glass. α–Al_2O_3 has a wide band gap of 7.3 eV, and so the enhancement of $\chi^{(3)}$ by the three–photon resonance can not be expected. It has been stated in the previous section that the three–photon resonance makes a great contribution to $\chi^{(3)}$ in α–Fe_2O_3, although the contribution is smaller than in PDA. Therefore, the large difference of $\chi^{(3)}$ between α–Fe_2O_3 and α–Al_2O_3 may be attributed to the presence of the three–photon resonance and the large refractive index of α–Fe_2O_3.

5. Conclusion

In this section, the third–order nonlinear optical properties of the sol–gel derived α–Fe_2O_3 thin films and α–Al_2O_3 single crystal $(11\bar{2}0)$ have been

investigated by the THG method. Mostly, the effect of corundum isomorph on the $\chi^{(3)}$ has been examined. The following results were obtained.

(1) The $\chi^{(3)}$ value of α–Fe_2O_3 thin films was 5.8×10^{-11} esu, which is the highest value among inorganic oxides reported so far. The high nonlinearity was ascribed to the optical band gap close to three–photon energy as well as the high refractive index.

(2) The $\chi^{(3)}$ of α–Al_2O_3 single crystal was 1.0×10^{-13} esu, which nearly three orders of magnitude lower than that for α–Fe_2O_3. It is found that the effect of corundum isomorph on the $\chi^{(3)}$ is small and instead the Fe element plays an important role in enhancement of the $\chi^{(3)}$.

References

[1] S. H. Wemple, *J. Chem. Phys.*, **67**, 2151 (1977).

[2] "Kessyou Kogaku Handbook", Kyoritu Syuppan, Tokyo, Japan, 1267 (1971).

[3] K. Kubodera and H. Kobayashi, *Mol. Cryst. Liq. Cryst.*, **182A**, 103 (1990).

[4] H. Nasu, K. Kubodera, M. Kobayashi, M. Nakamura and K. Kamiya, *J. Am. Ceram. Soc.*, **73**, 1794 (1990).

[5] G. R. Meredith, B. Buchalter and C. Hanzlik, *J. Chem. Phys.*, **78**, 1533 (1983).

[6] R. C. Miller, *Appl. Phys. Lett.*, **5**, 17 (1964).

[7] C. C. Wang, *Phys. Rev. B*, **2**, 2045 (1970).

[8] G. R. Meredith, *Phys. Rev. B*, **24**, 5522 (1981).

[9] N. Ueda, H. Kawazoe, Y. Watanabe, M. Takata, M. Yamane and K. Kubodera, *Appl. Phys. Lett.*, **59**, 502 (1991).

[10] S. H. Kim, T. Yoko and S. Sakka, *J. Am. Ceram. Soc.*, **76**, 2486 (1993).

[11] T. Kanetake, K. Ishikawa, T. Hasegawa, T. Koda, K. Takeda, M. Hasegawa, K. Kubodera and H. Kobayashi, *Appl. Phys. Lett.*, **54**, 2287 (1989).

[12] T. Kurihara, Y. Mori, T. Kaino, H. Murata, N. Takada, T. Tsutsui and S. Saito, *Chem. Phys. Lett.*, **183**, 534 (1991).

[13] J. S. Meth, H. Vanherzeele and Y. Wang, *Chem. Phys. Lett.*, **197**, 26 (1992).

[14] F. Kajzar and J. Messier, in "Nonlinear Optical Properties of Organic Molecules and Crystals, **2**", ed. by D. S. Chemla and J. Zyss, Academic Press, New York (1987) p. 51.

[15] M. E. Lines, *Phys. Rev. B*, **43**, 11978 (1991).

[16] M. E. Lines, *Phys Rev. B*, **41**, 3383 (1990).

[17] M. E. Lines, *J. Appl. Phys.*, **69**, 6876 (1991).

SECTION 3.2 COMPARISON OF $\chi^{(3)}$ BETWEEN α–Fe_2O_3, γ–Fe_2O_3 AND Fe_3O_4

1. Introduction

In Section 3.1, it was shown that α–Fe_2O_3 exhibits the highest $\chi^{(3)}$ among oxides reported so far. It is easily expected that other iron oxides, e.g. γ–Fe_2O_3 and Fe_3O_4, may also show high $\chi^{(3)}$.

In this section, the results of preparation of α–Fe_2O_3, γ–Fe_2O_3 and Fe_3O_4 thin films prepared on the SiO_2 glass substrates by the sol–gel method and the third–order nonlinear optical properties investigated by the THG method are presented. $\chi^{(3)}$ of iron oxides is discussed in terms of superexchange interaction between Fe^{3+} and Fe^{3+} ions though O^{2-} ions. For a better understanding and to ensure a reliable comparison, the data of α–Fe_2O_3 are remeasured in this section.

2. Experimental

2.1 Preparation of α–Fe_2O_3, γ–Fe_2O_3 and Fe_3O_4 Thin Films

α–Fe_2O_3, γ–Fe_2O_3 and Fe_3O_4 thin films were prepared by the sol–gel method. As starting solution, $Fe(NO_3)_3{\cdot}9H_2O$–$CH_3OCH_2CH_2OH$–$CH_3COCH_2COCH_3$ solution was selected for α–Fe_2O_3, γ–Fe_2O_3 and Fe_3O_4 films. The chemical compositions of the solutions were 1:20:2 in molar ratio. Iron (III) nitrate enneahydrate ($Fe(NO_3)_3{\cdot}9H_2O$) was dissolved in a solution of 2–methoxyethanol ($CH_3OCH_2CH_2OH$) and 2,4–pentanedione ($CH_3COCH_2COCH_3$). The coating solution was allowed to stand at 30 °C for 2 h prior to use.

Dip–coating was used for film formation. An SiO_2 glass substrate was immersed in the coating solution, and pulled up at a rate of 3 cm min^{-1}. The films were heated at 800 °C for 10 min immediately after each coating

procedure. This cycle was repeated 4–6 times to attain the desired film thickness. Sample embedded in carbon powders (No. 1) was heated at 600 °C for 5 h in N_2 (No. 2) [1] and further at 200–600 °C for 5 h in air (No. 3–7).

2.2 Characterization of α–Fe_2O_3, γ–Fe_2O_3 and Fe_3O_4 Thin Films

For reason mentioned in Chapter 1, an SiO_2 coating was further applied onto the α–Fe_2O_3, γ–Fe_2O_3 and Fe_3O_4 films and then the α–Fe_2O_3, γ–Fe_2O_3 or Fe_3O_4 and additional SiO_2 films on one face were removed. These films were characterized by resistivity, X–ray diffraction, ellipsometry, UV–visible spectrophotometry and THG measurements as gone into details in Chapter 1.

3. Results

3.1 Crystallization Behavior

Figure 1 shows the X–ray diffraction patterns of iron oxide thin films prepared by the sol–gel method. The crystalline phases precipitated in the sol–gel derived α–Fe_2O_3, γ–Fe_2O_3 and Fe_3O_4 thin films were identified referring to JCPDS–FILE 33–0664 (hexagonal), 19–0629 (cubic) and 39–1346 (cubic), respectively. Preferable orientation is not seen for α–Fe_2O_3, γ–Fe_2O_3 and Fe_3O_4 films. Reduction of α–Fe_2O_3 films (No. 1) yields Fe_3O_4 films (No. 2) and the sequent oxidation converts Fe_3O_4 films into γ–Fe_2O_3 films (No. 3–6). Note that the excess oxidation results in α–Fe_2O_3 films (No. 7). As summarized in Table 1, the final identification of crystalline phases precipitated in the films (No. 1–7) was made based on the combined results of the absorption spectra (Fig. 2) and the resistivity (Table 1). The crystallite sizes in the α–Fe_2O_3, γ–Fe_2O_3 and Fe_3O_4 films were ~35, ~30 and ~30 nm, respectively.

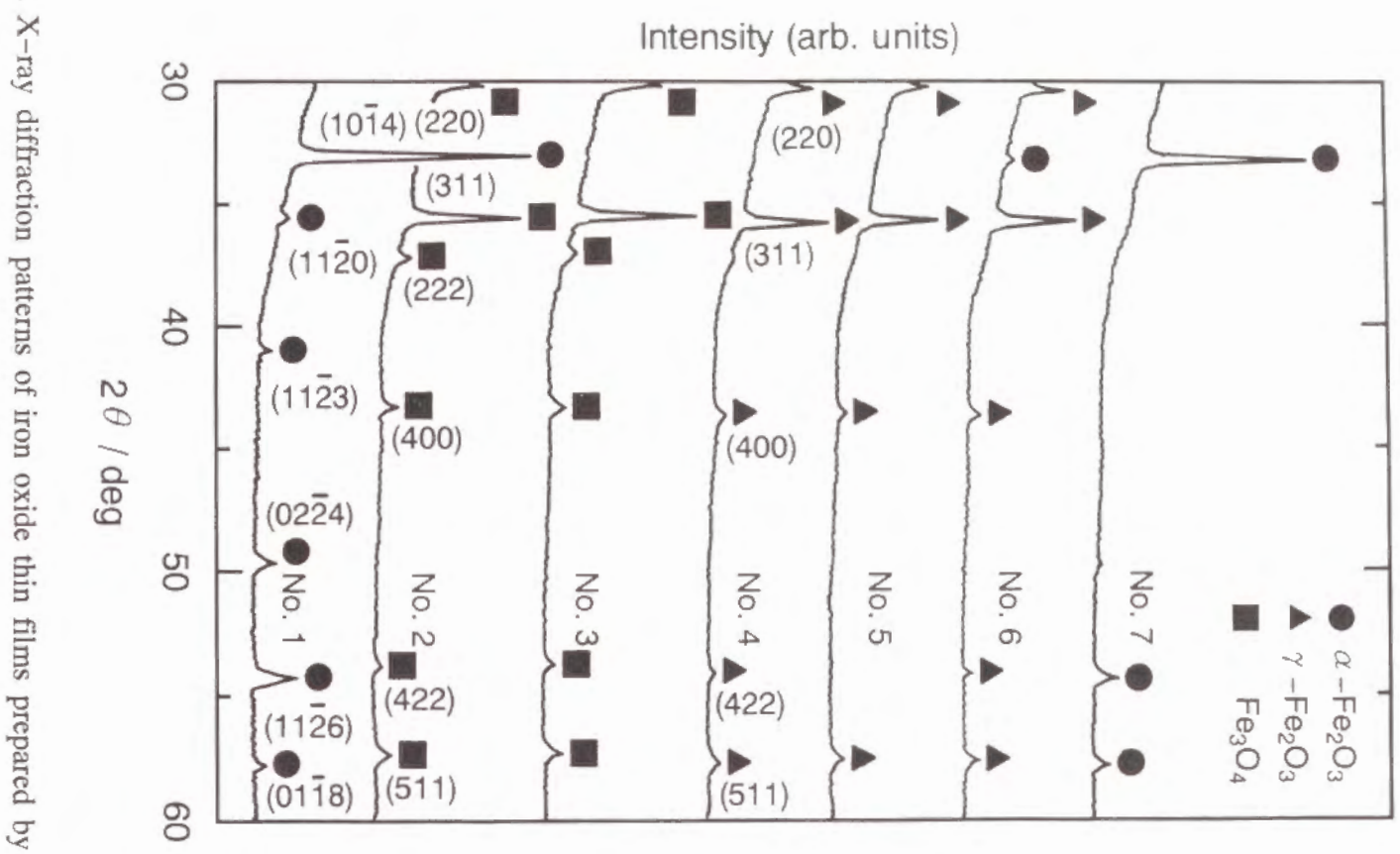

Fig. 1. X-ray diffraction patterns of iron oxide thin films prepared by the sol-gel method.

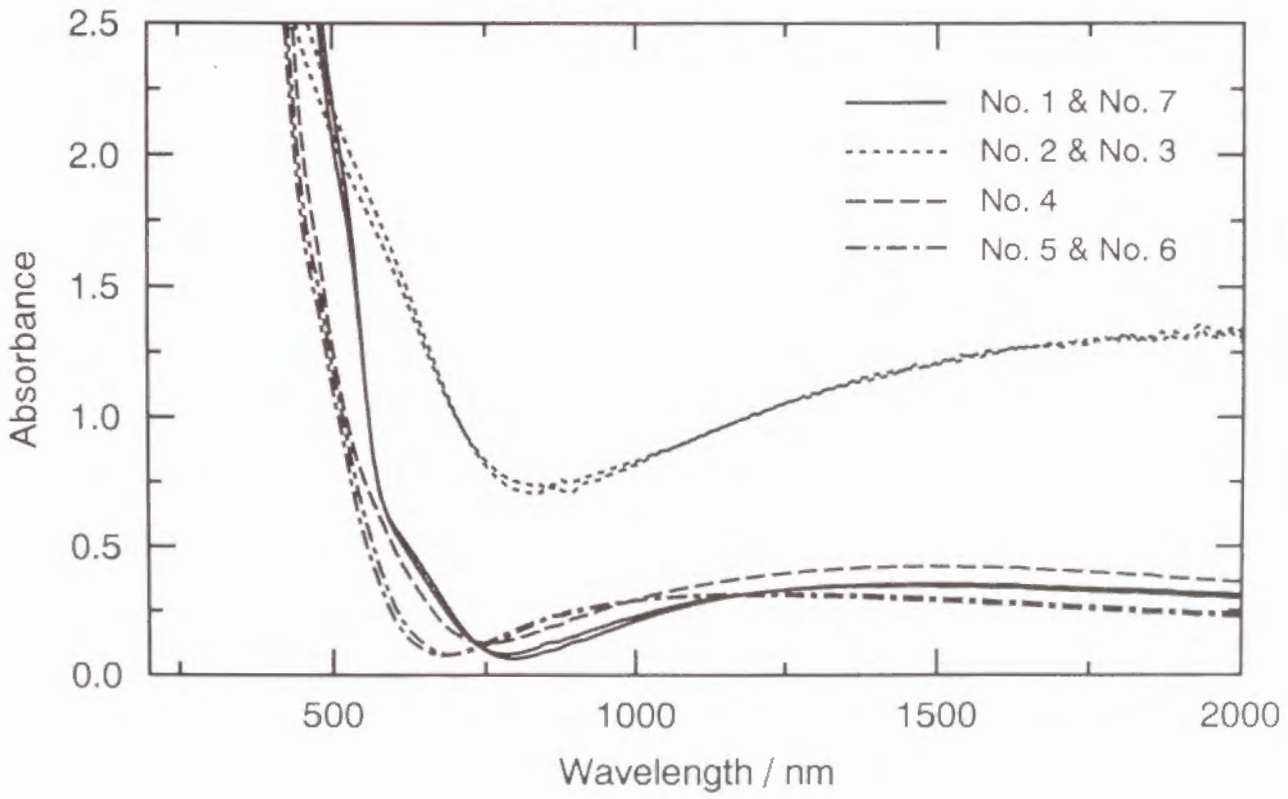

Fig. 2. Absorption spectra of iron oxide thin films prepared by the sol-gel method.

Table 1. Heat-treatment conditions for preparing various iron oxide thin films by the sol-gel method, and color and resistivity of the products.

Sample No.	1st heat-treatment (Air)	2nd heat-treatment (N_2)	3rd heat-treatment (Air)	Color	Resistivity / kΩ□	Product
1	800 °C, 10 min (×6)	---	---	Red brown	> 1000	α-Fe_2O_3
2	800 °C, 10 min (×6)	600 °C, 5 h	---	Black	~ 3	Fe_3O_4
3	800 °C, 10 min (×6)	600 °C, 5 h	200 °C, 5 h	Black	~ 15	Fe_3O_4, γ-Fe_2O_3
4	800 °C, 10 min (×6)	600 °C, 5 h	300 °C, 5 h	Light brown	> 1000	γ-Fe_2O_3, Fe_3O_4
5	800 °C, 10 min (×6)	600 °C, 5 h	400 °C, 5 h	Light brown	> 1000	γ-Fe_2O_3
6	800 °C, 10 min (×6)	600 °C, 5 h	500 °C, 5 h	Light brown	> 1000	γ-Fe_2O_3, α-Fe_2O_3
7	800 °C, 10 min (×6)	600 °C, 5 h	600 °C, 5 h	Red brown	> 1000	α-Fe_2O_3

3.2. Refractive Index and Optical Transmittance

The wavelength dependencies of refractive index, n, for α-Fe_2O_3, γ-Fe_2O_3 and Fe_3O_4 thin films are shown in Figure 3. It is seen that the refractive indices of α-Fe_2O_3 and γ-Fe_2O_3 films decrease with increasing wavelength as well known, while this is not the case for Fe_3O_4 films due to the broad and strong absorption band. Figure 4 presents the linear plots of $(n^2-1)^{-1}$ versus E^2 for α-Fe_2O_3, γ-Fe_2O_3 and Fe_3O_4 thin films based on Wemple's equation [2]

$$\frac{1}{n^2-1} = \frac{E_0}{E_d} - \frac{E^2}{E_0 E_d}, \qquad (1)$$

where E, E_0 and E_d are the photon energy, the average oscillator energy and dispersion energy in eV unit, respectively. E_0 and E_d are important optical properties of materials [2]. The refractive indices were estimated as $n_{3\omega}$=3.00 at 633 nm and n_ω=2.57 at 1900 nm, and the coherence length, ℓ_c=1.9/[6($n_{3\omega}$-n_ω)], was 0.7 μm for α-Fe_2O_3 films. In a similar manner, $n_{3\omega}$, n_ω and ℓ_c for γ-Fe_2O_3 films were estimated as 2.59, 2.31 and 1.1 μm, and for Fe_3O_4 films 2.47, 1.99 and 0.7 μm, respectively. The thickness of the α-Fe_2O_3, γ-Fe_2O_3 and Fe_3O_4 films obtained by 4 dippings was 0.07, 0.11 and 0.11 μm, respectively.

Figure 5 shows the absorption spectra of α-Fe_2O_3, γ-Fe_2O_3 and Fe_3O_4 thin films with and without additional SiO_2 coating. Most spectra have no mountains and troughs arising from the interference of light due to the small film thickness. It is seen that the additional SiO_2 coating effectively reduces the optical loss due to reflection at the surface especially in the wavelength region above ~600 nm. The optical band gaps, E_g, of α-Fe_2O_3 and γ-Fe_2O_3 films were estimated to be 2.1 and 2.2 eV, respectively. E_g of Fe_3O_4 was

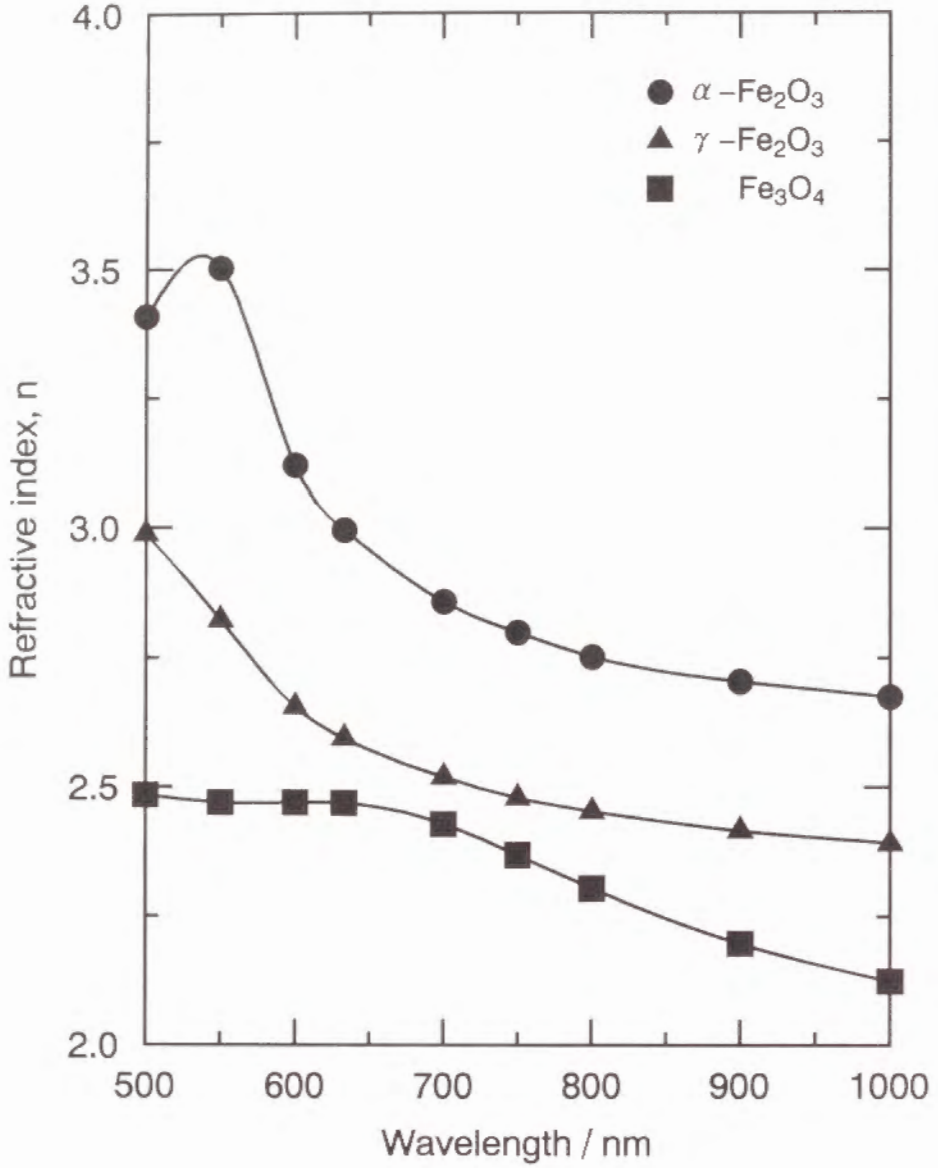

Fig. 3. Wavelength dependencies of refractive index, n, for α–Fe_2O_3, γ–Fe_2O_3 and Fe_3O_4 thin films.

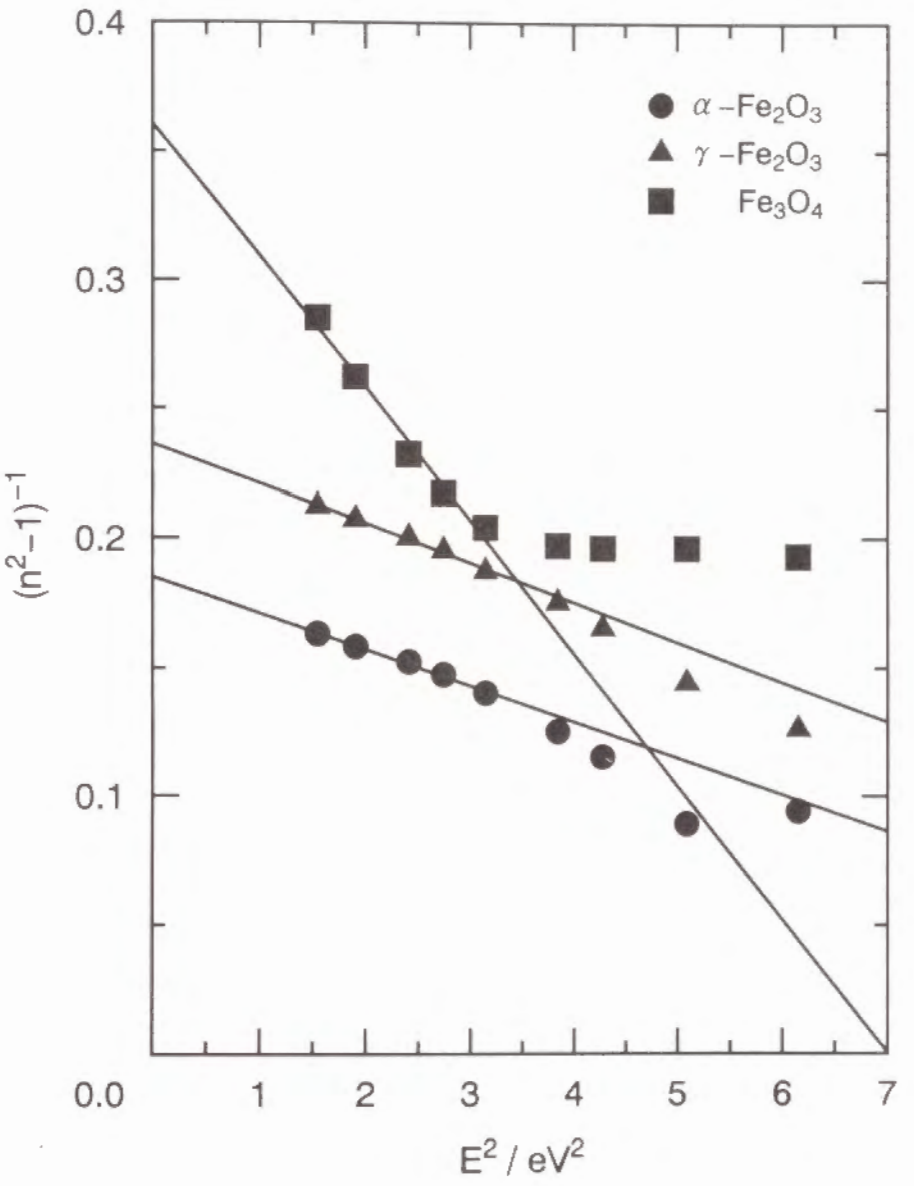

Fig. 4. Linear plots of $(n^2-1)^{-1}$ versus E^2 for α–Fe_2O_3, γ–Fe_2O_3 and Fe_3O_4 thin films.

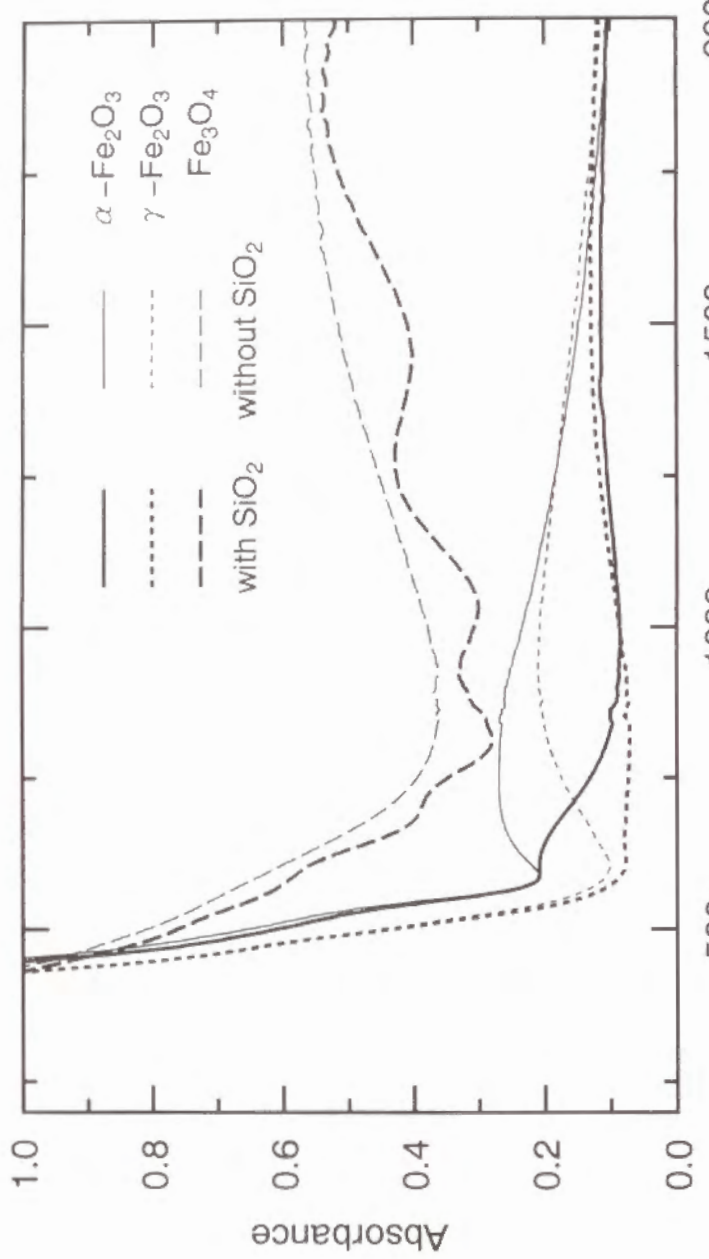

Fig. 5. Absorption spectra of α–Fe_2O_3, γ–Fe_2O_3 and Fe_3O_4 thin films with and without additional SiO_2 coating.

cited to be 0.3 eV [3], which is beyond the measurable wavelength region in the present study.

3.3 Evaluation of $\chi^{(3)}$ Values

The THG intensities as a function of the rotation angle for (a) α–Fe_2O_3 films, (b) γ–Fe_2O_3 films, (c) Fe_3O_4 films and (d) SiO_2 glass are given in Figure 6. The THG intensity patterns of α–Fe_2O_3 and γ–Fe_2O_3 films clearly show the interference between the THG lights from α–Fe_2O_3 (or γ–Fe_2O_3) films and SiO_2 glass substrate as previously reported [4], while the parabolic one with small modulation is observed for Fe_3O_4 films, because the THG signal of Fe_3O_4 films is much stronger than that of SiO_2 glass. The THG intensity was obtained by the least squares method as solid curve in Fig. 6.

In the present study, $\chi^{(3)}$ was determined by the equation [5]

$$\chi^{(3)}_{film} = \frac{2}{\pi}\chi^{(3)}_{SiO_2}\frac{\ell_{c,\,SiO_2}}{\ell}\sqrt{\frac{I_{3\omega,\,film}}{I_{3\omega,\,SiO_2}}}\sqrt{\frac{n^3_{\omega,\,film}n_{3\omega,\,film}T^3_{\omega,\,SiO_2}T_{3\omega,\,SiO_2}}{n^3_{\omega,\,SiO_2}n_{3\omega,\,SiO_2}T^3_{\omega,\,film}T_{3\omega,\,film}}}\ (esu)\ , \qquad (2)$$

where I denotes the THG peak intensity. The film thickness is used for ℓ, because the film thickness is less than the coherence length. The values of $\chi^{(3)}_{SiO_2}=2.8\times10^{-14}$ esu and $\ell_{c,SiO_2}=18.1$ μm were used for SiO_2 glass as both standard sample and substrate [6].

The intensities of THG signals generated from α–Fe_2O_3, γ–Fe_2O_3 and Fe_3O_4 films were determined by the equation [4]

$$I_{film} = \frac{I_{\max}+I_{\min}}{2} - \frac{I_{substrate}}{2} = \frac{I_{\max}+I_{\min}}{2} - \frac{I_{SiO_2}}{2}\ , \qquad (3)$$

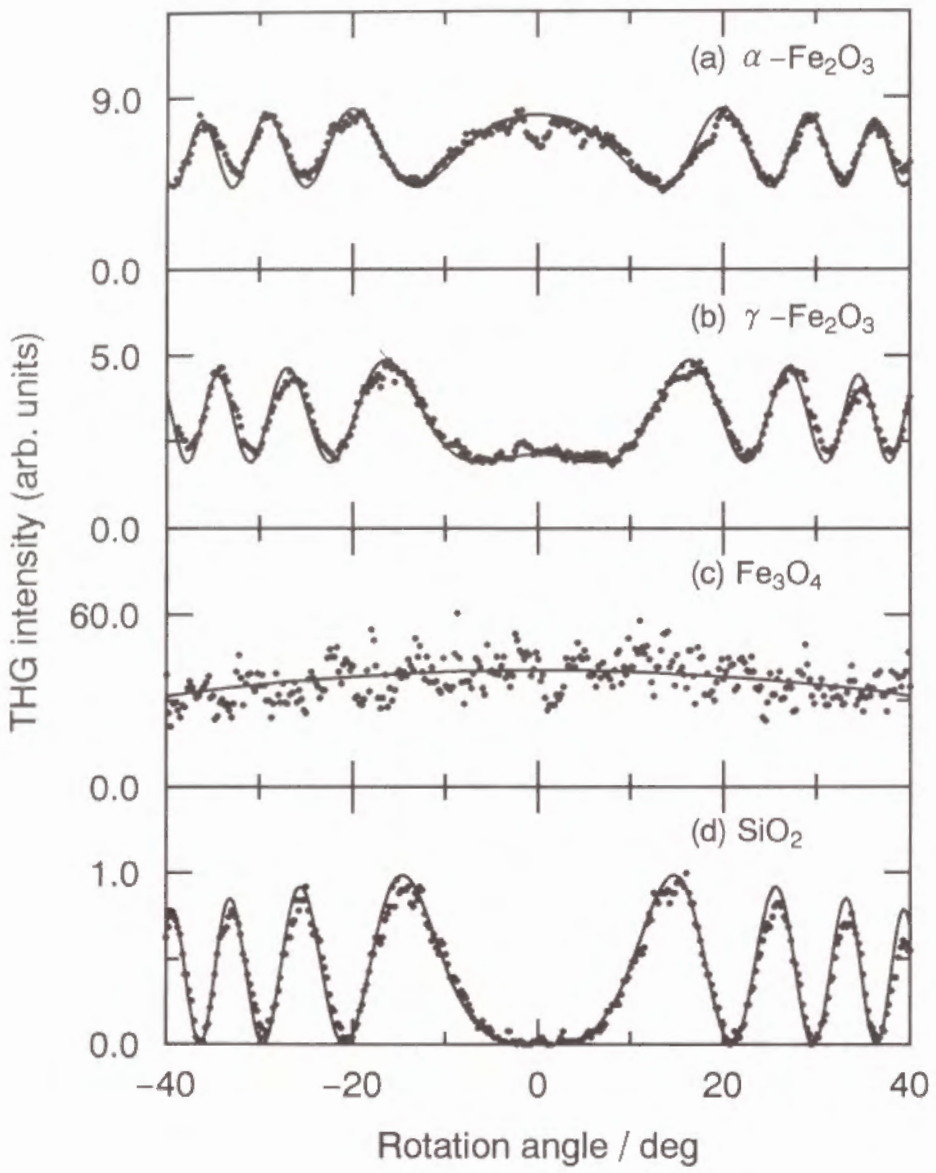

Fig. 6. THG intensities as a function of rotation angle for (a) α–Fe_2O_3 films, (b) γ–Fe_2O_3 films, (c) Fe_3O_4 films and (d) SiO_2 glass. Solid curves are computed using the least squares method.

where I_{max} and I_{min} are the upper and lower envelopes, respectively, of the superimposed THG intensity pattern. The THG light from the additional SiO_2 coating on the α–Fe_2O_3 (or γ–Fe_2O_3 and Fe_3O_4) films was neglected, because $\chi^{(3)}_{SiO_2}$ itself is very small and moreover the thickness of SiO_2 coating (less than ~0.2 μm) is much smaller than the coherence length (18.1 μm). The $\chi^{(3)}$ values of α–Fe_2O_3, γ–Fe_2O_3 and Fe_3O_4 films were determined to be 5.8×10^{-11}, 2.1×10^{-11} and 4.0×10^{-10} esu, respectively. Table 2 summarizes the obtained optical properties of α–Fe_2O_3, γ–Fe_2O_3 and Fe_3O_4 thin films.

4. Discussion

4.1 Relation between $\chi^{(3)}$ and Refractive Index, n

One can roughly predict $\chi^{(3)}$ of a material from refractive index, n, based on Miller's rule [7, 8]

$$\chi^{(3)} = [\chi^{(1)}]^4\times10^{-10}\ (esu)\ , \tag{4-a}$$

and

$$\chi^{(1)} = \frac{n^2-1}{4\pi}\ . \tag{4-b}$$

The $\chi^{(3)}$ values of 3.9×10^{-12}, 1.4×10^{-12} and 3.1×10^{-13} esu, which are predicted by Miller's rule for α–Fe_2O_3, γ–Fe_2O_3 and Fe_3O_4 thin films, respectively, as in the second row of Table 3, are inconsistent with the measured ones, 5.8×10^{-11}, 2.1×10^{-11} and 4.0×10^{-10} esu, as in the first row.

Figure 7 shows a relation between $\chi^{(3)}$ and refractive index, n_ω, at 1900 nm for α–Fe_2O_3, γ–Fe_2O_3 and Fe_3O_4 thin films together with other NLO materials reported so far [5, 6, 9–14]. Inorganic materials with the high

Table 2. Optical properties of α–Fe_2O_3, γ–Fe_2O_3 and Fe_3O_4 thin films.

Compound	$n_{3\omega}$	n_ω	$T_{3\omega}$ / %	T_ω / %	E_0 / eV	E_d / eV	E_g / eV	$\frac{I_{3\omega,film}}{I_{3\omega,SiO_2}}$	ℓ_c / μm	ℓ / μm	$\chi^{(3)}$ / esu
α–Fe_2O_3	3.00	2.57	62.4	78.2	3.6	19.4	2.1	5.98	0.7	0.07	5.8×10^{-11}
γ–Fe_2O_3	2.59	2.31	83.2	75.1	3.9	16.6	2.2	2.92	1.1	0.11	2.1×10^{-11}
Fe_3O_4	2.47	1.99	31.7	29.4	2.7	7.4	0.3	40.0	0.7	0.11	4.0×10^{-10}

The physical meanings of all the notations in the table are described in the section 3.
Transmittances are values for α–Fe_2O_3, γ–Fe_2O_3 and Fe_3O_4 thin films with additional SiO_2 coating.

Table 3. Comparison of the measured $\chi^{(3)}$ with the calculated $\chi^{(3)}$ for α–Fe_2O_3, γ–Fe_2O_3 and Fe_3O_4 thin films on the basis of three models.

	$\chi^{(3)}$ / esu		
	α–Fe_2O_3	γ–Fe_2O_3	Fe_3O_4
Measured value	5.8×10^{-11}	2.1×10^{-11}	4.0×10^{-10}
Miller's rule	3.9×10^{-12}	1.4×10^{-12}	3.1×10^{-13}
Band gap model	8.7×10^{-11}	4.2×10^{-11}	2.4×10^{-11}
Lines' model	1.3×10^{-11}	4.9×10^{-12}	4.3×10^{-12}

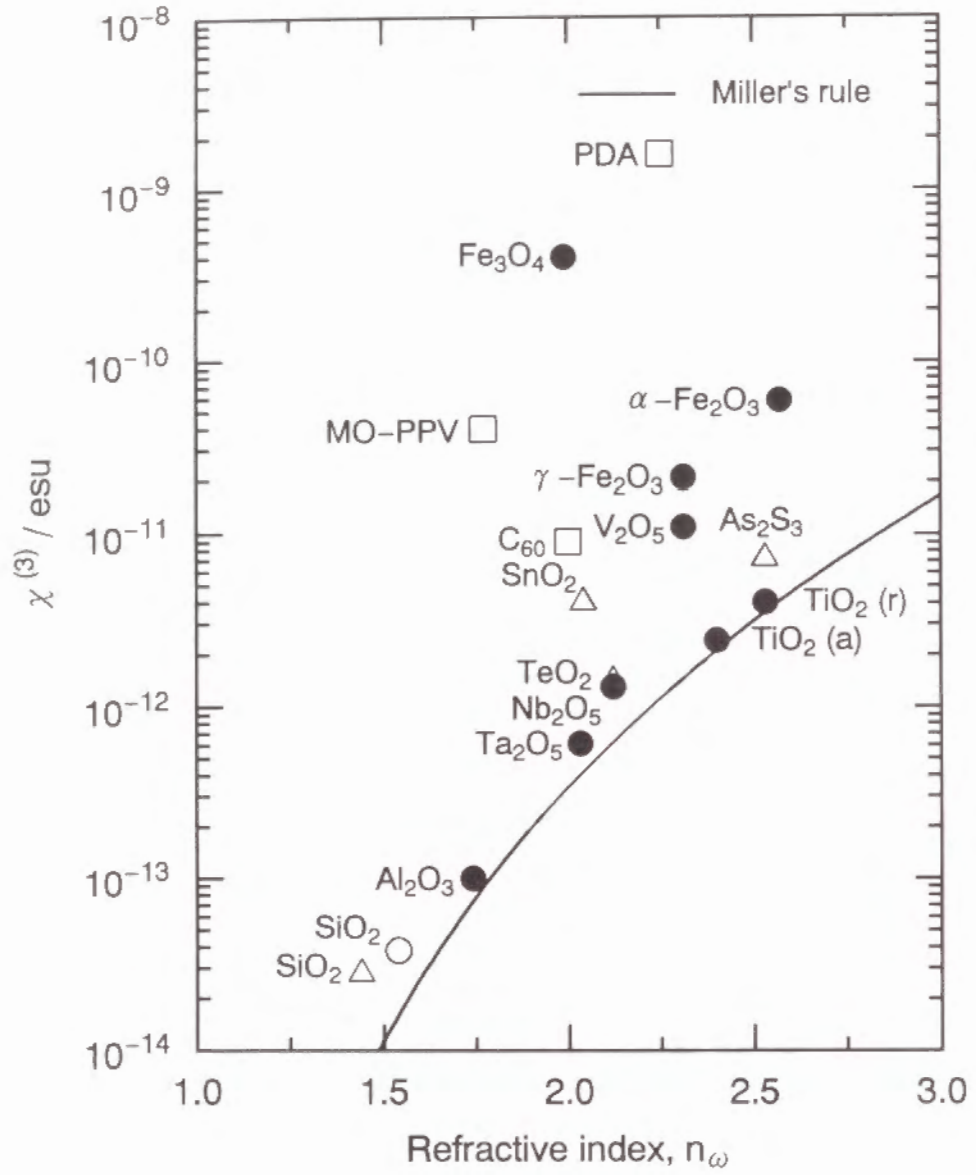

Fig. 7. Relation between $\chi^{(3)}$ and refractive index, n_ω, at 1900 nm for α–Fe_2O_3, γ–Fe_2O_3 and Fe_3O_4 thin films together with other NLO materials. Circles, triangles and squares denote inorganic crystals, inorganic amorphous materials and organic materials, respectively. Closed circles are data measured in the present study. Letters of r and a in parentheses denote rutile and anatase, respectively. PDA: polydiacetylene, MO–PPV: poly(2,5–dimethoxy *p*–phenylene vinylene).

refractive index tend to exhibit high $\chi^{(3)}$ while $\chi^{(3)}$ of organic polymers such as polydiacetylene (PDA) [12] and poly(2,5–dimethoxy *p*–phenylene vinylene) (MO–PPV) [13] deviates from Miller's rule to a considerable extent. The latter is due to the enhancement by the "so–called" three–photon resonance or near three–photon resonance [15]. Since $\chi^{(3)}$ of Fe_3O_4 saliently deviates from the relation, the THG process may also be enhanced by the resonance effect similarly to these organic compounds. This problem will be mentioned in more details in the next section.

4.2 Relation between $\chi^{(3)}$ and Optical Band Gap, E_g

An enhancement in $\chi^{(3)}(-3\omega;\omega,\omega,\omega)$ occurs when a frequency of interacting light approaches either one of one–, two– or three–photon resonance frequency according to the relation [15]

$$\chi^{(3)}(-3\omega;\omega,\omega,\omega) \propto \frac{N}{\hbar^3}\sum_{gnmn'} \rho(g)F(\omega)\Omega_{gn}\Omega_{nm}\Omega_{mn'}\Omega_{n'g}\ (esu)\ , \qquad (5\text{–a})$$

and

$$F(\omega) = \frac{1}{(E_{ng}-3\omega)(E_{mg}-2\omega)(E_{n'g}-\omega)} + \frac{1}{(E_{ng}+\omega)(E_{mg}-2\omega)(E_{n'g}-\omega)} + \frac{1}{(E_{ng}+\omega)(E_{mg}+2\omega)(E_{n'g}-\omega)} + \frac{1}{(E_{ng}+\omega)(E_{mg}+2\omega)(E_{n'g}+3\omega)}\ , \qquad (5\text{–b})$$

where $\rho(g)$, E_{ij} and Ω_{ij} are the density matrix element of fundamental state, the energy difference between states i and j in $\hbar$ ($=h/2\pi$, h: Planck's constant) unit and the transition matrix elements between states i and j, respectively. If the three–photon resonance is dominant in the THG process as in the case

of optical band gap, E_g, higher than three-photon energy, $3\hbar\omega$, one can obtain the most significant term due to the three-photon resonance in Eq. (5) as follows:

$$\chi^{(3)} = \frac{A}{(E_g-1.96)(E_g-1.31)(E_g-0.65)} \ (esu) \ (E_g>1.96) \ , \qquad (6)$$

where A is the phenomenological constant and a laser light of 1900 nm (0.65 eV) is used as incident beam.

Since the optical band gap of Fe_3O_4 of 0.3 eV is much narrower than one-photon energy of 0.65 eV, the THG process may be enhanced by both one- and three-photon resonances. However, it is not clear whether two-photon resonance contributes to the THG process, because a two-photon absorption band could not be measured in the present study.

Figure 8 gives a relation between $\chi^{(3)}$ and optical band gap, E_g, for α-Fe_2O_3, γ-Fe_2O_3 and Fe_3O_4 thin films together with other NLO materials shown in Fig. 7. For some organic materials, the absorption edge of exciton absorption for some materials is used instead of E_g. It is clear from Fig. 8 that $\chi^{(3)}$ of these materials increases asymptotically as the E_g approaches 1.96 eV corresponding to the three-photon energy in the present case. This change obeys Eq. (6) as shown in the figure by a solid line when the parameter, A, takes a value of 1.4×10^{-11}. From Eq. (6), the $\chi^{(3)}$ values were estimated to be 8.7×10^{-11}, 4.2×10^{-11} and 2.4×10^{-11} esu for α-Fe_2O_3, γ-Fe_2O_3 and Fe_3O_4, respectively, as in the third row of Table 3, which are in reasonable accordance with the measured ones, 5.8×10^{-11}, 2.1×10^{-11} and 4.0×10^{-10} esu, as in the first row. Since the band gap model is derived on the assumption of the three-photon resonance (E_g > 1.96 eV), the $\chi^{(3)}$ value calculated from the model for Fe_3O_4 is physically meaningless.

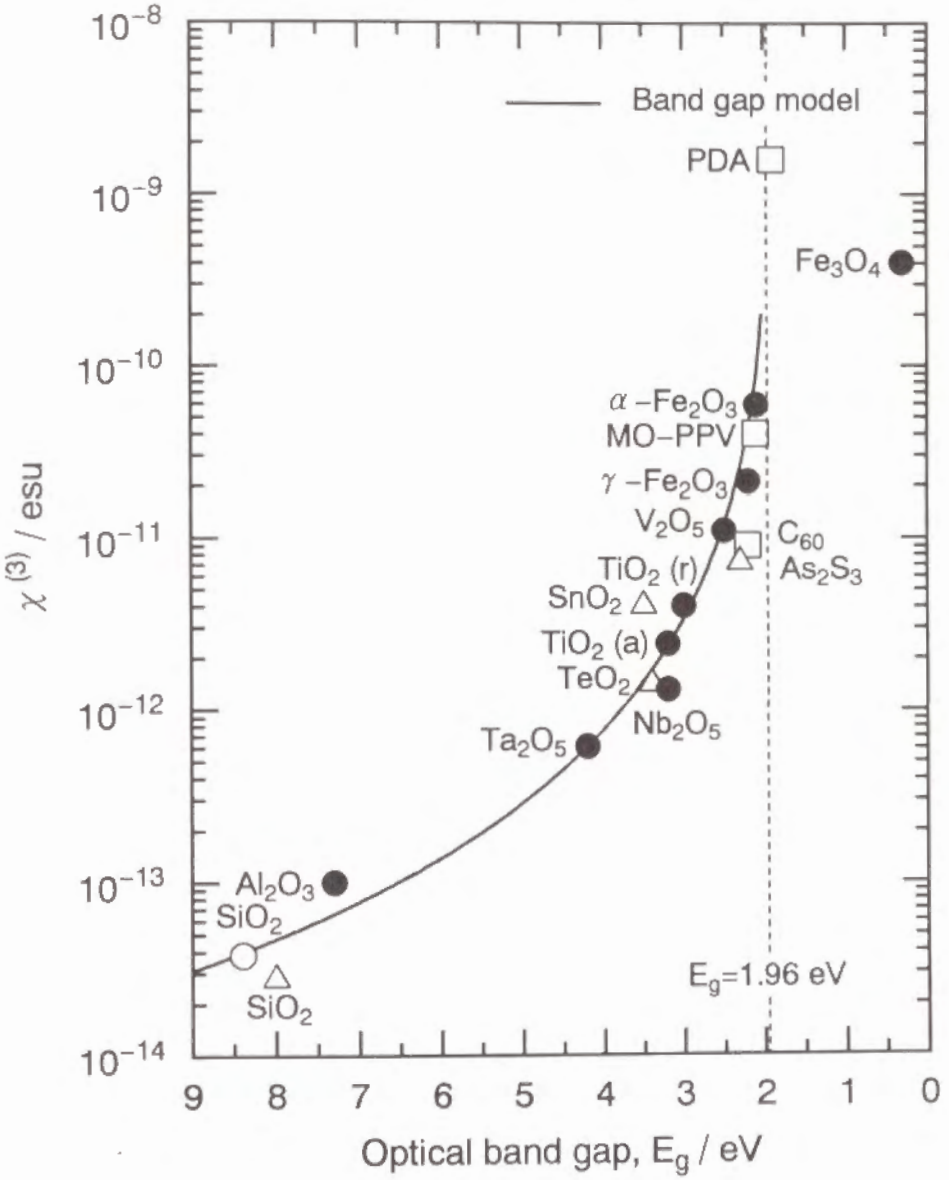

Fig. 8. Relation between $\chi^{(3)}$ and optical band gap, E_g, for α-Fe_2O_3, γ-Fe_2O_3 and Fe_3O_4 thin films together with other NLO materials. Notations are the same as in Fig. 7.

4.3 Calculation of $\chi^{(3)}$ Based on Lines' Model

Recently, Lines has proposed a model dealing with the contribution of the empty *d* orbitals in addition to *sp* orbitals to the linear and nonlinear optical properties based on a bond-orbital theory as follows [16, 17]:

$$\chi^{(3)} = \frac{2.5\times10^{-12}\ell_b^2(n_\omega^2-1)f_L^3E_S^6}{3\pi[E_S^2-E^2]^4} \ (esu) \ , \qquad (7)$$

where ℓ_b denotes the average bond length, $f_L=(n_\omega^2+2)/3$ the Lorentz local-field correction factor, E_S the Sellmeier gap which is in practice equal to the average oscillator energy, E_0, in Eq. (1). It is known that E_s/E_g is ~2 over a wide range of insulators and semiconductors with $E_s \geq 4$ eV. [18] From Eq. (7), one can obtain the $\chi^{(3)}$ values of 1.3×10^{-11}, 4.9×10^{-12} and 4.3×10^{-12} esu for α-Fe_2O_3, γ-Fe_2O_3 and Fe_3O_4 films, respectively, as in the fourth row of Table 3, which are not in accordance with the measured ones, 5.8×10^{-11}, 2.1×10^{-11} and 4.0×10^{-10} esu, as in the second row. Such large discrepancies indicate the improper application of Lines' model to these iron oxides with partially occupied *d* orbitals as expected [16, 17].

4.4 Comparison of $\chi^{(3)}$ between α-Fe_2O_3 and γ-Fe_2O_3

It was considered in the above sections that $\chi^{(3)}$ of Fe_3O_4 is enhanced by both one- and three-photon resonances, and much higher than that of α-Fe_2O_3 and γ-Fe_2O_3. $\chi^{(3)}$ of α-Fe_2O_3 and γ-Fe_2O_3 (E_g > 1.96 eV) can be related to the transition probability around 1.96 eV as will be discussed below.

It is expected that since the *d*-*d* transition in Fe^{3+} ions with $3d^5$ electronic configuration is Laporte- and spin-forbidden in nature, it does not contribute to the THG process. However, in practice the *d*-*d* transition

occurs with high transition probability and is the origin of the strong color in iron oxides containing Fe^{3+} ions. This is explicable in terms of a superexchange interaction between two neighboring Fe^{3+} ions though O^{2-} ion, which results from overlapping between Fe 3*d* and O 2*p* orbitals. [19] The overlapping between Fe 3*d* and O 2*p* orbitals relaxes Laporte-forbidden transition. However, it is obvious from Fig. 5 that the transition probability for spin-forbidden transitions ($^6A_1 \rightarrow {}^4T_1$ at 1.4 eV and $^6A_1 \rightarrow {}^4T_2$ at 1.9-2.0 eV [19, 20]) seems very low in these oxides. On the other hands, pair excitation process ($^6A_1+{}^6A_1 \rightarrow {}^4T_1+{}^4T_1$) [19-21] involving the simultaneous excitation of magnetically-coupled two neighboring Fe^{3+} ions is spin-allowed because of no change in the total spin quantum number, and gives rise to an absorption peak at 2.2-2.4 eV with the much higher transition probability than the spin-forbidden transition. Therefore, this pair excitation process may also be the most contributive to the THG process for α-Fe_2O_3 and γ-Fe_2O_3 even though the excitation energy for $^6A_1 \rightarrow {}^4T_2$ transition is very close to 1.96 eV.

Next, we discuss a difference in crystal structure between α-Fe_2O_3 and γ-Fe_2O_3 in relation to their NLO properties. An FeO_6 octahedron in α-Fe_2O_3 with a corundum structure is connected to the nearest neighboring ones via face-sharing bonds in addition to corner- and edge-sharing ones. (Figure 9) In γ-Fe_2O_3 with a defect spinel structure there are two kinds of polyhedra, an FeO_4 tetrahedron and an FeO_6 octahedron, and in the former a central Fe atom is surrounded by the corner-sharing oxygens only and the latter contains both corner- and edge-sharing oxygens. The presence of face-shared FeO_6 octahedra in α-Fe_2O_3 should enhance the transition probability in pair excitation process by the following two reasons. One is the more relaxed Laporte-forbidden transition in α-Fe_2O_3 due to the lower symmetry of FeO_6 octahedra. The other is the largest magnetic coupling between the neighboring Fe ions in face-shared FeO_6 octahedra through the three

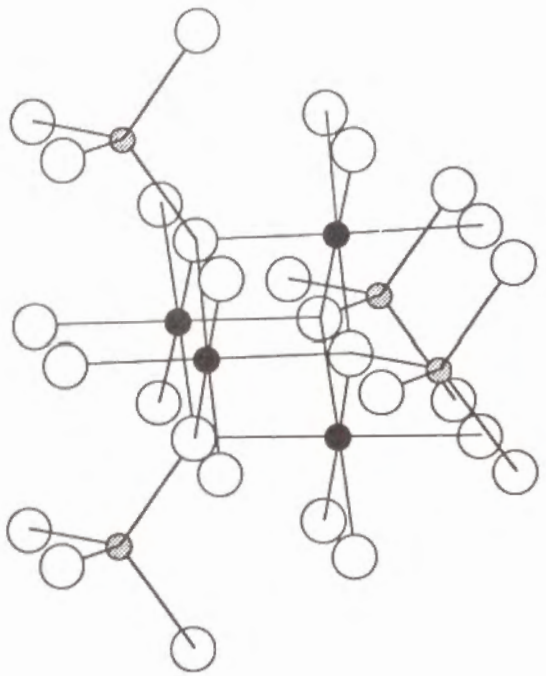

(b)

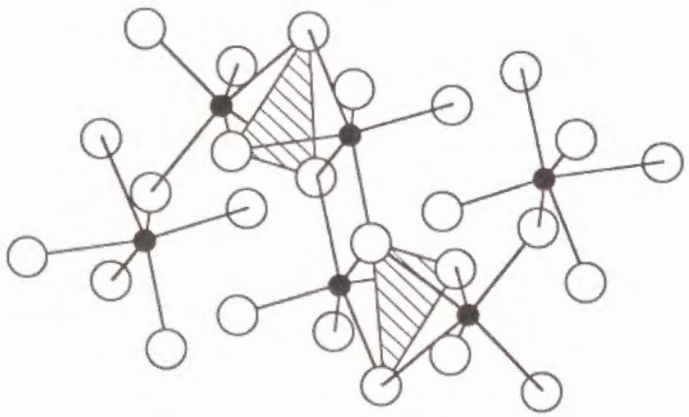

(a)

Fig. 9. Linkage mode of oxygen polyhedra in (a) corundum type α–Fe_2O_3 and (b) spinel type γ–Fe_2O_3 (or Fe_3O_4).

● Octahedral Fe^{3+} (Fe^{2+})

● Tetrahedral Fe^{3+}

○ O^{2-}

interacting bonds giving rise to the higher transition probability for spin–allowed transition in α–Fe_2O_3.

A Néel (or Curie) temperature of magnetic materials reflects the degree of the superexchange interaction as well known. Figure 10 represents a relation between Néel (or Curie) temperature and the number of unpaired electrons for iron oxides and other magnetic oxide materials. In fact, it is seen from Fig. 10 that a material with a smaller number of unpaired electrons shows a higher Néel (or Curie) temperature, and iron oxides containing Fe^{3+} ions have an exceptionally high transition temperature and moreover the Néel temperature for α–Fe_2O_3 is higher than the Curie temperature for γ–Fe_2O_3. This means that the pair excitation process in α–Fe_2O_3 can facilitate the THG process rather than in γ–Fe_2O_3.

5. Conclusion

In this section, the third–order nonlinear optical properties of the sol–gel derived α–Fe_2O_3, γ–Fe_2O_3 and Fe_3O_4 thin films have been investigated by the THG method. Primarily, the effect of the valence and coordination number of Fe ions on the $\chi^{(3)}$ has been examined. The following results were obtained.

(1) The $\chi^{(3)}$ values of α–Fe_2O_3, γ–Fe_2O_3 and Fe_3O_4 thin films were 5.8×10^{-11}, 2.1×10^{-11} and 4.0×10^{-10} esu, respectively, which are the highest values among inorganic oxides reported so far.

(2) $\chi^{(3)}$ of α–Fe_2O_3 and γ–Fe_2O_3 may be enhanced by the pair excitation process involving the simultaneous excitation of magnetically coupled two neighboring Fe^{3+} ions while $\chi^{(3)}$ of Fe_3O_4 by both one– and three–photon resonances. The difference in $\chi^{(3)}$ between α–Fe_2O_3 and γ–Fe_2O_3 may result from the presence of face–shared FeO_6 octahedra in α–Fe_2O_3.

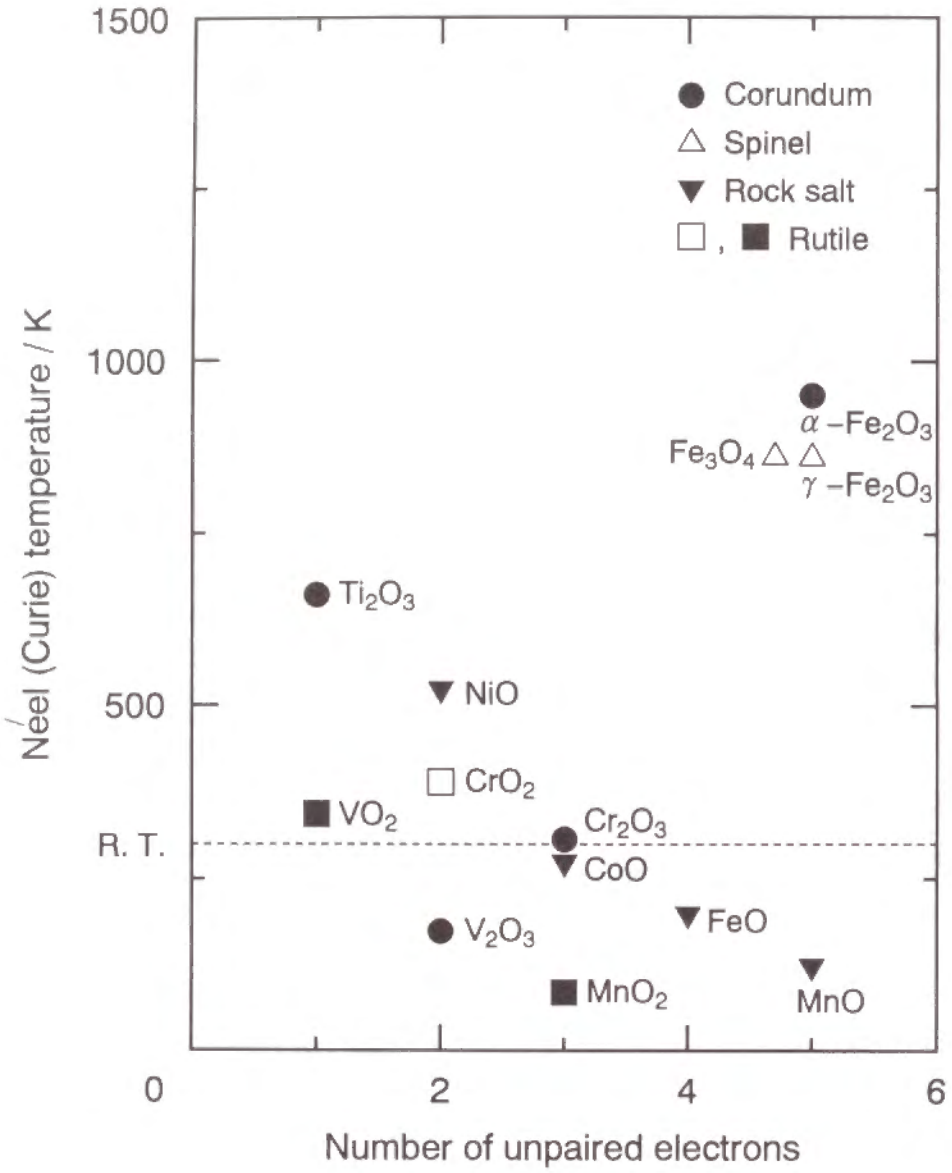

Fig. 10. Relation between Néel (or Curie) temperature and the number of unpaired electrons for iron oxides and other magnetic oxide materials with crystal structure distinguished by four types of marks. Closed and open marks means the antiferromagnetic (Néel) and ferrimagnetic or ferromagnetic (Curie) materials,

References

[1] K. Tanaka, T. Yoko, M. Atarashi, K. Kamiya, *J. Mater. Sci. Lett.*, **8**, 83 (1989).

[2] S. H. Wemple, *J. Chem. Phys.*, **67**, 2151 (1977).

[3] I. Balberg and J. I. Pankove, *Phys. Rev. Lett.*, **27**, 596 (1971).

[4] K. Kubodera and H. Kobayashi, *Mol. Cryst. Liq. Cryst.*, **182A**, 103 (1990).

[5] H. Nasu, K. Kubodera, M. Kobayashi, M. Nakamura and K. Kamiya, *J. Am. Ceram. Soc.*, **73**, 1794 (1990).

[6] G. R. Meredith, B. Buchalter and C. Hanzlik, *J. Chem. Phys.*, **78**, 1533 (1983).

[7] R. C. Miller, *Appl. Phys. Lett.*, **5**, 17 (1964).

[8] C. C. Wang, *Phys. Rev. B*, **2**, 2045 (1970).

[9] G. R. Meredith, *Phys. Rev. B*, **24**, 5522 (1981).

[10] N. Ueda, H. Kawazoe, Y. Watanabe, M. Takata, M. Yamane and K. Kubodera, *Appl. Phys. Lett.*, **59**, 502 (1991).

[11] S. H. Kim, T. Yoko and S. Sakka, *J. Am. Ceram. Soc.*, **76**, 2486 (1993).

[12] T. Kanetake, K. Ishikawa, T. Hasegawa, T. Koda, K. Takeda, M. Hasegawa, K. Kubodera and H. Kobayashi, *Appl. Phys. Lett.*, **54**, 2287 (1989).

[13] T. Kurihara, Y. Mori, T. Kaino, H. Murata, N. Takada, T. Tsutsui and S. Saito, *Chem. Phys. Lett.*, **183**, 534 (1991).

[14] J. S. Meth, H. Vanherzeele and Y. Wang, *Chem. Phys. Lett.*, **197**, 26 (1992).

[15] F. Kajzar and J. Messier, in "Nonlinear Optical Properties of Organic Molecules and Crystals, **2**", ed. by D. S. Chemla and J. Zyss, Academic Press, New York (1987) p. 51.

[16] M. E. Lines, *Phys. Rev. B*, **43**, 11978 (1991).

[17] M. E. Lines, *Phys Rev. B*, **41**, 3383 (1990).

[18] M. E. Lines, *J. Appl. Phys.*, **69**, 6876 (1991).

[19] D. M. Sherman and T. D. Waite, *Amer. Mineral*, **70**, 1262 (1985).

[20] R. V. Morris, H. V. Lauer, Jr., C. A. Lawson, E. K. Gibson, Jr., G. A. Nace and C. Stewart, *J. Geophys. Res.*, **90** 3126 (1985).

[21] H. J. Schugar, G. R. Rossman, J. Thibeault and H. B. Gray, *Chem. Phys. Lett.*, **6**, 26 (1970).

CHAPTER 4. THIRD-ORDER NONLINEAR OPTICAL PROPERTIES OF $FeTiO_3$ THIN FILMS

1. Introduction

It was found in Chapter 2 that $\chi^{(3)}$ of transition metal oxides with the empty *d* orbitals is dominated mainly by the metal-oxygen bond length rather than the valence of metal cation. It is therefore interesting whether this concept is applicable to transition metal oxide with the partially occupied *d* orbitals.

In Chapter 3, it was shown that iron oxides consisting of Fe ions in different local environments and with different valences exhibit the highest $\chi^{(3)}$ among oxides reported so far. A comparison of $\chi^{(3)}$ between them will reveal effects of the local environment and valence of Fe ions on the $\chi^{(3)}$. For this purpose $\chi^{(3)}$ data of Fe^{2+}-containing oxides are further required.

In this chapter, the results of the preparation of $FeTiO_3$ thin films on SiO_2 glass substrates by the sol-gel method and the third-order nonlinear optical properties investigated by the THG method are presented. $FeTiO_3$ (ilmenite) was selected, because it contains both Fe^{2+} and Ti^{4+} ions which are substituted for Al^{3+} ions in α-Al_2O_3 corundum structure. The effect of Fe ions (valence and coordination number) on $\chi^{(3)}$ is discussed in terms of the microscopic second-hyperpolarizability, γ.

2. Experimental

2.1 Preparation of $FeTiO_3$ Thin Films

$FeTiO_3$ thin films were prepared by the sol-gel method. As starting solution, $Fe(NO_3)_3 \cdot 9H_2O$-$Ti(OC_3H_7^i)_4$-$CH_3OCH_2CH_2OH$-$CH_3COCH_2COCH_3$ solutions were selected. The chemical composition of the solution was 1:1:40:4 in molar ratio. Iron (III) nitrate enneahydrate ($Fe(NO_3)_3 \cdot 9H_2O$) was

first dissolved in a solution of 2,4–pentanedione ($CH_3COCH_2COCH_3$) and half of a prescribed amount of 2–methoxyethanol ($CH_3OCH_2CH_2OH$). Then, titanium tetraisopropoxide ($Ti(OC_3H_7^i)_4$) which was diluted by the remainder of $CH_3OCH_2CH_2OH$ in advance was mixed with the solution. Coating solutions were allowed to stand at 60 °C for 24 h prior to use.

Dip–coating was used for film formation. A SiO_2 glass substrate was immersed in a coating solution, and pulled up at a rate of 3 cm min^{-1}. The films were heated at 800 °C for 10 min immediately after each coating procedure. This cycle was repeated 10 times to attain the desired film thickness.

2.2 Characterization of $FeTiO_3$ Thin Films

For reason mentioned in Chapter 1, an SiO_2 coating was further applied onto the $FeTiO_3$ films and then the $FeTiO_3$ and additional SiO_2 films on one face were removed. These films were characterized by X–ray diffraction, ellipsometry, UV–visible spectrophotometry and THG measurements as gone into details in Chapter 1.

3. Results

3.1 Crystallization Behavior

Figure 1 shows the X–ray diffraction pattern of $FeTiO_3$ thin films prepared by the sol–gel method. The crystalline phase precipitated in the sol–gel derived $FeTiO_3$ thin films was identified referring to JCPDS–FILE 29–0733 (hexagonal). Preferable orientation is not seen for $FeTiO_3$ films. The main crystalline phase was $FeTiO_3$ (ilmenite) although small amounts of Fe_2TiO_5 (pseudobrookite), $Fe_2Ti_3O_9$ (pseudorutile) and TiO_2 (rutile) phases were precipitated. In the present study, Ti–containing solution was added to Fe–containing solution. The reversed mixing lead to the increased TiO_2 phase. The reducing treatment of the resultant films was further attempted

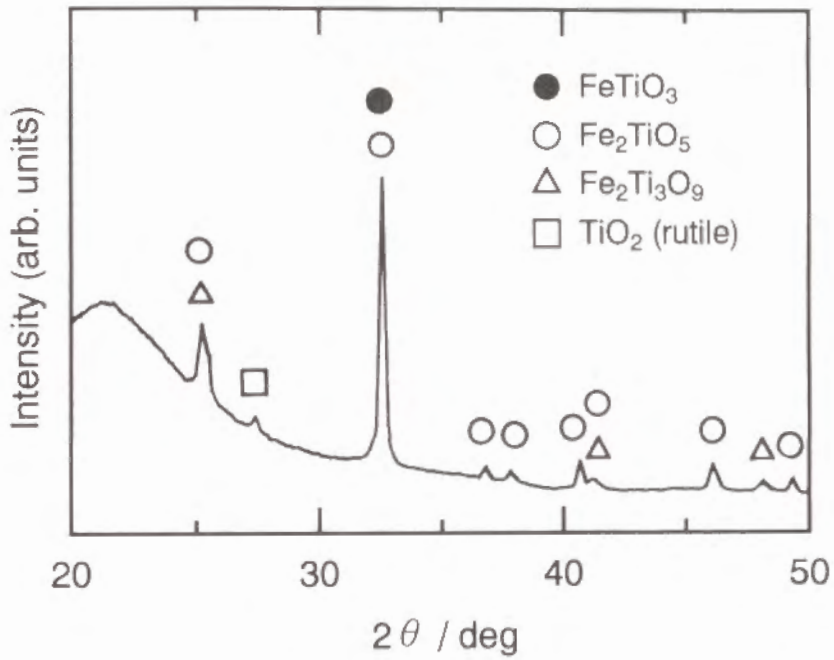

Fig. 1. X–ray diffraction pattern of $FeTiO_3$ thin films.

in order to convert the residual Fe^{3+} to Fe^{2+} ions. Although impurity phases such as Fe_2TiO_5 and $Fe_2Ti_3O_9$ decreased, the films became slightly blackish in color probably due to the formation of the reduced species such as Fe metal or Ti^{3+} ion, which could not be detected by an X-ray diffraction. The crystallite size in the $FeTiO_3$ films was ~30 nm.

3.2 Refractive Index and Optical Transmittance

The wavelength dependencies of refractive index, n, for $FeTiO_3$ thin films is shown in Figure 2. It is seen that the refractive index of $FeTiO_3$ films decreases with increasing wavelength. Figure 3 presents a linear plot of $(n^2-1)^{-1}$ versus E^2 for $FeTiO_3$ thin films based on Wemple's equation [3]

$$\frac{1}{n^2-1} = \frac{E_0}{E_d} - \frac{E^2}{E_0 E_d}, \qquad (1)$$

where E, E_0 and E_d are the photon energy, the average oscillator energy and dispersion energy in eV unit, respectively. E_0 and E_d are important optical properties of materials [3]. The refractive indices of $FeTiO_3$ films were estimated as $n_{3\omega}$=2.33 at 633 nm and n_{ω}=2.17 at 1900 nm, and the coherence length, $\ell_c=1.9/[6(n_{3\omega}-n_{\omega})]$, was 2.0 μm. The thickness of the $FeTiO_3$ films obtained by 10 dippings was typically 0.27 μm.

Figure 4 shows the absorption spectra of $FeTiO_3$ thin films with and without additional SiO_2 coating. Both spectra have a number of mountains and troughs arising from the interference of light. It is seen that the additional SiO_2 coating reduces the optical loss due to reflection especially in the wavelength region above ~400 nm. Fe^{2+} and Fe^{3+} ions in octahedral coordination are known to show absorption bands around 1100 and 800 nm, respectively [4]. The difference in absorbance due to reflection loss between

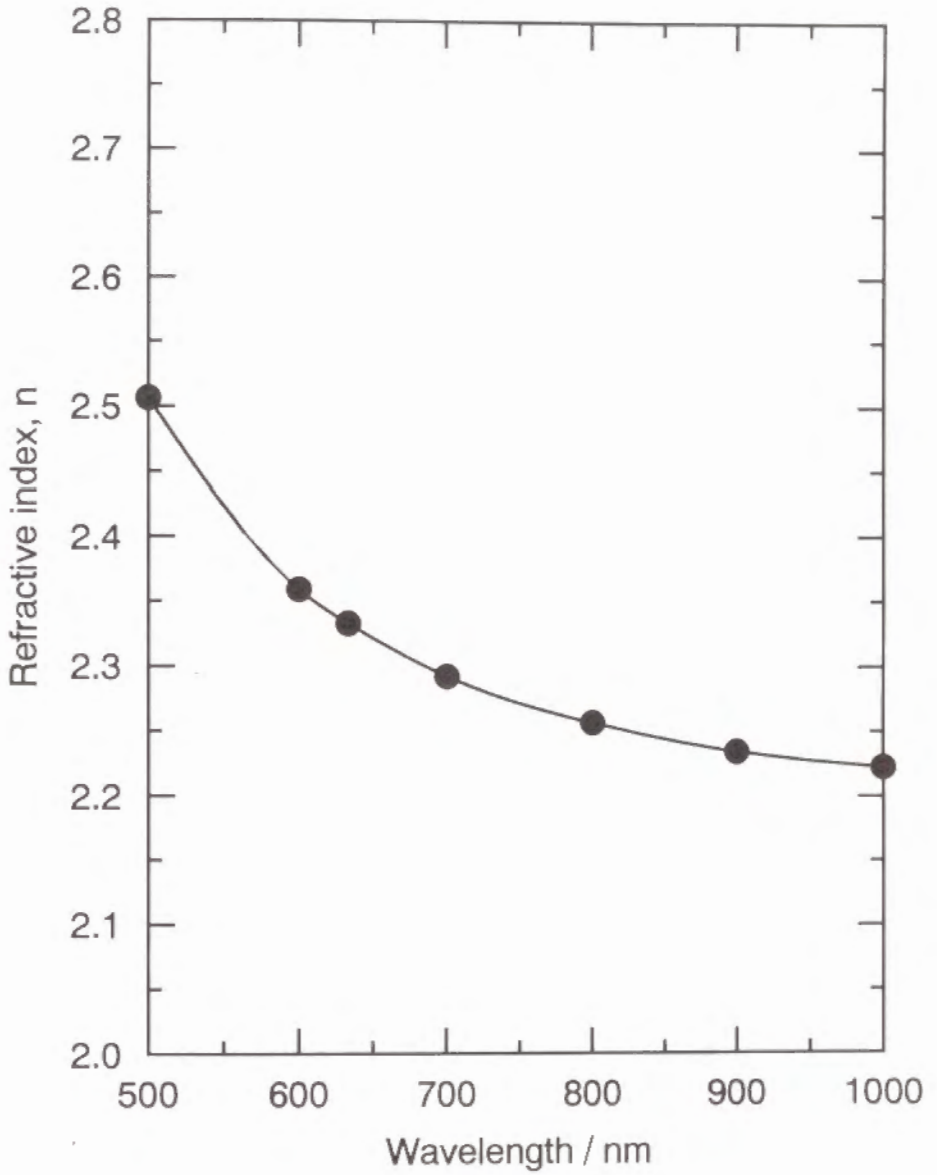

Fig. 2. Wavelength dependence of refractive index, n, for $FeTiO_3$ thin films.

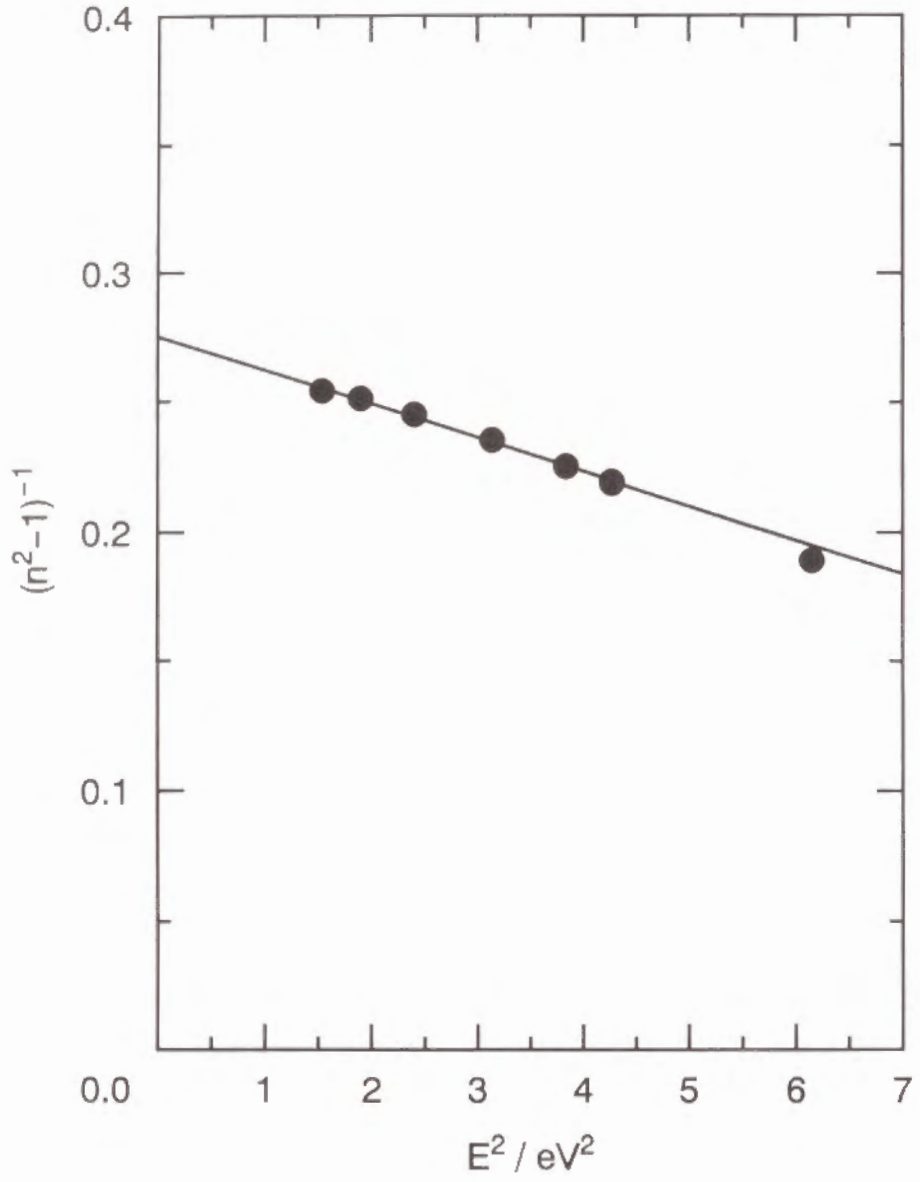

Fig. 3. Linear plot of $(n^2-1)^{-1}$ versus E^2 for $FeTiO_3$ thin films.

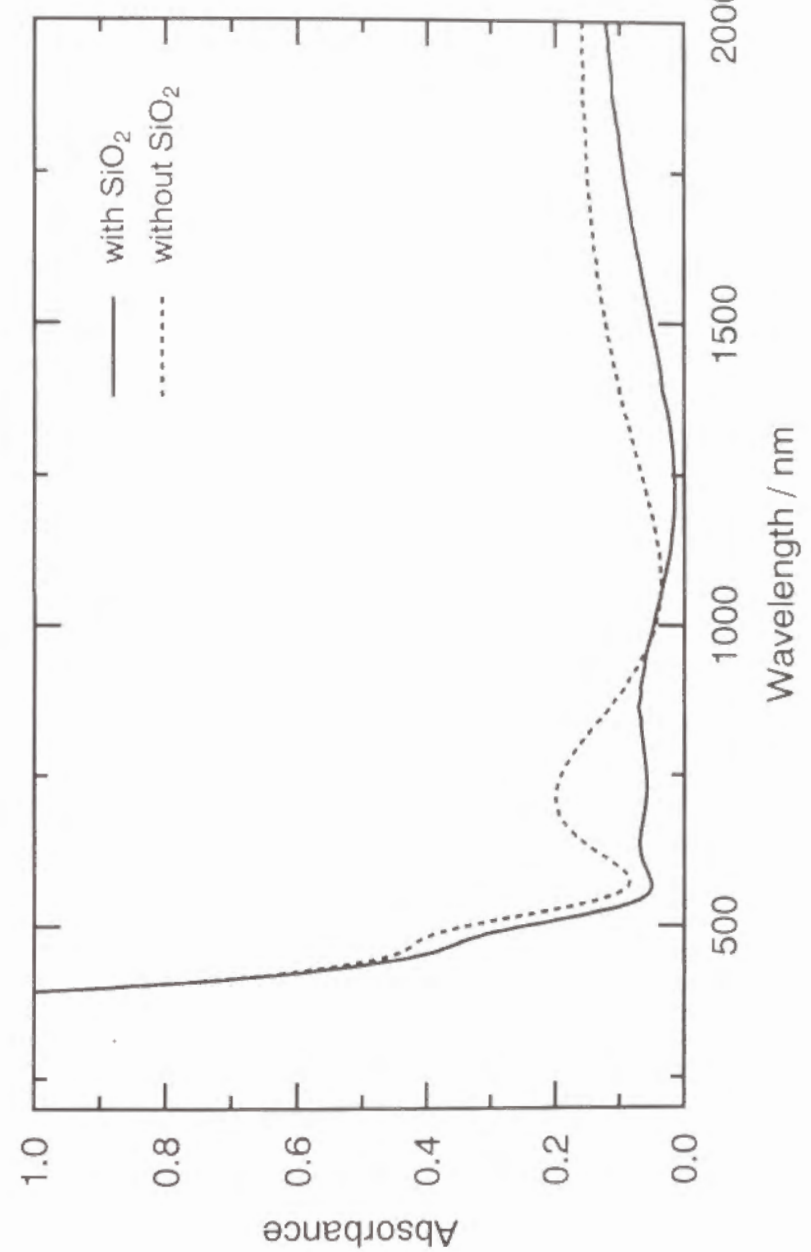

Fig. 4. Absorption spectra of $FeTiO_3$ thin films with and without additional SiO_2 coating.

both spectra is relatively small around 1100 and 800 nm, indicating that the present $FeTiO_3$ films include other Fe^{3+}-containing compounds as indicated by the result of X-ray diffraction measurement. The optical band gap, E_g, of $FeTiO_3$ films was estimated to be 2.2 eV.

3.3 Evaluation of $\chi^{(3)}$ Value

The THG intensities as a function of the rotation angle are given for (a) $FeTiO_3$ films and (b) SiO_2 glass in Figure 5. The THG intensity pattern of $FeTiO_3$ films clearly shows the interference between the THG lights from $FeTiO_3$ films and SiO_2 glass substrate as previously reported [5]. The THG intensity was obtained by the least squares method as solid line in Fig. 5.

In the present study, $\chi^{(3)}$ value was determined by the equation [6]

$$\chi^{(3)}_{film} = \frac{2}{\pi}\chi^{(3)}_{SiO_2}\frac{l_{c,\,SiO_2}}{l}\sqrt{\frac{I_{3\omega,\,film}}{I_{3\omega,\,SiO_2}}}\sqrt{\frac{n^3_{\omega,\,film}n_{3\omega,\,film}T^3_{\omega,\,SiO_2}T_{3\omega,\,SiO_2}}{n^3_{\omega,\,SiO_2}n_{3\omega,\,SiO_2}T^3_{\omega,\,film}T_{3\omega,\,film}}}\ (esu)\ , \qquad (2)$$

where I denotes the THG peak intensity. The film thickness is used for ℓ, because the film thickness is less than the coherence length. The values of $\chi^{(3)}{}_{SiO_2}=2.8\times10^{-14}$ esu and $\ell_{c,SiO_2}=18.1\ \mu$m were used for SiO_2 glass as both standard sample and substrate [7].

The intensity of THG signals generated from $FeTiO_3$ films was determined by the equation [5]

$$I_{film} = \frac{I_{max}+I_{min}}{2} - \frac{I_{substrate}}{2} = \frac{I_{max}+I_{min}}{2} - \frac{I_{SiO_2}}{2}\ , \qquad (3)$$

where I_{max} and I_{min} are the upper and lower envelopes of the superimposed THG intensity pattern. The THG light from the additional SiO_2 coating on

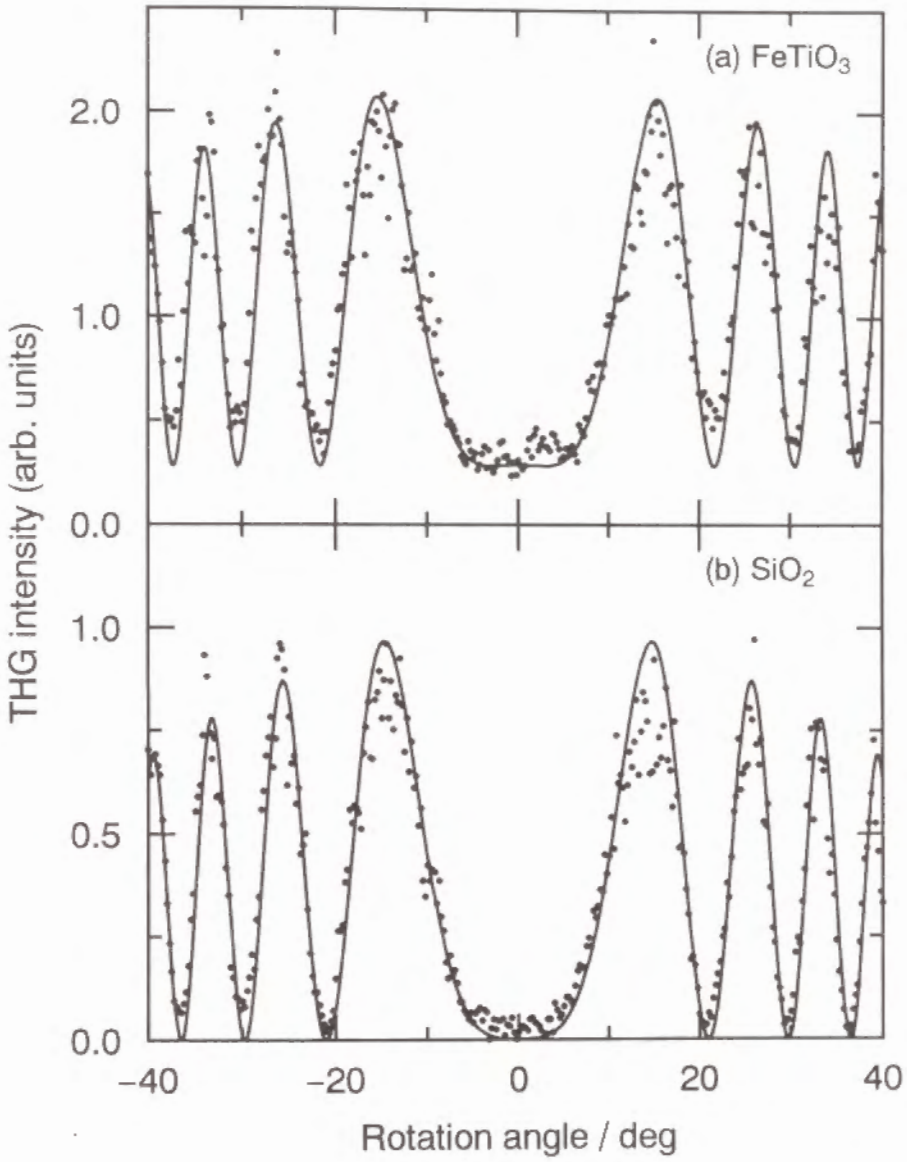

Fig. 5. THG intensities as a function of rotation angle for (a) $FeTiO_3$ films and (b) SiO_2 glass. Solid curves are computed using the least squares method.

the $FeTiO_3$ films was neglected, because $\chi^{(3)}_{SiO_2}$ is low and the thickness of SiO_2 coating (less than ~0.2 μm) is much smaller than the coherence length. The $\chi^{(3)}$ value of $FeTiO_3$ films was determined to be 3.3×10^{-12} esu. Table 1 summarizes the optical properties of $FeTiO_3$ thin films.

4. Discussion

4.1 Relation between $\chi^{(3)}$ and Refractive Index, n

It is possible to estimate $\chi^{(3)}$ of a material from refractive index, n, according to Miller's rule [1, 2]

$$\chi^{(3)} = [\chi^{(1)}]^4\times10^{-10}\ (esu)\ , \tag{4-a}$$

and

$$\chi^{(1)} = \frac{n^2-1}{4\pi}\ . \tag{4-b}$$

The $\chi^{(3)}$ value of 7.6×10^{-13} esu, which are predicted by Miller's rule for $FeTiO_3$ thin films, as in the second row of Table 2, is not in good accordance with the measured one, 3.3×10^{-12} esu, as in the first row.

Figure 6 shows a relation between $\chi^{(3)}$ and refractive index, n_ω, at 1900 nm for $FeTiO_3$ thin films and other nonlinear optical materials reported so far [6–13]. It is seen that inorganic materials with high refractive index inherently exhibit high optical nonlinearity.

The $\chi^{(3)}$ values of organic polymers such as polydiacetylene (PDA) [11] and poly(2,5–dimethoxy *p*–phenylene vinylene) (MO–PPV) [12] deviate from the relation to a considerable extent, due to the enhancement by the so–called three–photon resonance or near three–photon resonance [14]. Since the

Table 1. Optical properties of $FeTiO_3$ thin films.

Compound	$n_{3\omega}$	n_ω	$T_{3\omega}$ / %	T_ω / %	E_0 / eV	E_d / eV	E_g / eV	$\frac{I_{3\omega,film}}{I_{3\omega,SiO_2}}$	ℓ_c / μm	ℓ / μm	$\chi^{(3)}$ / esu
$FeTiO_3$	2.33	2.17	85.3	77.5	4.6	16.8	2.2	0.71	2.0	0.27	3.3×10^{-12}

The physical meanings of all the notations in the table are described in the section 3.
Transmittances are values for $FeTiO_3$ thin films with additional SiO_2 coating.

Table 2. Comparison of the measured $\chi^{(3)}$ with the calculated $\chi^{(3)}$ for $FeTiO_3$ thin films on the basis of three models.

	$\chi^{(3)}$ / esu
	$FeTiO_3$
Measured value	3.3×10^{-12}
Miller's rule	7.6×10^{-13}
Band gap model	4.2×10^{-11}
Lines' model	2.4×10^{-12}

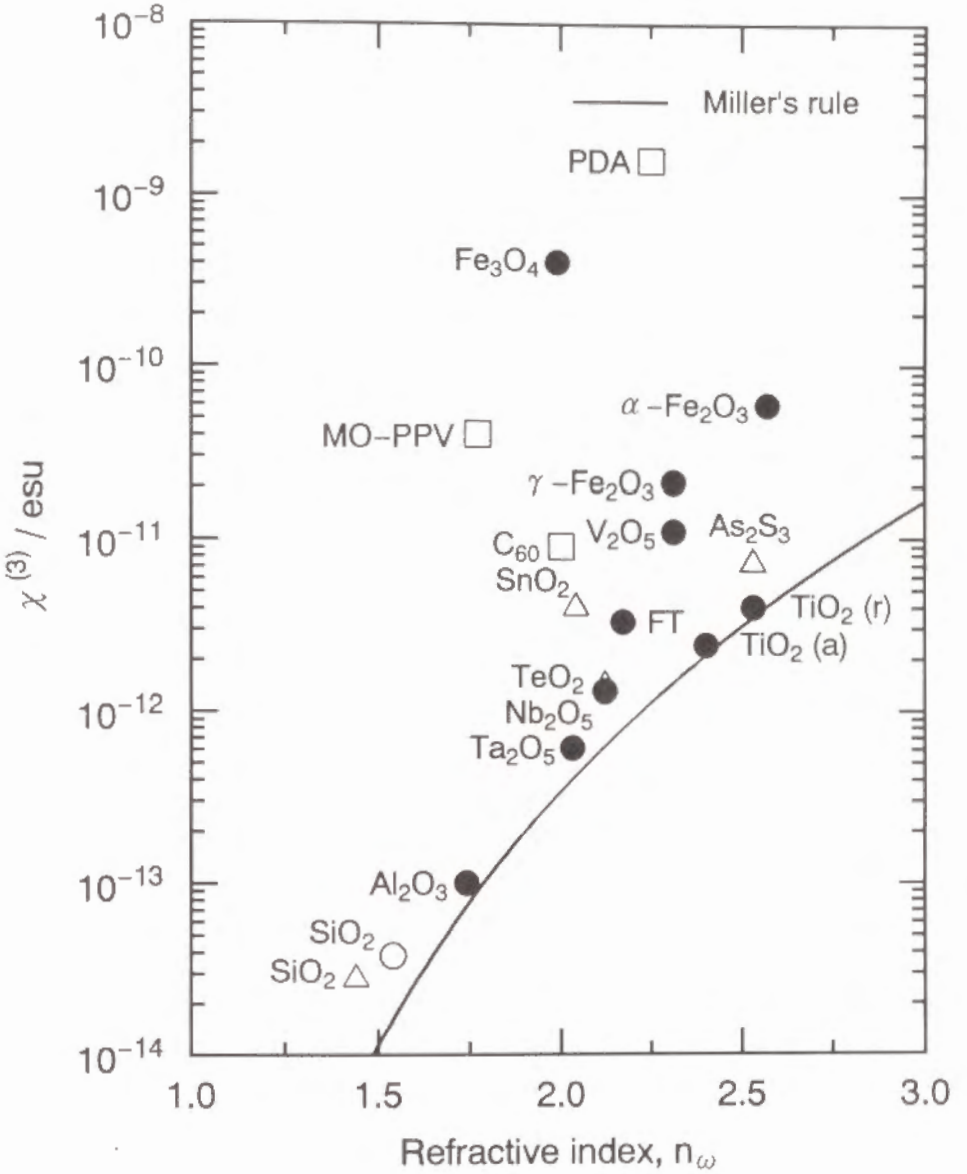

Fig. 6. Relation between $\chi^{(3)}$ and refractive index, n_ω, at 1900 nm for $FeTiO_3$ thin film together with other NLO materials. Circles, triangles and squares denote inorganic crystals, inorganic amorphous materials and organic materials, respectively. Closed circles are data measured in the present study. The letters of r and a in parentheses denote rutile and anatase, respectively. FT: $FeTiO_3$, PDA: polydiacetylene, MO-PPV: poly(2,5-dimethoxy *p*-phenylene vinylene).

measured $\chi^{(3)}$ includes the significant contribution of the imaginary part, there are no simple relations between $\chi^{(3)}$ and refractive index for these organic materials, that is, Miller's rule does not hold.

4.2 Relation between $\chi^{(3)}$ and Optical Band Gap, E_g

One can expect that an enhancement in $\chi^{(3)}(-3\omega;\omega,\omega,\omega)$ occurs when in a material a frequency of interacting light approaches either one of one-, two- or three-photon resonance frequencies according to the relation [14]

$$\chi^{(3)}(-3\omega;\omega,\omega,\omega) \propto \frac{N}{\hbar^3}\sum_{gnmn'} \rho(g)F(\omega)\Omega_{gn}\Omega_{nm}\Omega_{mn'}\Omega_{n'g}\ (esu)\ , \qquad (5\text{-a})$$

and

$$F(\omega) = \frac{1}{(E_{ng}-3\omega)(E_{mg}-2\omega)(E_{n'g}-\omega)} + \frac{1}{(E_{ng}+\omega)(E_{mg}-2\omega)(E_{n'g}-\omega)} + \frac{1}{(E_{ng}+\omega)(E_{mg}+2\omega)(E_{n'g}-\omega)} + \frac{1}{(E_{ng}+\omega)(E_{mg}+2\omega)(E_{n'g}+3\omega)}\ , \qquad (5\text{-b})$$

where $\rho(g)$, E_{ij} and Ω_{ij} are the density matrix element of fundamental state, the energy difference between states i and j in $\hbar$ ($=h/2\pi$, h: Planck's constant) unit and the transition matrix elements between states i and j, respectively. For materials having optical band gap, E_g, higher than three-photon energy, 3ω, the three-photon resonance makes the greatest contribution to the enhancement of $\chi^{(3)}$. Then, to a good approximation, the most significant term due to the three-photon resonance in Eq. (5) may be expressed as follows:

$$\chi^{(3)} = \frac{A}{(E_g-1.96)(E_g-1.31)(E_g-0.65)}\ (esu)\ (E_g>1.96)\ , \qquad (6)$$

where A is the phenomenological constant.

Figure 7 gives a relation between $\chi^{(3)}$ and optical band gap, E_g, for $FeTiO_3$ thin films and other nonlinear optical materials shown in Fig. 6. In Fig. 7, for organic materials the absorption edge of exciton absorption is used instead of E_g. In this figure, the $\chi^{(3)}$ values of these materials show a clear tendency to increase asymptotically as the E_g approaches 1.96 eV corresponding to the photon energy of THG signal. This change obeys Eq. (6) when the parameter, A, takes a value of 1.4×10^{-11}. From Eq. (6), the $\chi^{(3)}$ value was estimated to be 4.2×10^{-11} esu for $FeTiO_3$, as in the third row of Table 2, which is not in accordance with the measured one, 3.3×10^{-12} esu, as in the first row.

The above discussion indicates that the large $\chi^{(3)}$ value of 3.3×10^{-12} esu for $FeTiO_3$ films, which is comparable to those for TiO_2 polymorphs (rutile and anatase), is explained by the balanced contributions of two opposite effects, the lower refractive index (negative contribution) and the narrower optical band gap (positive contribution) compared with TiO_2 polymorphs. On the other hand, the $\chi^{(3)}$ value of $FeTiO_3$ films is one order of magnitude lower than that of α-Fe_2O_3 because of the lower refractive index and the wider optical band gap compared with α-Fe_2O_3.

4.3 Calculation of $\chi^{(3)}$ Based on Lines' Model

Lines introduced a bond-orbital theory dealing with the contribution of empty *d* orbital in addition to *sp* orbitals to linear and nonlinear optical properties, giving the following equation to estimate $\chi^{(3)}$ [15, 16]:

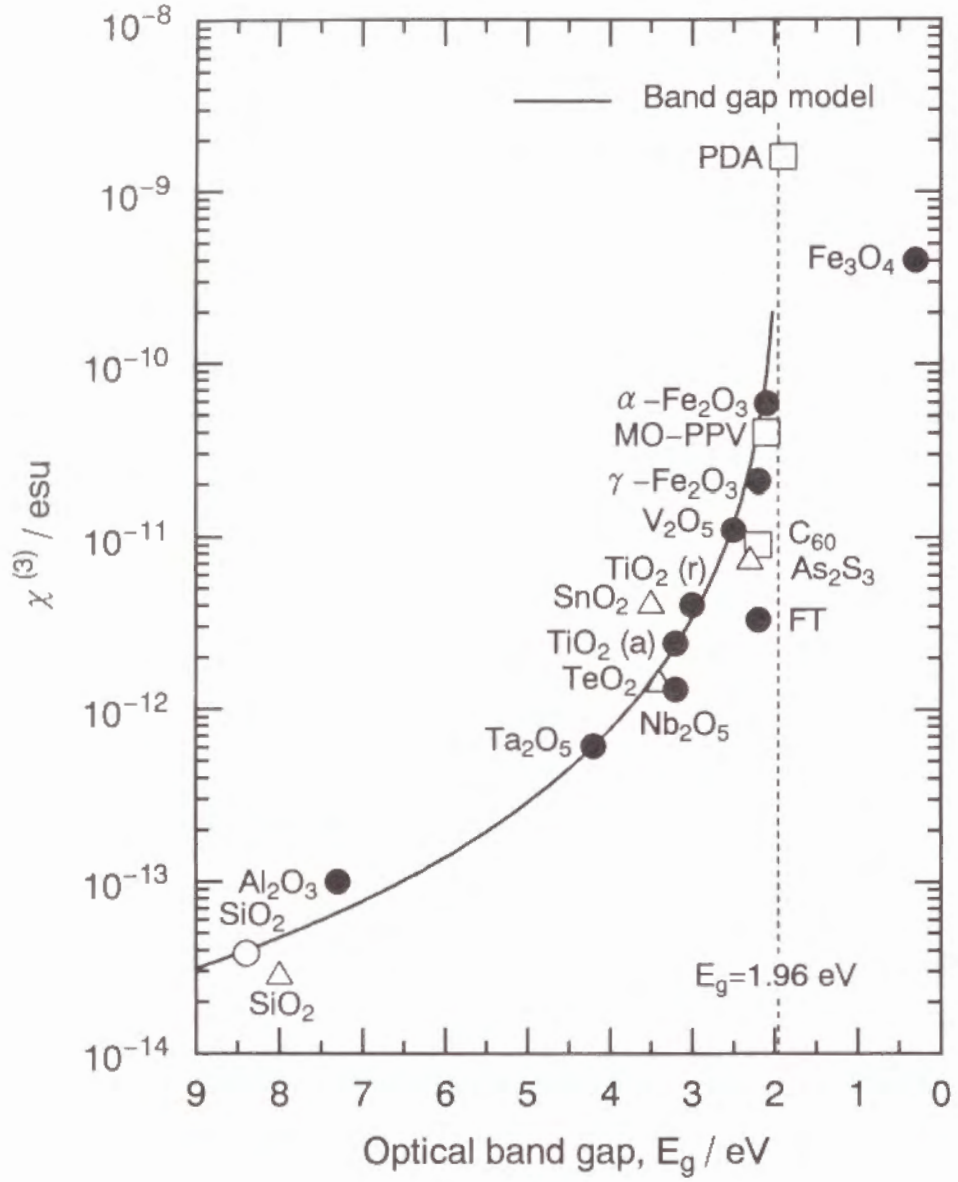

Fig. 7. Relation between $\chi^{(3)}$ and optical band gap, E_g, for $FeTiO_3$ thin films together with other NLO materials. Notations are the same as in Fig. 6.

$$\chi^{(3)} = \frac{2.5\times10^{-12}\ell_b^2(n_\omega^2-1)f_L^3E_S^6}{3\pi[E_S^2-E^2]^4}\ (esu)\ , \tag{7}$$

where ℓ_b denotes the bond length between cation and anion, $f_L=(n_\omega^2+2)/3$ the Lorentz local–field correction factor, E_S the Sellmeier gap which is in practice equal to the average oscillator energy, E_0, in Eq. (1). From Eq. (7), one can obtain $\chi^{(3)}$ value of 2.4×10^{-12} esu for $FeTiO_3$ films, as in the fourth row, which is in reasonable accordance with the measured value of 3.3×10^{-12} esu, as in the second row, compared with those calculated by the above two models. This is possibly because two important optical properties (refractive index and Sellmeier gap) are included in Eq. (7).

Weak absorption bands around 1,100 nm (1.13 eV) and 800 nm (1.55 eV) due to the presence of Fe^{2+} and Fe^{3+} ions, respectively, do not always cause two–photon resonance at 1.31 eV, because the process requires parity opposite to one and three–photon related ones. Also, Kajzar et al. [14] reported that as for PDA the effect of two–photon resonance on the third–order nonlinear optical susceptibility is smaller than that of three–photon resonance.

4.4 Effect of Valence and Coordination Number of Fe Ions on $\chi^{(3)}$

In order to make the effect of the valence and coordination number of Fe ions on the third–order nonlinear optical properties clear, microscopic second–hyperpolarizability, γ, has to be taken into account, because macroscopic $\chi^{(3)}$ depends on both γ_i and the number density, N_i of the *i*th constituent as follows [17, 18]:

$$\chi^{(3)} = \frac{f_L^4}{24}\sum_i N_i\gamma_i\ (esu), \tag{8}$$

For a metal oxide, M_xO_y, γ per $M_{x/y}O$ formula unit, $\gamma(M_{x/y}O)$, can be derived as follows:

$$\gamma(M_{x/y}O) = \frac{1944\chi^{(3)}M_w}{N_A(n_\omega^2+2)^4 yD} \ (esu\ cm^3), \tag{9}$$

where M_w, D and N_A are the molecular weight and density of M_xO_y and Avogadro's number, respectively. Table 3 summarizes microscopic and macroscopic nonlinear optical properties of Fe–containing oxides together with other NLO materials.

The $\gamma(Fe^{3+}_{2/3}O)_{oct}$ and $\gamma(Fe^{2+}O)_{oct}$ values of Fe^{3+} and Fe^{2+} ions in FeO_6 octahedra, which were calculated using $\chi^{(3)}$ values of α–Fe_2O_3, $FeTiO_3$ and TiO_2, were estimated to be 3.5×10^{-34} and 9.8×10^{-35} esu cm^3, respectively. $\gamma(Fe^{3+}_{2/3}O)_{oct}$ is three to four times as high as $\gamma(Fe^{2+}O)_{oct}$. Therefore, $\chi^{(3)}$ of transition metal oxides with partially occupied *d* orbitals is also influenced by the bond length as in the case of the transition metal oxides with empty *d* orbitals. This result may be attributed to the larger *p*–*d* overlapping resulting from the shorter Fe–O bond length of the former. This short distance is due to the smaller ionic radius of Fe^{3+} ions compared Fe^{2+} ions. In fact, the bond lengths of Fe–O and Ti–O in $FeTiO_3$ are 0.209 and 0.203 nm [19], respectively, whereas those in α–Fe_2O_3 and TiO_2 are 0.203 [19] and 0.195–0.196 nm [20], respectively. Since the Ti–O bond length in $FeTiO_3$ was assumed to be the same as that in TiO_2 on calculation of $\gamma(Fe^{2+}O)$ value, the true $\gamma(Ti^{4+}_{1/2}O)$ value for $FeTiO_3$ should be lower than that in TiO_2 and then the $\gamma(Fe^{2+}O)$ value should be larger than 9.8×10^{-35} esu cm^3. Therefore, it can be said that the $\chi^{(3)}$ value of $FeTiO_3$ may be governed by the $\gamma(Fe^{2+}O)$ rather than $\gamma(Ti^{4+}_{1/2}O)$.

Table 3. Microscopic and macroscopic nonlinear optical properties of Fe–containing oxides together with other NLO materials.

Compound	$\gamma(M_xO)$ / esu cm^3	$\chi^{(3)}$ / esu	N_i / cm^{-3}	n_ω	D / g cm^{-3}	M_w / g mol^{-1}
α–Fe_2O_3	3.5×10^{-34}	5.8×10^{-11}	5.9×10^{22}	2.57	5.26	159.70
γ–Fe_2O_3	2.5×10^{-34}	2.1×10^{-11}	5.5×10^{22}	2.31	4.90	159.70
Fe_3O_4	1.1×10^{-32}	4.0×10^{-10}	5.4×10^{22}	1.99	5.18	231.55
$FeTiO_3$	4.8×10^{-35}	3.3×10^{-12}	6.5×10^{22}	2.17	5.50	151.73
TiO_2 (rutile)	2.5×10^{-35}	4.0×10^{-12}	6.4×10^{22}	2.53	4.23	79.88
TiO_2 (anatase)	2.2×10^{-35}	2.4×10^{-12}	5.9×10^{22}	2.40	3.89	79.88
SiO_2 glass	4.5×10^{-36}	2.8×10^{-14}	4.4×10^{22}	1.44	2.21	60.09
Hypothetical crystal						
FeO (octahedral)	9.8×10^{-35} *1	---	---	---	---	71.85
Fe_2O_3 (tetrahedral)	8.9×10^{-35} *1	---	---	---	---	159.70
Fe_4O_5 (octahedral) *2(a)	1.8×10^{-32} *1	---	---	---	---	303.40
Fe_4O_5 (octahedral) *2(b)	2.5×10^{-34} *1	---	---	---	---	303.40

*1: These $\gamma(Fe_{x/y}O)$'s are values for hypothetical crystals consisting of oxygen polyhedra indicated in parentheses.
*2: Octahedral sites of Fe_4O_5 are occupied by (a) $Fe^{2.5+}$ ions and (b) discrete Fe^{2+} and Fe^{3+} ions.

Analogously, $\gamma(Fe^{3+}_{2/3}O)$ values was calculated using $\chi^{(3)}$ value of γ–Fe_2O_3 to be 2.5×10^{-34} esu cm^3. If one assumes the independent contributions of $\gamma(Fe^{3+}_{2/3}O)$ for Fe^{3+} ions in FeO_6 octahedra and FeO_4 tetrahedra for γ–Fe_2O_3 to the total $\chi^{(3)}$, $\gamma(Fe^{3+}_{2/3}O)_{tet}$ value of Fe^{3+} ions in oxygen tetrahedra is calculated to be 8.9×10^{-35} esu cm^3 using $\gamma(Fe_{2/3}{}^{3+}O)$ and $\gamma(Fe^{3+}_{2/3}O)_{oct}$ values. $\gamma(Fe^{3+}_{2/3}O)_{oct}$ is four times as high as $\gamma(Fe^{3+}O)_{tet}$. This may be ascribed to the effective p–d overlapping due to the p–d hybridization (sp^3d^2) in Fe^{3+} ions in octahedral sites, which is not available for Fe^{3+} ions in tetrahedral sites (sp^3), and in part to the longer Fe–O bond length in octahedral sites, because $\gamma(M_{x/y}O)$ is proportional to the cube of the M–O bond length as is known from Eq. (9).

Fe_3O_4 contains Fe^{2+} and Fe^{3+} ions octahedrally coordinated by oxygens and tetrahedrally coordinated Fe^{3+} ions. It is considered that above Verwey temperature at 120 K the octahedral sites are occupied by $Fe^{2.5+}$ ions rather than discrete Fe^{2+} and Fe^{3+} ions, because the electron hopping on a time scale is short compared with pulse width of laser. [21] $\gamma(Fe^{8/3+}_{3/4}O)$ value was calculated using $\chi^{(3)}$ value of Fe_3O_4 to be 1.1×10^{-32} esu cm^3 and $\gamma(Fe^{2.5+}_{4/5}O)_{oct}$ values of $Fe^{2.5+}$ ion in FeO_6 octahedra was obtained to be 1.8×10^{-32} esu cm^3 using $\gamma(Fe^{8/3+}{}_{3/4}O)$ and $\gamma(Fe^{3+}_{2/3}O)_{tet}$ values. $\gamma(Fe^{2.5+}_{4/5}O)'_{oct}$, which is weighted–average between $\gamma(Fe^{2+}O)_{oct}$ and $\gamma(Fe^{3+}_{2/3}O)_{oct}$, is 2.5×10^{-34} esu cm^3 but lower than $\gamma(Fe^{2.5+}_{4/5}O)_{oct}$ by two orders of magnitude. The physical meaning of this value is the average contribution of $\gamma(Fe_{x/y}O)$ for the Fe^{2+} and Fe^{3+} ions in FeO_6 octahedra to the $\chi^{(3)}$ of Fe_3O_4 below Verwey temperature. Therefore, it is predicted from Eq. (8) and Table 5 that $\chi^{(3)}$ of Fe_3O_4 is ~7×10^{-12} esu below Verwey temperature on the assumption of the constant refractive index and density. It is necessary to examine $\chi^{(3)}$ of Fe_3O_4 at low temperatures below Verwey temperature by means of Z–scan method [22].

5. Conclusion

In this chapter, the third–order nonlinear optical properties of the sol–gel derived $FeTiO_3$ thin films have been investigated by the THG method. Primarily, the effect of valence and coordination number of Fe ions on the $\chi^{(3)}$ has been examined. The following results were obtained.

(1) The $\chi^{(3)}$ value of $FeTiO_3$ thin films was 3.3×10^{-12} esu, which is comparable to those for TiO_2 polymorphs (rutile and anatase), but one order of magnitude lower than that of α–Fe_2O_3.

(2) The $\gamma(Fe^{2+}O)$ was ~4 times as large as $\gamma(Ti^{4+}{}_{1/2}O)$, indicating that the $\chi^{(3)}$ value of $FeTiO_3$ is governed by the $\gamma(Fe^{2+}O)$ rather than $\gamma(Ti^{4+}{}_{1/2}O)$.

(3) The higher $\gamma(Fe_{x/y}O)$ is obtained when Fe ions are 3+ rather than 2+ and octahedrally rather than tetrahedrally coordinated by oxygens. It is expected that $\gamma(Fe^{2.5+}_{4/5}O)$ under the resonant condition is extremely high.

References

[1] R. C. Miller, *Appl. Phys. Lett.*, **5**, 17 (1964).

[2] C. C. Wang, *Phys. Rev. B*, **2**, 2045 (1970).

[3] S. H. Wemple, *J. Chem. Phys.*, **67**, 2151 (1977).

[4] T. Bates, "Modern Aspects of the Vitreous State, **2**", ed. by J. D. Mackenzie, Butterworths, London (1962) p. 195.

[5] K. Kubodera and H. Kobayashi, *Mol. Cryst. Liq. Cryst.*, **182A**, 103 (1990).

[6] H. Nasu, K. Kubodera, M. Kobayashi, M. Nakamura and K. Kamiya, *J. Am. Ceram. Soc.*, **73**, 1794 (1990).

[7] G. R. Meredith, B. Buchalter and C. Hanzlik, *J. Chem. Phys.*, **78**, 1533 (1983).

[8] G. R. Meredith, *Phys. Rev. B*, **24**, 5522 (1981).

[9] N. Ueda, H. Kawazoe, Y. Watanabe, M. Takata, M. Yamane and K. Kubodera, *Appl. Phys. Lett.*, **59**, 502 (1991).

[10] S. H. Kim, T. Yoko and S. Sakka, *J. Am. Ceram. Soc.*, **76**, 2486 (1993).

[11] T. Kanetake, K. Ishikawa, T. Hasegawa, T. Koda, K. Takeda, M. Hasegawa, K. Kubodera and H. Kobayashi, *Appl. Phys. Lett,*, **54**, 2287 (1989).

[12] T. Kurihara, Y. Mori, T. Kaino, H. Murata, N. Takada, T. Tsutsui and S. Saito, *Chem. Phys. Lett.*, **183**, 534 (1991).

[13] J. S. Meth, H. Vanherzeele and Y. Wang, *Chem. Phys. Lett.*, **197**, 26 (1992).

[14] F. Kajzar and J. Messier, "Nonlinear Optical Properties of Organic Molecules and Crystals, **2**", ed. by D. S. Chemla and J. Zyss, Academic Press (1987) p. 51.

[15] M. E. Lines, *Phys Rev. B*, **41**, 3383 (1990).

[16] M. E. Lines, *Phys. Rev. B*, **43**, 11978 (1991).

[17] N. L. Boling, A. J. Glass and A. Owyoung, *IEEE J. Quant. Electron.*, **QE-14**, 601 (1978).

[18] R. Adair, L. L. Chase and S. A. Payne, *Phys. Rev. B*, **39**, 3337 (1989).

[19] R. Kiriyama, "Kozomukikagaku, **III**", Kyoritu Zensyo, Tokyo (1978) p. 51.

[20] J. K. Burdett, T. Hughbanks, G. J. Miller, J. W. Richardson, Jr. and J. V. Smith, *J. Am. Chem. Soc.*, **109**, 3639 (1987).

[21] R. G. Strens and B. J. Wood, *Miner. Mag.*, **43**, 347 (1979).

[22] M. Sheik-Bahae, A. A. Said, T. H. Wei, D. J. Hagan, E. W. Van Stryland, *IEEE J. Quant. Electron.*, **26**, 760 (1990).

CHAPTER 5. THIRD-ORDER NONLINEAR OPTICAL PROPERTIES OF Pb-COMPLEX PEROVSKITE THIN FILMS

SECTION 5.1 THIRD-ORDER NONLINEAR OPTICAL PROPERTIES OF α-PbO THIN FILMS

1. Introduction

In Chapter 2, it was revealed that $\chi^{(3)}$ of transition metal oxides with the empty *d* orbitals is dominated mainly by the metal-oxygen bond length rather than the valence of metal cation. It was also predicted on the basis of Lines' model that transition metal oxides with the shortest bond length exhibit the highest $\chi^{(3)}$ while non-transition metal oxides with the longest ones do the highest $\chi^{(3)}$. The latter prediction states that oxides containing large cation such as PbO show the high $\chi^{(3)}$. One expects that PbO consisting of Pb ions with high polarizability may be exhibit the high $\chi^{(3)}$ as well as high refractive index. Although there are some studies on $\chi^{(3)}$ of PbO-containing glasses [1-3], the third-order optical nonlinearity of single component PbO itself has not been discussed except Vogel's study by means of DFWM method (1064 nm) [4, 5]. Her data however dose not include any information on polymorph and refractive index and moreover the wavelength of incident beam differs from 1900 nm employed in the present study. Therefore, it is indispensable to determine $\chi^{(3)}$ and refractive index at 1900 nm of a known PbO polymorph in order to estimate the contribution of Pb^{2+} ions to the $\chi^{(3)}$.

In this section, the results of the preparation of α-PbO thin films on SiO_2 glass substrates by the sol-gel method and the third-order nonlinear optical properties studied by the THG method are presented.

2. Experimental

2.1 Preparation of α-PbO thin films

α-PbO thin films were prepared by the sol-gel method. As a starting solution, $Pb(OCOCH_3)_2 \cdot 3H_2O$-$CH_3OCH_2CH_2OH$-$HNO_3$ solution was selected

for α-PbO films. The chemical composition of the solution was 1:60:0.1 in molar ratio. In α-PbO solution, lead acetate trihydrate $Pb(OCOCH_3)_2 \cdot 3H_2O$ was dissolved in a mixture of 2-methoxyethanol ($CH_3OCH_2CH_2OH$) and HNO_3aq (~15 N). Coating solution was allowed to stand for 2 h at 30 °C prior to use.

Dip-coating was used for film formation. A SiO_2 glass substrate was immersed into a coating solution, and pulled up at a rate of 3 cm min^{-1}. The films were heated at 400 °C for 10 min immediately after each coating procedure. This cycle was repeated 10 times to attain the desired film thickness.

2.2 Characterization of α-PbO Thin Films

An SiO_2 coating was not further applied onto the α-PbO films to avoid reaction of α-PbO films with the additional SiO_2 coating as usually formed and then the α-PbO films on one face were removed. These films were characterized by X-ray diffraction, ellipsometry, UV-visible spectrophotometry and THG measurements as described in detail in Chapter 1.

3. Results

3.1 Crystallization Behavior

Figure 1 shows the X-ray diffraction pattern of α-PbO thin films prepared by the sol-gel method. The crystalline phase precipitated in the sol-gel derived α-PbO thin films was identified referring to JCPDS-FILE 5-0561 (tetragonal). Preferable orientation along the (002) plane is seen for α-PbO films. The crystallite size in the α-PbO films was ~20 nm.

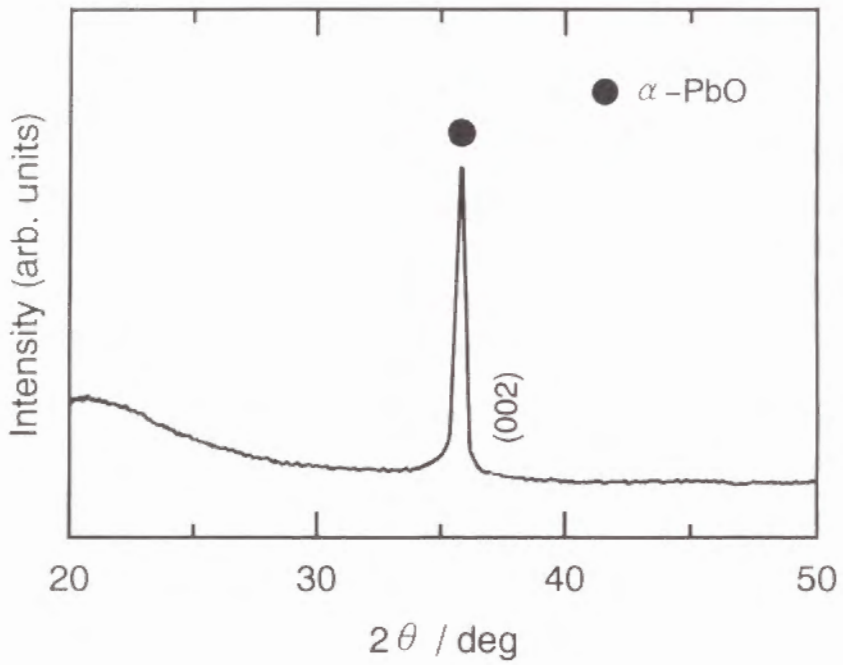

Fig. 1. X-ray diffraction pattern of α-PbO thin films prepared by the sol-gel method.

3.2 Refractive Index and Optical Transmittance

The wavelength dependence of refractive index, n, for α-PbO thin films is shown in Figure 2. It can be seen that the refractive index of α-PbO films strongly depends on the wavelength as well-known. Figure 3 presents the linear plot of $(n^2-1)^{-1}$ versus E^2 for α-PbO thin films based on Wemple's equation [6]

$$\frac{1}{n^2-1} = \frac{E_0}{E_d} - \frac{E^2}{E_0 E_d}, \qquad (1)$$

where E, E_0 and E_d are the photon energy, the average oscillator energy and dispersion energy in eV unit, respectively. E_0 and E_d are important optical properties of materials [6]. The refractive indices were estimated as $n_{3\omega}$=2.13 at 633 nm and n_ω=1.92 at 1900 nm, and the coherence length, ℓ_c=1.9/[6($n_{3\omega}$-n_ω)], was 1.5 μm for α-PbO films. The thickness of the α-PbO films obtained by 10 dippings was 0.10 μm.

Figure 4 shows the absorption spectrum of α-PbO thin films without additional SiO_2 coating. This spectrum has no mountains and troughs arising from the interference of light due to the small film thickness. The optical band gap, E_g, of α-PbO films was estimated to be 3.0 eV.

3.3 Evaluation of $\chi^{(3)}$ Value

The THG intensities as a function of the rotation angle for (a) α-PbO films and (b) SiO_2 glass are given in Figure 5. The THG intensity pattern of α-PbO films clearly shows the interference between the THG lights from α-PbO films and SiO_2 glass substrate as previously reported [7]. The THG intensity was obtained by the least squares method as solid curve in Fig. 5.

In the present study, $\chi^{(3)}$ was determined by the equation [8]

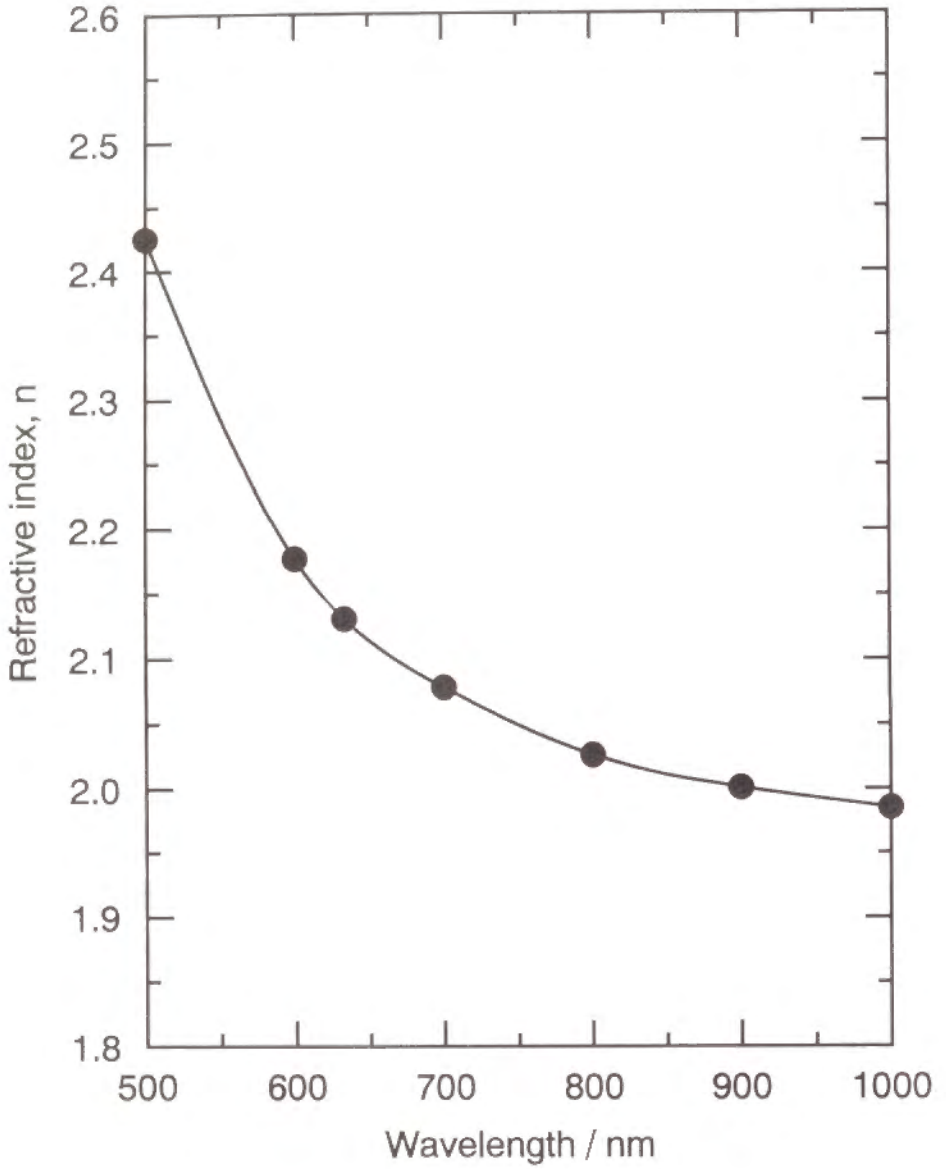

Fig. 2. Wavelength dependence of refractive index, n, for α–PbO thin films.

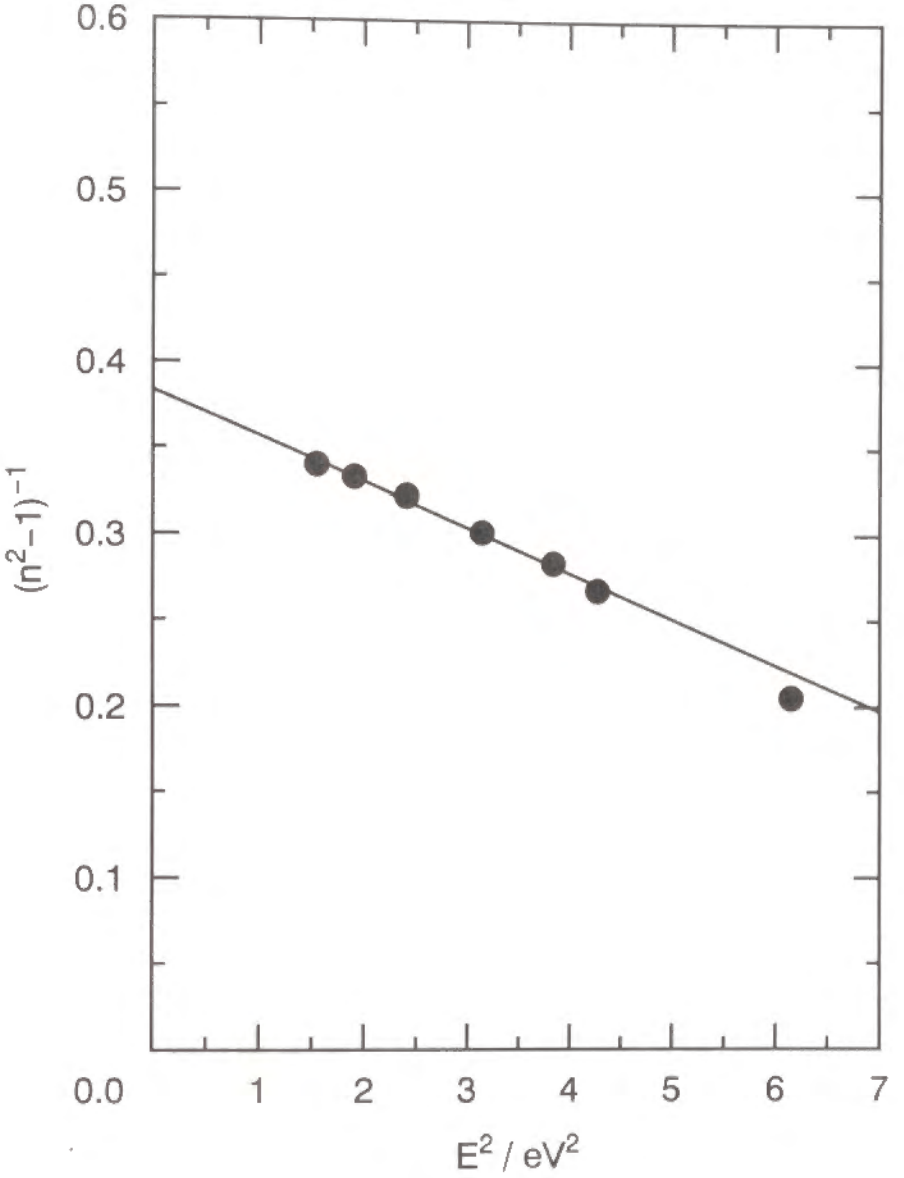

Fig. 3. Linear plot of $(n^2-1)^{-1}$ versus E^2 for α–PbO thin films.

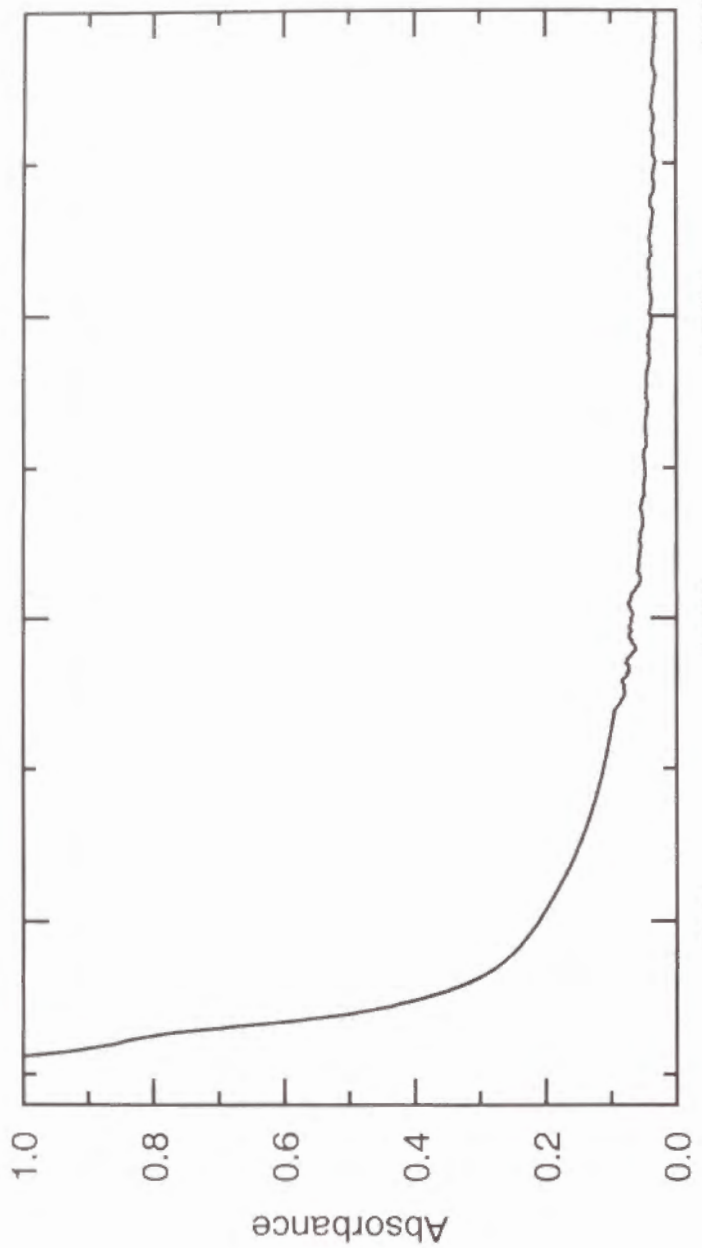

Fig. 4. Absorption spectrum of α–PbO thin films without additional SiO_2 coating.

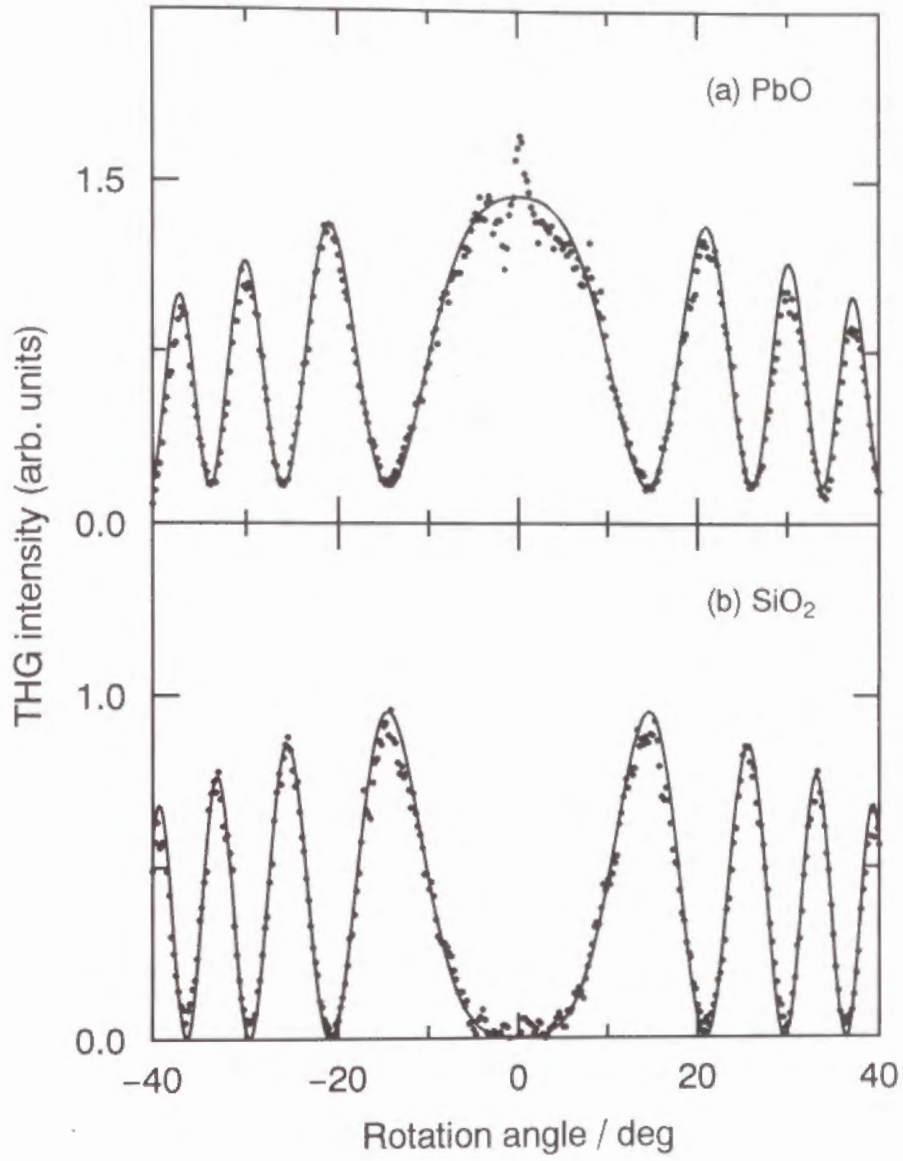

Fig. 5. THG intensities as a function of rotation angle for (a) α–PbO films, (b) SiO_2 glass. Solid curves are computed using the least squares method.

$$\chi^{(3)}_{film} = \frac{2}{\pi}\chi^{(3)}_{SiO_2}\frac{\ell_{c,\,SiO_2}}{\ell}\sqrt{\frac{I_{3\omega,\,film}}{I_{3\omega,\,SiO_2}}}\sqrt{\frac{n^3_{\omega,\,film}n_{3\omega,\,film}T^3_{\omega,\,SiO_2}T_{3\omega,\,SiO_2}}{n^3_{\omega,\,SiO_2}n_{3\omega,\,SiO_2}T^3_{\omega,\,film}T_{3\omega,\,film}}}\ (esu)\ , \qquad (2)$$

where I denotes the THG peak intensity. The film thickness is used for ℓ, because the film thickness is less than the coherence length. The values of $\chi^{(3)}_{SiO_2}=2.8\times10^{-14}$ esu and $\ell_{c,SiO_2}=18.1$ μm were used for SiO_2 glass as both standard sample and substrate [9].

The intensity of THG signals generated from α–PbO films was determined by the equation [7]

$$I_{film} = \frac{I_{max}+I_{min}}{2} - \frac{I_{substrate}}{2} = \frac{I_{max}+I_{min}}{2} - \frac{I_{SiO_2}}{2}\ , \qquad (3)$$

where I_{max} and I_{min} are the upper and lower envelopes, respectively, of the superimposed THG intensity pattern. The $\chi^{(3)}$ value of α–PbO films was determined to be 3.8×10^{-12} esu. Table 1 summarizes the obtained optical properties of α–PbO thin films. The present value is lower than that after Vogel (1.4×10^{-11} esu), because the present α–PbO films have the much lower refractive index (2.13) compared to single crystal (~2.6 after JCPDS–FILE 5–0561). The $\chi^{(3)}$ value corrected using the following equation given in Chapter 1 turn out to be ~2.7×10^{-11} esu, which is in reasonable accordance with Vogel's data.

$$\chi^{(3)}_{dense} = \chi^{(3)}_{porous}\left(\frac{100}{100-p}\right)^4\ (esu)\ . \qquad (4\text{–a})$$

and

Table 1. Optical properties of α–PbO thin films.

Compound	$n_{3\omega}$	n_ω	$T_{3\omega}$ / %	T_ω / %	E_0 / eV	E_d / eV	E_g / eV	$\frac{I_{3\omega,film}}{I_{3\omega,SiO_2}}$	ℓ_c / μm	ℓ / μm	$\chi^{(3)}$ / esu
α–PbO	2.13	1.92	71.2	93.0	3.8	9.9	3.0	0.32	1.5	0.10	3.8×10^{-12}

The physical meanings of all the notations in the table are described in the section 3.
Transmittance of α–PbO is value for thin films without additional SiO_2 coating.

$$p = \left(1 - \frac{n_p^2 - 1}{n_s^2 - 1}\right) \times 100\ (\%)\ , \qquad (4\text{–b})$$

Since refractive indices at arbitrary wavelengths of α–PbO is not known, $\chi^{(3)}$ value for porous α–PbO films will be used in the following discussion.

4. Discussion

4.1 Relation between $\chi^{(3)}$ and Refractive Index, n

One can roughly predict $\chi^{(3)}$ of a material from refractive index, n, based on Miller's rule [10, 11]

$$\chi^{(3)} = [\chi^{(1)}]^4 \times 10^{-10}\ (esu)\ , \qquad (5\text{–a})$$

and

$$\chi^{(1)} = \frac{n^2 - 1}{4\pi}\ . \qquad (5\text{–b})$$

The $\chi^{(3)}$ value of 2.1×10^{-13} esu, which is predicted by Miller's rule for α–PbO thin films, as in the second row of Table 2, is inconsistent with the measured one, 3.8×10^{-12} esu, as in the first row.

Figure 6 shows a relation between $\chi^{(3)}$ and refractive index, n_ω, at 1900 nm for α–PbO thin films together with other NLO materials reported so far [8, 9, 12–17]. It is found that the α–PbO is one of the inorganic materials with much larger $\chi^{(3)}$ values than expected from Miller's rule. Inorganic materials with the high refractive index tend to exhibit high $\chi^{(3)}$ while $\chi^{(3)}$ of organic polymers such as polydiacetylene (PDA) [15] and poly(2,5–dimethoxy *p*–phenylene vinylene) (MO–PPV) [16] deviates from Miller's rule

Table 2. Comparison of the measured $\chi^{(3)}$ with the calculated $\chi^{(3)}$ for α–PbO thin films on the basis of three models.

	$\chi^{(3)}$ / esu
	α–PbO
Measured value	3.8×10^{-12}
Miller's rule	2.1×10^{-13}
Band gap model	3.4×10^{-12}
Lines' model	2.0×10^{-12}

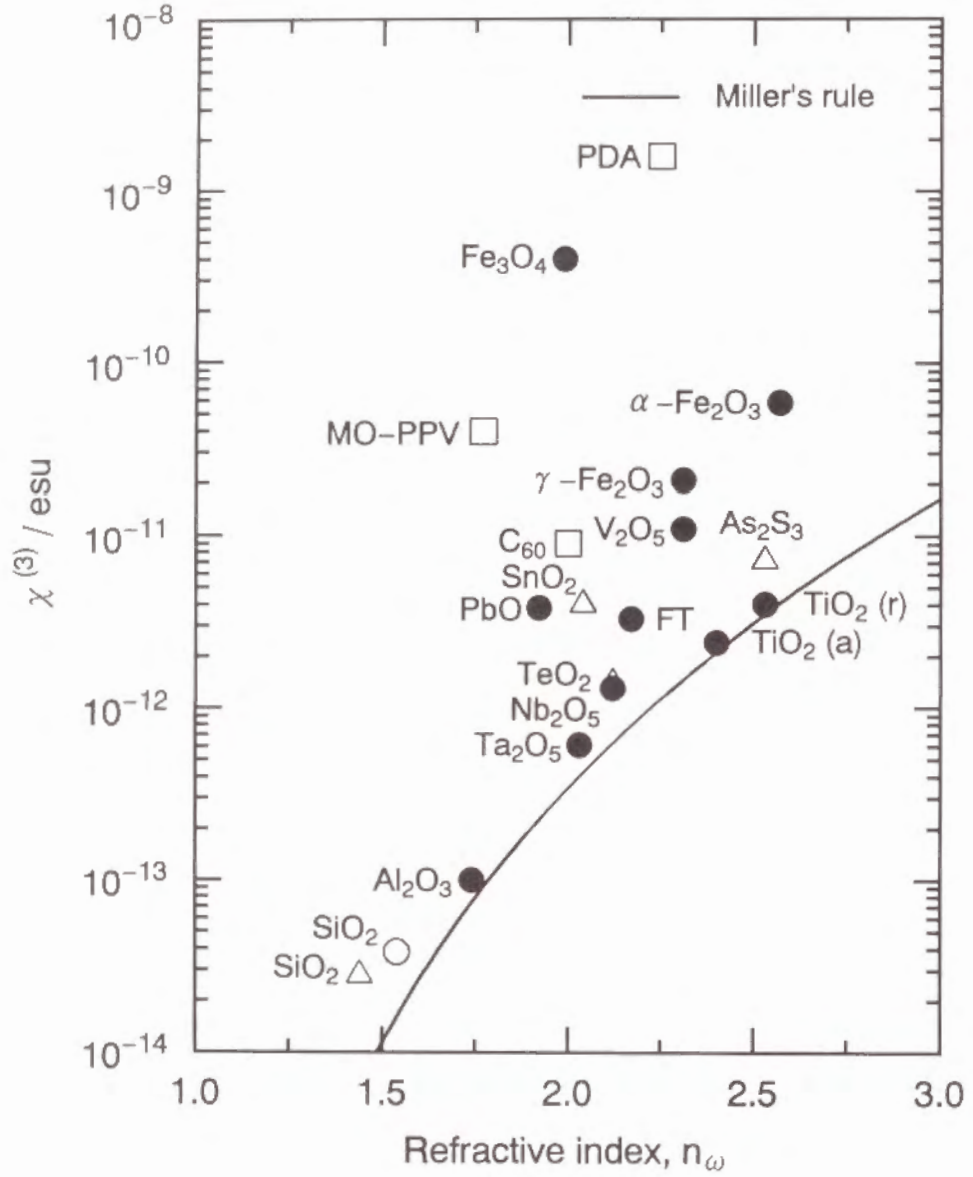

Fig. 6. Relation between $\chi^{(3)}$ and refractive index, n_ω, at 1900 nm for α–PbO thin films together with other NLO materials. Circles, triangles and squares denote inorganic crystals, inorganic amorphous materials and organic materials, respectively. Closed circles are data measured in the present study. Letters of r and a in parentheses denote rutile and anatase, respectively. FT: $FeTiO_3$, PDA: polydiacetylene, MO–PPV: poly(2,5–dimethoxy *p*–phenylene vinylene).

to a considerable extent. The latter is due to the enhancement by the "so–called" three–photon resonance or near three–photon resonance [18].

4.2 Relation between $\chi^{(3)}$ and Optical Band Gap, E_g

An enhancement in $\chi^{(3)}(-3\omega;\omega,\omega,\omega)$ occurs when a frequency of interacting light approaches either one of one–, two– or three–photon resonance frequency according to the relation [18]

$$\chi^{(3)}(-3\omega;\omega,\omega,\omega) \propto \frac{N}{\hbar^3}\sum_{gnmn'} \rho(g)F(\omega)\Omega_{gn}\Omega_{nm}\Omega_{mn'}\Omega_{n'g}\ (esu)\ , \tag{6–a}$$

and

$$F(\omega) = \frac{1}{(E_{ng}-3\omega)(E_{mg}-2\omega)(E_{n'g}-\omega)} + \frac{1}{(E_{ng}+\omega)(E_{mg}-2\omega)(E_{n'g}-\omega)} + \frac{1}{(E_{ng}+\omega)(E_{mg}+2\omega)(E_{n'g}-\omega)} + \frac{1}{(E_{ng}+\omega)(E_{mg}+2\omega)(E_{n'g}+3\omega)}\ , \tag{6–b}$$

where $\rho(g)$, E_{ij} and Ω_{ij} are the density matrix element of fundamental state, the energy difference between states i and j in $\hbar$ (=h/2π, h: Planck's constant) unit and the transition matrix elements between states i and j, respectively. If the three–photon resonance is dominant in the THG process as in the case of optical band gap, E_g, higher than three–photon energy, $3\hbar\omega$, one can obtain the most significant term due to the three–photon resonance in Eq. (6) as follows:

$$\chi^{(3)} = \frac{A}{(E_g-1.96)(E_g-1.31)(E_g-0.65)}\ (esu)\ (E_g>1.96)\ , \tag{7}$$

where A is the phenomenological constant and a laser light of 1900 nm (0.65 eV) is used as incident beam.

Figure 7 gives a relation between $\chi^{(3)}$ and optical band gap, E_g, for α–PbO thin films together with other NLO materials shown in Fig. 6. For some organic materials, the absorption edge of exciton absorption for some materials is used instead of E_g. It is clear from Fig. 7 that $\chi^{(3)}$ of these materials increases asymptotically as the E_g approaches 1.96 eV corresponding to the three–photon energy in the present case. It is also seen that α–PbO is one of transparent inorganic oxides with the highest $\chi^{(3)}$ reported so far. This change obeys Eq. (7) as shown in the figure by a solid line when the parameter, A, takes a value of 1.4×10^{-11} as determined in Chapter 1. From Eq. (7), the $\chi^{(3)}$ value was estimated to be 3.4×10^{-12} esu for α–PbO, as in the third row of Table 2, which is in good accordance with the measured one, 3.8×10^{-12} esu, as in the first row.

4.3 Calculation of $\chi^{(3)}$ Based on Lines' Model

Recently, Lines has proposed a model dealing with the contribution of the empty *d* orbitals in addition to *sp* orbitals to the linear and nonlinear optical properties based on a bond–orbital theory as follows [14, 15]:

$$\chi^{(3)} = \frac{2.5\times10^{-12}\ell_b^2(n_\omega^2-1)f_L^3E_S^6}{3\pi[E_S^2-E^2]^4}\ (esu)\ , \tag{8}$$

where ℓ_b denotes the average bond length, $f_L=(n_\omega^2+2)/3$ the Lorentz local–field correction factor, E_S the Sellmeier gap which is in practice equal to the average oscillator energy, E_0, in Eq. (1). It is known that E_s/E_g is ~2 over a wide range of insulators and semiconductors with $E_s \geq 4$ eV. [16] From Eq. (8), one can obtain the $\chi^{(3)}$ values of 2.0×10^{-12} esu for α–PbO films as in the

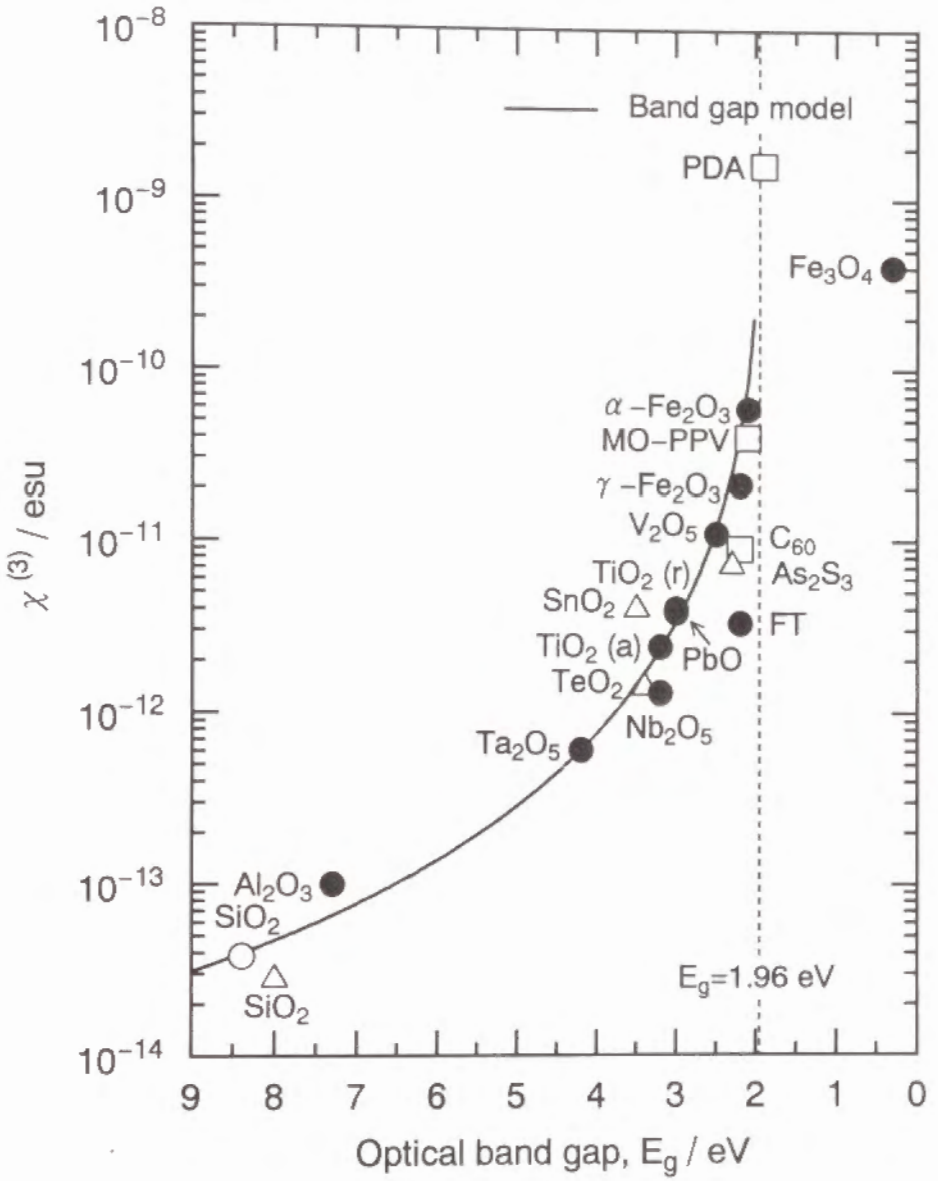

Fig. 7. Relation between $\chi^{(3)}$ and optical band gap, E_g, for α–PbO thin films together with other NLO materials. Notations are the same as in Fig. 6.

fourth row of Table 2, which is reasonable accordance with the measured one, 3.8×10^{-12} esu, as in the second row.

5. Conclusion

In this section, the third-order nonlinear optical properties of the sol-gel derived α-PbO thin films have been investigated by the THG method. As a result, the $\chi^{(3)}$ value of α-PbO thin films was 3.8×10^{-12} esu. It was found that α-PbO has high $\chi^{(3)}$ as expected from Lines' model.

References

[1] H. Nasu, T. Uchigaki, K. Kamiya, H. Kanbara and K. Kubodera, *Jpn. J. Appl. Phys.*, **31**, 3899 (1992).

[2] V. V. Dimitrov, S.-H. Kim, T. Yoko and S. Sakka, *J. Ceram. Soc. Jpn.*, **101**, 59 (1993).

[3] J. Yumoto, S. G. Lee, B. Kippelen, N. Peyghambarian, B. G. Aitken and N. F. Borrelli, *Appl. Phys. Lett.*, **63**, 2630 (1993).

[4] E. M. Vogel, M. J. Weber and D. M. Krol, *Phys. Chem. Glasses*, **32**, 231 (1991).

[5] E. M. Vogel, S. G. Kosinski, D. M. Krol, J. L. Jackel, S. R. Friberg, M. K. Oliver and J. D. Powers, *J. Non-Cryst. Solids*, **107**, 244 (1989).

[6] S. H. Wemple, *J. Chem. Phys.*, **67**, 2151 (1977).

[7] K. Kubodera and H. Kobayashi, *Mol. Cryst. Liq. Cryst.*, **182A**, 103 (1990).

[8] H. Nasu, K. Kubodera, M. Kobayashi, M. Nakamura and K. Kamiya, *J. Am. Ceram. Soc.*, **73**, 1794 (1990).

[9] G. R. Meredith, B. Buchalter and C. Hanzlik, *J. Chem. Phys.*, **78**, 1533 (1983).

[10] R. C. Miller, *Appl. Phys. Lett.*, **5**, 17 (1964).

[11] C. C. Wang, *Phys. Rev. B*, **2**, 2045 (1970).

[12] G. R. Meredith, *Phys. Rev. B*, **24**, 5522 (1981).

[13] N. Ueda, H. Kawazoe, Y. Watanabe, M. Takata, M. Yamane and K. Kubodera, *Appl. Phys. Lett.*, **59**, 502 (1991).

[14] S. H. Kim, T. Yoko and S. Sakka, *J. Am. Ceram. Soc.*, **76**, 2486 (1993).

[15] T. Kanetake, K. Ishikawa, T. Hasegawa, T. Koda, K. Takeda, M. Hasegawa, K. Kubodera and H. Kobayashi, *Appl. Phys. Lett.*, **54**, 2287 (1989).

[16] T. Kurihara, Y. Mori, T. Kaino, H. Murata, N. Takada, T. Tsutsui and S. Saito, *Chem. Phys. Lett.*, **183**, 534 (1991).

[17] J. S. Meth, H. Vanherzeele and Y. Wang, *Chem. Phys. Lett.*, **197**, 26 (1992).

[18] F. Kajzar and J. Messier, in "Nonlinear Optical Properties of Organic Molecules and Crystals, **2**", D. S. Chemla and J. Zyss, ed. by, Academic Press, New York (1987) p. 51.

[19] M. E. Lines, *Phys. Rev. B*, **43**, 11978 (1991).

[20] M. E. Lines, *Phys Rev. B*, **41**, 3383 (1990).

[21] M. E. Lines, *J. Appl. Phys.*, **69**, 6876 (1991).

SECTION 5.2 THIRD-ORDER NONLINEAR OPTICAL PROPERTIES OF $Pb(Fe_{1/2}Nb_{1/2})O_3$ AND $Pb_3Nb_4O_{13}$ THIN FILMS

1. Introduction

As easily expected from Chapter 2 oxides consisting of small transition metal cations and large non-transition metal cations may show high $\chi^{(3)}$. Pb-complex perovskites such as $Pb(Fe_{1/2}Nb_{1/2})O_3$ and $Pb(Fe_{2/3}W_{1/3})O_3$ meet the above requirements. These compounds have several interesting features as follows. (1) Simultaneous realization of high $\chi^{(3)}$ and optical transparency differing from α-Fe_2O_3 with highest $\chi^{(3)}$ and relatively low optical transparency. (2) Change in $\chi^{(3)}$ as cubic phase (paraelectricity) transforms to tetragonal phase (ferroelectricity). (3) Most of Pb-complex perovskites in tetragonal phase refer to "relaxor", which is a ferroelectric or antiferroelectric material accompanied with diffuse phase transition. Pb-complex perovskites without inversion symmetry are an important material for not only third-order NLO but also second-order NLO.

In this section, the results of the preparation of Pb-complex perovskite ($Pb(Fe_{1/2}Nb_{1/2})O_3$) thin films on SiO_2 glass substrates by the sol-gel method and the third-order nonlinear optical properties studied by the THG method are presented. The third-order nonlinear optical properties of pyrochlore $Pb_3Nb_4O_{13}$ thin films, which are often formed on preparing $Pb(Fe_{1/2}Nb_{1/2})O_3$ as an undesirable phase were also examined. Chiefly, for complex oxides such as $Pb(Fe_{1/2}Nb_{1/2})O_3$ and $Pb_3Nb_4O_{13}$ comparison of the measured $\chi^{(3)}$ measured with the theoretical $\chi^{(3)}$ calculated using second-hyperpolarizabilities, which are estimated from $\chi^{(3)}$ of single oxides treated in Chapters 1 to 5, are given.

2. Experimental

2.1 Preparation of $Pb(Fe_{1/2}Nb_{1/2})O_3$ and $Pb_3Nb_4O_{13}$ Thin Films

$Pb(Fe_{1/2}Nb_{1/2})O_3$ and $Pb_3Nb_4O_{13}$ thin films were prepared by the sol-gel method. As starting solution, $Pb(OCOCH_3)_2{\cdot}3H_2O$-$Fe(NO_3)_3{\cdot}9H_2O$-$Nb(OC_2H_5)_5$-$CH_3OCH_2CH_2OH$-$HNO_3$ and $Pb(OCOCH_3)_2{\cdot}3H_2O$-$Nb(OC_2H_5)_5$-$CH_3OCH_2CH_2OH$-$HNO_3$ solutions were selected for $Pb(Fe_{1/2}Nb_{1/2})O_3$ and $Pb_3Nb_4O_{13}$ films, respectively. The chemical compositions of the solutions were 1.2:0.5:0.5:70:0.1 and 3.6:4:220:0.3 in molar ratio. In preparing the former solution, Iron (III) nitrate enneahydrate ($Fe(NO_3)_3{\cdot}9H_2O$) and $Nb(OC_2H_5)_5$ were separately dissolved in 2-methoxyethanol ($CH_3OCH_2CH_2OH$) and $Pb(OCOCH_3)_3{\cdot}3H_2O$ was in a solution of $CH_3OCH_2CH_2OH$ and HNO_3. After stirring for 15 h these solutions were mixed together. The latter solution was prepared in the same way as the former solution. The coating solution was allowed to stand at 30 °C for 2 h prior to use.

Dip-coating was used for film formation. An SiO_2 glass substrate was immersed in the coating solution, and pulled up at a rate of 3 cm min^{-1}. The films were heated at 800 °C for 10 min immediately after each coating procedure. This cycle was repeated 4-6 times to attain the desired film thickness.

2.2 Characterization of $Pb(Fe_{1/2}Nb_{1/2})O_3$ and $Pb_3Nb_4O_{13}$ Thin Films

For reason mentioned in Chapter 1, an SiO_2 coating was further applied onto the $Pb(Fe_{1/2}Nb_{1/2})O_3$ and $Pb_3Nb_4O_{13}$ films and then the coating films on one face were removed. These films were characterized by X-ray diffraction, ellipsometry, UV-visible spectrophotometry and THG measurements as described in Chapter 1.

3. Results

3.1 Crystallization Behavior

Figure 1 shows the X-ray diffraction patterns of (a) $Pb(Fe_{1/2}Nb_{1/2})O_3$ and (b) $Pb_3Nb_4O_{13}$ thin films prepared by the sol-gel method. The crystalline phases precipitated in the sol-gel derived $Pb(Fe_{1/2}Nb_{1/2})O_3$ and $Pb_3Nb_4O_{13}$ thin films were identified referring to JCPDS-FILE 32-0522 (cubic) and 25-0443 (cubic), respectively. Preferable orientation is not seen for both films. The crystallite sizes in the $Pb(Fe_{1/2}Nb_{1/2})O_3$ and $Pb_3Nb_4O_{13}$ films were ~40 and ~30 nm, respectively.

3.2 Refractive Index and Optical Transmittance

The wavelength dependencies of refractive index, n, for $Pb(Fe_{1/2}Nb_{1/2})O_3$ and $Pb_3Nb_4O_{13}$ thin films are shown in Figure 2. It is seen that the refractive indices of $Pb(Fe_{1/2}Nb_{1/2})O_3$ and $Pb_3Nb_4O_{13}$ films decrease with increasing wavelength as well known. Figure 3 presents the linear plots of $(n^2-1)^{-1}$ versus E^2 for $Pb(Fe_{1/2}Nb_{1/2})O_3$ and $Pb_3Nb_4O_{13}$ thin films based on Wemple's equation [1]

$$\frac{1}{n^2-1} = \frac{E_0}{E_d} - \frac{E^2}{E_0 E_d}, \qquad (1)$$

where E, E_0 and E_d are the photon energy, the average oscillator energy and dispersion energy in eV unit, respectively. E_0 and E_d are important optical properties of materials [1]. The refractive indices were estimated as $n_{3\omega}$=2.41 at 633 nm and n_ω=2.27 at 1900 nm, and the coherence length, ℓ_c=1.9/[6 ($n_{3\omega}-n_\omega$)], was 2.2 μm for $Pb(Fe_{1/2}Nb_{1/2})O_3$ films. In a similar manner, $n_{3\omega}$, n_ω and ℓ_c for $Pb_3Nb_4O_{13}$ films were estimated as 2.27, 2.13 and 2.3 μm. The thickness of the $Pb(Fe_{1/2}Nb_{1/2})O_3$ and $Pb_3Nb_4O_{13}$ films obtained by 10 dippings

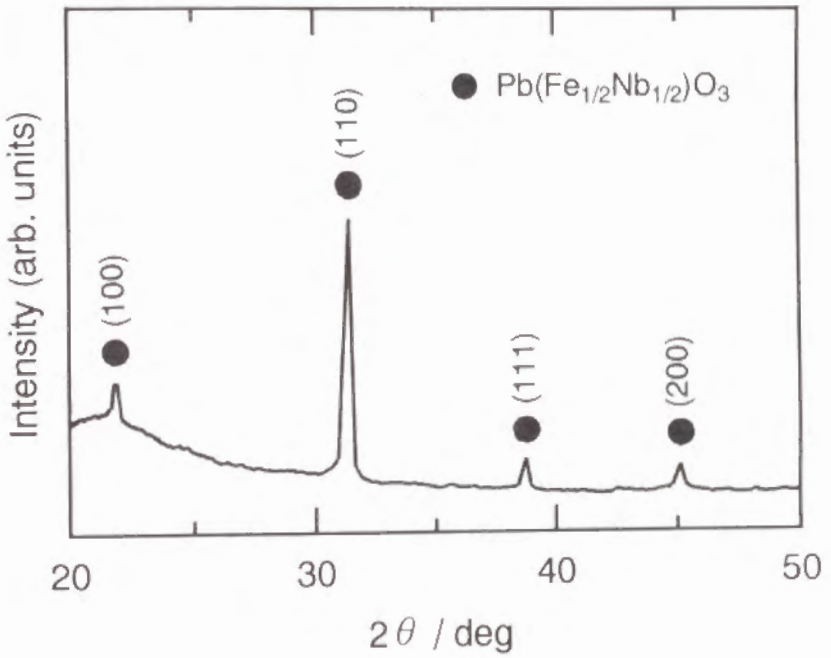

Fig. 1(a). X-ray diffraction pattern of $Pb(Fe_{1/2}Nb_{1/2})O_3$ thin films.

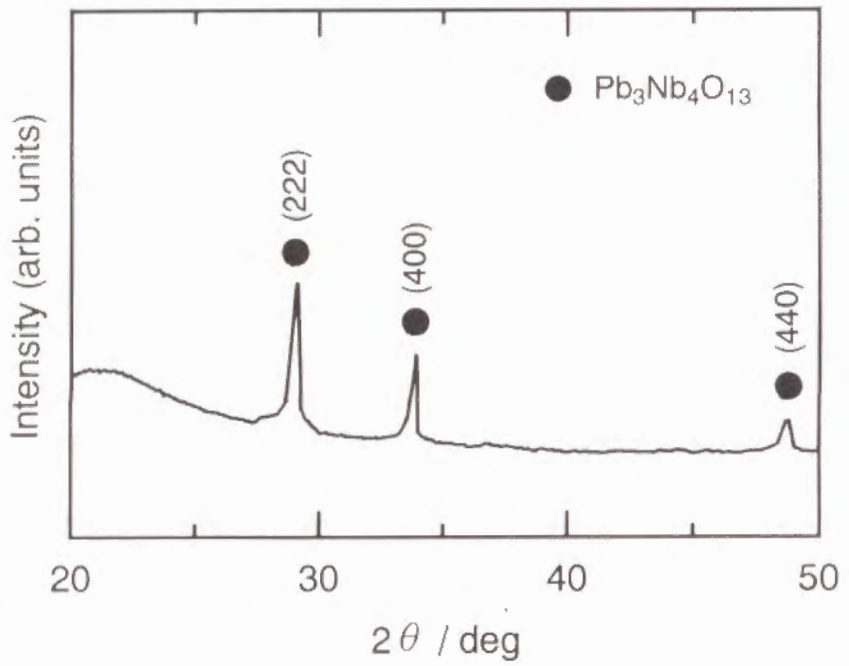

Fig. 1(b). X-ray diffraction pattern of $Pb_3Nb_4O_{13}$ thin films.

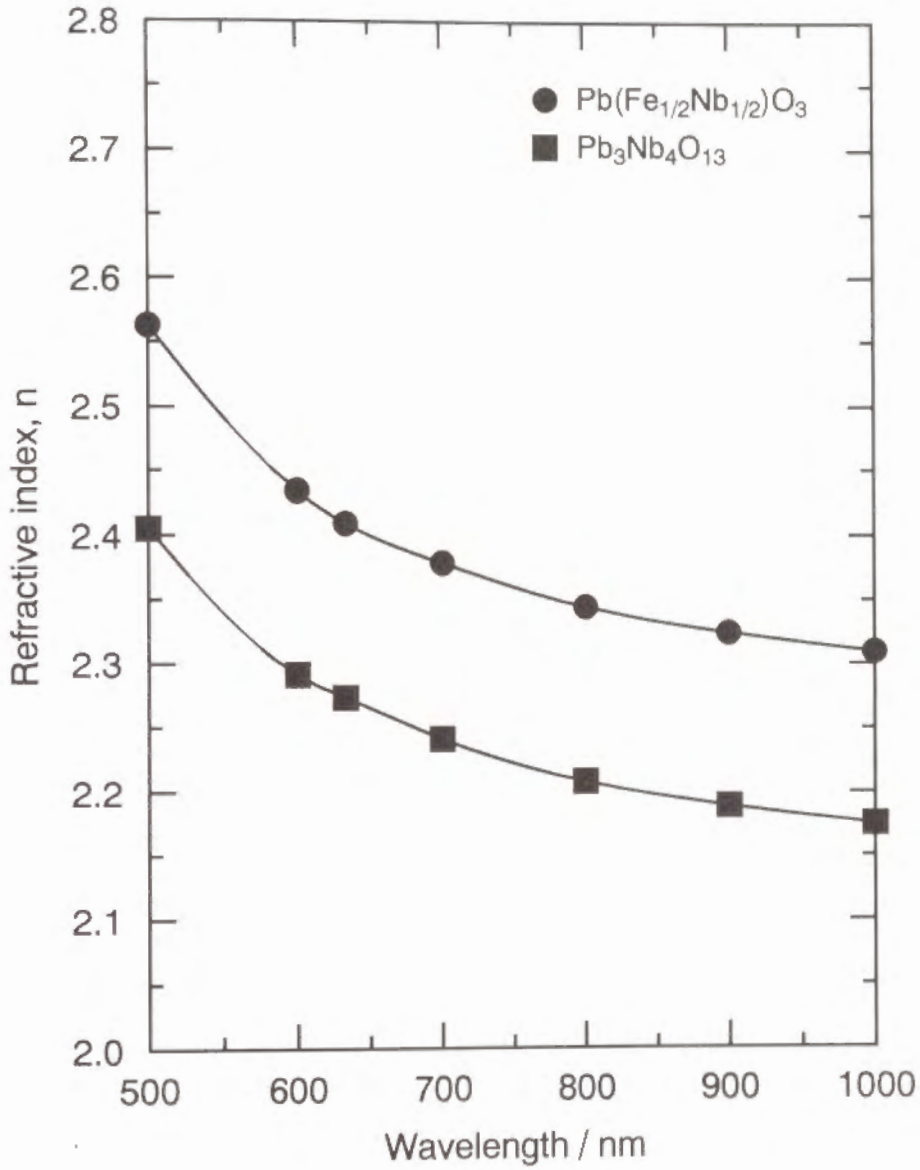

Fig. 2. Wavelength dependencies of refractive index, n, for $Pb(Fe_{1/2}Nb_{1/2})O_3$ and $Pb_3Nb_4O_{13}$ thin films.

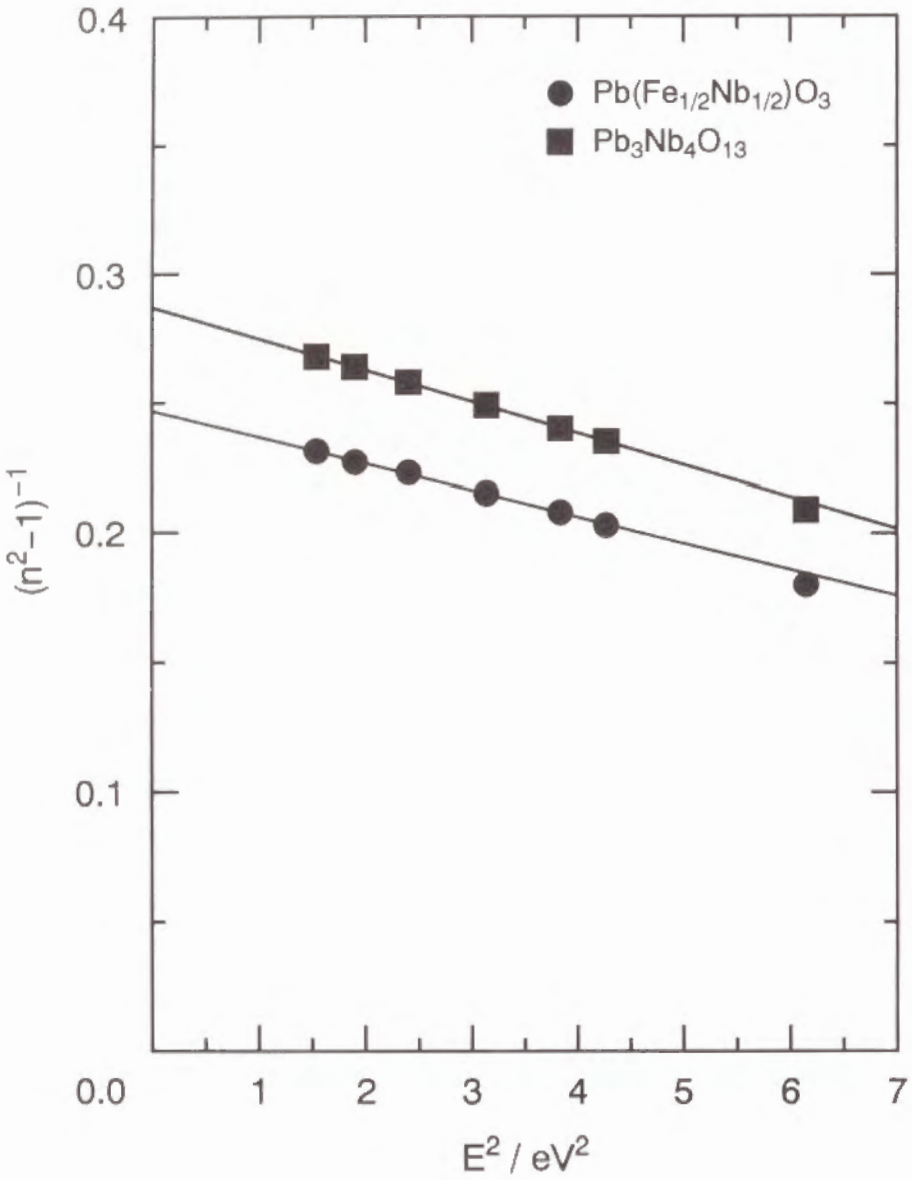

Fig. 3. Linear plots of $(n^2-1)^{-1}$ versus E^2 for $Pb(Fe_{1/2}Nb_{1/2})O_3$ and $Pb_3Nb_4O_{13}$ thin films.

was 0.19 and 0.27 μm, respectively.

Figure 4 shows the absorption spectra of $Pb(Fe_{1/2}Nb_{1/2})O_3$ and $Pb_3Nb_4O_{13}$ thin films with and without an additional SiO_2 coating. Most spectra have mountains and troughs arising from the interference of light. It is seen that the additional SiO_2 coating effectively reduces the optical loss due to reflection at the surface especially in the wavelength region above ~600 nm. The optical band gaps, E_g, of $Pb(Fe_{1/2}Nb_{1/2})O_3$ and $Pb_3Nb_4O_{13}$ films were estimated to be 2.6 and 3.1 eV, respectively.

3.3 Evaluation of $\chi^{(3)}$ Values

The THG intensities as a function o the rotation angle for (a) $Pb(Fe_{1/2}Nb_{1/2})O_3$ films, (b) $Pb_3Nb_4O_{13}$ films and (c) SiO_2 glass are given in Figure 5. The THG intensity patterns of $Pb(Fe_{1/2}Nb_{1/2})O_3$ and $Pb_3Nb_4O_{13}$ films clearly show the interference between the THG lights from $Pb(Fe_{1/2}Nb_{1/2})O_3$ (or $Pb_3Nb_4O_{13}$) films and SiO_2 glass substrate as previously reported [2]. The THG intensity was obtained by the least squares method as solid curve in Fig. 5.

In the present study, $\chi^{(3)}$ was determined by the equation [3]

$$\chi^{(3)}_{film} = \frac{2}{\pi}\chi^{(3)}_{SiO_2}\frac{l_{c,\,SiO_2}}{l}\sqrt{\frac{I_{3\omega,\,film}}{I_{3\omega,\,SiO_2}}}\sqrt{\frac{n^3_{\omega,\,film}n_{3\omega,\,film}T^3_{\omega,\,SiO_2}T_{3\omega,\,SiO_2}}{n^3_{\omega,\,SiO_2}n_{3\omega,\,SiO_2}T^3_{\omega,\,film}T_{3\omega,\,film}}}\ (esu)\ , \qquad (2)$$

where I denotes the THG peak intensity. The film thickness is used for ℓ, because the film thickness is less than the coherence length. The values of $\chi^{(3)}{}_{SiO_2}=2.8\times10^{-14}$ esu and $\ell_{c,SiO_2}=18.1$ μm were used for SiO_2 glass as both standard sample and substrate [4].

The intensities of THG signals generated from $Pb(Fe_{1/2}Nb_{1/2})O_3$ and $Pb_3Nb_4O_{13}$ films were determined by the equation [2]

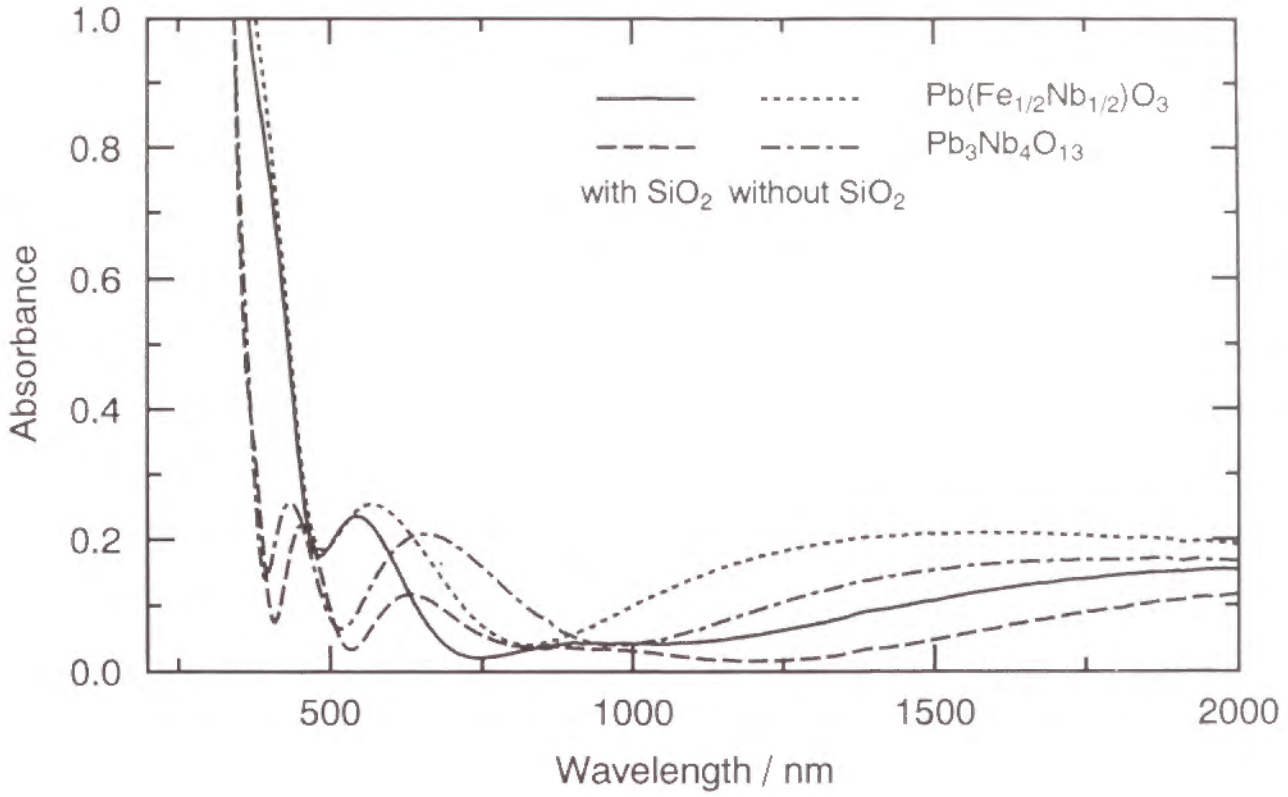

Fig. 4. Absorption spectra of $Pb(Fe_{1/2}Nb_{1/2})O_3$ and $Pb_3Nb_4O_{13}$ with and without additional SiO_2 coating.

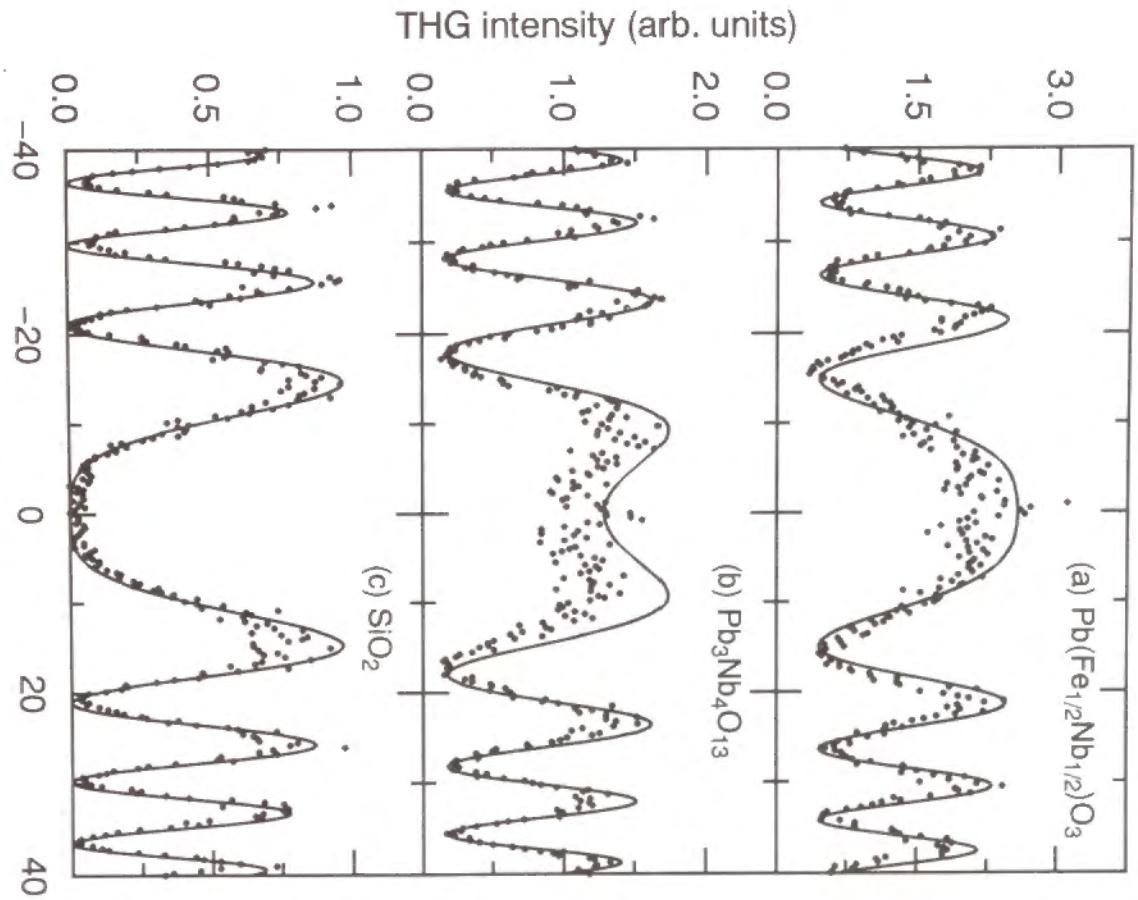

Fig. 5. THG intensities as a function of rotation angle for (a) $Pb(Fe_{1/2}Nb_{1/2})O_3$ films, (b) $Pb_3Nb_4O_{13}$ films and (b) SiO_2 glass. Solid curves are computed using the least squares method.

$$I_{film} = \frac{I_{max}+I_{min}}{2} - \frac{I_{substrate}}{2} = \frac{I_{max}+I_{min}}{2} - \frac{I_{SiO_2}}{2} , \quad (3)$$

where I_{max} and I_{min} are the upper and lower envelopes, respectively, of the superimposed THG intensity pattern. The THG from the additional SiO_2 films on the $Pb(Fe_{1/2}Nb_{1/2})O_3$ (or $Pb_3Nb_4O_{13}$) films was neglected, because $\chi^{(3)}_{SiO_2}$ itself is very small and moreover the thickness of SiO_2 coating (less than ~0.2 μm) is much smaller than the coherence length (18.1 μm). The $\chi^{(3)}$ values of $Pb(Fe_{1/2}Nb_{1/2})O_3$ and $Pb_3Nb_4O_{13}$ films were determined to be 7.4×10^{-12} and 2.8×10^{-12} esu, respectively. Table 1 summarizes the obtained optical properties of $Pb(Fe_{1/2}Nb_{1/2})O_3$ and $Pb_3Nb_4O_{13}$ thin films.

4. Discussion

4.1 Relation between $\chi^{(3)}$ and Refractive Index, n

It is possible to estimate $\chi^{(3)}$ of a material from refractive index, n, according to Miller's rule [5, 6]

$$\chi^{(3)} = [\chi^{(1)}]^4\times10^{-10} \ (esu) , \quad (4\text{–a})$$

and

$$\chi^{(1)} = \frac{n^2-1}{4\pi} . \quad (4\text{–b})$$

The $\chi^{(3)}$ values of 1.2×10^{-12} and 6.4×10^{-13} esu, which are predicted by Miller's rule for $Pb(Fe_{1/2}Nb_{1/2})O_3$ and $Pb_3Nb_4O_{13}$ thin films, respectively, as in the second row of Table 2, are inconsistent with the measured ones, 7.4×10^{-12} and 2.8×10^{-12} esu, as in the first row.

Table 1. Optical properties of $Pb(Fe_{1/2}Nb_{1/2})O_3$ and $Pb_3Nb_4O_{13}$ thin films.

Compound	$n_{3\omega}$	n_ω	$T_{3\omega}$ / %	T_ω / %	E_0 / eV	E_d / eV	E_g / eV	$\frac{I_{3\omega,film}}{I_{3\omega,SiO_2}}$	ℓ_c / μm	ℓ / μm	$\chi^{(3)}$ / esu
$Pb(Fe_{1/2}Nb_{1/2})O_3$	2.41	2.27	76.7	70.5	4.9	20.1	2.6	1.01	2.2	0.19	7.4×10^{-12}
$Pb_3Nb_4O_{13}$	2.27	2.13	76.2	78.0	4.9	17.0	3.1	0.47	2.3	0.27	2.8×10^{-12}

The physical meanings of all the notations in the table are described in the section 3.
Transmittances are values for $Pb(Fe_{1/2}Nb_{1/2})O_3$ and $Pb_3Nb_4O_{13}$ thin films with additional SiO_2 coating.

Table 2. Comparison of the measured $\chi^{(3)}$ with the calculated $\chi^{(3)}$ for $Pb(Fe_{1/2}Nb_{1/2})O_3$ and $Pb_3Nb_4O_{13}$ thin films on the basis of three models.

	$\chi^{(3)}$ / esu	
	$Pb(Fe_{1/2}Nb_{1/2})O_3$	$Pb_3Nb_4O_{13}$
Measured value	7.4×10^{-12}	2.8×10^{-12}
Miller's rule	1.2×10^{-12}	6.4×10^{-13}
Band gap model	8.7×10^{-12}	2.8×10^{-12}
Lines' model	2.6×10^{-12}	1.8×10^{-12}

Figure 6 shows a relation between $\chi^{(3)}$ and refractive index, n_ω, at 1900 nm for $Pb(Fe_{1/2}Nb_{1/2})O_3$ and $Pb_3Nb_4O_{13}$ thin films together with other NLO materials reported so far [3, 4, 7–12]. Inorganic materials with the high refractive index tend to exhibit high $\chi^{(3)}$ while $\chi^{(3)}$ of organic polymers such as polydiacetylene (PDA) [10] and poly(2,5-dimethoxy p-phenylene vinylene) (MO-PPV) [11] deviates from Miller's rule to a considerable extent. The latter is due to the enhancement by the "so-called" three-photon resonance or near three-photon resonance [13]. This problem will be mentioned in more details in the next section.

4.2 Relation between $\chi^{(3)}$ and Optical Band Gap, E_g

An enhancement in $\chi^{(3)}(-3\omega;\omega,\omega,\omega)$ occurs when a frequency of interacting light approaches either one of one-, two- or three-photon resonance frequency according to the relation [13]

$$\chi^{(3)}(-3\omega;\omega,\omega,\omega) \propto \frac{N}{\hbar^3}\sum_{gnmn'}\rho(g)F(\omega)\Omega_{gn}\Omega_{nm}\Omega_{mn'}\Omega_{n'g}\ (esu)\ , \tag{5-a}$$

and

$$F(\omega) = \frac{1}{(E_{ng}-3\omega)(E_{mg}-2\omega)(E_{n'g}-\omega)}+\frac{1}{(E_{ng}+\omega)(E_{mg}-2\omega)(E_{n'g}-\omega)} + \frac{1}{(E_{ng}+\omega)(E_{mg}+2\omega)(E_{n'g}-\omega)}+\frac{1}{(E_{ng}+\omega)(E_{mg}+2\omega)(E_{n'g}+3\omega)}\ , \tag{5-b}$$

where $\rho(g)$, E_{ij} and Ω_{ij} are the density matrix element of fundamental state, the energy difference between states i and j in $\hbar$ (=h/2π, h: Planck's constant) unit and the transition matrix elements between states i and j, respectively.

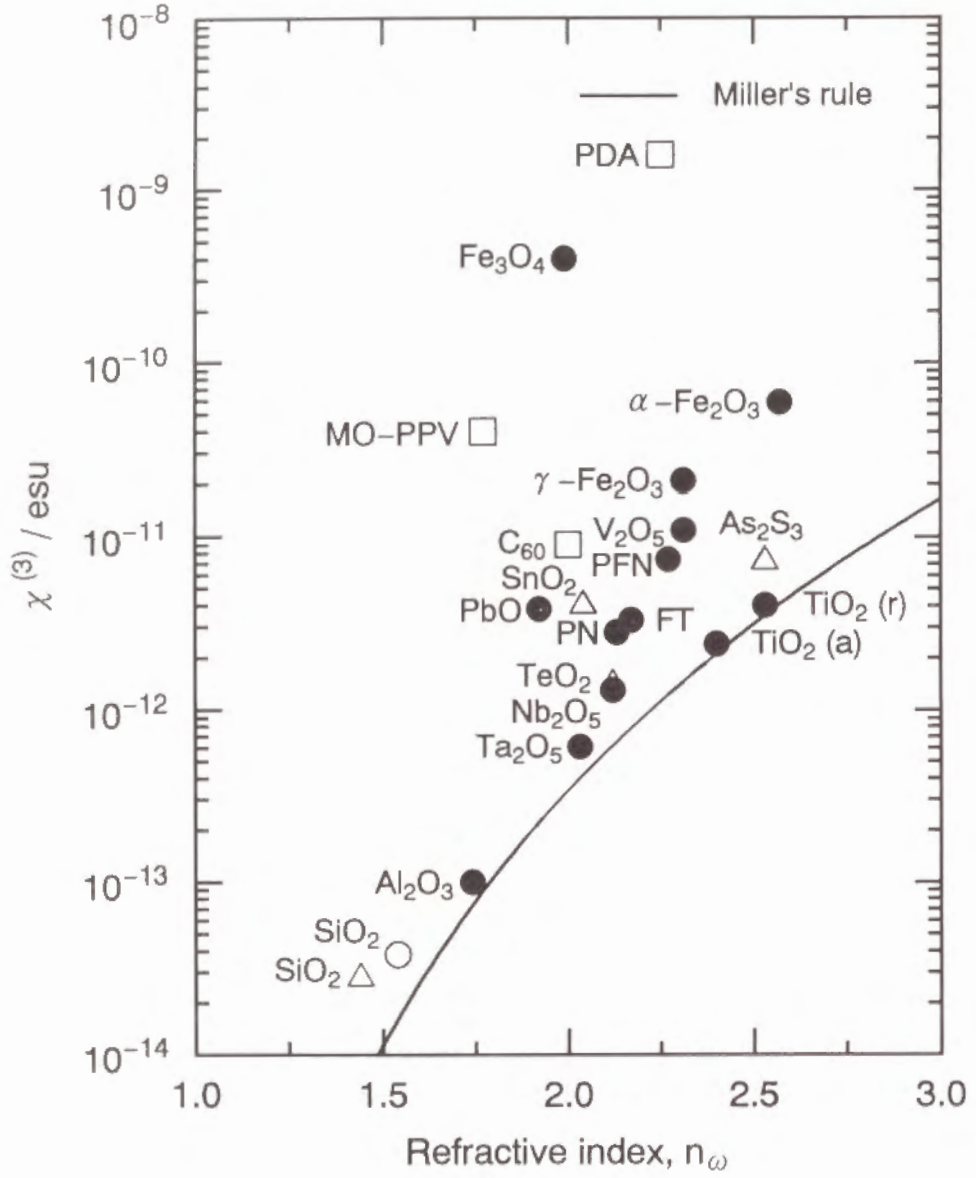

Fig. 6. Relation between $\chi^{(3)}$ and refractive index, n_ω, at 1900 nm for $Pb(Fe_{1/2}Nb_{1/2})O_3$ and $Pb_3Nb_4O_{13}$ thin films together with other NLO materials. Circles, triangles and squares denote inorganic crystals, inorganic amorphous materials and organic materials, respectively. Closed circles are data measured in the present study. Letters of r and a in parentheses denote rutile and anatase, respectively. FT: $FeTiO_3$, PFN: $Pb(Fe_{1/2}Nb_{1/2})O_3$, PN: $Pb_3Nb_4O_{13}$, PDA: polydiacetylene, MO–PPV: poly(2,5–dimethoxy *p*–phenylene vinylene).

If the three–photon resonance is dominant in the THG process as in the case of optical band gap, E_g, higher than three–photon energy, $3\hbar\omega$, one can obtain the most significant term due to the three–photon resonance in Eq. (5) as follows:

$$\chi^{(3)} = \frac{A}{(E_g-1.96)(E_g-1.31)(E_g-0.65)}\ (esu)\ \ (E_g>1.96)\ , \tag{6}$$

where A is the phenomenological constant and a laser light of 1900 nm (0.65 eV) is used as incident beam.

Figure 7 gives a relation between $\chi^{(3)}$ and optical band gap, E_g, for $Pb(Fe_{1/2}Nb_{1/2})O_3$ and $Pb_3Nb_4O_{13}$ thin films together with other NLO materials shown in Fig. 6. For some organic materials, the absorption edge of exciton absorption for some materials is used instead of E_g. It is clear from Fig. 7 that $\chi^{(3)}$ of these materials increases asymptotically as the E_g approaches 1.96 eV corresponding to the three–photon energy in the present case. This change obeys Eq. (6) as shown in the figure by a solid line when the parameter, A, takes a value of 1.4×10^{-11}. From Eq. (6), the $\chi^{(3)}$ values were estimated to be 8.7×10^{-12} and 2.8×10^{-12} esu for $Pb(Fe_{1/2}Nb_{1/2})O_3$ and $Pb_3Nb_4O_{13}$, respectively, as in the third row of Table 2, which are in good accordance with the measured ones, 7.4×10^{-12} and 2.8×10^{-12} esu, as in the first row.

4.3 Calculation of $\chi^{(3)}$ Based on Lines' Model

Recently, Lines has proposed a model dealing with the contribution of the empty *d* orbitals in addition to *sp* orbitals to the linear and nonlinear optical properties based on a bond–orbital theory as follows [14, 15]:

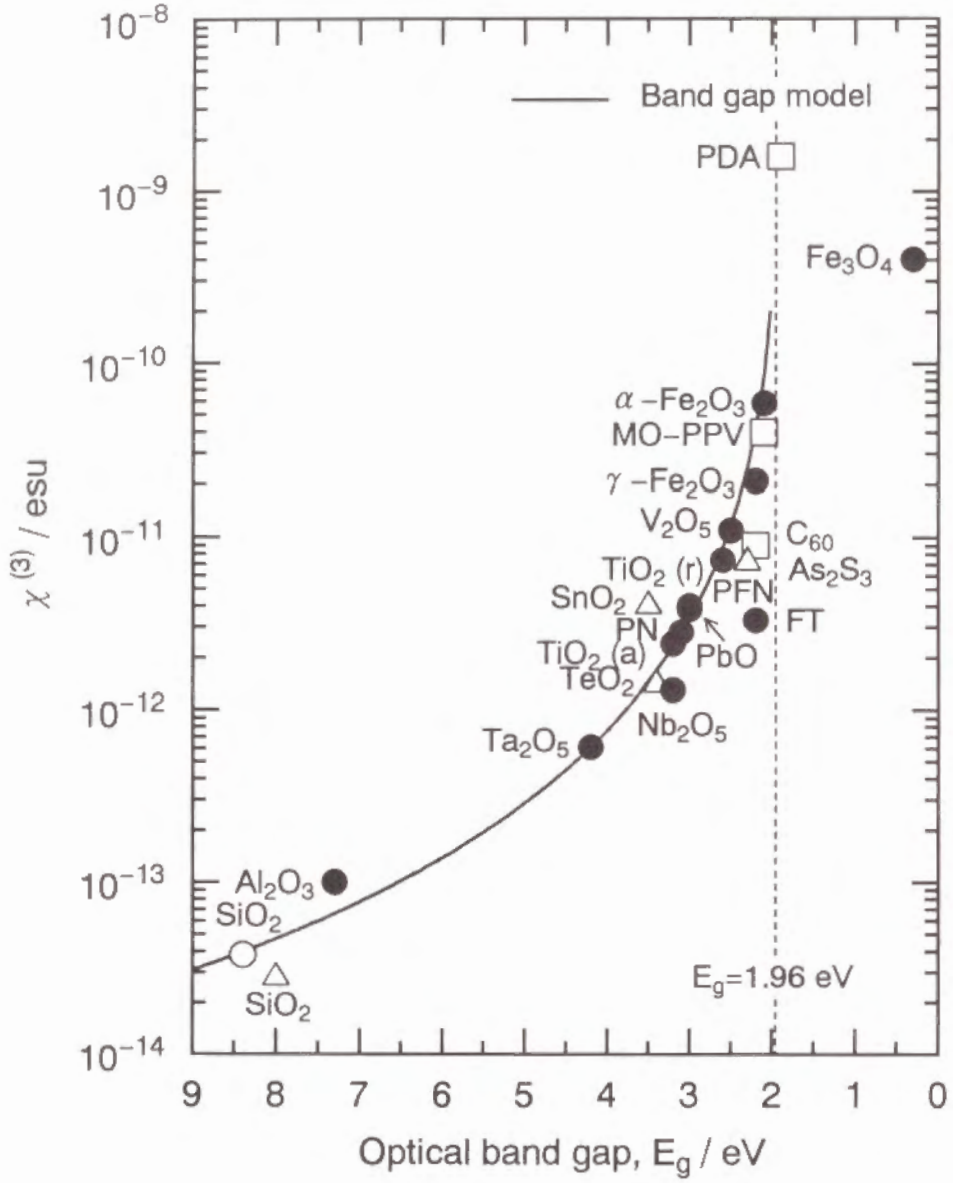

Fig. 7. Relation between $\chi^{(3)}$ and optical band gap, E_g, for $Pb(Fe_{1/2}Nb_{1/2})O_3$ and $Pb_3Nb_4O_{13}$ thin films together with other NLO materials. Notations are the same as in Fig. 6.

$$\chi^{(3)} = \frac{2.5\times10^{-12}\ell_b^2(n_\omega^2-1)f_L^3E_S^6}{3\pi[E_S^2-E^2]^4}\ (esu)\ , \tag{7}$$

where ℓ_b denotes the average bond length, $f_L=(n_\omega^2+2)/3$ the Lorentz local–field correction factor, E_S the Sellmeier gap which is in practice equal to the average oscillator energy, E_0, in Eq. (1). It is known that E_s/E_g is ~2 over a wide range of insulators and semiconductors with $E_s \geq 4$ eV. [16] From Eq. (7), one can obtain the $\chi^{(3)}$ values of 2.6×10^{-12} and 1.8×10^{-12} esu for $Pb(Fe_{1/2}Nb_{1/2})O_3$ and $Pb_3Nb_4O_{13}$ films, respectively, as in the fourth row of Table 2, which are in reasonable accordance with the measured ones, 7.4×10^{-12} and 2.8×10^{-12} esu, as in the second row. As seen for iron oxides in Chapter 3, the larger discrepancy for $Pb(Fe_{1/2}Nb_{1/2})O_3$ than for $Pb_3Nb_4O_{13}$ indicates the improper application of Lines' model to $Pb(Fe_{1/2}Nb_{1/2})O_3$ containing Fe^{3+} ions with partially occupied *d* orbitals as expected [14, 15].

4.4 Contribution of Constitutional Ions to $\chi^{(3)}$

In order to make the effect of the valence and coordination number of Fe ions on the third–order nonlinear optical properties clear, microscopic second–hyperpolarizability, γ, has to be taken into account, because macroscopic $\chi^{(3)}$ depends on both γ_i and the number density, N_i of the *i*th constituent as follows [17, 18]:

$$\chi^{(3)} = \frac{f_L^4}{24}\sum_i N_i\gamma_i\ (esu), \tag{8}$$

For a metal oxide, M_xO_y, γ per $M_{x/y}O$ formula unit, $\gamma(M_{x/y}O)$, can be derived as follows:

$$\gamma(M_{x/y}O) = \frac{1944\chi^{(3)}M_w}{N_A(n_\omega^2+2)^4 yD} \quad (esu\ cm^3), \tag{9}$$

where M_w, D and N_A are the molecular weight and density of M_xO_y and Avogadro's number, respectively. Table 3 summarizes microscopic and macroscopic nonlinear optical properties of $Pb(Fe_{1/2}Nb_{1/2})O_3$ and $Pb_3Nb_4O_{13}$ thin films together with other NLO materials.

The $\chi^{(3)}$ values of $Pb(Fe_{1/2}Nb_{1/2})O_3$ and $Pb_3Nb_4O_{13}$ were calculated using $\gamma(M_{x/y}O)$ values of α–PbO, α–Fe_2O_3 and Nb_2O_5 and α–PbO to be 1.5×10^{-11} and 3.9×10^{-12} esu, respectively. These values are in reasonable accordance with the measured ones, 7.4×10^{-12} and 2.8×10^{-12} esu, respectively. The discrepancy between the calculated and measured values may arise partly from the rough assumption that γ(PbO) values for α–PbO (4–coordinated Pb^{2+}), $Pb(Fe_{1/2}Nb_{1/2})O_3$ (12–coordinated Pb^{2+}) and $Pb_3Nb_4O_{13}$ (8–coordinated Pb^{2+}) are all the same.

5. Conclusion

In this section, the third–order nonlinear optical properties of the sol–gel derived $Pb(Fe_{1/2}Nb_{1/2})O_3$ and $Pb_3Nb_4O_{13}$ thin films have been investigated by the THG method. The following results were obtained.

(1) The $\chi^{(3)}$ values of $Pb(Fe_{1/2}Nb_{1/2})O_3$ and $Pb_3Nb_4O_{13}$ thin films were 7.4×10^{-12} and 2.8×10^{-12} esu, respectively. It was shown that oxides consisting of small transition metal cations and large non–transition metal cations show high $\chi^{(3)}$.

(2) The $\chi^{(3)}$ values of complex oxides can be estimated from the $\gamma(M_{x/y}O)$ values of the corresponding single oxides.

Table 3. Microscopic and macroscopic nonlinear optical properties of $Pb(Fe_{1/2}Nb_{1/2})O_3$ and $Pb_3Nb_4O_{13}$ thin films together with other NLO materials.

Compound	$\gamma(M_{x/y}O)$ / esu cm^3	$\chi^{(3)}$ / esu	N_i / cm^{-3}	n_ω	D / g cm^{-3}	M_w / g mol^{-1}
TiO_2 (rutile)	2.5×10^{-35}	4.0×10^{-12}	6.4×10^{22}	2.53	4.23	79.88
TiO_2 (anatase)	2.2×10^{-35}	2.4×10^{-12}	5.9×10^{22}	2.40	3.89	79.88
V_2O_5	1.4×10^{-34}	1.1×10^{-11}	5.5×10^{22}	2.31	3.32	181.88
Nb_2O_5	2.5×10^{-35}	1.3×10^{-12}	5.6×10^{22}	2.12	4.97	265.82
Ta_2O_5	1.5×10^{-35}	6.1×10^{-13}	5.7×10^{22}	2.03	8.35	441.88
α–Fe_2O_3	3.5×10^{-34}	5.8×10^{-11}	5.9×10^{22}	2.57	5.26	159.70
γ–Fe_2O_3	2.5×10^{-34}	2.1×10^{-11}	5.5×10^{22}	2.31	4.90	159.70
Fe_3O_4	1.1×10^{-32}	4.0×10^{-10}	5.4×10^{22}	1.99	5.18	231.55
$FeTiO_3$	4.8×10^{-35}	3.3×10^{-12}	6.5×10^{22}	2.17	5.50	151.73
α–PbO	2.8×10^{-34}	3.8×10^{-12}	2.5×10^{22}	1.92	9.35	223.00
$Pb(Fe_{1/2}Nb_{1/2})O_3$	1.2×10^{-34}	7.4×10^{-12}	4.6×10^{22}	2.27	8.46	329.58
$Pb_3Nb_4O_{13}$	6.7×10^{-35}	2.8×10^{-12}	4.4×10^{22}	2.13	6.78	1201.24
SiO_2 glass	4.5×10^{-36}	2.8×10^{-14}	4.4×10^{22}	1.44	2.21	60.09

References

[1] S. H. Wemple, *J. Chem. Phys.*, **67**, 2151 (1977).

[2] K. Kubodera and H. Kobayashi, *Mol. Cryst. Liq. Cryst.*, **182A**, 103 (1990).

[3] H. Nasu, K. Kubodera, M. Kobayashi, M. Nakamura and K. Kamiya, *J. Am. Ceram. Soc.*, **73**, 1794 (1990).

[4] G. R. Meredith, B. Buchalter and C. Hanzlik, *J. Chem. Phys.*, **78**, 1533 (1983).

[5] R. C. Miller, *Appl. Phys. Lett.*, **5**, 17 (1964).

[6] C. C. Wang, *Phys. Rev. B*, **2**, 2045 (1970).

[7] G. R. Meredith, *Phys. Rev. B*, **24**, 5522 (1981).

[8] N. Ueda, H. Kawazoe, Y. Watanabe, M. Takata, M. Yamane and K. Kubodera, *Appl. Phys. Lett.*, **59**, 502 (1991).

[9] S. H. Kim, T. Yoko and S. Sakka, *J. Am. Ceram. Soc.*, **76**, 2486 (1993).

[10] T. Kanetake, K. Ishikawa, T. Hasegawa, T. Koda, K. Takeda, M. Hasegawa, K. Kubodera and H. Kobayashi, *Appl. Phys. Lett.*, **54**, 2287 (1989).

[11] T. Kurihara, Y. Mori, T. Kaino, H. Murata, N. Takada, T. Tsutsui and S. Saito, *Chem. Phys. Lett.*, **183**, 534 (1991).

[12] J. S. Meth, H. Vanherzeele and Y. Wang, *Chem. Phys. Lett.*, **197**, 26 (1992).

[13] F. Kajzar and J. Messier, in "Nonlinear Optical Properties of Organic Molecules and Crystals, **2**", D. S. Chemla and J. Zyss, ed. by, Academic Press, New York (1987) p. 51.

[14] M. E. Lines, *Phys. Rev. B*, **43**, 11978 (1991).

[15] M. E. Lines, *Phys Rev. B*, **41**, 3383 (1990).

[16] M. E. Lines, *J. Appl. Phys.*, **69**, 6876 (1991).

[17] N. L. Boling, A. J. Glass and A. Owyoung, *IEEE J. Quant. Electron.*, **QE–14**, 601 (1978).

[18] R. Adair, L. L. Chase and S. A. Payne, *Phys. Rev. B*, **39**, 3337 (1989).

SUMMARY

This thesis presents the results of studies on the third-order nonlinear optical properties of transition metal oxide thin films prepared by the sol-gel method. In this study, the third-order nonlinear optical susceptibility, $\chi^{(3)}$, of the sol-gel derived simple and complex oxides containing Ti, V, Nb, Ta, Fe and Pb has been measured by the third-harmonic generation (THG) method and the results have been discussed on the basis of the linear optical properties, microscopic local structures and electronic structures of these oxides.

In Chapter 1, the third-order nonlinear optical properties of the sol-gel derived TiO_2 thin films of rutile and anatase phases have been investigated by the THG method. Chiefly, the effects of TiO_2 polymorph (rutile and anatase) and porosity on $\chi^{(3)}$ has been examined. The measured $\chi^{(3)}$ values of rutile and anatase thin films were 1.4×10^{-12} and 9.7×10^{-13} esu, respectively. The $\chi^{(3)}$ values corrected for porosity were 4.0×10^{-12} (rutile) and 2.4×10^{-12} esu (anatase), which are ~100 times as high as that of SiO_2 glass. The much higher $\chi^{(3)}$ values of both TiO_2 polymorphs compared with SiO_2 glass were ascribed to the higher refractive index and the narrower optical band gap of the former due to the significant contribution of Ti 3*d* orbital as a result of the large *p*–*d* overlapping caused by the short Ti–O bond length of 0.195–0.196 nm. The slightly higher $\chi^{(3)}$ value of rutile compared with anatase was also attributed to the higher refractive index and the narrower optical band gap of the former, which both possibly arise from the broader Ti 3*d* conduction band as a result of the formation of the straight chains of TiO_6 octahedra in rutile, as distinct from the zigzag chains of TiO_6 octahedra in anatase. Phase-matching for the THG of rutile single crystal (110) have been also examined in view of the practical application in optical devices in

Chapter 1. As a result, third-harmonic generation with a visible red light was clearly observed, indicating that TiO_2 is one of the most promising NLO materials.

In Chapter 2, the third-order nonlinear optical properties of the sol-gel derived V_2O_5, Nb_2O_5 and Ta_2O_5 thin films have been investigated by the THG method. Mainly, the effect of the local structures (metal-oxygen bond length and valence of cation) on $\chi^{(3)}$ of transition metal oxides with empty *d* orbitals have been examined in comparison with non-transition metal oxides. The $\chi^{(3)}$ values of V_2O_5, Nb_2O_5 and Ta_2O_5 thin films are 1.1×10^{-11}, 1.3×10^{-12} and 6.1×10^{-13} esu, respectively, which is in reverse relation to an increase of the average bond length in the order of V–O (ℓ_b=0.183 nm), Nb–O (ℓ_b=0.200 nm) and Ta–O (ℓ_b=0.204 nm). The above relation is also applicable to TiO_2 polymorphs ($\chi^{(3)}=4.0\times10^{-12}$ esu, ℓ_b=0.196 nm for rutile: $\chi^{(3)}=2.4\times10^{-12}$ esu, ℓ_b=0.195 nm for anatase) with the different valence of metal cation from the above metal cations. The results indicate that $\chi^{(3)}$ of these transition metal oxides with the empty *d* orbitals is dominated mainly by the metal-oxygen bond length rather than the valence of metal cation. It is predicted on the basis of Lines' model that transition metal oxides with the shortest ℓ_b have the highest $\chi^{(3)}$ while non-transition metal oxides with the longest ℓ_b do the highest $\chi^{(3)}$.

In Chapter 3, the third-order nonlinear optical properties of the sol-gel derived α–Fe_2O_3 thin films and α–Al_2O_3 single crystal $(11\bar{2}0)$ have been investigated by the THG method. Mostly, the effect of corundum isomorph on the $\chi^{(3)}$ has been examined. The $\chi^{(3)}$ value of α–Fe_2O_3 thin films was 5.8×10^{-11} esu, which is the highest value among inorganic oxides reported so far. The high nonlinearity was ascribed to the optical band gap close to three-photon energy as well as the high refractive index. The $\chi^{(3)}$ of α–Al_2O_3 single crystal was 1.0×10^{-13} esu, which nearly three orders of magnitude

lower than that for α–Fe_2O_3. It is found that the effect of corundum isomorph on the $\chi^{(3)}$ is small and the Fe element plays an important role in enhancement of the $\chi^{(3)}$. The third–order nonlinear optical properties of the sol–gel derived α–Fe_2O_3, γ–Fe_2O_3 and Fe_3O_4 thin films have been also investigated by the THG method. The $\chi^{(3)}$ values of α–Fe_2O_3, γ–Fe_2O_3 and Fe_3O_4 thin films were 5.8×10^{-11}, 2.1×10^{-11} and 4.0×10^{-10} esu, respectively, which are the highest values among inorganic oxides reported so far. $\chi^{(3)}$ of α–Fe_2O_3 and γ–Fe_2O_3 may be enhanced by the pair excitation process involving the simultaneous excitation of magnetically coupled two neighboring Fe^{3+} ions while $\chi^{(3)}$ of Fe_3O_4 by both one– and three–photon resonances. The difference in $\chi^{(3)}$ between α–Fe_2O_3 and γ–Fe_2O_3 may result from the presence of face–shared FeO_6 octahedra in α–Fe_2O_3.

In Chapter 4, the third–order nonlinear optical properties of the sol–gel derived $FeTiO_3$ thin films have been investigated by the THG method. Primarily, the effect of valence and coordination number of Fe ions on the $\chi^{(3)}$ has been examined. The $\chi^{(3)}$ value of $FeTiO_3$ thin films was 3.3×10^{-12} esu, which is comparable to those for TiO_2 polymorphs (rutile and anatase), but one order of magnitude lower than that of α–Fe_2O_3. The $\gamma(Fe^{2+}O)$ was ~4 times as large as $\gamma(Ti^{4+}_{1/2}O)$, indicating that the $\chi^{(3)}$ value of $FeTiO_3$ is governed by the $\gamma(Fe^{2+}O)$ rather than $\gamma(Ti^{4+}_{1/2}O)$. It is found from the results obtained in Chapters 3 and 4 that the higher $\gamma(Fe_{x/y}O)$ is obtained when Fe ions are 3+ rather than 2+ and octahedrally rather than tetrahedrally coordinated by oxygens. It is expected that $\gamma(Fe^{2.5+}_{4/5}O)$ under the resonant condition is extremely high.

In Chapter 5, the third–order nonlinear optical properties of the sol–gel derived α–PbO thin films have been investigated by the THG method. As a result, the $\chi^{(3)}$ value of α–PbO thin films was 3.8×10^{-12} esu. It was found that α–PbO containing large Pb^{2+} cation has high $\chi^{(3)}$ as expected from Lines'

model. The third–order nonlinear optical properties of the sol–gel derived $Pb(Fe_{1/2}Nb_{1/2})O_3$ and $Pb_3Nb_4O_{13}$ thin films have been also investigated by the THG method. The $\chi^{(3)}$ values of $Pb(Fe_{1/2}Nb_{1/2})O_3$ and $Pb_3Nb_4O_{13}$ thin films were 7.4×10^{-12} and 2.8×10^{-12} esu, respectively. It was shown that oxides consisting of small transition metal cations and large non–transition metal cations show high $\chi^{(3)}$. The $\chi^{(3)}$ values of complex oxides can be estimated from the $\gamma(M_{x/y}O)$ values from the corresponding single oxides.

In summarizing, it has been found from Lines' model that transition metal oxides with the shortest ℓ_b have the highest $\chi^{(3)}$ while non–transition metal oxides with the longest ℓ_b do the highest $\chi^{(3)}$. Lines model dealing with refractive index and Sellmeier (or optical band) gap gave better prediction of $\chi^{(3)}$ for most of materials with empty *d* orbitals than Miller's and band gap models. However, simple band gap model was superior to Lines' model for transition metal oxides with partly occupied *d* orbitals, because Lines model is applicable only to transition metal oxides with empty *d* orbitals in nature. Finally, it should be noted that calculation of $\chi^{(3)}$ using second–hyperpolarizability, γ, is very useful, because it does not require any empirical parameters in contrast to the above three models.

LIST OF PUBLICATIONS

CHAPTER 1

"Sol–Gel Preparation and Third–Order Nonlinear Optical Properties of TiO_2 Thin Films", T. Hashimoto, T. Yoko and S. Sakka, *Bull. Chem. Soc. Jpn.*, **67**, 653 (1994).

"Phase–Matching of Rutile Single Crystal", T. Hashimoto and T. Yoko, to be submitted to *Appl. Phys. Lett.*

CHAPTER 2

"Third–Order Nonlinear Optical Properties of Sol–Gel Derived V_2O_5, Nb_2O_5 and Ta_2O_5 Thin Films",T. Hashimoto and T. Yoko, *Appl. Opt.* in press.

CHAPTER 3

"Third–Order Nonlinear Optical Susceptibility of α–Fe_2O_3 Thin Film Prepared by the Sol–Gel Method", T. Hashimoto, T. Yoko and S. Sakka, *J. Ceram. Soc. Jpn.*, **101**, 64 (1993).

"Third–Order Nonlinear Optical Properties of Sol–Gel Derived α–Fe_2O_3, γ–Fe_2O_3 and Fe_3O_4 Thin Films", T. Hashimoto, T. Yamada and T. Yoko, submitted to *Phys. Rev. B*.

CHAPTER 4

"Third–Order Nonlinear Optical Properties of Sol–Gel Derived $FeTiO_3$ Thin Films", T. Hashimoto, T. Yoko and S. Sakka, *Bull. Inst. Chem. Res., Kyoto Univ.*, **71**, 420 (1994).

CHAPTER 5

"Third–Order Nonlinear Optical Properties of Pb–Complex Perovskite Thin Films Prepared by Sol–Gel Method", T. Hashimoto, K. Ishibashi and T. Yoko, to be submitted to *J. Sol–Gel Sci. Technol.*

ACKNOWLEDGMENTS

The present thesis has been carried out under the direction of Professor Toshinobu Yoko and Emeritus Professor Sumio Sakka at Division of Molecular Engineering, Graduate School of Engineering in Kyoto University.

The author wishes to express his sincere gratitude to Professor Toshinobu Yoko and Emeritus Professor Sumio Sakka for valuable and helpful guidance, suggestion and discussion throughout this thesis. The author also is indebted to Professor Satohiro Yoshida and Professor Naohiro Soga for their instructive discussion.

The author thanks Dr. Hiromitsu Kozuka and Mr. Fumiaki Miyaji for their encouragement and advice. Hearty thanks are also made to Mr. Keiji Ishibashi and Mr. Tetsuya Yamada and the students of Yoko's and Sakka's Lab. for collaboration.

Finally, the author expresses his sincere gratitude to his parents, Mr. Jiro Hashimoto and Mrs. Yoshiko Hashimoto for their continuous understanding an encouragement.

Tadanori Hashimoto